UNIVERSITÀ
DEGLI STUDI
FIRENZE

PhD in

Earth Sciences

CYCLE XXXV

Geochemistry and petrology to understand the evolution of the Stratoid and younger volcanism in Afar

Doctoral Candidate

Dr. Tortelli Gianmaria

Supervisor

Prof. Anna Gioncada

Co-Supervisor

Prof. Carolina Pagli

Prof. Derek Keir

Coordinator

Prof. Sandro Moretti

Years 2019/2022

Tables of content

Abstract

In rift settings, magmatism and tectonics play a key role during continental breakup leading to oceanic spreading. A control by mantle plumes is commonly invoked for the flood basalt volcanism taking place during rifting. However, given the possible mixing of melts derived from different mantle reservoirs and the spatial and temporal variability of the magmatic activity in rift setting, depicting the nature and variation of the magmatism in the rifting cycle is challenging. Furthermore, the transition from widespread continental flood basalt to localized rift volcanism during rift migration and localization is still a matter of debate. The Afar depression (Ethiopia) is a rift-rift-rift triple junction located at the intersection of the Red Sea, Gulf of Aden and East African Rift System (EARS), where the continent-ocean transition is currently represented by the ongoing activity of the magmatic segments. It therefore represents an excellent place to study magmatism and its relation with rift evolution from continental breakup to oceanic spreading.

In my thesis I investigated the petrology of the Stratoid flood basalt and younger volcanism (4.5-0.6 Ma; i.e., the activity preceding the current magmatic segments) associated with the Red Sea branch in Afar, by means of field observations and petrographic, geochemical, isotopical and microanalytical studies. In particular I studied the characteristics of the mantle source and the reservoir/s involved during the partial melting to identify the relation between magmatic activity and the continent-ocean transition in Southern and Central Afar. I then studied the evolution of the magmatic system during the continental breakup in Central Afar. Lastly, I studied the magmatic activity close to the Afar boarded faults to investigate the development of rift segments at the margin of the depression and their relation with the silicic central volcanoes.

The systematic geochemical study carried out in this work reveals for the first time the variable petrological nature of the Stratoid Series. This work indicates that the temporal distinctions between Lower and Upper Stratoid Series (Kidane et al., 2003) is related to changes in the conditions of primitive magma genesis and also points out inner variability within the Series. Differences in garnet-compatible elements indicate a shallower melting column for the oldest and youngest products (4.5-2.6 Ma Lower Stratoid Series; 1.1-0.6 Ma Gulf Series) with respect to a deeper melting column for the products erupted at 2.6-1.1 Ma

(Upper Stratoid Series). Accordingly, the isotopic signature indicates a more depleted mantle source and a major involvement of the lithospheric component for the Lower Stratoid and Gulf Series with respect to a more plume-like mantle source for the Upper Stratoid. The geochemical study is integrated with independent geophysical and stratigraphic evidence, explaining the results with rift relocalization and focusing: the Pliocene rift phase of localized extension in Southern Afar leads to melting of the shallow mantle reservoirs and, consequently, to the observed shallow melting column for the Lower Stratoid. At 2.6 Ma the Pleistocene rift jumped to Central Afar under a less-extended lithosphere leading to a major involvement of the deep Afar plume for the Upper Stratoid. Subsequently, the stretching of the lithosphere and rift progressively focusing in Central Afar along the Tendaho graben led to the shallowing of the melting column and to the major involvement of the shallower mantle reservoirs as observed for the Afar Gulf Series.

In Central Afar the microanalytical study revealed a lower crustal, moderately zoned, melt-rich magmatic system for the Upper Stratoid with magma rising mostly directly to the surface, similar to the models of flood basalt magmatic systems. This phase was followed by the formation of several shallow silicic magma chambers of the central volcanoes and, subsequently, by the development of a lower crustal, polybaric, interconnected, crystal-rich magmatic system for the Afar Gulf. I interpreted these variations as related to an increase of the intruded material during the Afar Gulf activity and to the development of crystal mushes in the crust during rift focalization with respect to the Upper Stratoid.

List of figures

List of tables

Supplementary material

All the supplementary material can be found at the following google drive link:

https://drive.google.com/drive/folders/1Y0LmQoUyIzXf7Ew5O0yI_2_VGQBoKAb-?usp=share_link

List of supplementary figures

List of supplementary tables

Thesis organization

The thesis is composed of a total of seven chapters:

Chapter 1 - Brief introduction regarding the main thematics of this work and the geological and volcanological background of the East African rift and Afar. In chapter 1.3 the aims of my PhD are listed.

Chapter 2 - Here, all the information regarding the samples, the methodology and analytical techniques used in this work are reported.

Chapter 3 - This chapter is focused on the study of the mantle source/s and composition of the Stratoid and Afar Gulf of Central and Southern Afar (4.5-0.6 Ma) by means of major and trace elements and isotopic analyses of whole rock lavas.

Chapter 4 - This chapter is dedicated to the study of the crustal magmatic systems of the Stratoid and Afar Gulf in Central Afar (2.6-0.6 Ma) by means of textural and mineral chemistry investigations and on the major and trace element compositional profiles of plagioclase phenocrysts.

Chapter 5 - This chapter is focused on the study of the volcanological evolution of the Ma'Alalta volcanic field in the marginal area of the depression (< 0.55 Ma) by means of satellite-based mapping and relative stratigraphy reconstruction, major and trace element geochemistry, geothermobarometry and structures and seismicity analysis.

Chapter 6 - This chapter presents the discussion and interpretation of the origin of the Stratoid flood basalt. Furthermore, integrating the results and discussions of chapters 3, 4 and 5, the dynamics of the mantle source and the crustal magmatic systems during rift evolution is presented and interpreted to reconstruct the evolution of the Red Sea rift in the last 4.5 Ma in Central and Southern Afar.

Chapter 7 - In this chapter I summarize the main findings of my thesis addressing the objectives set out in the previous chapter.

PART I - Introduction to the thesis

1. Aims and study area

1.1. Introduction

The transition from continental rifting to seafloor spreading in rift systems is a key aspect of the Wilson Cycle. To understand this fundamental aspect of plate tectonics, several petrological, geological and geophysical studies, together with analog and numerical modeling, of active continental rift have been carried out (e.g., Corti 2009, 2012; Rooney, 2020a; Maestrelli 2022; Brune 2017; Wright et al., 2012). However, how rifts initiate and evolve remains a matter of debate due to the complex interaction between the extensional driving mechanisms and the inhomogeneous continental lithosphere. Extension from subduction, mantle convection or rising mantle plumes, and possibly localised by inherited weaknesses of the lithosphere, can induce lithosphere breakup (e.g., Morgan, 1972; Buck, 1986; Brune et al., 2023). After that, the geodynamic evolution of the rift is guided by a series of processes that can weaken (e.g., strain softening, magmatism production and surface processes) or strengthen (e.g., isostasy and cooling) the rifting lithosphere (Brune et al., 2023). The interplay between these processes creates complex interaction between the magmatic and tectonic activity (e.g., Corti et al., 2003), the partial melting of different mantle reservoirs (e.g., Rooney 2020a) and the migration and localization of rift segments (e.g., Wolfenden et al., 2005; Stab et al., 2016). Nevertheless, investigating these aspects is fundamental in order to understand how rift evolve and how the breakup process occur.

1.2. The Afar rift in the East Africa

East Africa and the Arabian peninsula have been splitting up along the Red Sea, Gulf of Aden and East African Rift System (EARS) since the arrival of the Eocene magmatic pulse in Southern Ethiopia (Fig. 1.1a). In the Red Sea and Gulf of Aden rifting started at ~27.5-23 Ma and ~35 Ma respectively, and continuous seafloor spreading is currently separating the Arabian peninsula from East Africa (e.g., Autin et al., 2010; d'Acremont et al., 2010; Bosworth et al., 2005; Cochran, 1983). The EARS is instead tearing apart East Africa in a zone from Ethiopia to Mozambique, through a series of diachronous continental rift segments

(e.g., Main Ethiopian Rift, Eastern Branch, Western Branch, Malawi and Okavango rifts; Fig. 1.1a).

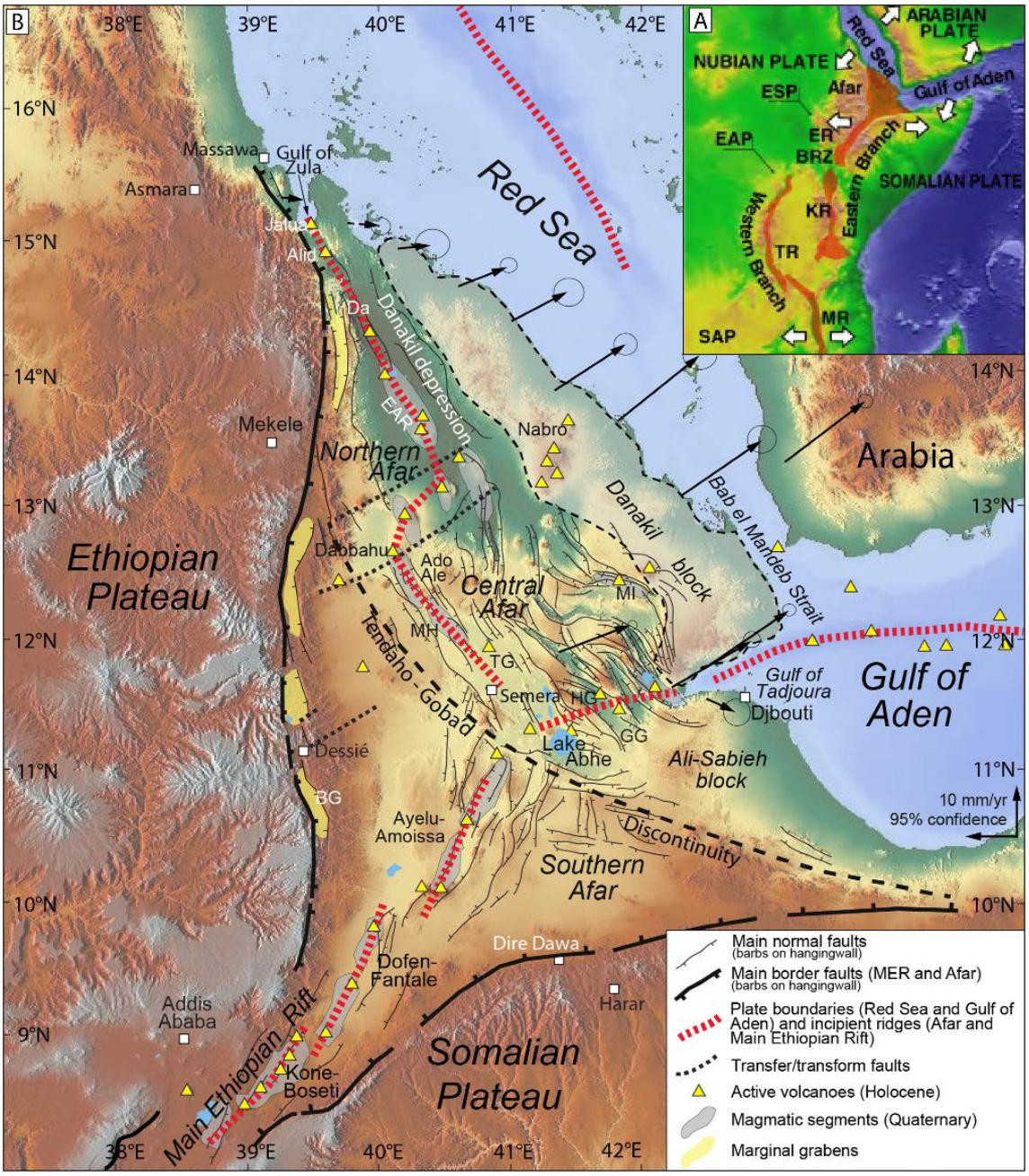

Fig. 1.1 (a) Topographic map of the East African Rift System with plate boundary, name, and spreading vector. BRZ, Broadly Rifted Zone; EAP, East African Plateau; ER, Ethiopian Rift; ESP, Ethiopian–Somalian plateaus; KR, Kenya Rift; MR, Malawi Rift; SAP, Southern African Plateau; TR, Tanganyika Rift. (b) Afar triple junction with reported faults, volcanoes, magmatic segments and GPS field velocity of the Danakil Block from Sani et al. (2017). BG, Borkena graben; Da, Dallol; EAR, Erta Ale range; GG, Gaddale graben; HG, Hanle graben; MH, Manda–Hararo; MI, Manda-Inakir rift; TG, Tendaho graben.

The Afar depression is located at the intersection of the Red Sea, Gulf of Aden and EARS, and is a rift-rift-rift triple junction created by the divergent motion of the Arabia, Somalian and

Nubian plates (Fig. 1.1b; McClusky et al., 2010; Saria et al., 2014; Vigny et al., 2006). The triple junction is subaerial, allowing to study the on-land evolution and interaction of the rifts and the associated magmatic activity (Fig. 1.1b; Corti et al., 2015a). The extension in Afar began at ~25 Ma (Stab et al., 2016; Wolfenden et al., 2005; Bosworth et al., 2005), after the arrival of the Afar mantle plume that triggered the eruption of the Ethiopian flood basalt over ~1 Myr at about 30 Ma (Ebinger et al., 1993; Eid et al., 2021; C. Hofmann et al., 1997; Kieffer et al., 2004; Marty et al., 1996; Pik et al., 1999; Steiner et al., 2022; Zumbo et al., 1995).

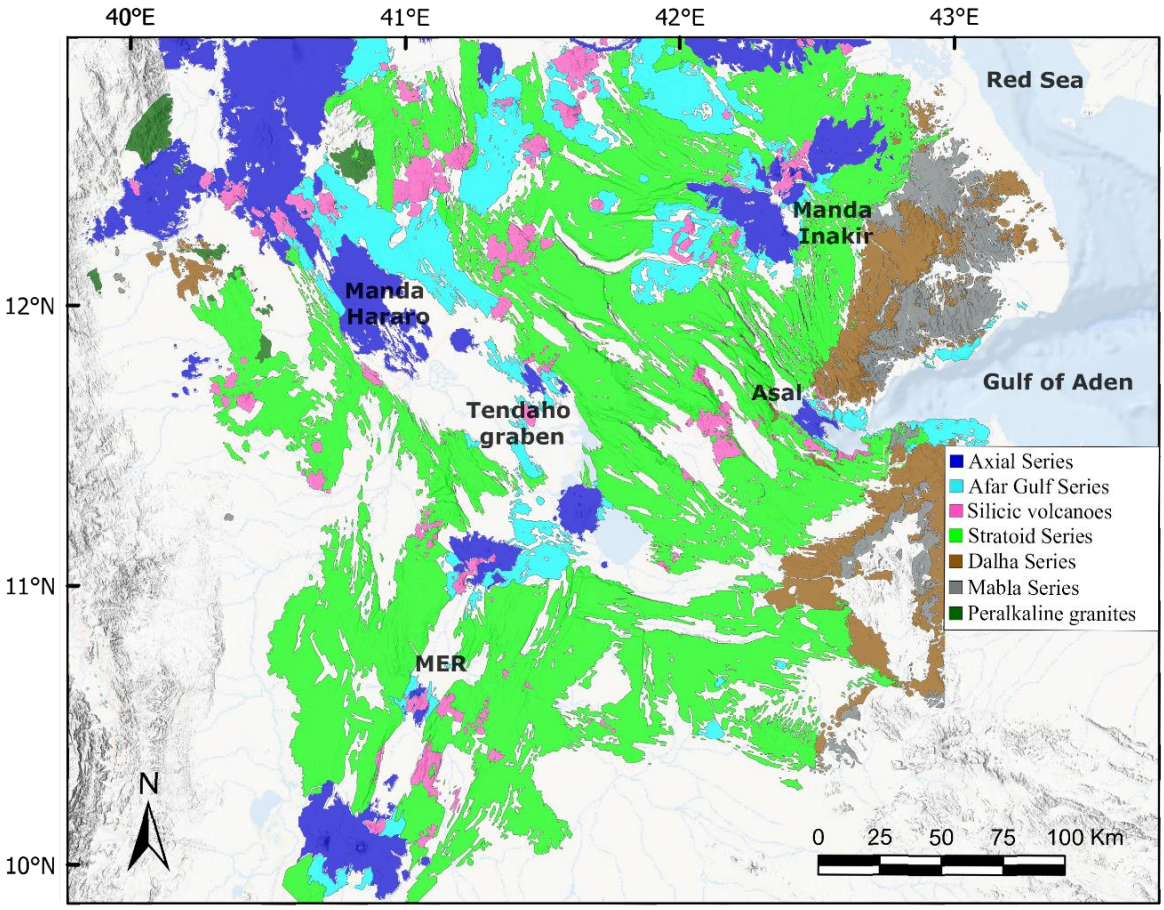

Fig. 1.2 Simplified geological map of the Afar depression (modified from Varet, 1978 and Stab et al., 2016). MER, Main Ethiopian Rift.

The magmatism associated with the formation of the rift margin (Mabla Series, 20-10 Ma) and with the development of rift marginal basins (Dalha Series, 10-3.9 Ma) is now exposed at the margins of the depression (Rooney, 2020b; Fig. 1.2). The central area of Afar is instead dominated by the Stratoid flood basalt Series (4.5-1.1 Ma, ~55,000 km^2; Barberi and Santacroce, 1980), temporally distinct in Lower (4.5-2.6 Ma) and Upper (2.6-1.1 Ma) Stratoid and, to a lesser extent, by several silicic volcanoes (around 1 Ma). Most recent products are

the mainly mafic Afar Gulf (1.1-0.6 Ma) and Axial (<0.6 Ma) Series (Fig. 1.1; Fig. 1.2), localized to rift axis. The southernmost portion of the Afar region is currently affected by the NE-SW activity of the Main Ethiopian Rift (MER) (Wolfenden et al., 2004; Bonini et al., 2005; Corti, 2009). Northern and Central Afar are mainly influenced by the interaction between the inland propagation of the Red Sea (trending NNW-SSE) and Gulf of Aden (trending ENE-WSW) rifts, marking the transition from continental rifting to oceanic spreading (Bastow and Keir, 2011; Bastow et al., 2018; Makris and Ginzburg, 1987). The continent-ocean transition is currently represented by the ongoing activity of the magmatic segments (i.e., Erta Ale and Manda Hararo for the Red Sea and Asal and Manda Inakir for the Gulf of Aden; Fig. 1.1; Fig. 1.2).

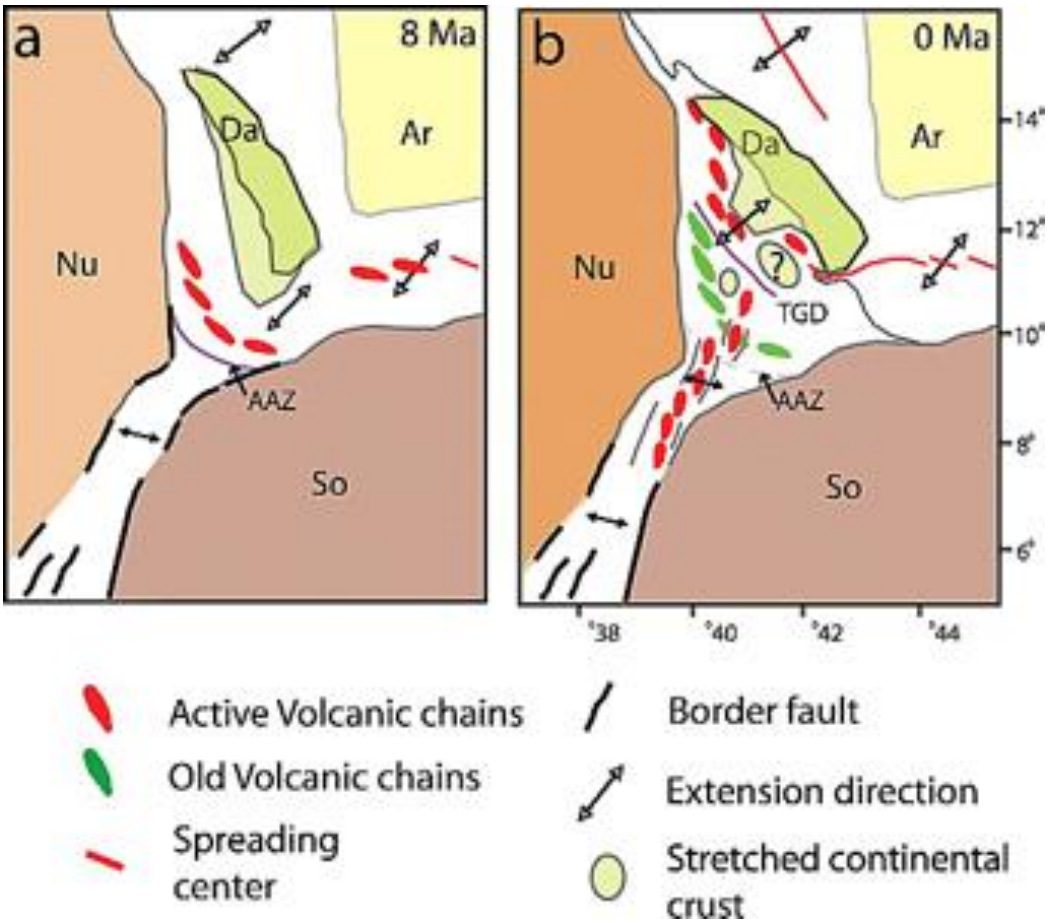

Fig. 1.3 Cartoon from Hammond et al. (2011) proposing the model of Afar depression evolution from 8 Ma (a) to present day (b). AAZ, Arcuate Accommodation Zone; TGD, Tendaho-Gob'a Discontinuity; Da, Danakil block; So, Somalia; Nu, Nubia; Ar, Arabia.

By means of tectonic reconstruction Wolfenden et al. (2005) indicate that, from 16 to 7 Ma, the Southern Red Sea branch migrated eastward, from the western border into the central areas of the depression, accompanied by a narrowing of the active zone of extension. Based

on geophysical observation on the crustal thickness, Hammond et al. (2011) suggested a migration of the Red Sea branch from South to Central Afar starting from 8 Ma (Fig. 1.3). Stab et al. (2016) used tectonic reconstruction to suggest the presence of a *wide rift* during the early Miocene, which started to localize in Central Afar at ~1 Ma. Furthermore Lahitte et al. (2003a) find a temporal relation between the silicic volcanoes and rift segment development suggesting that the silicic volcanoes are precursors of the rift development.

However, in this scenario the geological significance of the Stratoid flood basalts and their role in the rifting cycle is unclear. Furthermore, no petrological and geochemical studies constrain the mantle source evolution of the Red Sea branch nor the relation between magmatic activity and crustal modification due to rift migration and localization during continental breakup.

1.3. Objective of the study

During my PhD I focused on the recent magmatic activity (<4.5 Ma) of Central and Southern Afar and studied mainly the mafic volcanic products of the Stratoid and the younger volcanism by means of petrographic, microanalytic, geochemical and isotopic analyses. This study aims to investigate:

I) The geological and geochemical characteristics of the widespread Stratoid flood basalts in order to make an accurate and systematic description of the Series and compare it with the other volcanic phases of Afar.

II) The mantle source/s and composition of the Stratoid and younger volcanism in order to characterize the nature of their mantle reservoir/s and establish their relation with the continent-ocean transition.

III) The plumbing system and magma dynamics of the Stratoid and younger volcanism in order to explore the evolution of crustal magmatic systems during rift focusing and continental breakup.

IV) The genesis and development of post Stratoid magmatic activity at the marginal areas of Afar in order to investigate the behavior of the rift at the margins of the depression and the role of silicic central volcanoes in rift propagation.

V) The results of the petrological studies conducted during my PhD, together with geophysical and stratigraphic evidence from literature, in order to reconstruct the geodynamic evolution of the on land Red Sea rift branch in Afar in the last 4.5 Ma.

Author's note: One additional objective of my PhD was also to improve the existing age dataset and constrain the geodynamic reconstruction of this work with new Ar-Ar ages that I carried out at the Natural Environment Research Council (NERC) laboratories in Scotland. Unfortunately, due to delay in the samples preparation caused by the COVID19 restrictions, this data will be available in the next few months and therefore not presented in this thesis.

PART II - Sampling and analytical techniques

2. Materials and methods

2.1. Field campaign and UniPi Afar repository

A field campaign was carried out during February 2020 aimed at the sampling of Stratoid and Gulf Series in Central and Southern Afar (Fig. 2.1). The campaign was planned in order to cover the largest portion of the Stratoid and Gulf area. During the fieldtrip we collected 85 samples (48 Stratoid, 8 Gulf, 9 Axial, 20 samples from silicic central volcanoes; Tab. 2.1; Tab. S2.1). A second campaign planned for 2021 and aimed to sample vertical sections of the Stratoid escarpment was canceled due to COVID19 restrictions. Therefore, to improve the sampling distribution, and for the study of the Ma'Alalta volcanic field (hereafter MVF), additional samples from the Afar Repository of the University of Pisa (https://repositories.dst.unipi.it/index.php/home-afar) have been used (Tab. 2.1; Tab. S2.1).

Fig. 2.1 Team that carried out the Afar 2020 campaign. From left to right, Tortelli Gianmaria, Anna Gioncda, Giovanna Moratti, Eleonora Braschi. Federico Sani, Giacomo Corti, Ermias Filfilu Gebru and Derek Keir (not in the photo).

These samples were collected between 1967 and 1973 during the Italian-French campaigns of the CNR and CNRS teams, and the sampling sites have been identified using the original sampling map. Furthermore, previous major element analysis of 46 samples of the Stratoid Series from Santarnecchi (1978, unpublished thesis of the University of Pisa) were included (Tab. S2.1).

With respect to the Gulf Series, I took into consideration only the lavas outcropping in the Tendaho and Immino grabens and not in the Tadjoura Gulf. Thus, in this work I name these Gulf Series lavas as Central Afar Gulf Series.

Tab. 2.1 List of Axial, Central Afar Gulf, Stratoid and Ma'Alalta volcanic field samples used in this thesis. Different analyses for each sample are marked with an "X". Bas, Basalt; Bas-And, Basaltic-andesite; And, Andesite; Tra, Trachyte; Rhy, Rhyolite. All samples signed "AF-20" has been collected during the February 2020 field campaign while the others are from the Afar Repository of the University of Pisa.

Sample	*Lat.*	*Long.*	*Petrography*	*Trace element*	*Sr-Nd-Pb isotopic ratios*	*EPMA*	*LA-ICP-MS*	*Rock type*
				Axial				
AF20-08	11.78	41.03	X	X				Bas
AF20-30	11.82	41.08						
AF20-31	11.82	41.08	X	X				Bas
AF20-32	11.83	41.05						
AF20-76	11.81	41.02	X	X	X			Bas
AF20-77	11.81	41.02						
AF20-78	11.81	41.02	X	X				Bas
AF20-01	9.88	40.52						
AF20-02a	10.29	40.73						
				Central Afar Gulf				
AF20-22	11.66	41.48	X	X	X			Bas
AF20-23	11.66	41.48	X					
AF20-25	11.65	41.54	X	X	X	X	X	Bas
AF20-29	11.59	41.42	X	X				Bas-And
AF20-46	12.27	41.15	X	X	X	X	X	Bas
AF20-64	12.14	42.03	X					
AF20-65	12.14	42.03	X	X	X			Bas
AF20-66	12.07	41.95	X	X		X		Bas
A238	11.81	41.32	X	X	X			Bas
H216	11.20	41.43	X	X		X		Bas
H307	11.58	41.43	X	X	X			Bas
				Lower Stratoid				
AF20-03	10.44	40.72	X	X	X			Bas
AF20-60a	11.44	40.77	X					
AF20-60b	11.44	40.77	X	X	X			Bas
AF20-61	11.43	40.76	X	X	X			And
AF20-62a	11.43	40.76	X	X				And
AF20-62b	11.43	40.76	X					
AF20-79	11.20	40.75	X					
AF20-80	11.13	40.76	X	X				Bas

Tab. 2.1 (continued)

Sample	Lat.	Long.	Petrography	Trace element	Sr-Nd-Pb isotopic ratios	EPMA	LA-ICP-MS	Rock type
H323	10.86	41.30	X	X				Bas
H332	10.86	41.30	X	X	X			Bas
H436	10.89	41.69	X	X	X	X		Bas
H449	10.84	41.87	X	X	X			Bas
Ma'Alalta Volcanic Field								
D170	13.04	40.15	X	X		X		Bas
D171	13.03	40.15	X					
D172	No location		X					
D173	13.04	40.15	X					
D174	13.04	40.15	X					
G35	13.08	40.17	X					
D169	13.04	40.15	X					Rhy
K32	13.16	40.08	X					
K35	13.04	40.11	X					
K37	12.99	40.12	X					
G28	13.01	40.20	X	X				Bas
G31	13.01	40.20	X					
G33	13.01	40.20	X	X				Rhy
T7	No location		X					
G27	13.01	40.21	X					
G29	13.01	40.21	X					
G34	13.01	40.19	X					
G32	13.01	40.20	X					
K39	Caldera rim		X	X		X		
G16	12.97	40.15	X	X				Bas
G17	12.96	40.15	X					
G22	12.96	40.18	X					
G23	12.96	40.17	X	X				Rhy
G24	12.97	40.17	X					
T5	No location		X					
T1	No location		X					
G2	12.94	40.25	X					
G3	12.94	40.25	X	X				Tra
G4	12.94	40.25	X					
G5	12.94	40.24	X					
G7	12.95	40.22	X					
G8	12.96	40.21	X	X		X		Bas
G9	12.96	40.21	X					
G10	12.96	40.21	X	X				Rhy

Tab. 2.1 (continued)

Sample	Lat.	Long.	Petrography	Trace element	Sr-Nd-Pb isotopic ratios	EPMA	LA-ICP-MS	Rock type
G12	12.95	40.20	X					
G14	12.95	40.20	X	X				Rhy
G15	12.95	40.21	X					
D175	12.99	40.23	X					
D177	12.99	40.22	X	X				Tra
G13	12.96	40.21	X					
G18	12.91	40.21	X	X				Rhy
G19	12.90	40.22	X					
G20	12.90	40.22	X	X		X		Bas
T4	No location		X					
				Silicic Volcanoes				
AF20-26	11.63	41.49						
AF20-27	11.60	41.48						
AF20-28	11.58	41.47						
AF20-35	12.20	41.19						
AF20-36	12.20	41.19	X					
AF20-37	12.20	41.19						
AF20-38	12.20	41.19						
AF20-39	12.20	41.19						
AF20-40	12.20	41.19						
AF20-41	12.25	41.17	X					
AF20-42	12.25	41.17	X					
AF20-43	12.30	41.12						
AF20-44	12.30	41.12						
AF20-45	12.30	41.12	X					
AF20-47	12.26	41.15						
AF20-48	12.26	41.15						
AF20-49	12.26	41.15	X					
AF20-52	12.37	41.16						
AF20-53	12.30	41.17	X					
AF20-21	11.64	41.41						
				Upper Stratoid				
AF20-04	11.68	40.97	X	X	X	X	X	Bas
AF20-05	11.68	40.97						
AF20-06	11.68	40.96	X					
AF20-07	11.68	40.96	X					
AF20-11	11.66	40.97	X					
AF20-10	11.66	40.97						
AF20-09	11.66	40.97	X	X	X			Bas

Tab. 2.1 (continued)

Sample	Lat.	Long.	Petrography	Trace element	Sr-Nd-Pb isotopic ratios	EPMA	LA-ICP-MS	Rock type
AF20-13	11.68	40.97						
AF20-14a	11.47	41.68	X					
AF20-14b	11.47	41.68	X					
AF20-14c	11.47	41.68	X	X	X			Rhy
AF20-15	11.47	41.68	X	X				Bas
AF20-16	11.47	41.68	X					
AF20-16a	11.47	41.68						
AF20-18	11.47	41.68						
AF20-19	11.47	41.68	X	X	X	X		Bas
AF20-17	11.47	41.68						
AF20-20	11.47	41.68	X	X	X			Bas
AF20-33	11.99	41.30						
AF20-34	11.99	41.30	X	X				Bas-And
AF20-50	12.26	41.15	X	X	X			Bas
AF20-51	12.37	41.16	X	X				Bas
AF20-54	11.62	40.91	X	X	X			Bas
AF20-55	11.62	40.91						
AF20-56	11.62	40.91	X					
AF20-57	11.61	40.91	X					
AF20-58	11.61	40.91						
AF20-59	11.61	40.91	X	X				Bas
AF20-63	11.90	41.72						
AF20-67	11.95	41.82	X	X	X			Bas
AF20-68	11.83	41.89	X	X				Bas
AF20-69a	11.82	41.87	X	X	X			Tra
AF20-69b	11.82	41.87	X					
AF20-70	11.82	41.87	X					
AF20-71	12.20	41.19	X	X	X			Bas
AF20-72	12.20	41.19	X	X				Bas
AF20-73	12.16	41.19						
AF20-74	12.08	41.25	X	X				Bas
AF20-75	12.04	41.26						
Z4	11.60	41.68	X	X				Bas
Z137	11.60	41.68	X	X	X			Bas
Z135	11.60	41.68	X	X	X			Bas
Z131	11.60	41.68	X	X		X	X	Bas
Z16	11.60	41.68	X	X		X		Bas

2.2. Mapping from satellite images

Due to the absence of first-hand field observations of the MVF I investigated the spatial distribution of the erupted products using satellite images. I obtained a detailed map of the different lava flows of MVF by determining the type of erupted products through petrographic observations and reconstructing the spatial distribution of the products with Landsat satellite panchromatic images. I mapped all the volcanic and tectonic features, and by draping the satellite images onto the SRTM DEM (resolution of 1 arc-second, ~30 m) I interpreted the relative stratigraphy of the volcanic deposits.

2.3. Seismicity analysis

For the MVF I studied the seismicity distribution using a combined dataset of local seismicity acquired during 2005-2013 in Afar (Fig. 2.2) in order to identify the active structural trend of the MVF. The data were collected using consecutive local seismic networks during 2005-2006 (Ebinger et al., 2008), 2007-2009 (Belachew et al., 2011) and 2011-2013 (Illsley-Kemp et al., 2018). The latter seismic network was more sensitive to earthquakes in MVF, as the closest station was ~23 km from the stratovolcano, while the minimum distance was ~50 km during the earlier networks. I used the published earthquake catalogs from the above studies and isolated all the earthquakes that occurred near the MVF between longitude 39.90E-40.35E and latitude 12.70N-13.20N, giving a total of 229 events (Fig. 2.2), of which 34 were recorded between 2005-2006, 26 during 2007-2009 and 169 in 2011-2013.

2.4. Petrography, whole rock major and trace element geochemical analyses

A total of about 150 lava samples have been investigated at the polarized light optical microscope. A selection of 111 samples, based on their petrographic characteristics and location, have been described with regard to their phenocryst abundance, mineral assemblage, and micro-texture (Tab. S2.1). The phenocrysts and micro-phenocrysts have been identified based on their size, and relation with the groundmass. The phenocryst abundance has been evaluated qualitatively by comparison with volume % estimation diagrams. Rock samples with phenocrysts less than 2% have been considered aphyric.

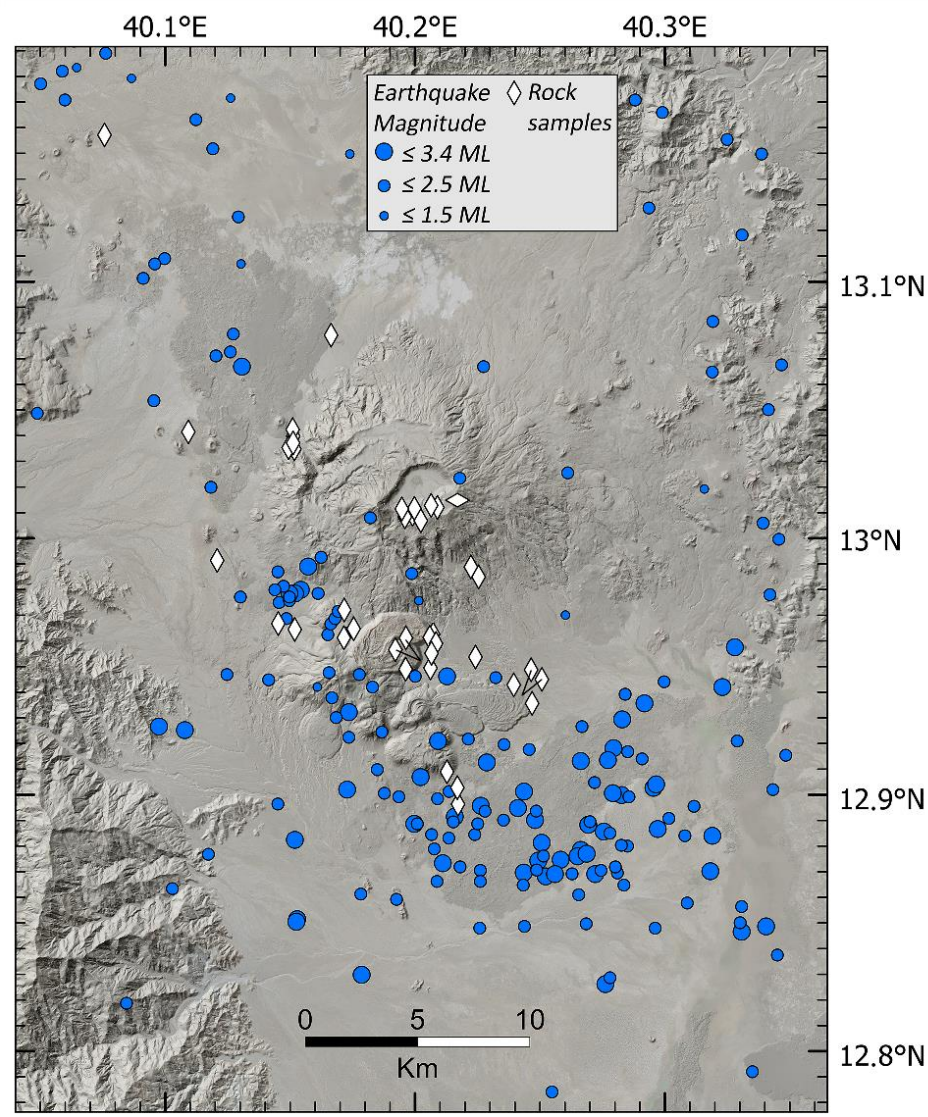

Fig. 2.2 Topography of MVF. Blue dots are the earthquakes scaled by magnitude (see text for references). White diamonds are the location of the rock samples from the Afar Repository of the University of Pisa (http://repositories.dst.unipi.it/index.php/afar-repositories). The horizontal orientated diamond is representative of sample K39, not located in the original sampling map but collected at the "Ma'Alalta volcano caldera wall" according to Barberi et al. (1974a).

Major and trace element analyses has been carried out on 60 samples (Tab. S2.1). The pulp was prepared by crushing and milling the samples in agate jars in the rock preparation laboratories of the Earth Science Department of Pisa. Major element analysis were carried by means of X-ray fluorescence spectroscopy (XRF) using the spectrometer ARL 9400 XP of the University of Pisa, Earth Sciences Department (Loss on Ignition LOI was determined at 950 °C) according to Lezzerini et al. (2013) and by means of inductively coupled plasma-optical emission spectroscopy (ICP-OES) by Activation Laboratories Ltd. (Ontario, Canada) whole rock analysis. Trace element analysis were carried out at the ICP-MS laboratories of

the Earth Sciences Department, University of Pisa. Following the procedure used at the ICP-MS laboratory for igneous rocks, 50–60 mg of each powdered sample was dissolved by means of multiple steps in a mixture of HF and HNO3 on a hot plate at ~170°C in a screw-top perfluoroalkoxy (PFA) vessel. Ultrapure Milli-Q water was used for diluting the solution. The samples were analyzed using inductively coupled plasma mass spectrometry (ICP-MS) with a PerkinElmer NexION 300X (Fig. 2.3). A procedural blank and three reference samples underwent the same procedure. The geochemical references materials used are RGM-1 (Rhyolite Glass Mountain) (Govindaraju 1994) and WS-E (Whin Sill Dolerite) (Govindaraju 1994) to verify the accuracy of the analysis and BE-N (alkali basalt) (Govindaraju 1980) to calibrate the equipment (Tab. S2.1). A solution containing 103Rh, 187Re, and 209Bi has been added to my samples, to the blank and to the reference samples, to be used as an internal standard. For some samples, trace element analysis were carried out at Activation Laboratories Ltd. (Ontario, Canada) by means of pulverization in mild steel and inductively coupled plasma mass spectrometry (ICP-MS; Tab. S2.1).

Fig. 2.3 PerkinElmer NexION 300X at the Inductively coupled plasma mass spectrometry laboratory of the Earth Science department of the University of Pisa (Italy).

2.5. Whole rock Sr-Nd-Pb isotope geochemical analysis

Sr, Nd and Pb isotopes on 25 selected samples (Tab. S2.1) were determined at the Radiogenic Isotope Laboratory of the Dipartimento di Scienze della Terra, Università degli Studi di Firenze (Italy), using the new thermal ionization Thermo-Finnigan Triton-Plus mass

spectrometer equipped with nine collectors coupled with 1011 and 1013 Ω movable amplifiers (Fig. 2.4). Samples were processed in an ultraclean laboratory environment (Class 1000) using the standard digestion technique for silicate matrices reported in Avanzinelli et al. (2005). To accommodate the suitable amount for measurements of each element (Sr, Nd and Pb) in the final sample solution a variable amount of 100-150g of powder was weighed for each sample. A previous leaching step with diluted HCl (1N) was also performed to remove possible secondary impurities. The dissolution procedure consists of sequential additions of HF–HNO_3–HCl concentrated ultrapure-quality acid to each sample placed in teflon beakers. After acid addition each beaker was sealed and placed on a hot plate up to 140 C° and finally evaporated to be diluted for sample loading in chromatographic columns for elemental selection. Prior columns loading each sample was diluted to a stock solution that was split in two different aliquots for the Sr vs Nd and Pb collection. Sr and Nd were purified and collected following standard liquid chromatographic techniques using Einchrom AGW-8X (200– 400 mesh) cation exchange resins and Ln-resin (150 mesh), respectively. The procedure included multiple additions of properly diluted HCl and HNO_3 (of suprapur quality) acids, as described in Avanzinelli et al. (2005) (Fig. 2.5).

Fig. 2.4 Thermal ionization Thermo-Finnigan Triton-Plus mass spectrometer at the Radiogenic Isotope Laboratory of the Earth Science department of the University of Firenze (Italy).

Pb have been selected separately using a specific ultra-clean Einchrom AG1-8X cation exchange resin in dedicated columns that were properly prepared at each run. The procedure included multiple additions of properly diluted HCl and HBr acids of ultrapure quality. $^{87}Sr/^{86}Sr$ were measured in dynamic mode using 10^{11} amplifiers for all masses allowing amplifier rotation during measurement. $^{143}Nd/^{144}Nd$ were measured in static mode using 10^{11} amplifiers for all the masses except for ^{147}Sm that was measured with the 10^{13} amplifier and rotation of the amplifiers during measurement. Pb isotope ratios were measured in static mode using 10^{11} amplifiers for 206, 207, 208 masses and 10^{13} amplifiers for 204. The setting of the cup configurations and amplifier are shown in Tab. S2.1.

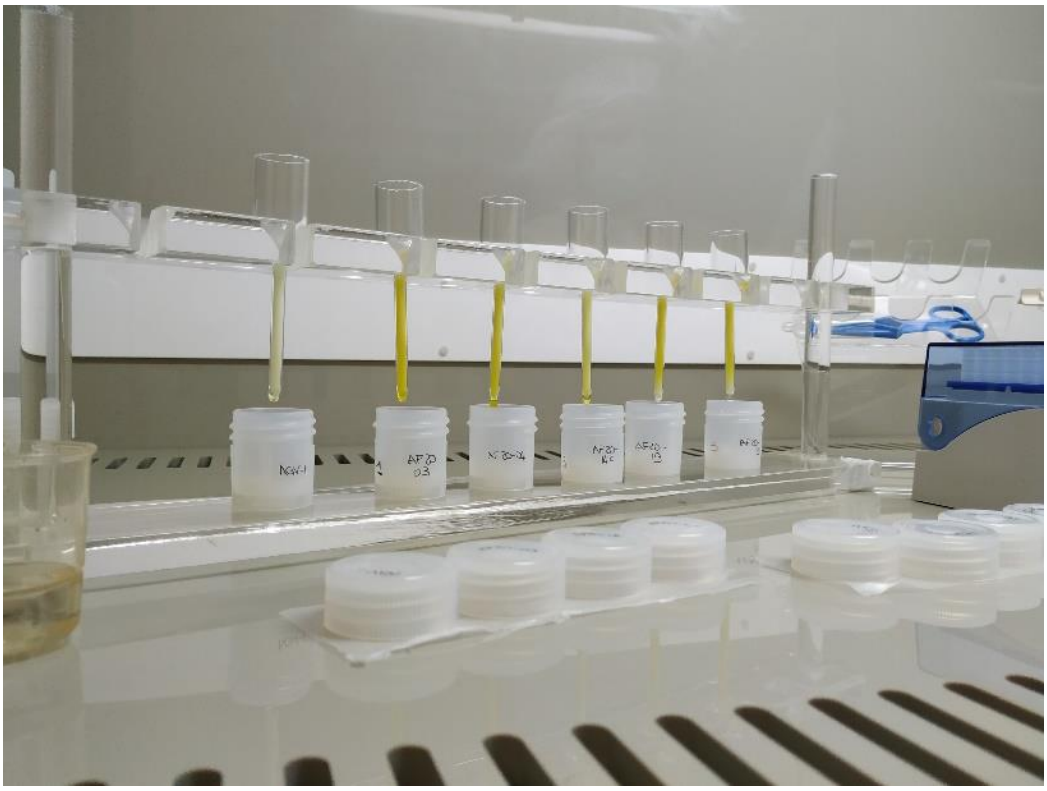

Fig. 2.5 Samples preparation by addition of diluted HCl and HNO_3 for the Sr-Nd-Pb analysis.

Mass bias was corrected using an exponential mass fractionation law and normalized to $^{86}Sr/^{88}Sr = 0.1194$ and $^{143}Nd/^{144}Nd = 0.7219$, respectively. Pb isotopes were corrected for mass bias using replicate analyses of NIST SRM 981 standard yielding within-run averages of $^{206}Pb/^{204}Pb = 16.898 \pm 0.011$, $^{207}Pb/^{204}Pb = 15.438 \pm 0.014$ and $^{208}Pb/^{204}Pb = 36.529 \pm 0.047$ (2σ, $n = 13$). An average fractionation factor of 0.130% and 0.155% per mass unit, relative to the reference values of Baker et al. (2004) and Thirlwall (2000), was applied to Pb isotope ratios depending on measurement conditions. Every single result is the average of 120, 300 and 180 measurements for Sr, Nd and Pb respectively that allow excellent precision (2SE) of

the acquired data (<10 ppm). Within run replicate measurements of international NBS987 and NBS981 and internal NdFi and international AGV-1 standards gave mean values well comparable with those reported in literature (Tab. S2.1). All uncertainty reported are 2SE (2 standard error of the mean) for single data precisions and 2SD (2 standard deviation) for standard reproducibility. The Sr and Pb analytical blank measured during this study is 120pg and 55pg respectively, which is in agreement with the blank reproducibility of the laboratory for whole rocks samples. All data were age corrected to obtain the initial isotope value, according to their ages, and uncertainty were fully propagated using a Monte Carlo simulation spreadsheet.

2.6. Mineral chemistry for major and trace elements

Polished thin sections were prepared for 15 lava samples, selected based on the presence and representativeness of phenocrysts. These samples were studied at the Center for Instrument Sharing of the University of Pisa (CISUP) laboratory by mean of scanning electron microscopy-back scattered electron imaging (SEM-BSEI) and energy dispersive X-ray spectroscopy (EDS) microanalysis with the field emission scanning electron microscope FEI Quanta 450 ESEM-FEG provided with a Bruker QUANTAX XFlash Detector 6/10 (Fig. 2.6).

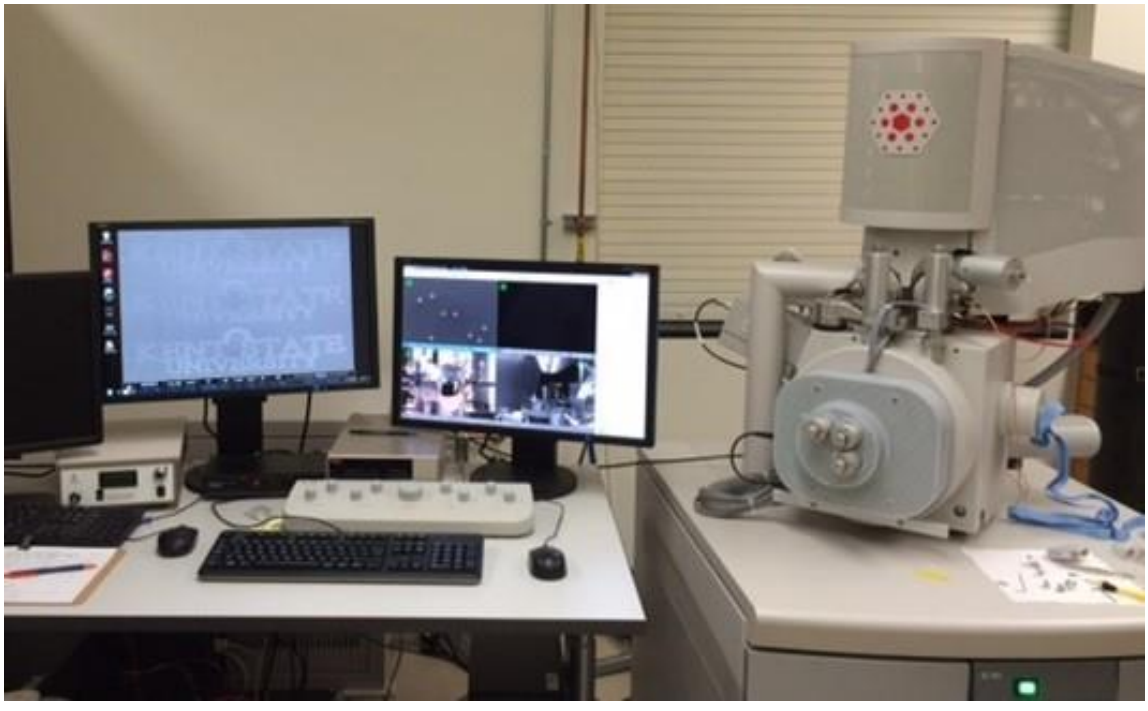

Fig. 2.6 FEI Quanta 450 ESEM-FEG at the Center for Instrument Sharing of the University of Pisa laboratory (Italy).

Based on the SEM observations, the samples were then analyzed at the CNR-IGG “Filippo Olmi'' laboratories (Department of Earth Sciences of Florence) by means of the JEOL JAX8600—EMPA device (Fig. 2.7; Tab. S2.1). The analytical conditions were 15 kV of accelerating voltage with 20 nA of beam current and 3 µm beam size for olivine, pyroxene, and oxide and 10 nA beam current and 5 µm beam size for plagioclase. The counting time is 15 s on peak and 7 s in the background for the major element (Si, Ti, Al, Fe, Mg, Ca, K) with the exception of Na where the counting time is 10 s on peak and 5 s in the background. For the minor elements (Mn, Sr, Ba) the counting time is 30-40 s on peak and 15-20 s in the background. The standards used for the calibration are Albite Astimex for Si and Na, Plagioclase Astimex for the Al, Olivine Astimex for the Mg, Diopside Asimex for the Ca, Sanidine Astimex for K, Ilmenite Smithsonian for Ti and Fe, Baryte Astimex for the Ba, Celestite Astimex for the Sr. Five samples (the MVF samples) were analyzed using the Electron Probe MicroAnalyzer (EPMA) 8200 Super Probe at the Department of Earth Sciences “Ardito Desio'' of the University of Milan. Analytical conditions for minerals were 15 kV accelerating voltage, 5 nA beam current, 3 µm beam size and counting time of 20 s on peaks and 10 s in background.

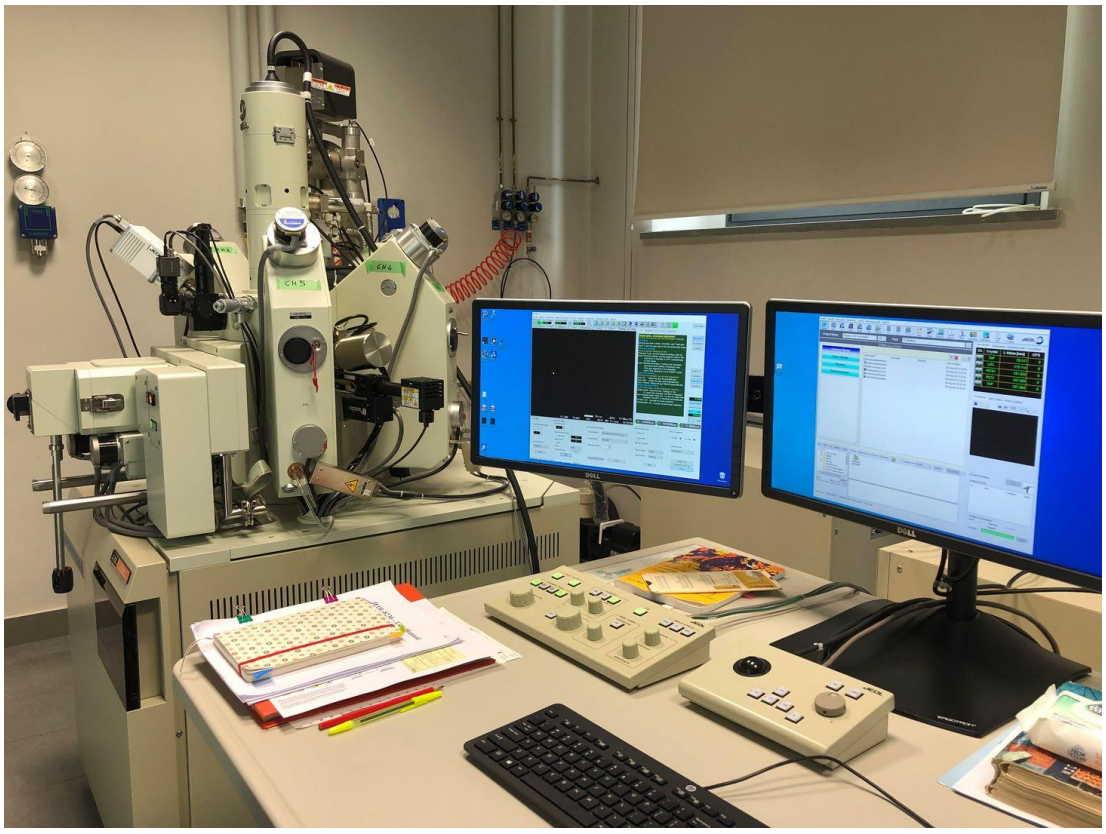

Fig. 2.7 JEOL JAX8600—Electron Probe MicroAnalyzer at the CNR-IGG “Filippo Olmi'' laboratories, Department of Earth Sciences of Florence (Italy).

In-situ trace element analysis has been performed on plagioclase phenocrysts of five samples previously analyzed by means of EPMA (Tab. S2.1). The laser ablation-ICP-MS analyses were performed using a PerkinElmer NexION 2000 ICP-MS coupled with a NWR-193 AR-F 193 nm excimer laser (Fig. 2.8) at the Center for Instrument Sharing of the University of Pisa (CISUP) in the Earth Science Department of Pisa. Ultrapure He was used as carrier gas and Ar added to improve plasma stabilization and analytical sensitivity. The ablation was performed with a spot size of 50-60 µm, fluency of 6 J cm−2, warm up time of 20 s, ablation time of 25 s and wash out time of 25 s. The NIST612 glass reference material was used as calibration standard, the data reduction was carried out with Iolite v.2.5 (Paton et al., 2011) in quantitative mode and Ca concentrations (analyzed by means EPMA) were used as internal standard. The accuracy of the analyses were performed analyzing the NIST610 reference material as a standard. Precision and accuracy of the NIST610 reference material trace elements of the sessions are reported in Tab. S2.1.

Fig. 2.8 PerkinElmer NexION 2000 ICP-MS coupled with a NWR-193 AR-F 193 nm excimer laser at the Center for Instrument Sharing of the University of Pisa (CISUP) in the Earth Science Department of Pisa (Italy).

PART III - Geochemistry, petrology and mineral chemistry of the Afar depression

3. Magma sources in Central and Southern Afar

3.1. Introduction

Magmatism in rift systems plays a key role along with tectonics in breaking up the continental lithosphere and eventual initiation of oceanic spreading (Acocella, 2014; Bosworth et al., 2005; Corti et al., 2015; Hayward and Ebinger, 1996; Manighetti et al., 1997; Stab et al., 2016; Wolfenden et al., 2005). However, ambiguity remains about the origin of one of the largest magmatic provinces associated with continental rifting, the Stratoid flood basalts in Afar, and how rifting evolved in space and time during the magma production. Both in Afar and globally, it is debated whether flood basalts associated with continental breakup are driven by the activity of a thermally anomalous mantle plume, or by plate extension and related thinning causing decompression melting (Buck, 1991; Corti et al., 2003; Farnetani and Hofmann, 2014; Frizon de Lamotte et al., 2015; Griffiths and Campbell, 1991; Koptev et al., 2016; Schmeling, 2010; Turcotte et al., 1983). Geochemical, petrological and volcanological studies are crucial to characterize the magmatism (e.g., magma source/s, magma productivity, magma storage and ascent) in order to understand the links with rift related processes.

In this chapter I target the spatial and temporal variations of the Stratoid Series erupted over Southern and Central Afar at 4.5-1.1 Ma (Barberi and Santacroce, 1980; Varet, 2018) and the following Gulf Series erupted at 2.8-0.3 Ma near the current rift axis (Kidane et al., 2003; Rooney, 2020b). These Series allow to investigate the origin of the widespread basaltic volcanism and the transition to the formation of narrow magmatic segments at the Afar Rift-Rift-Rift triple junction. In this work, I present new results of petrographic, microanalytical and geochemical analyses as well as field observations from a regional campaign in Central and Southern Afar in February 2020. Furthermore, I complement this dataset with new analyses of samples collected during the French-Italian campaigns in 1967–1973 (https://repositories.dst.unipi.it/index.php/afar-repositories). This geochemical work is based on samples that are temporally and spatially distributed over the Stratoid and the Gulf

Series and hence allow me to identify variations in the mantle source between these previously undistinguished Series.

These observations have therefore been used to better understand the origin of the Stratoid flood basalt volcanism, constrain the mantle reservoirs of the 4.5-0.6 Ma magmatism and interpret the evolution of the rift in Central and Southern Afar. My results are also compared to independent stratigraphic reconstruction of the Afar basins and crustal thickness models derived from seismic imaging, to explore links between the shifts in volcanism and tectonics.

3.2. Geological and volcanological background

At the northern end of the EARS (East African Rift System) the Red Sea, Gulf of Aden, and Main Ethiopian Rift (Fig. 3.1) intersect at the Afar depression and represent a classic example of a rift-rift-rift triple junction at the transition from continental rifting to oceanic spreading (Bastow and Keir, 2011; Bastow et al., 2018; Makris and Ginzburg, 1987). Volcanism in EARS began around 45 Ma in central and southern Ethiopia with the emplacement of the Ethiopian flood basalts and kimberlite magmas along the margins of the Tanzanian craton. During the Oligocene the flood basalt volcanism mainly emplaced over only ~1 Myr, at about 30 Ma, associated with the arrival of a mantle plume and the onset of rifting (Ebinger et al., 1993; Eid et al., 2021; Hofmann et al., 1997; Kieffer et al., 2004; Marty et al., 1996; Pik et al., 1999; Steiner et al., 2022; Zumbo et al., 1995).

Rifting in Afar is thought to have started ∼29 Ma, with tectono-magmatic reconstructions suggesting that the locus of strain of the southern Red Sea rift migrated eastward, from the western Afar border fault system toward the rift center (Wolfenden et al., 2005). This migration was associated with a progressive narrowing of the active zone of extension and magmatism until 7 Ma by which time strain was mainly accommodated through dike intrusion (Wolfenden et al., 2005). The migration of extension was not only caused by strain localization, but also due to triple junction tectonics. Using regional structural analysis, Tesfaye et al. (2003) reconstruct a ∼160 km northeast migration of the triple junction, from southernmost Afar (10°N-40°E) to the current position near Lake Abbe (11.2°N-41.8°E) in central Afar. Supporting this hypothesis, detailed stratigraphic reconstructions carried out for anthropological studies in the Woranso-Mille region and Awash valley (Fig. 3.1) reveal a northeast migration of the paleo-depocenter formation across Southern Afar during ∼10-3

Ma (Kalb, 1995) until the development of the Hadar Basin depocenter (ca. 3.8–2.9 Ma; DiMaggio et al., 2015; Wynn et al., 2008; Fig. 3.1). The sedimentary succession of the Hadar basin is topped by an angular unconformity separating it from the overlying Busidima Formation (ca. 2.7–0.15 Ma) and marking an important change in fluvial sedimentary processes in Afar (Campisano, 2012; Quade et al., 2008; Wynn et al., 2008). Wynn et al. (2008) and Campisano (2012) suggest that the changes following the Hadar Basin deposition were the response of a major tectonic reorganization in Afar.

Volcanism in Afar started at ~31-29 Ma with the eruption of the Ethiopia-Yemen flood basalt province (Baker et al., 1996; Hofmann et al., 1997). From 20 to 10 Ma the Mabla Series was emplaced, outcropping today along the Afar rift margins. The Mabla Series was dominated by the explosive silicic activity (Stab et al., 2016; Wolfenden et al., 2005). Then the Dalha Series succession (10-5.6 Ma) began with mainly silicic activity and was followed by the basaltic fissural activity of the Dalhoid Series (5.6-3.9 Ma; Rooney, 2020a). In the Pliocene starting at 4.5 Ma, the largest volcanic succession of Afar was erupted, the Stratoid Series covering an area of ~55.000 km^2 in Central and Southern Afar and reaching ~1000 m in thickness. The Stratoid are mostly made of flat lying fissural basalts, minor rhyolitic lavas and pyroclastics. The basaltic emission centres have not been identified in the field and the base of the lava succession is not exposed (Barberi and Santacroce, 1980; Varet, 2018). The Stratoid Series are dissected by graben-forming normal faults, striking NW-SE to NNW-SSE in Central Afar (Red Sea trend), while south of the Tendaho Goba'Ad Discontinuity (T.G.D., separating the E-W extension direction of the MER from the NE-SW one of the Red Sea) the faults mainly strike NNE-SSW (Main Ethiopian Rift trend) (Fig. 3.1). The precise timing of the Stratoid Series emplacements is still not well established (mainly due to the inaccessibility of some areas and uncertainties regarding their spatial and vertical distribution). Overall, the literature data indicate ages ranging from 4.5 ± 0.19 Ma to 1.25 ± 0.09 Ma (Barberi et al., 1975; Courtillot et al., 1984; Feyissa et al., 2019; Kidane et al., 2003; Kunz et al., 1975; Lahitte et al., 2003a; Zumbo et al., 1995). Acocella (2010) indicated a rejuvenation of the Stratoid Series along a direction perpendicular to the Dobi and the Tendaho graben, with ages getting younger toward the inner portions of the graben. Kidane et al. (2003) divided the Stratoid Series based on their age and morphology in Upper and Lower Stratoid Series (hereafter US and LS), respectively younger and older than 2.6 Ma. Towards the end of the Stratoid Series,

central silicic volcanoes produced effusive and pyroclastic products (Barberi and Santacroce, 1980; Lahitte et al., 2003b).

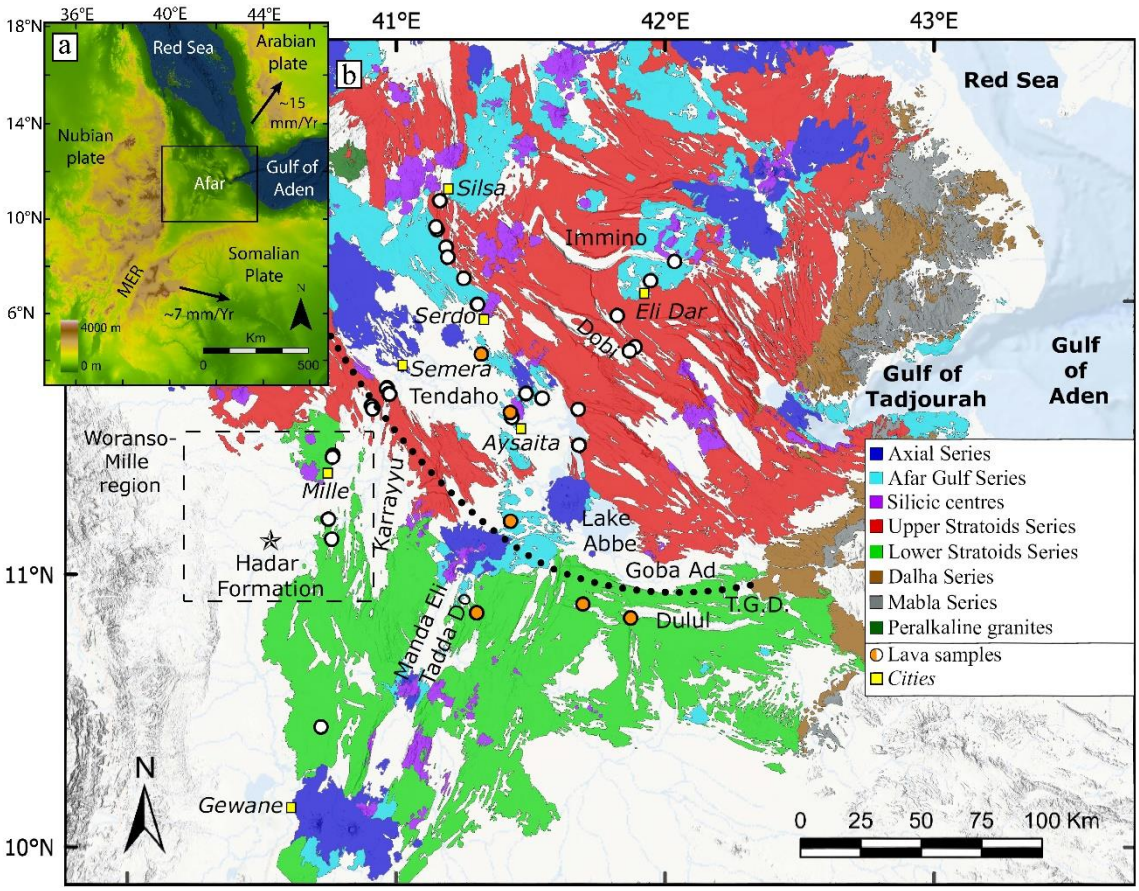

Fig. 3.1 (a) Topographic map of the East African Rift System with plate boundary, name and spreading vector with respect to Nubia fixed plate. The black box encloses the Afar depression represented in picture (b). (b) Geological map of the Afar depression modified from Varet (1978), Kidane et al. (2003) and Stab et al. (2016). Lava samples are from the 2020 campaign (white circles) and the Afar repository of the University of Pisa (orange circles). All the Afar Gulf samples in the figure are from Central Afar (i.e., Central Afara Gulf; CAG). The dashed box represents the approximate location of the Woranso-Mille region. Dotted line indicates the Tendaho Goba Ad Discontinuity (T.G.D.). Datum WGS1984, background Multi-Directional Hillshade.

After the Stratoid Series, the Gulf Series are emplaced. These were previously identified as the upper part of the Stratoid Series (Varet et al., 1978) and later distinguished based on their younger age (2.8-0.3 Ma) and the decrease in the volume of the flows with respect to the Stratoid Series (Daoud et al., 2011; Kidane et al., 2003; Lahitte et al., 2003a; Le Gall et al., 2015; Rooney, 2020a). The Gulf Series volcanism is located along the faults of the main grabens in central Afar and in the Gulf of Tadjoura (Fig. 3.1) (i.e., Tendaho-Manda Hararo, Tat'Ali, Manda Inakir). Gasse et al. (1983) and Stab et al. (2016) hypothesized that the Gulf Series are the first products associated with the progressive localization of the extension from a diffuse distribution (i.e., Stratoid Series) to a discrete distribution (i.e., magmatic

segments), starting at ~1.1 Ma in central Afar (hereafter Central Afar Gulf, CAG Series) (Kidane et al., 2003; Lahitte et al., 2003a) and at ~3 Ma in the Gulf of Tadjoura (Daoud et al., 2011; Le Gall et al., 2015). The Gulf Series products cover a much smaller area than the Stratoid lavas (Fig. 3.1).

The Stratoid and Gulf Series basalts are both originated from transitional to subalkaline magmas modified by fractional crystallisation processes with major and trace elements (e.g., REE, La_N/Sm_N and Zr/Nb) and isotopic composition ($^{143}Nd/^{144}Nd$, $^{87}Sr/^{86}Sr$, $^{206}Pb/^{204}Pb$, $^{207}Pb/^{204}Pb$ and $^{208}Pb/^{204}Pb$) that largely overlap (Barberi and Santacroce 1980; Feyissa et al., 2019; Rooney 2020a). Based on the observed geochemical patterns (Ba peak, U-Th trough, and Nb-Ta peak), isotopic compositions (Sr-Nd-Pb) and modelled patterns of primitive, depleted and lithospheric mantle partial melting, Stratoid and Gulf Series lavas have been identified as a mixture of Afar plume, depleted mantle, and African lithosphere (Rooney 2020a, 2020b; Rooney et al., 2012a, 2014, 2017; Feyissa et al., 2019). Furthermore, Rooney (2020a) recognized a group of Stratoid Series samples within the Woranso-Mille region (Fig. 3.1) and the Hayyabley basalts (near Djibouti) of the Gulf Series as lavas originated from a source extremely depleted in the most incompatible element and enriched in LILE (type VI).

Seismic imaging studies sensitive to discontinuities struggle to image the lithosphere-asthenosphere boundary (LAB) beneath Afar. However, a weak discontinuity at ~65-70 km depth has been interpreted as potentially the LAB (Lavayssiere et al., 2018). Seismic tomography beneath Afar shows slow velocity lobes of ~100-150 km length scale in the uppermost asthenosphere that are interpreted as the melt zone (Chambers et al., 2022; Gallacher et al., 2016). The slow seismic velocities are interpreted as partial melt at ~60-110 km depth (Chambers et al., 2022; Fig. 3.2), broadly consistent with the presence of a melt zone directly beneath the lithosphere. This geophysical observation is consistent with the partial melting depth derived from modelling REE compositions of young basaltic rocks in Afar (~95 km; Ferguson et al., 2013). The crust beneath most of central and southern Afar is ~25-30 km, but locally thins to ~20 km beneath the magmatic segments and beneath previous zone of strain such as the Woranso-Mille region (Ahmed et al., 2022; Hammond et al., 2011; Wang et al., 2021). Furthermore, tectonic studies and receiver function analysis (Stab et al., 2016; Wang et al., 2021) suggest presence of lower crustal intrusions/magmatic

underplating near the Moho in the Afar Depression, that could potentially play an important role in the magmatic evolution of the erupted products.

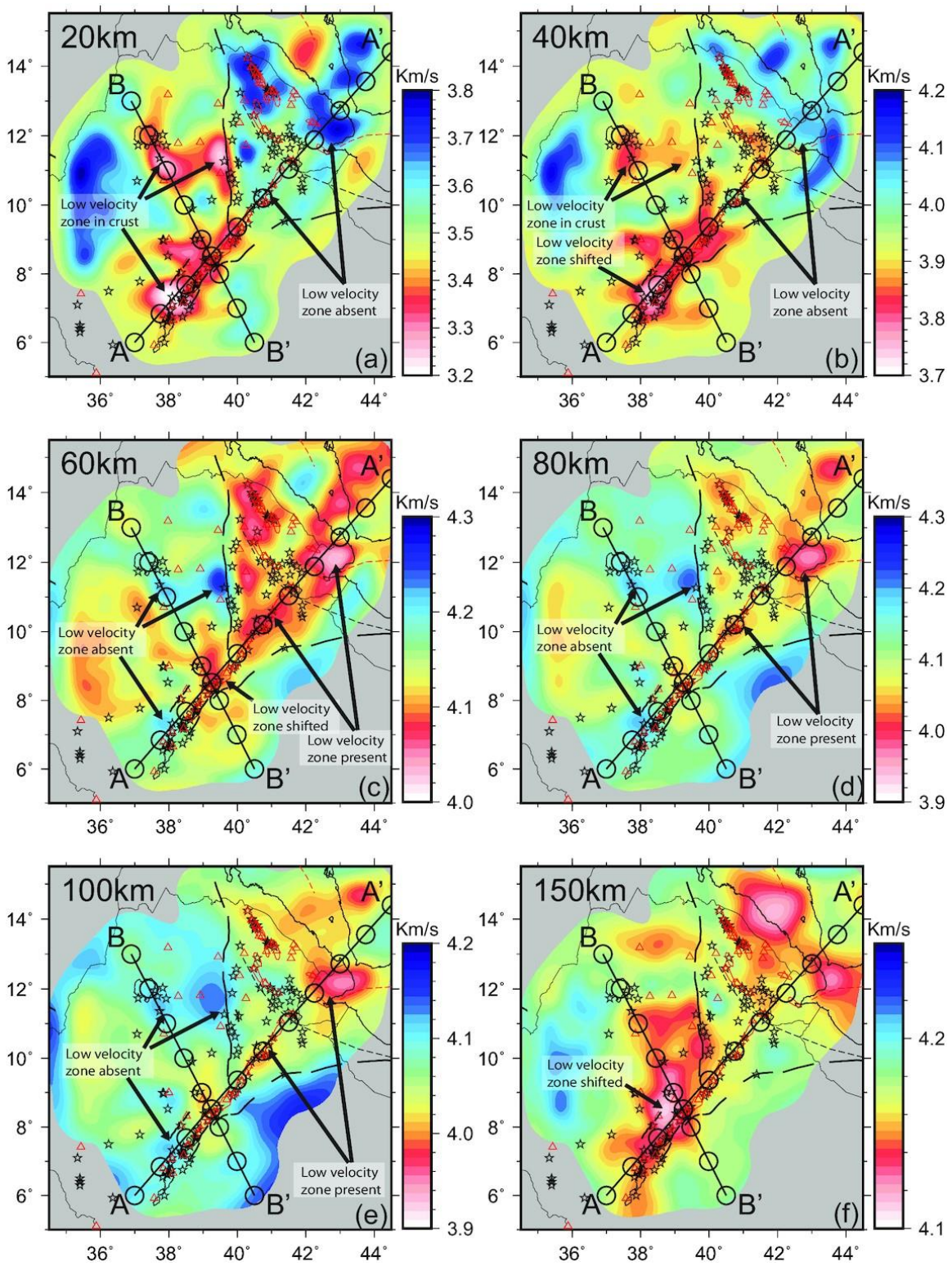

Fig. 3.2 Interpolated absolute shear wave velocity at 20, 40, 60, 80, 100 and 150 km depth showing the depth of partial melting in Ethiopia from Chambers et al. (2022).

3.3. Results

3.3.1. Field observation

A schematic stratigraphic column of the studied Series (LS, US and CAG) volcanic products and of the more recent and older volcanic activity (Axial, Dalha and Mabla Series), outcropping in Central and Southern Afar, is presented in Fig. 3.3.

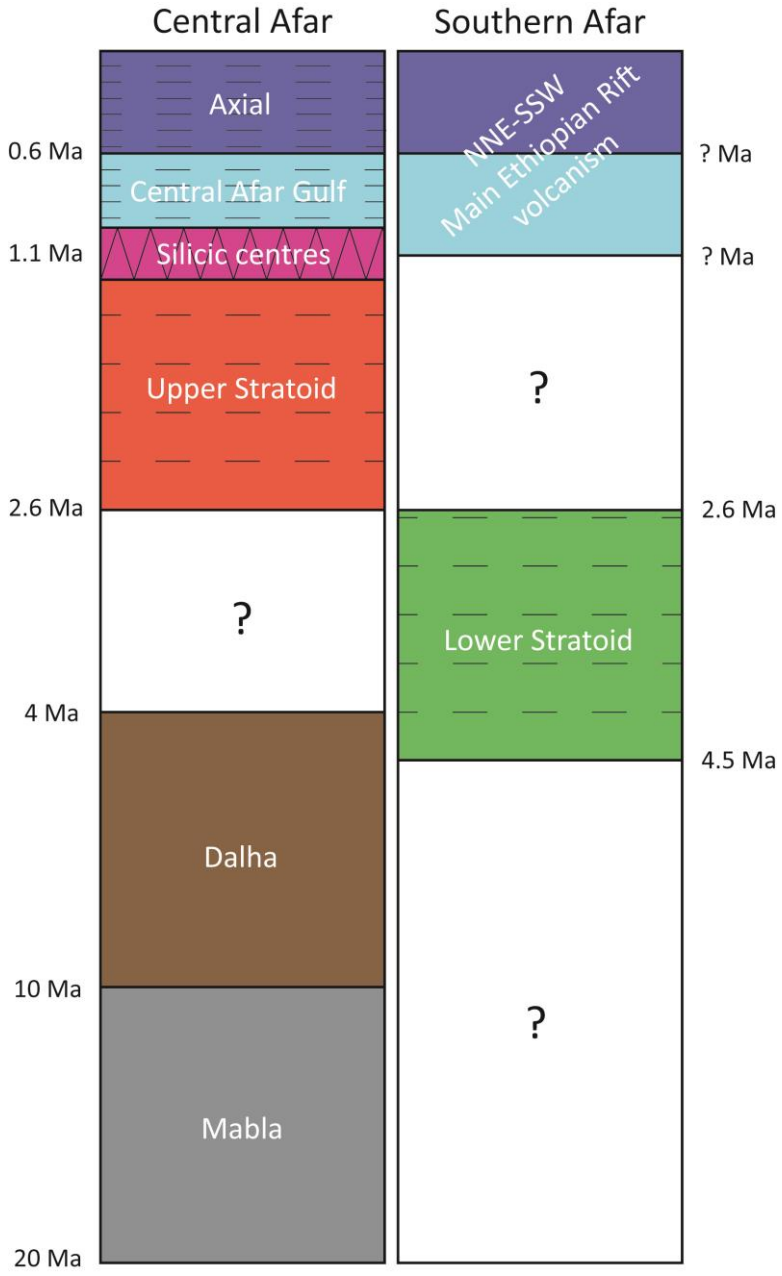

Fig. 3.3 Schematic stratigraphic column of the volcanic products outcropping in Southern and Central Afar. For the Southern Afar is reported also the recent volcanism related to the Main Ethiopian Rift branch.

The LS Series lavas have been observed in outcrops along the road from Gewane to Mille (Fig. 3.1). They consist of horizontally-jointed and massive blocky-jointed lava flows, reaching thickness of a few meters (Fig. 3.4a; Fig. S3.1). The thickness of the observed lava successions is moderate (~5 m), but to the east a lava succession of up to 400/500 m thick occurs (e.g., Karrayyu and Manda Eli Adda Do graben; satellite observations). The US Series have been observed mainly along the Tendaho and Dobi graben escarpments with observed flow thickness on the order of ten meters (Fig. 3.4b, c; Fig. S3.1). The thick succession of sheet flows is cut by up to 1000-meter-high graben-bounding faults in the Tendaho graben. The thickness of the single flows and the total volume (55,000 km^3; Lahitte et al., 2003b) are, however, smaller with respect to the typical flood basalt volcanism, e.g., the Oligocene Ethiopian trap reaching pluri-decametric thick single flows for a total volume of ~720,000 km^3 (Krans et al., 2018; Mohr, 1983; Rooney, 2017). The US lava flows are rather homogeneous, tabular, mainly massive, and predominantly blocky-jointed (Fig. 3.4b, c; Fig. S3.1). However, horizontal jointed and, to a small extent, well-formed columnar-jointed deposits have also been observed. Some flows show an increase in vesiculation toward the top. Subordinate pillow lavas have also been found, suggesting that water bodies may have existed during the US emplacement and therefore an environment with episodic depressed areas and humid conditions. No evidence of long hiatuses, such as the ones marked by thick sedimentary deposit interbedded with basalt flows in the Awash valley (Alemseged et al., 2020; DiMaggio et al., 2015), has been recognized on the observed outcrops. This suggests an overall high eruption rate, which potentially also contributed to forming a relatively flat surface morphology. The CAG Series lava flows are overall less thick with respect to the Stratoid Series flows and show inner variations in structure and vesiculation. In central Tendaho, north-east of Aysaita, and in the Immino area (Fig. 3.1) meter-thick (up to 2 m) massive and blocky-jointed flows interlayered with thin vesiculated facies were observed (Fig. 3.4d; Fig. S3.1). In Tendaho, a subaqueous lava forming hummocky-like flows (e.g., Self et al., 1998) shows clinker, tilted block and pressure ridges suggesting flow inflation (Duraiswami et al., 2001; Rossi and Gudmundsson, 1996; Walker, 1991). Near Eli Dar (Fig. 3.1) a reworked volcaniclastic deposit has been observed at the base of the meter-thick massive flow, suggesting a period of stasis in the magmatic activity. In the same area, Varet (2018) observed an erosive boundary and clastic sedimentation between the Stratoid Series and the CAG Series.

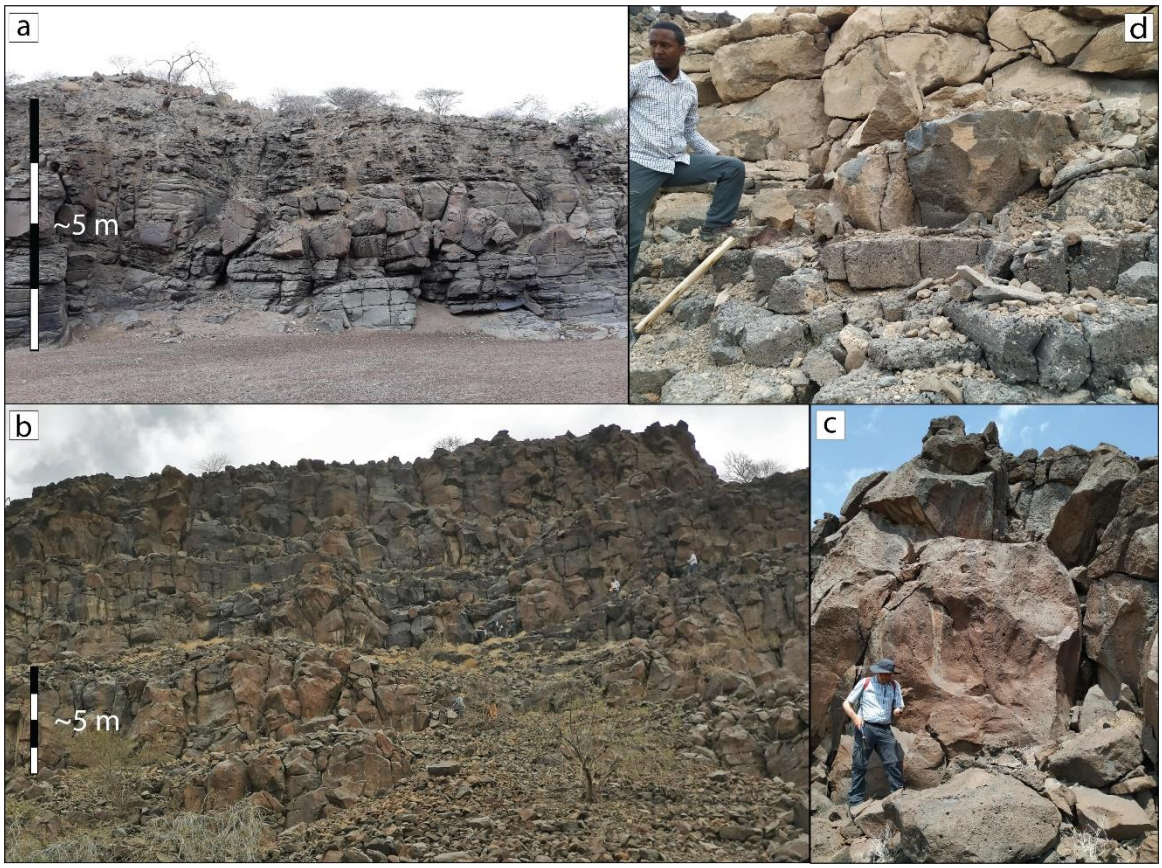

Fig. 3.4 Field photographs of the three Series. (a) LS Series massive blocky-jointed lava flows. (b) US Series typical blocky-jointed flows escarpment. (c) Closer look of the top flow of panel (b). (d) CAG Series lava flows alternating vesiculated and massive portions, less voluminous with respect to the Stratoid Series. More field photographs in Fig. S3.1.

Overall, the Stratoid Series, have the characteristics of flood basalt volcanism, such as the thick, massive, and jointed sheet flows, but they are less voluminous with respect to the typical flood basalt province (e.g., Deccan Traps, Columbia River Basalt province). Sporadic pillow lavas indicate episodes of subaqueous activity while the absence of hiatuses is consistent with continuous volcanic activity. Based on observed reworked volcaniclastic deposit a stasis can be instead suggested between the Stratoid and the CAG Series. The CAG Series shows an important decrease in total and single flow thickness with respect to the Stratoid Series, and more variable features with respect to the more homogeneous lavas of the Stratoid Series.

3.3.2. Petrography and mineral chemistry

Overall, the analyzed samples of the three Series in the Total Alkali-Silica (TAS) classification diagram are mainly basalt-basaltic andesite, with few samples reaching more evolved composition (andesite, trachyte and rhyolite fields; Fig. 3.5; Tab. S2.1).

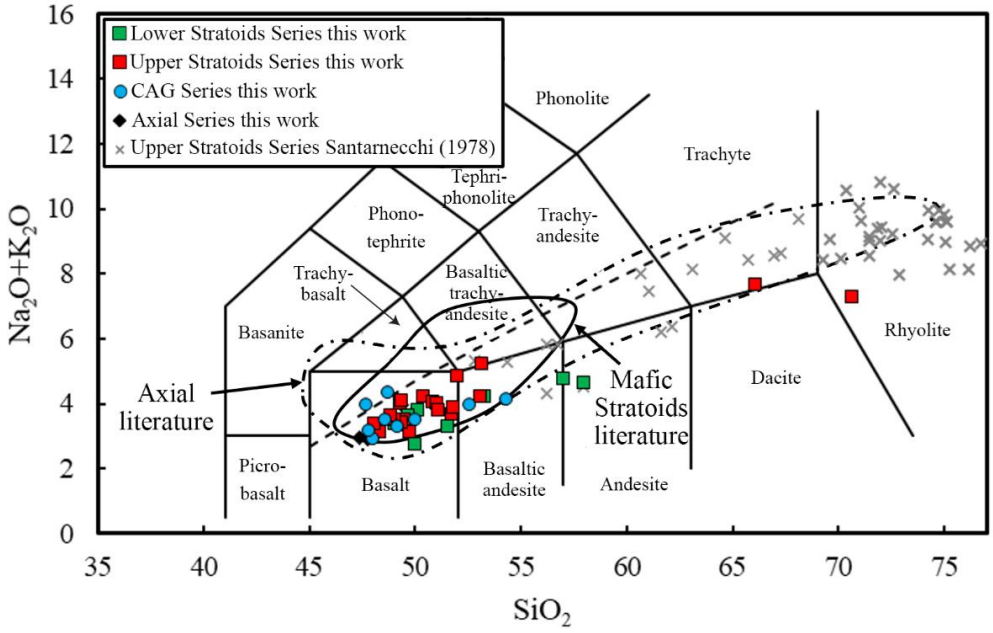

*Fig. 3.5 TAS (Total Alkali vs Silica, wt%) classification diagram for LS, US, CAG and Axial Series. Data recalculated to 100% on a water-free basis. Total iron as FeOtot = FeO+Fe_2O_3*0.8998. The dashed line marks the limit between subalkaline-alkaline fields (Irvine and Baragar, 1971). Data of silicic central volcanoes intercalated in the upper part of the US Series are from Santarnecchi (1978) and reported in Tab. S2.1. Stratoid Series literature data of Central and Southern Afar (solid line) are from Barberi and Santacroce (1980); Deniel et al. (1994); Feyissa et al. (2019). Axial literature data of Manda Hararo and Manda Inakir (dashed line) are from Barrat et al. (2003); Deniel et al. (1994); Feyissa et al. (2019).*

The LS Series are mainly aphyric or micro-porphyritic, with some scarcely porphyritic samples (Tab. S2.1). The populations of phenocrysts and microphenocrysts are dominated by plagioclase with minor olivine and clinopyroxene. The plagioclase phenocrysts are often sieve-textured and external resorption features are common (Fig. 3.6a; Fig. S3.1). Fe-Ti oxides and apatite are accessory minerals. The groundmass is mostly intergranular with subordinate hyalopilitic samples, and it is composed of plagioclase, olivine, clinopyroxene and Fe-Ti oxides.

The lavas of the US Series, similarly to the LS Series, are mainly aphyric and micro-porphyritic (Tab. S2.1). Four US samples are scarcely porphyritic and only one sample (AF20-12) reaches 35% of phenocryst abundance with phenocrysts of plagioclase and olivine. The most

abundant phase is plagioclase, with minor olivine and clinopyroxene (Fig. 3.6b; Fig. S3.1). In some samples, plagioclase phenocrysts show internal and external resorption features. With regard to accessory minerals, Fe-Ti oxides have been observed in most of the samples, apatite in the more evolved samples, while sulfides (pyrrhotite and Cu-rich sulfide) have been found in two mafic samples (AF20-04 and AF20-19). The groundmass is mostly intergranular with subordinate intersertal samples and composed of plagioclase, olivine, clinopyroxene and Fe-Ti oxides. The five more evolved lava samples are porphyritic and dominated by plagioclase with minor clinopyroxene and olivine, also found as glomerocrysts. Fe-Ti oxides and apatite are accessory phases. The groundmass is mostly intersertal and, subordinately, intergranular and is composed of plagioclase, olivine, clinopyroxene and Fe-Ti oxides.

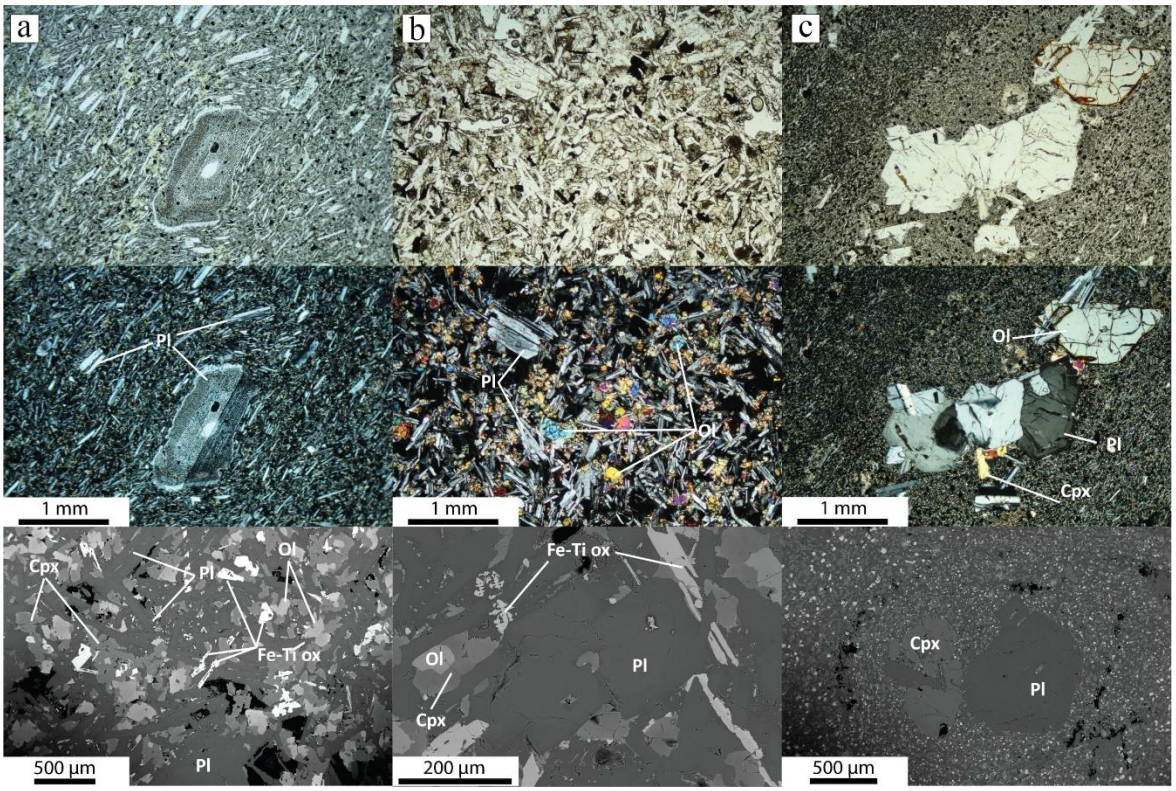

Fig. 3.6 Transmitted light petrographic (PPL and XPL) and SEM images (from top to the bottom) of the three Series respectively. (a) LS Series sieved and resorbed plagioclase in hyalopilitic groundmass. Note that the SEM image is not from the same sample of the petrographic images. (b) US Series sample with phenocryst and micro-phenocryst in intergranular groundmass. (c) CAG Series porphyritic lava. Pl, plagioclase; Cpx, clinopyroxene; Ol olivine; Fe-Ti ox, Fe-Ti oxides. More petrographic and SEM images in Fig. S3.1.

The CAG Series lavas are instead generally porphyritic and micro-porphyritic, with only two aphyric samples (Tab. S2.1). One sample has an ophitic texture with plagioclase enclosed in clinopyroxene. As for the Stratoid Series, plagioclase is the most abundant phenocryst

mineral, but olivine and clinopyroxene phenocrysts are also common (Fig. 3.6c; Fig. S3.1). In some samples, plagioclase phenocrysts have sieve textures and/or show external resorption features, together with olivine and clinopyroxene they form glomerocrysts. Quartz xenocrysts with pyroxene corona have been found in one sample. Fe-Ti oxides have been observed as accessory minerals. The groundmass is mostly intergranular and subordinately intersertal and composed of plagioclase, olivine, clinopyroxene and Fe-Ti oxides.

Six samples have been analyzed for mineral chemistry, two lava flows of the US Series (AF20-04 and AF20-19, respectively MgO 4.76 wt% and 4.54 wt%), one flow of the LS Series (H436, MgO 5.44 wt%) and three lava flows of the CAG Series (AF20-46, AF20-66 and AF20-25, respectively MgO 5.17 wt%, 4.69 wt% and 5.84 wt%) (Tab. S2.1). They have been selected based on composition (most of the mafic lavas range between MgO 4.5 wt% and 6.5 wt%) and on the presence of phenocrysts and micro-phenocryst (Fig. 3.7).

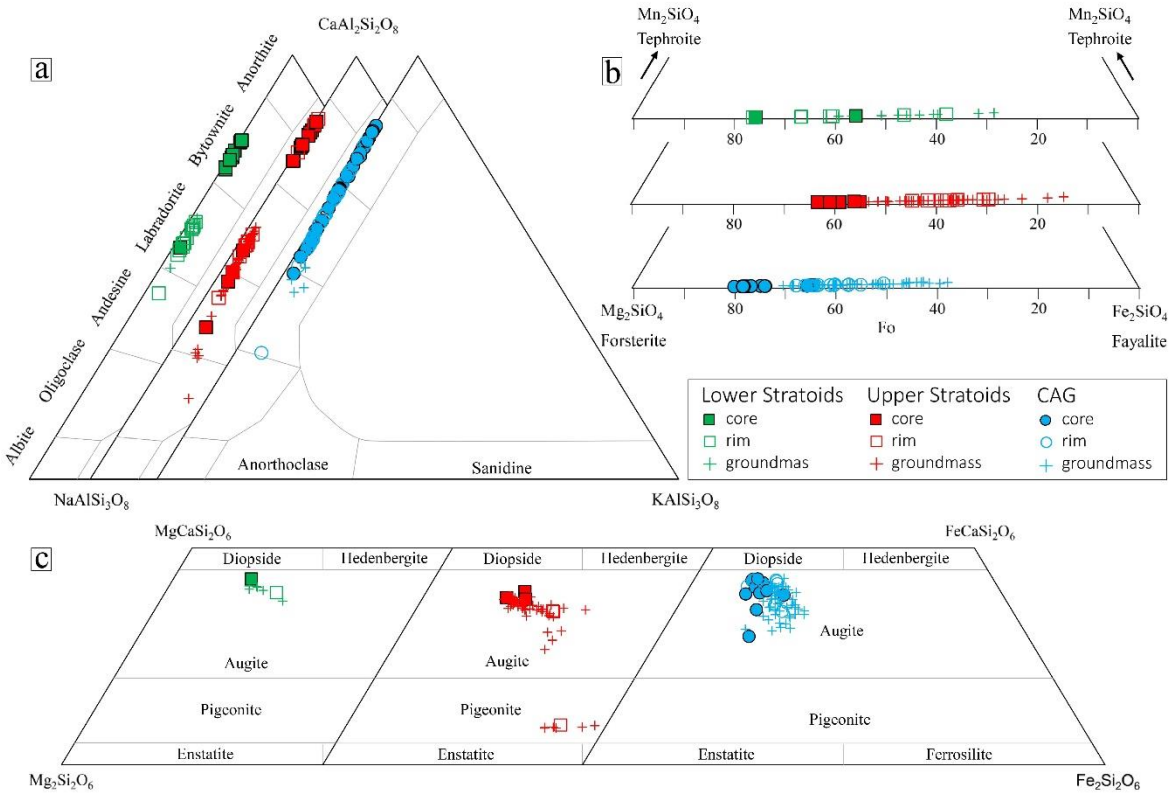

Fig. 3.7 (a) Feldspar (An-Ab-Or), (b) olivine (Fo-Fa-Tep) and (c) clinopyroxene (En-Fs-Hd-Di) classification diagrams of the three Series: LS Series (green), US Series (red) and CAG Series (blue). Different symbols identify phenocrysts core (full symbols), rim (empty symbols) and groundmass (crosses).

Both in the US and LS Series, plagioclase crystals are normally zoned with a compositional gap between the bytownite and the labradorite fields (Fig. 3.7a). The cores are mainly bytownite ranging from An 75 to An 85 and the rims are mainly andesine-labradorite (An 43-

58) with some bytownitic composition (An 76-85) (Fig. 3.7a). The CAG Series plagioclase crystals are mostly normally zoned, with mainly bytownitic cores and some reaching more evolved compositions (An 50-65). Rims are mainly labradoritic (An 50-70) and no compositional gap has been observed (Fig. 3.7a). The groundmass plagioclase has overall similar compositions for the three Series (Fig. 3.7a). The olivine crystals of the US Series are normally zoned, with cores Fo 54-63 and rims Fo 29-44 (Fig. 3.7b). The olivine crystals in the LS Series are normally zoned, and cores reach more Fo-rich composition with respect to the US Series (up to Fo 76). The olivine crystals in the CAG Series are normally zoned with overlapping compositional ranges for cores (Fo 62-79) and rims (Fo 54-69). The groundmass olivine are overall similar between LS and US Series, while they are more mafic for the CAG Series (Fig. 3.7b). The clinopyroxene is mainly augite for all the Series, with the exception of pigeonite in the US Series groundmass and rim (Fig. 3.7c). The CAG Series and the LS Series reach more diopsidic composition with respect to the US Series (Fig. 3.7c). The presence of only few clinopyroxene and olivine phenocrysts in the LS Series does not allow a robust comparison with the other Series. LS and US Series have both ilmenite and titanomagnetite and in sample AF20-04 the titanomagnetite forms preferentially the rims around an ilmenite core. For the CAG Series, AF20-46 have titanomagnetite only while in AF20-66 and AF20-25 both ilmenite and titanomagnetite are present (Tab. S2.1).

3.3.3. Major element and trace elements

The Stratoid and CAG Series analyzed samples are subalkaline, with transitional to tholeiitic affinity. Overall, the samples of the three Series overlap and in the Total Alkali-Silica (TAS) classification diagram they are mainly basalt-basaltic andesite, with two andesite, one trachyte and one rhyolite (Fig. 3.5; Tab. S2.1). The CAG Series is on average more mafic (Tab. 3.1; Tab. S2.1) and includes the most primitive samples (up to MgO 8.38 wt%, 345 ppm of Cr and 168 ppm of Ni) compared to the LS and US Series (respectively up to MgO 6.47 wt% and 6.60 wt%; Fig. 3.8; Tab. 3.1; Tab. S2.1). The LS and US Series basalts are mainly Qz-normative and subordinately Hy-Ol normative, while the CAG Series is mainly Hy-Ol normative.

Tab. 3.1 Summary table of the main petrographic and chemical characteristics of the LS, US and CAG Series. The complete datasets are presented in Tab. S2.1.

Petrography													
Series		Mafic samples						Silicic samples					
	N° of	*mean vol% ph*			*mean vol% mph*			*N° of samples*			*mean vol% ph*		
LS	12	1.8			7.3			0			-		
US	25	2.5			5.8			5			20		
CAG	11	9.6			0.7			0			-		
NORM and major element chemistry													
	N° of	*NORM*			*MgO wt%*			*TiO_2 wt%*			*Tot. alk. wt%*		
					min	*mean*	*max*	*min*	*mean*	*max*	*min*	*mean*	*max*
LS	9	Mainly Qz norm			3.75	4.85	6.47	1.42	2.61	3.41	2.68	3.68	4.66
US	20	Mainly Qz norm			0.58	4.54	6.60	0.82	2.89	3.61	2.95	4.04	7.13
CAG	9	Mainly Hy-Ol norm			4.69	6.03	8.38	1.60	2.68	4.15	2.89	3.58	4.33
MgO > 4 wt% trace element chemistry													
	N° of	*Sr ppm*			*Nb ppm*			*Th ppm*			*Nb/Ta*		
		min	*mean*	*max*	*min*	*mean*	*max*	*min*	*mean*	*max*	*min*	*mean*	*max*
LS	7	197	239	291	14.24	27.53	39.29	1.05	3.14	6.74	11.76	15.29	16.05
US	15	295	341	390	23.20	34.46	44.78	1.79	2.78	3.93	15.28	15.96	16.52
CAG	9	272	338	458	17.99	30.35	44.51	0.88	2.40	4.54	14.49	15.82	17.15
MgO > 4 wt% trace element chemistry													
	N° of	*Ti/Y*			*Nb/U*			*Rb/Nb*			*Ce/Pb **		
		min	*mean*	*max*	*min*	*mean*	*max*	*min*	*mean*	*max*	*min*	*mean*	*max*
LS	7	369	420	512	8.01	42.39	53.10	0.14	0.76	3.06	8.18	22.83	28.38
US	15	255	468	558	44.25	50.32	59.14	0.12	0.41	0.57	10.94	23.54	31.61
CAG	9	329	418	493	22.52	58.97	81.54	0.17	0.46	1.04	24.79	28.23	32.84

*Note. *Due to Pb being below the detection limit, Ce/Pb values are the means of 5 LS samples, 6 US samples and 3 CAG samples.*

The major element distributions of the three Series in variation diagrams are rather scattered, particularly for TiO_2, FeO P_2O_5 and Al_2O_3, and no single trend for each Series is recognized (Fig. 3.8; Fig. S3.2; Tab. S2.1). CaO, Na_2O and K_2O have overall similar trends for the three Series with CaO showing a more scattered behavior for the CAG Series (Fig. 3.8; Fig. S3.2).

A group of samples, formed by two CAG Series samples from the Tendaho graben (AF20-22 and AF20-29) and two LS Series samples from the Woranso-Mille region (AF20-61 and AF20-62a) can be distinguished outside of the overall trend. The group is remarkably depleted in TiO_2 and FeO_t and enriched in SiO_2, Al_2O_3, K_2O with respect to the rest of the samples for the same MgO wt%, (Fig. 3.8; Fig. S3.2) and is hereafter called the low Ti-Fe samples group.

Concerning trace elements, a marked discrimination among the three Series is provided by the Sr content, which is higher in the CAG and US Series with respect to the LS Series (Fig. 3.8). Incompatible trace elements are positively correlated with Zr showing overall overlapping trends for the three Series, except for Y and HREE (Fig. S3.3; Tab. S2.1). Furthermore, the low Ti-Fe samples show definitely different incompatible trace element contents and ratios (i.e., higher Th, U and Rb for the same Zr) with respect to their respective Series (Fig. S3.3).

The incompatible trace element and REE patterns, normalized to primitive mantle and chondrite concentrations respectively (McDonough and Sun, 1995), are presented in Fig. 3.9. The LS and US Series basalts have E-MORB type REE patterns and are characterized by a slight U-Th trough and a Nb-Ta peak. The CAG Series also shows E-MORB-type REE patterns, but the Nb-Ta peak and U-Th though are more pronounced with respect to the Stratoid Series (Fig. 3.9). The four low Ti-Fe samples have a positive peak in Th-U, high K and Rb, high La/Sm and low and scarcely fractionated MREE and HREE (Fig. 3.9; Tab. S2.1). Moreover, two of the low Ti-Fe samples have positive anomalies in Pb (for the other two samples Pb is below the detection limit; Fig. 3.9; Tab. S2.1).

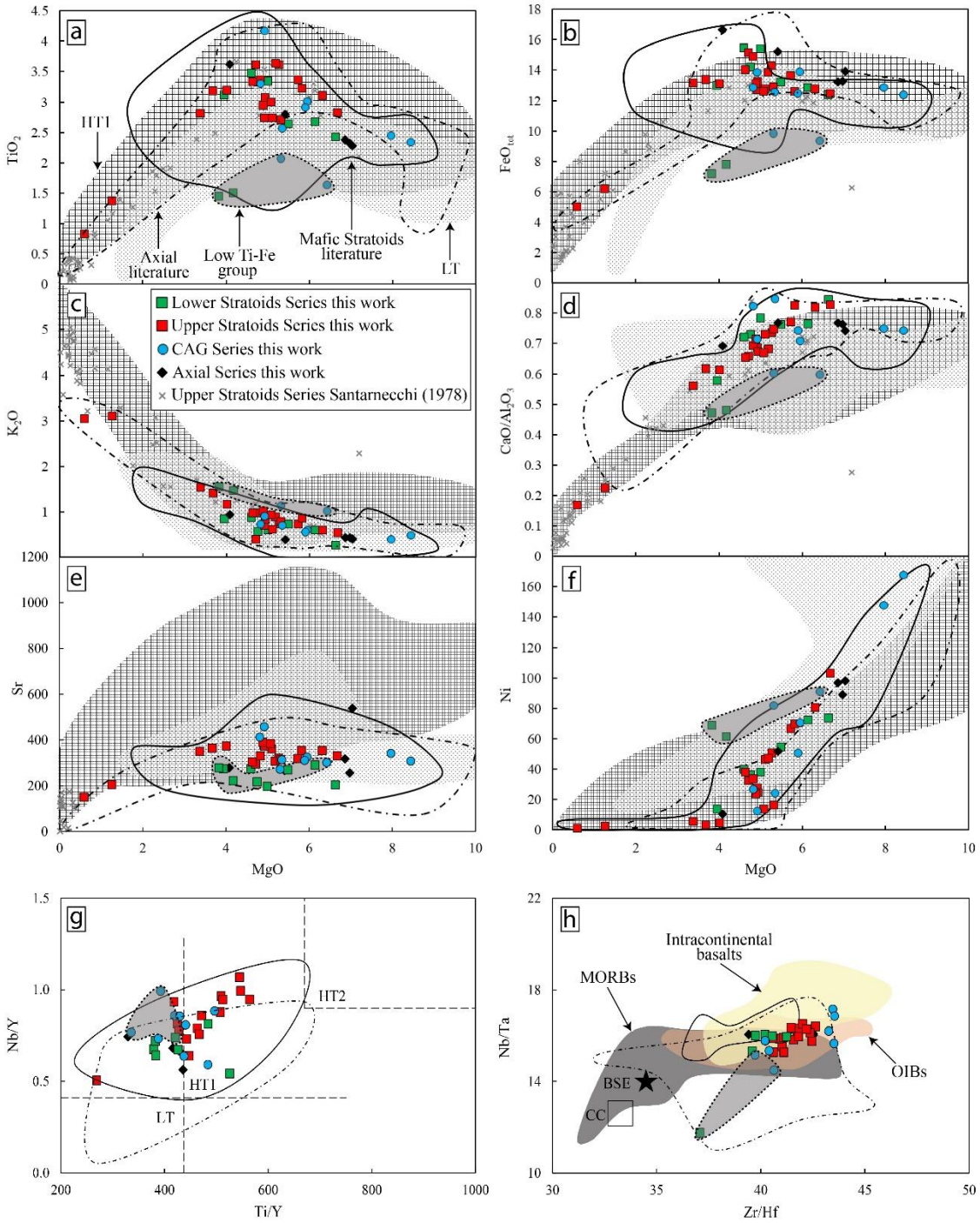

Fig. 3.8 (a-f) Major (wt%) and compatible trace element (ppm) binary diagrams of Stratoid, CAG and Axial Series. Data of silicic central volcanoes intercalated in the upper part of the US Series are from Santarnecchi (1978) and reported in Tab. S2.1. LT and HT1 fields are from Kieffer et al. (2004) and Pik et al. (1998). (g) Classification diagram Nb/Y vs. Ti/Y from Pik et al., 1998 (LT, low-Ti type; HT1, high-Ti1 type; HT2, high-Ti2 type) for mafic rock (MgO > 4 wt%) of Stratoid, CAG and Axial Series. (h) Nb/Ta vs. Zr/Hf diagram for mafic rock (MgO > 4 wt%) of Stratoid, CAG and Axial Series. Fields for MORBs, OIBs and intracontinental basalts are from Pfänder et al. (2012). CC is continental crust (Rudnick and Gao, 2003), and BSE is the Bulk Silicate Earth. Stratoid Series literature data of Central and Southern Afar (solid line) are from Barberi and Santacroce (1980); Deniel et al. (1994); Feyissa et al. (2019). Axial literature data of Manda Hararo and Manda Inakir (dashed line) are from Barrat et al. (2003); Deniel et al. (1994); Feyissa et al. (2019).

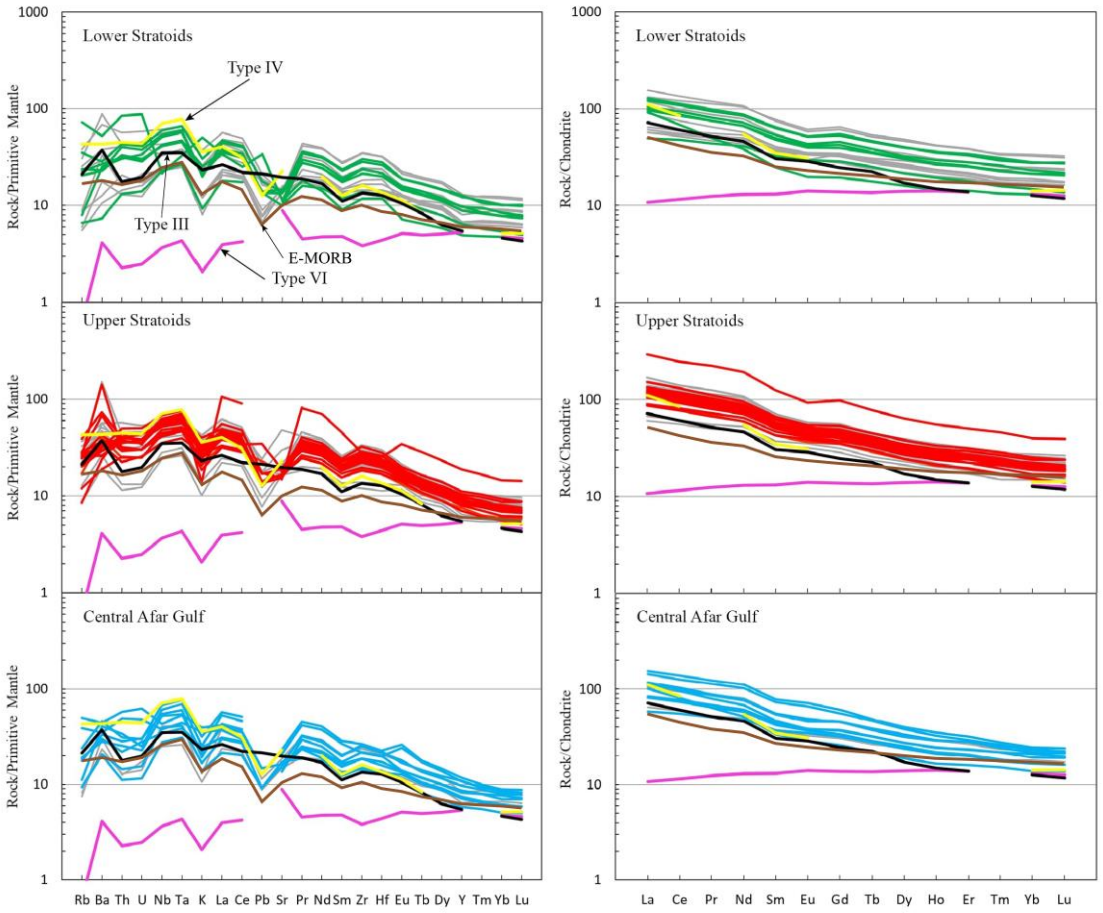

Fig. 3.9 Chondrite-normalized REE patterns and primitive mantle-normalized trace element spider diagrams of LS, US and CAG Series. Grey lines are from Feyissa et al. (2019) and the distinction between US and LS Series has been made based on their location and the map of Kidane et al. (2003). Magma types III, IV and VI of Rooney (2020a) are shown for comparison. E-MORB composition is from Gale et al. (2013). Normalizing values after McDonough and Sun (1995).

Overall, the analyzed samples exhibit characteristics of Enriched-MORB and correspond to the type III (a mixture of plume, depleted mantle, and African lithosphere) and IV (a hybrid between type III and more OIB-like magmas) of Rooney (2020a, b) EARS magmatism classification (Fig. 3.9). The three Series have similar trends and ratios of many incompatible elements but show notable differences in HREE and Y (Fig. S3.3). The samples belong overall to the HT1 group (High-Ti group 1 of Pik et al., 1998) with lower Ti content for the LS Series (Fig. 3.8g). Overall, the three Series broadly overlap with the OIB, MORB and intracontinental basalt fields (Fig. 3.8h). However, part of the US have higher Nb/Ta and Zr/Hf indicating, according to their partition coefficient during partial melting (Hart and Dunn, 1993; McDade et al., 2003; van Westrenen et al., 2001), a slightly more intracontinental affinity with respect to the LS, possibly suggesting two different stages of the rift evolution (Fig. 3.8h).

Nevertheless, not all the CAG show a more MORB affinity with respect to the US. Despite the rather scattered behavior of the three Series, the major and trace elements suggest an evolution dominated by fractional crystallization of the minerals observed in thin sections, starting from the most primitive basalts (Fig. 3.8; Fig. S3.2). The trend is well constrained by the evolved and intermediate samples of Santarnecchi (1978), that studied the silicic central volcanoes intercalated in the upper part of the Stratoid Series (e.g., Gad Elu, Ado Ale, Oyma, Katahelu; Tab. S2.1), partially covering the Daly gap commonly observed in the Afar and Main Ethiopian Rift volcanism (Peccerillo et al., 2003, 2007). The constant decrease of Ni and Cr suggests fractionation of olivine from the most mafic terms. At 6% MgO a decrease in CaO and Al_2O_3 is observed suggesting fractionation of plagioclase and clinopyroxene, without a decrease in Sr. The decrease of TiO_2 and FeO at 5% MgO and of P_2O_5 at 4% MgO respectively indicate fractionation of Fe-Ti oxides and apatite, respectively.

3.3.4. Sr, Nd, Pb isotopic data

The results obtained on the analyzed samples show a moderate variation range for $^{87}Sr/^{86}Sr$ (0.7033-0.7040) and $^{143}Nd/^{144}Nd$ (0.51284-0.51298) and a relatively wider range for $^{206}Pb/^{204}Pb$, $^{207}Pb/^{204}Pb$ and $^{208}Pb/^{204}Pb$ (18.23-19.03, 15.51-15.58 and 38.26-39.11 respectively), overall overlapping with the available published data of Central and Southern Afar (Fig. 3.10; Tab. S2.1; Feyissa et al., 2019).

Regarding the Sr vs Nd (Fig. 3.10a), the three Series partially overlap, defining a general inverse correlation trend between the two isotopes, consistent with the global mantle array. In detail the LS and CAG show overall a more depleted composition, reaching the highest $^{143}Nd/^{144}Nd$ and the lowest $^{87}Sr/^{86}Sr$ (respectively 0.51298 and 0.7033; Fig. 3.10a). The US are overall less scattered than the LS and CAG, ranging from 0.51290 to 0.51294 for $^{143}Nd/^{144}Nd$ at from 0.7034 to 0.7036 for $^{87}Sr/^{86}Sr$, with the exception of three US samples having the lowest $^{143}Nd/^{144}Nd$ and the highest $^{87}Sr/^{86}Sr$ of the three Series (down to 0.51284 and up to 0.7040 respectively; Fig. 3.10a).

Regarding Pb isotopes, in the $^{208}Pb/^{204}Pb$ vs $^{206}Pb/^{204}Pb$ diagram the three series are distributed along a single array, subparallel to the Northern Hemisphere Reference Line (NHRL; Fig. 3.10b). The US have overall a more enriched composition with respect to the LS and CAG reaching the highest $^{208}Pb/^{204}Pb$ and $^{206}Pb/^{204}Pb$ (39.11 and 19.03 respectively).

Three US samples show a distinctly more depleted signature, grouping at the lowest $^{208}Pb/^{204}Pb$ and $^{206}Pb/^{204}Pb$ (38.26 and 18.23 respectively; Fig. 3.10b). They are the same samples that scattered towards more radiogenic $^{87}Sr/^{86}Sr$ and lower $^{143}Nd/^{144}Nd$, confirming their peculiarity, with a distinct isotopic composition with respect to the other US. Similarly, in the $^{207}Pb/^{204}Pb$ vs $^{206}Pb/^{204}Pb$ diagram, the US samples have a generally more enriched signature with respect to LS and CAG, but the overall sample behavior do not show correlation between the two isotopes. The samples of the three Series have indeed an overall constant $^{207}Pb/^{204}Pb$ (~15.55), with variable $^{206}Pb/^{204}Pb$. This behavior is enhanced by the scattering of the three US samples (the US with the lower $^{206}Pb/^{204}Pb$; Fig. 3.10c).

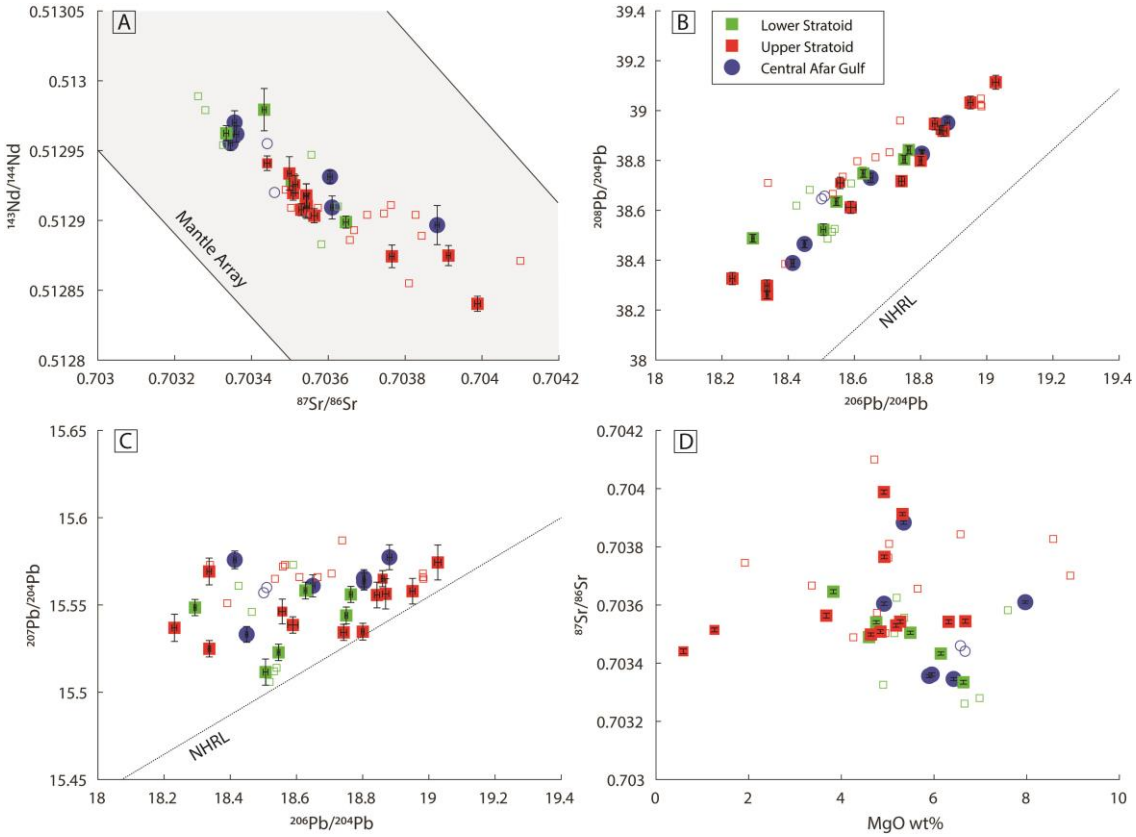

Fig. 3.10 Isotopic variations of the US, LS and CAG. Error bars represent the standard deviation (2SE) for each mean value (Tab. S2.1). a) $^{87}Sr/^{86}Sr$ vs. $^{143}Nd/^{144}Nd$. b) $^{206}Pb/^{204}Pb$ vs. $^{207}Pb/^{204}Pb$. c) $^{206}Pb/^{204}Pb$ vs. $^{208}Pb/^{204}Pb$. d) $^{87}Sr/^{86}Sr$ vs. MgO wt%. The black line in (b) and (c) is the North Hemisphere Reference Line (NHRL) from Hart (1984).

To evaluate isotopic variations due to crustal contamination, the $^{87}Sr/^{86}Sr$ has been plotted versus the magnesium number (Fig. 3.10d). An increase in $^{87}Sr/^{86}Sr$ (and decrease in $^{143}Nd/^{144}Nd$) at the decreasing of Mg# has been observed for the LS, while no correlation with Mg# has been observed for the US and CAG. Furthermore, scattering between and

within the Series at broadly the same Mg# confirm the variable nature of some samples or group of samples (Fig. 3.10d).

3.4. Discussion

3.4.1. Mantle sources of the Stratoid Series and CAG Series magmatism

The LS, US and CAG Series have similar characteristics in terms of lava composition. The lavas are mainly mafic, covering a similar differentiation range between 4.5 and 6.5 wt% MgO with few more primitive compositions (MgO up to 8 wt%). All basalts are subalkaline, Hy-Ol or Qz normative. The three Series also display overall similar trends of major and trace elements (excepting the four low Ti-Fe lavas). The mafic lavas, according to the Ba and Nb-Ta peaks, the negative K anomaly and to the U-Th trough (Fig. 3.9), are classified as type III and IV of Rooney (2020a, b), representative of lavas erupted under conditions of lithospheric thinning by a mixing of plume, depleted mantle, and African lithosphere. Despite the samples not being primitive, crustal contamination did not have an important effect on magma evolution during its possible stationing at the base of the crust (i.e., magma underplating) nor in the shallower magma chambers during its ascent (Fig. 3.11a; Fig. S3.4). Most of the samples fall in the MORB-OIB range (Nb/U 37-57, and Ce/Pb 20-30; Hofmann et al., 1986). The only exceptions are the two evolved US Series samples having low Nb/U and high Rb/Nb, and the four Low Ti-Fe lavas having low Nb/U, Ce/Pb and high La/Nb, Rb/Nb (Fig. 3.11a). However, the isotopic signature ($^{87}Sr/^{86}Sr$ vs $^{143}Nd/^{144}Nd$) do not show clear sign of crustal contamination for the Low Ti-Fe lavas, that could suggest similar isotopic signature. All the Series, in agreement with the literature data and with Nb/U and Ce/Pb ratios (Fig. 3.11a), fall in between the MORB and OIB fields (Fig. 3.11b; Fig. S3.4). In Fig. 3.11b the LS has higher Zr/Nb and lower La_N/Sm_N indicating a more MORB-like mantle source with respect to the US Series and therefore possibly suggesting two different stages of the rift evolution. Overall, the CAG has a more scattered distribution. However, considering only the samples collected at the Tendaho graben and excluding therefore the two samples of the Immino graben (Zr/Nb < 6; Fig. 3.1; Fig. 3.11b) and the two Low Ti-Fe samples (affected by crustal contamination), the CAG also has a more MORB-like affinity with respect to the US. At the same time, all the Series have a marked negative anomaly in K and the positive peak in Ba and Nb-Ta, interpreted as indicative of amphibole and/or phlogopite in the mantle source

(Furman and Graham, 1999; Rooney et al., 2017; Späth et al., 2001). The ratios Na_2O/K_2O and Ba/Rb can be used to discriminate between melting of phlogopite- and amphibole-bearing mantle sources, respectively lower and higher than 1 (Foley et al., 1999; Green, 1973; Rosenthal et al., 2009) and 11 (primitive mantle value from Sun and McDonough, 1989; Furman and Graham, 1999). The $Na_2O/K_2O > 1$, the Ba/Rb > 11 and the K/Th variation obtained by modelling a partial melting process of a mantle source with and without amphibole (Shaw, 1970, eq. 15; Fig. 3.11c) indicate an amphibole-bearing sub continental lithospheric mantle (SCLM) involved in partial melting. The amphibole is stable in the mantle up to 3 GPa and 1050-1150 °C (Class and Goldstein, 1997; Green et al., 2010; Niida and Green, 1999), therefore indicating a contribution of a relatively cold SCLM source during the partial melting for all three Series. Therefore, I suggest that the presence of the anomalously hot Afar mantle (1350-1500 °C; Ferguson et al., 2013; Feyissa et al., 2019; Rooney et al., 2012a) induced amphibole metasomatism (Furman et al., 2016; Rooney et al., 2017) of the SCLM in Afar. Consequently, melting of the Afar plume and depleted mantle (Ferguson et al., 2013; Feyissa et al., 2019; Rooney 2020b) together with the upper, easily-fusible (Pilet et al., 2008), amphibole-bearing SCLM produced the observed type III and IV magmatism of Rooney (2020a, b).

The four low Ti-Fe samples, instead, lack the diagnostic positive anomalies in Nb-Ta and negative in K of type III and IV mantle source, but show positive anomalies in Th-U and Rb and high La/Sm (Fig. 3.9). Furthermore, the low Ti-Fe lavas require the involvement of a crustal component (low Ce/Pb and high Rb/Nb; Fig. 3.11c; Fig. S3.4). In addition, two low Ti-Fe samples of the Woranso-Mille region, together with another sample of that region (AF20-60b), have low Zr and Nb for the same MgO wt% with respect to the other LS samples and low and scarcely fractionated MREE-HREE (Fig. 3.9; Tab. S2.1). These characteristics resemble a group of samples of the Woranso-Mille region described by Rooney (2020b) as a rare occurrence of a depleted component “intrinsic” to the Afar plume (type VI). My data confirm the observation made by Rooney (2020b) and seem to enhance the geochemical complexity of lavas in the Woranso-Mille area.

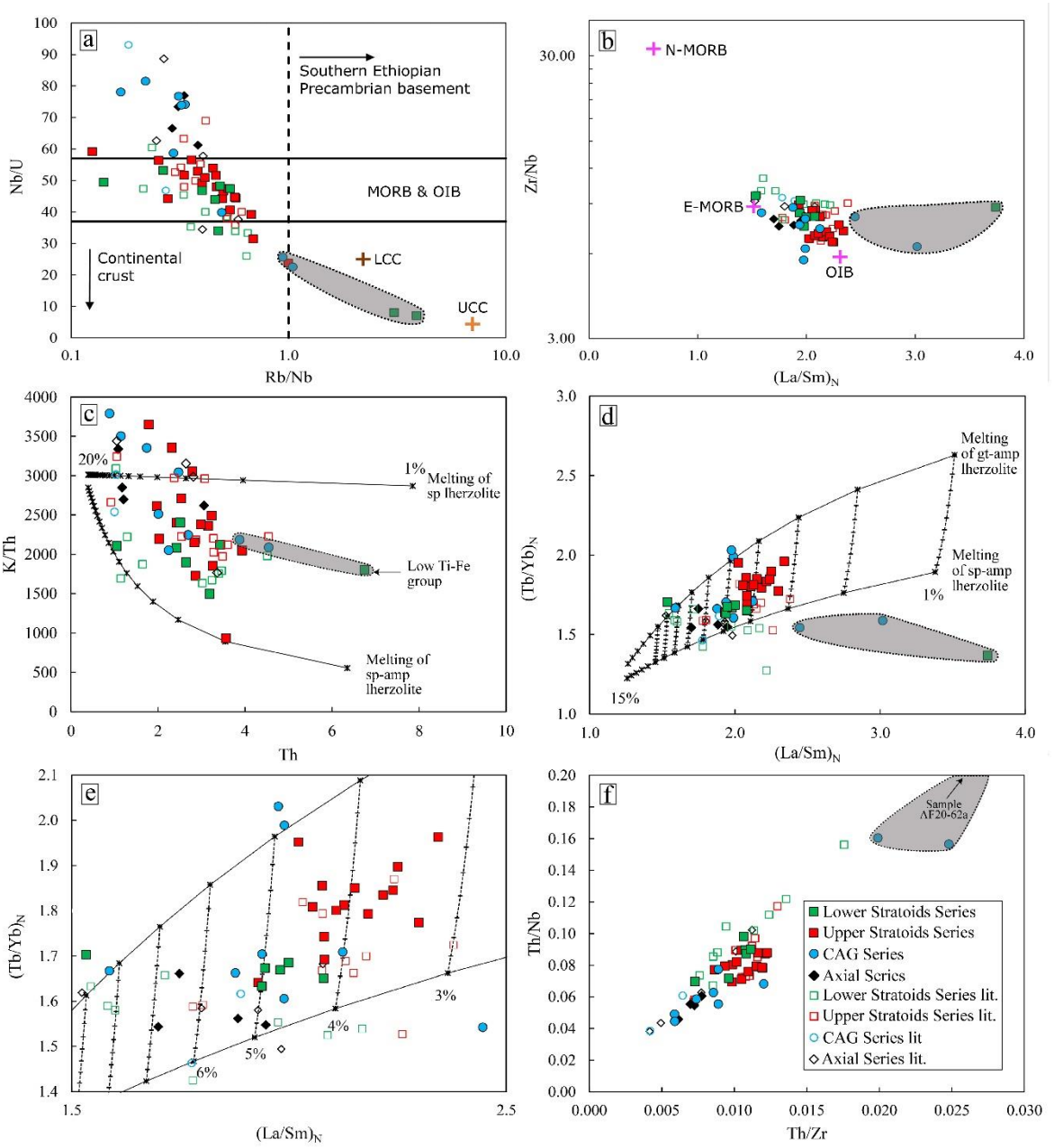

Fig. 3.11 (a) Nb/U vs. Rb/Nb indicating a minor role of crustal contamination on magma evolution for Stratoid, CAG and Axial Series. The MORB and OIB field (Nb/U 37-57) is from Hofmann et al. (1986). The Southern Ethiopian Precambrian basement (Rb/Nb >1) is from Peccerillo et al. (1998). UCC and LCC are respectively the upper continental crust and the lower continental crust (Rudnick and Gao, 2003). (b) Zr/Nb vs. La_N/Sm_N show variation in the degree of enrichment of lavas from the Stratoid, CAG and Axial Series mafic rock (MgO > 4 wt%). OIB, N-MORB and E-MORB values from Sun and McDonough (1989). Normalizing values after McDonough and Sun (1995). (c) K/Th vs. Th for Stratoid, CAG and Axial Series mafic rock (MgO > 4 wt%) in order to distinguish between a spinel lherzolite and spinel-amphibole lherzolite source. Partial melting of primitive mantle (McDonough and Sun, 1995) is calculated using the non-modal batch melting model of Shaw (1970), the partition coefficients from McKenzie and O'Nions (1991), and the following amphibole-garnet and -spinel lherzolites source mineral modes: garnet lherzolite: 0.58 Ol, 0.15 Opx, 0.20 Cpx, 0.02 Gt, 0.05 amp that melts in the proportion 0.10 Ol, 0.20 Opx, 0.40 Cpx, 0.10 Gt, 0.20 amp; spinel lherzolite: 0.58 Ol, 0.15 Opx, 0.20 Cpx, 0.02 sp., 0.05 amp that melts in the proportion 0.10 Ol, 0.20 Opx, 0.40 Cpx, 0.10 sp., 0.20 amp. Solid lines show the variation of the degree of partial melting from 1% to 20%. Literature data are from Feyissa et al. (2019) and

the distinction between US and LS Series has been made based on their location and the map of Kidane et al. (2003). (d-e) Tb_N/Yb_N vs. La_N/Sm_N mafic rock (MgO > 4 wt%) show variation in the depth of the melting column and in the degree of partial melting between the Series. (e) Enlargement of panel (d). Solid lines show the variation of the degree of partial melting from 1% to 15% while dashed lines identify the mixing trend from 100% amphibole-garnet lherzolite to 100% amphibole-spinel lherzolite. Primitive mantle, melting model, partition coefficient, mineral modes and literature data are the same as panel (c). Normalizing values after McDonough and Sun (1995). (f) Th/Nb vs. Th/Zr diagram shows the distinction between the CAG Series and the LS and US Series mafic rock (MgO > 4 wt%) due to the Th being slightly more incompatible than Nb during partial melting ($D_{Th}^{cpx/melt}$ = 0.0001, $D_{Th}^{ol/melt}$ = 0.00026, $D_{Th}^{gt/melt}$ = 0.0001, $D_{Nb}^{cpx/melt}$ = 0.05, $D_{Nd}^{ol/melt}$ = 0.01 McKenzie and O'Nions, 1991). One of the LS Series low Ti-Fe samples is out of the graph range (AF20-62a, Th/Zr 0.05 and Th/Nb 0.47). Literature data as in panel (c).

Considering the three Series, marked differences in garnet-compatible elements (e.g., Tb_N/Yb_N, Zr/Y; Fig. 3.11d, e) and small but systematic differences in highly incompatible elements ratios (e.g., Th/Nb, Th/Zr; Fig. 3.11f) have been observed in the lavas with MgO> 4 wt%. The Tb/Yb ratio is used as a proxy of the partial melting depth as Yb (as the other HREE and Y) is highly compatible in garnet (Salters and Longhi, 1999) and, thus, partial melting of a garnet-bearing mantle source, with residual garnet, translates in the increase of Tb_N/Yb_N ratio in the melt with respect to a spinel-bearing source. There are, however, other factors that can influence the Tb_N/Yb_N ratio in the melt that have to be taken in consideration. Variation to the Tb_N/Yb_N ratio due to melting of a garnet-bearing lower crust or to fractionation of garnet or amphibole in water-saturated conditions (Alonso-Perez et al., 2009) can be ruled out for Central-Southern Afar due to the low crustal thickness (Hammond et al., 2011). Furthermore, no garnet nor amphibole have been observed in the thin sections. High pressure clinopyroxene fractionation, behaving similarly to the garnet, could influence Tb_N/Yb_N ratio, but this process could also be ruled out due to its lower efficiency in fractionating MREE-HREE. Lastly, amphibole variations during partial melting can influence Tb_N/Yb_N ratio, however, its effect could also be ruled out as no variation is observed in other amphibole-compatible elements (e.g., K, Fig. 3.9; Fig. 3.11c). Similarly, the effect of clinopyroxene fractionation on La/Sm could be ruled out as no variations between the Series has been observed in other clinopyroxene-compatible elements, such as V.

I therefore used the Tb/Yb ratio as a diagnostic parameter to discriminate the different depths of the magma-source melting column. In Fig. 3.11d and 3.8e a marked distinction is evident within my samples at Tb_N/Yb_N ~1.7, with the US Series having overall higher values and the LS Series and the CAG Series having clear lower values. I model the batch melting

process (Shaw, 1970, eq. 15) of the spinel and garnet-bearing mantle sources for various degrees of partial melting and mixing between the two source types using the mass balance equation (Fig. 3.11d, e). The US Series are well encompassed by the model with 3.5-4.5% of a prevalently garnet-bearing mantle source (70-50% garnet-bearing), while most of the LS and CAG Series basalt require a degree of partial melting higher than 4.5% of a mantle source primarily out of the garnet stability field (50-80% spinel-bearing source). According to the experimental studies of Klemme and O'Neill (2000) and to the Afar mantle temperature ranging between 1050-1150 °C (residual amphibole) and 1500°C (Ferguson et al., 2013; Feyissa et al., 2019; Rooney et al., 2012a), I identify the spinel-garnet transition between 16-27 Kbar (60-100 Km). Therefore, the US Series basalts were mainly generated at relatively larger depths (greater than (>) 60-100 km-deep), while the LS Series and CAG Series are derived from shallower (less than (<) 60-100 km-deep) partial melting, and broadly consistent with the ~100 km-deep, base of melt zone constrained using seismology and geochemical modelling for the present day (Chambers et al., 2022; Ferguson et al., 2013). Notably, some samples of the US Series, with ages around 1.1 Ma (Feyissa et al., 2019; Kidane et al., 2003) have Tb_N/Yb_N values intermediate between CAG and US Series, suggesting a gradual shallowing of the melting column at the transition between the two Series (samples collected between the cities of Serdo and Silsa; Fig. 3.1; Tab. S2.1).

I stress out that only the two CAG lava flows analyzed from the Immino graben show Tb_N/Yb_N of 1.99 and 2.03, indicating a deeper melting column than the rest of the CAG. This suggests less lithosphere extension and thinning in the Immino graben compared to Tendaho graben, the historically active zone (e.g., Keir et al., 2009). Further studies on samples from the CAG Series and Stratoid Series in the Immino and neighboring grabens are however necessary to validate this hypothesis.

Highly incompatible element ratios, such as Th/Nb and Th/Zr, show a clear distinction between US and CAG Series, suggesting variations in the primitive melts (Fig. 3.11f). According to the partition coefficient of McKenzie and O'Nions (1991), Th is slightly more incompatible than Nb during partial melting. The lower values in Th/Nb and Th/Zr of the CAG Series basalts with respect to the US Series, coupled with the lower values in La_N/Sm_N, indicate an increase of the degree of melting after the eruption of the US Series.

In summary, the 4.5-0.6 Ma mafic magmatism of Central and Southern Afar is related to partial melting of a metasomatized SCLM that melted (or dripped into the asthenosphere; Furman et al., 2016) together with depleted mantle and the rising Afar plume, originating the three components observed in the lavas (Fig. 3.9; Fig. 3.10). Despite the sustained stretching and thinning of the lithosphere preceding the Stratoid volcanism in Afar (e.g., Armitage et al., 2015) and the similarity of the involved mantle reservoirs (Fig. 3.8; Fig. 3.11), the LS and US Series are produced by two distinct mantle sources, respectively with a shallower and deeper melting column (Fig. 3.11). The CAG Series basalts were generated from a shallower partial melting column and a higher degree of partial melting with respect to the US Series, suggesting more rift focusing and lithosphere thinning for the LS Series and CAG (Fig. 3.11).

3.4.2. Melt evolution of the Stratoid Series and CAG Series magmatism

The mafic and intermediate samples of the three Series overlap in most of the major and trace element variations diagrams (Fig. 3.8) and no clear distinct trend between the Series has been recognized except for Sr. At the same time, different primitive magmas have been revealed by the trace element composition of the mafic lavas, and multiple evolutionary paths are suggested by the compositional spread of the samples with intermediate degree of evolution. Since the samples are aphyric or scarcely porphyritic, this variable composition cannot be attributed to mechanisms of phenocryst accumulation, except for one sample with high Al_2O_3 and CaO and 35% of plagioclase phenocrysts. A significant interaction with the crust can be excluded based on the element's ratios Nb/U, Rb/Nb, Ce/Pb (Tab. 3.1), except the four low Ti-Fe samples.

I use rhyolite-MELTS algorithm (Asimow et al., 2004; Ghiorso and Sack, 1995) to model the liquid line of descent for a range of pressures (0.5-3.5 Kbar), water content (0.5-2 wt%) and oxygen fugacity (QFM+1-QFM-2), starting from the most mafic sample for each Series, to investigate fractional crystallization conditions for mafic-intermediate products. Except for the four low Fe-Ti samples, the range of conditions that best fit each individual Series are similar, with pressure varying between 1.5 and 2.5 Kbar, the oxygen fugacity between QFM and QFM-1 and H_2O from 0.5 to 1 wt% (Fig. S3.5a, b, c). These models suggest that there is no variation in time between the Series regarding the hydration state of the mantle nor

regarding the oxygen fugacity. According to MELTS simulations, the variation of TiO_2 and FeO at 4-5 MgO wt% within the US could be explained by an increase of the water content (up to 1 H_2O wt%) that, however, fails to fit the Al_2O_3 content (Fig. S3.5b). Moreover, it is difficult to explain the variation in Sr between the Series with different conditions of fractional crystallization considering the similarities of the other elements (i.e., Al_2O_3). Based on the MELTS modelling results (at 2 Kbar, QFM-0.5 and H_2O 0.5 wt%) olivine precipitates only for the CAG Series at ~8.3 MgO wt%. Clinopyroxene starts fractionating at ~7.14 MgO wt% for the CAG Series and at ~6.4-6.6 MgO wt% for the Stratoid Series. Plagioclase precipitates at ~6.9 MgO wt% for the CAG Series and at ~5.9-6.1 MgO wt% for the Stratoid Series. Spinel precipitates at ~5 MgO wt% for the CAG and the US Series and at ~4.4 MgO wt% for the LS Series.

Despite the presence of only few phenocrysts of plagioclase, clinopyroxene and olivine in the samples (particularly for the LS Series), the mineral chemistry indicates possible differences in the plumbing system between the Series. My data reveal that the CAG and the LS Series lavas host mafic mineral phases (Fo-rich olivine and Mg#-rich clinopyroxene) suggesting an early differentiation stage not observed instead in the US Series(Fig. 3.7). However, given the scarcity of the clinopyroxene phase (Tab. S2.1) and the lack of equilibrium with the bulk rock for the Stratoid Series, I only use the plagioclase phenocrysts analyses of the six samples to calculate the pressure of crystallization by means of mineral-melt geothermobarometer (Putirka, 2008, Eq. 25a). For the modelling I used the whole rock analysis as melt composition (Putirka 2008) and a water concentration of 0.5 wt%. The equilibrium was checked based on the distribution coefficient $KD_{(An-Ab)}^{pl-liq} = 0.10 \pm 0.05$ at T < 1050 °C and 0.27 ± 0.11 at T ≥ 1050 °C (Putirka, 2008). Plagioclase-melt equilibrium is never observed for the US Series suggesting a fast magma ascent leading to low phenocrysts content and plagioclase-liquid disequilibrium (La Spina et al., 2016). Plagioclase-melt equilibrium is instead observed for the LS Series ranging from 1.3 to 1.9 ± 3.8 kbar, and for the CAG Series ranging from 2.3 to 4.2 ± 3.8 kbar. Therefore, I suggest that during its ascent magma possibly ponded at first at the base of the crust and then, rising toward the surface, at ~ 5-7 Km depth for the LS Series and at 9-16 Km depth for the CAG Series. The two-plagioclase populations observed in the LS and US Series could be related to an abrupt release of water driven by a decompression-induced crystallization from a H_2O-rich melt.

This scenario will induce a rapid transition toward the crystallization of more Na-rich plagioclase (Lange et al., 2009).

3.4.3. Mantle sources composition of the Stratoid Series and CAG Series magmatism: constraints from Sr, Nd and Pb isotopic ratios

The Sr, Nd and Pb isotopic compositions of the three Series are overall similar but the LS and CAG have some samples showing more depleted composition, in contrast with the US samples that reach instead more enriched compositions (Fig. 3.10). Furthermore, a group of US have a distinct and peculiar isotopic signature with respect to the other US, reaching the most enriched composition in the Sr vs Nd diagram and the most depleted in the $^{208}Pb/^{204}Pb$ vs $^{206}Pb/^{204}Pb$ diagram (Fig. 3.10). US and CAG isotopic ratios show no correlation with Mg# while an increase in $^{87}Sr/^{86}Sr$ (and decrease in $^{143}Nd/^{144}Nd$) at the decrease of Mg# has been observed for the LS (Fig. 3.10). However, the large age range covered by the LS (ranging from 4.5 to 2.6 Ma) and their wide aerial distribution (Fig. 3.1) suggest different crustal magmatic systems for their emplacement, implying therefore a similar effect due to crustal assimilation for the whole LS Series or that the observed trend is a fortuitous observation. The absence of correlation between the isotopic variations and Nb/U argue against the involvement of crustal contamination for the LS. Variations have been observed instead for the same degree of evolution within and between the sample groups belonging to the different Series (Fig. 3.10). Therefore, besides the similarities of the three series, these observations could suggest variation in the mantle source/s.

3.4.3.1. Mantle components In the Afar region

The presence of a mantle plume in the EARS is inferred by the high $^{3}He/^{4}He$ of magmas (e.g., Halldórsson et al., 2014; Castillo et al., 2020) and by the anomalously high mantle temperature (>150 C°; e.g., Ferguson et al., 2013; Armitage et al., 2015; Feyissa et al., 2019). In Afar, the mantle plume is commonly proposed as the source promoting magmatism and affecting the geochemical signatures of magmas and at present is generally accepted to be located in the area of Lake Abhe (Hart et al., 1989; Schilling et al., 1992; Pik et al., 2006; Rooney et al., 2012b; Nelson et al., 2019; Castillo et al., 2020). The high titanium flood basalt (HT2) has been taken as the best representation of the Afar plume composition (Meshesha

and Shinjo, 2008; Pik et al., 1998). This choice is supported by the high $^{3}He/^{4}He$ values observed in HT2 magmatism (Marty et al., 1993; Marty et al., 1996; Pik et al., 2006; Rogers et al., 2010). Based on recent magmatism lead and helium isotopes trend, Rooney et al. (2012b) identified the common reservoirs (C; Hanan and Graham, 1996), as the unique composition of the Afar plume (Alene et al., 2017; Ayalew et al., 2018; Feyissa et al., 2017; Nelson et al., 2012). However, the isotopic signature of the Afar magmatism could not be explained by the C reservoir alone and a mix between the deep Afar plume and a shallow mantle reservoir in which both a depleted mantle component (DMM) and an enriched SCLM (Pan-African continental Lithosphere, according to Schilling et al., 1992) has been suggested (Rooney et al., 2012b; Rooney, 2020a), as also proposed for the Mid-Atlantic ridge (e.g., Andres et al., 2004; Blichert-Toft et al., 2005) and the Indian ridge (e.g., Graham et al., 2006; Hanan et al., 2004). Lithospheric detachment (Rooney at al., 2012b) or lithospheric dripping into the asthenosphere (Furman et al., 2016) could contaminate at different amounts and at different scales the DMM during rifting evolution toward the oceanic spreading. In general, in the more mature stages of the rift, this will produce magmas with relatively unradiogenic $^{207}Pb/^{204}Pb$, $^{208}Pb/^{204}Pb$ and $^{87}Sr/^{86}Sr$, and radiogenic $^{143}Nd/^{144}Nd$ due to a progressively minor involvement of the lithosphere (Rooney, 2020a). However, given the variable interplay of the three components due to temporal and spatial variations of the rift system and the different metasomatic events affecting the lithosphere before and during rift evolution, the study of the isotopic signature and variability in detail can be challenging but, at the same time, fundamental for final interpretation. However, considering the relatively small spatial distribution (Central and Southern Afar) and short time interval (4.5-0.6 Ma) investigated in this work, I can exclude that the observed chemical and isotopic variations are due to the documented heterogeneity within the Afar plume (Furman et al., 2006; Meshesha and Shinjo, 2008; Nelson et al., 2012; Natali et al., 2016; Beccaluva et al., 2009). I also can exclude that the variations could be related to the effect of the decreasing activity of the Afar plume away from the Lake Abhe (Ayalew et al., 2016; Nelson et al., 2019; Rooney et al., 2012b; Schilling et al., 1992) due to the location of the three Series, being very close to each other. Lastly, I exclude that the isotopic imprint could be related to variably metasomatized lithosphere (Nelson et al., 2019; Rooney et al., 2014), as the three Series have the same metasomatic signature (Fig. 3.9).

I discuss here, together with trace elements and spatial and temporal constraints, the isotopic variations observed within and between the Series and refer to DMM as the depleted asthenosphere, to PAL (Pan-African Lithosphere) as the enriched SCLM of Pan-African age, and Afar plume as the anonymously hot rising mantle, according to the values of Rooney et al. (2012b).

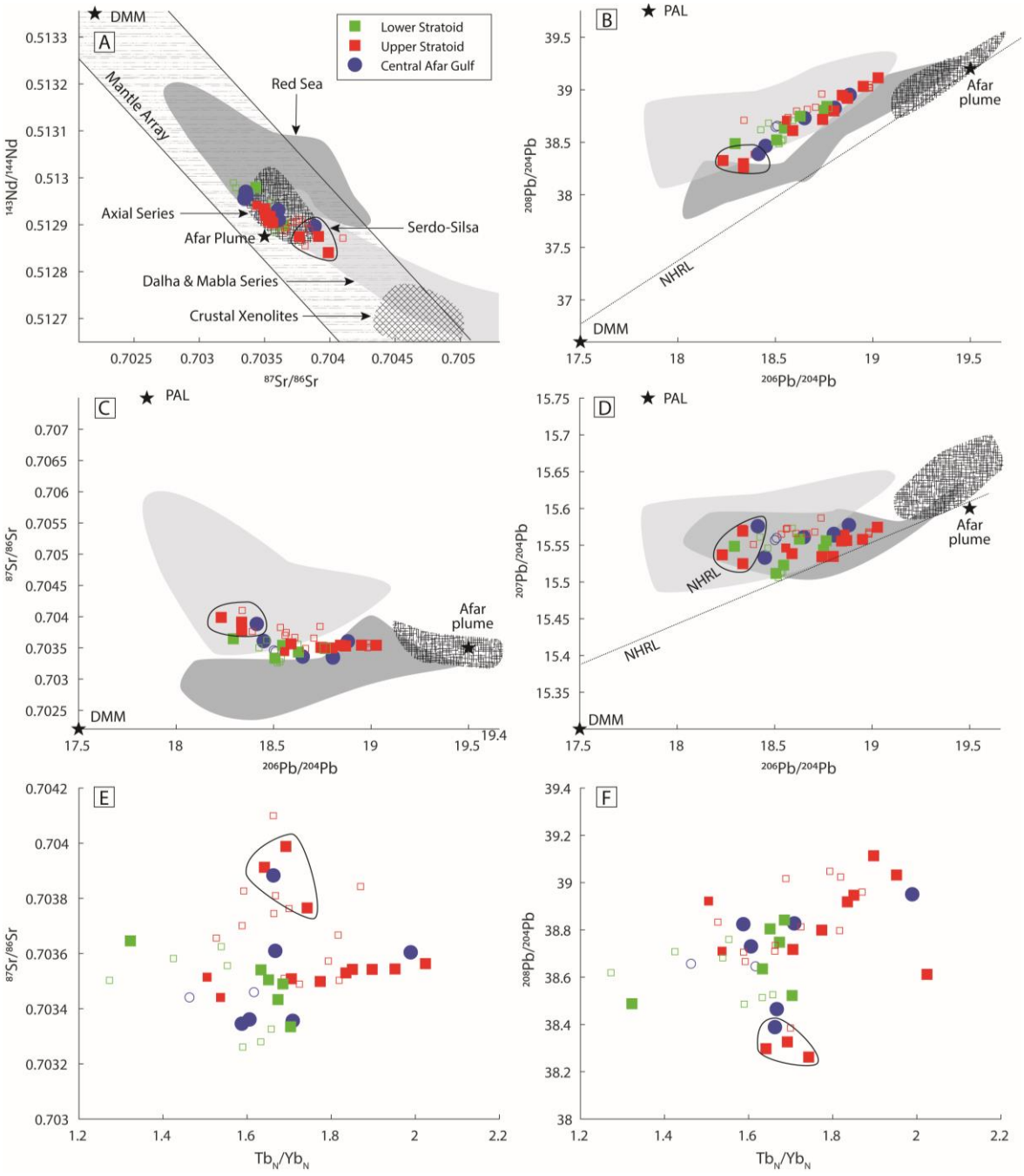

Fig. 3.12 a-d) Isotopic variations of the US, LS and CAG. The circled samples are the lavas from the region between the towns of Serdo and Silsa (Fig. 3.1). The fields indicate the isotopic variations of Red Sea (Petrini et al., 1988; Rogers, 1993; Volker et al., 1997; Barrat et al., 1990; Haase et al., 2000; Altherr et al., 2000), Axial Series (Watts et al., 2020; Lowenstern et al., 2006; Hagos et al., 2016; Duffield et al., 1997; Ayalew et al., 2019; Barrat et al., 1998, 2003; Castillo et al., 2020), Dalha and Mabla Series (Rooney et al., 2013; Barrat et al., 1993;

Chernet and Hart, 1999; Deniel et al., 1994; Feyissa et al., 2017; Hart et al., 1989) and crustal xenoliths (Teklay et al., 2010). The US, LS and CAG literature values are from Feyissa et al. (2019) and the distinction between US and LS Series has been made based on their location and the map of Kidane et al. (2003). The DMM, PAL and Afar plume reservoir values are from Rooney (2012b). a) $^{87}Sr/^{86}Sr$ vs. $^{143}Nd/^{144}Nd$. B) $^{206}Pb/^{204}Pb$ vs. $^{208}Pb/^{204}Pb$. C) $^{206}Pb/^{204}Pb$ vs. $^{207}Pb/^{204}Pb$. D) $^{87}Sr/^{86}Sr$ vs. $^{206}Pb/^{204}Pb$. The black line in (b) and (c) is the North Hemisphere Reference Line (NHRL) from Hart (1984). E-f) Isotopic and trace element variations of the US, LS and CAG. E) Tb_N/Yb_N vs. $^{87}Sr/^{86}Sr$. f) Tb_N/Yb_N vs. $^{208}Pb/^{204}Pb$. The circled samples are the lavas from the region between the towns of Serdo and Silsa (Fig. 3.1). Normalizing values after McDonough and Sun (1995).

3.4.3.2. Mantle sources isotopic signature

Overall, according to trace element ratios (e.g., Nb/U, Rb/Nb; Fig. 3.11a) and isotopic composition (e.g., $^{87}Sr/^{86}Sr$ vs $^{143}Nd/^{144}Nd$; Fig. 3.12a), LS, US and CAG do not show sign of contamination, unlike the older Dalha and Mabla Series (~20-4 Ma) that show instead a clear trend of crustal contamination (Fig. 3.12; Rooney, 2020b). This suggests an important decrease of crustal contamination starting from the beginning of the Stratoid activity.

Overall, for all the isotopic systematic, my samples range in between the Afar plume, the DMM and the PAL component, suggesting a mix of these three mantle sources for the genesis of the magmas, as already proposed by Rooney (2020a, b). However, the Sr vs Nd, $^{208}Pb/^{204}Pb$ vs $^{206}Pb/^{204}Pb$ and $^{206}Pb/^{204}Pb$ vs $^{87}Sr/^{86}Sr$ systematics seem to indicate a major involvement of the DMM source for the LS and CAG with respect to the US that instead plots broadly closer to the Afar plume (with the exception of a group of US samples behaving differently and treated separately in the next paragraph; Fig. 3.12a, b, c). Similarly, $^{207}Pb/^{204}Pb$ vs $^{206}Pb/^{204}Pb$ shows an increase in the DMM but also in the PAL (high $^{207}Pb/^{204}Pb$) contribution for the LS and CAG with respect to the US (Fig. 3.12d). These observations are in agreement with the Zr/Nb ratio, indicating a more MORB-like mantle source for LS and CAG and an OIB-like mantle source for the US (Fig. 3.10b). Furthermore, according to the Tb_N/Yb_N modeling (chapter 3) the increase of the DMM (and possibly PAL according to $^{207}Pb/^{204}Pb$ vs $^{206}Pb/^{204}Pb$) component in the LS and CAG, is associated with a shallower melting column with respect to the US (Fig. 3.11d, e; Fig. 3.12e, f). A decrease of the radiogenic $^{208}Pb/^{204}Pb$ and $^{87}Sr/^{86}Sr$, and an increase in the radiogenic $^{143}Nd/^{144}Nd$ is also observed within the US together with the shallowing of the melting column (Fig. 3.12e, f). Lastly, the deep melting column of the US (Tb_N/Yb_N > ~1.8) shows a moderate isotopic variability with respect to the shallower depths of melting (Fig. 3.12). I therefore suggest that the observed isotopic variations are related to the different involvement of the Afar

plume, DMM and PAL reservoirs in relation to the different depths of partial melting. Based on my observations, the shallower partial melting column of LS and CAG favored a major degree of DMM and possibly a sub continental, Pan-African lithospheric mantle involvement (according to $^{207}Pb/^{204}Pb$ vs $^{206}Pb/^{204}Pb$) with respect to the deeper and more homogeneous US melting column that was instead more prone to sample the Afar plume component.

As pointed out, the US samples plot overall closer to the Afar plume component with respect to the LS and CAG, and show a small trend towards the depleted signature of the DMM (Fig. 3.12). However, three scattered US samples show distinctive characteristics in all diagrams and a different behavior with respect to the US. These samples scatter toward the PAL enriched end-member according to Sr vs Nd, toward the DMM end-member according to the $^{208}Pb/^{204}Pb$ vs $^{206}Pb/^{204}Pb$ and toward somewhere in between these two end-member in the $^{207}Pb/^{204}Pb$ vs $^{206}Pb/^{204}Pb$ diagram (Fig. 3.12). These observations suggest an increase of both DMM and PAL during partial melting of these US lavas. According to the trace element ratios Nb/U, Rb/Nb and Ce/Pb these lavas do not show signs of crustal assimilation (respectively 44-52, 0.46-0.57 and 23) with the exception of one sample having lower Ce/Pb (11; Fig. 3.10a; Fig. S3.4). This confirms the minor role of crustal assimilation influencing isotopic composition and supports the idea that source heterogeneity is the main factor controlling isotopes variability. Interestingly, these isotopically distinct samples have the lowest Tb_N/Yb_N (1.64-1.74) of the US (i.e., shallowest melting column; Fig. 3.10d, e; Fig. 3.12e, f), and have been collected on top of the US succession and in the area between the towns of Serdo and Silsa (Fig. 3.1), where ages are around 1 Ma (Feyissa et al., 2019; Kidane et al., 2003; Lahitte et al., 2003b). Their shallow partial melting and young ages suggest that the shallowing of the melting column had already begun in the last period of the US activity (i.e., before the CAG) at least in the area between Serdo-Silsa. To confirm the peculiarity of this area, one CAG sample collected in this region has similar signatures both in terms of isotopes and Tb_N/Yb_N to the three US samples (Fig. 3.12e, f). This evidence could be explained, as for the CAG, by a higher DMM involvement during partial melting with respect to the other US (Pb-Pb diagrams; Fig. 3.12) samples. However, differently from the main CAG these lavas show an increase of the PAL component (Fig. 3.12a, c, d). I speculate that, being these, the first products melting at shallow level and possibly involving lithosphere weakened by the persistent US activity, this could explain the major involvement of PAL with

respect to the CAG. The consumption of the destabilized lithosphere and the consequent involvement of shallower, colder and less weakened lithosphere during the CAG activity, led to the observed decrease in the PAL components.

Lastly I point out the peculiar behavior of one CAG sample, that represents the only one not collected along the Tendaho graben but at the Immino graben, to the north (Fig. 3.1). This sample is the only CAG having high Tb_N/Yb_N (~2) and show isotopic characteristics more similar to the US (high $^{208}Pb/^{204}Pb$, $^{207}Pb/^{204}Pb$ and $^{206}Pb/^{204}Pb$ and $^{87}Sr/^{86}Sr$ and low $^{143}Nd/^{144}Nd$) rather than CAG of the Tendaho, underlining, together with the observation made on the Serdo-Silsa samples, the temporal and spatial complexity of rift systems. The results obtained on the lavas collected at Serdo-Silsa indicate that mantle source variations due to the involvement of different components (PAL, DMM and plume) could take place over short periods of time and limited regions. The mantle source characteristics of the Immino CAG suggests that, beside the temporal and geological affinity with the Tendaho CAG, the rifting in Afar show different evolutionary stages between Immino and Tendaho, possibly due to the different evolutionary history of the two rift branches (Red-Sea and Gulf of Aden). These observations therefore suggest caution when comparing different stages of the rift or different rift segments.

3.5. Conclusive remarks

Overall, the LS, US and CAG Series are generated by a mixing of plume, depleted mantle, and African lithosphere (amphibole-bearing SCLM; Fig. 3.11) but systematic differences have been observed. The LS and CAG have a shallower melting column (< 60-100 km-deep; Fig. 3.11), a more MORB-like mantle source (Fig. 3.11) and major involvement of the DMM source and, to a lesser extent, of the PAL component (Fig. 3.12) with respect to the US that have instead a deeper melting column (> 60-100 km-deep), a more OIB-like mantle source (Fig. 3.11) and a major involvement of the Afar plume component (Fig. 3.12). These observations indicate variation in the mantle source between the three Series. Both trace element and isotopic composition indicate that crustal contamination did not have an important effect for the three Series, with possible the exception of the four Low Ti-Fe lavas (Fig. 3.10; Fig. 3.11; Fig. 3.12). A group of US samples of the Serdo-Silsa area, having age around 1 Ma, show a shallower partial melting and an isotopic composition scattering

toward the PAL and the DMM end-member with respect to the other US (Fig. 3.12) indicating variation in the mantle source toward the end of the US activity. Lastly the mantle source and depth of partial melting of the two CAG samples collect at the Immino graben are similar to the Tendaho US with respect to other CAG, possible revealing different evolutionary stage for the two rift branches.

4. The crustal magmatic systems in Central Afar

4.1. Introduction

Studies of crustal magmatic systems, together with the mantle characteristics and melting conditions, is a key aspect in order to investigate the continental breakup processes and rift evolution. The spatial and temporal variation of the volcanic magmatic systems, the architecture of the magmatic reservoirs and the magma ascending paths, are important petrological constraints that can provide information regarding the breakup processes and the transition from continental rifting to oceanic spreading. Therefore, these petrological studies could also give insight into the crustal response during rift evolution. Furthermore, petrological studies of the voluminous eruptions taking place in rift settings are of primarily importance in order to understand the causes of the now widely recognized temporal relation between continental flood basalts (CFB) and perturbation of the planet ecosystem (i.e., climate shifts, environmental changes, mass extinctions; e.g., Clapham and Renne, 2019; Black and Gibson, 2019).

Emplacement of CFB has been long associated with the rifting and continental breakup process (e.g., Courtillot et al., 1999; Hooper, 1990). Petrological and geophysical studies reveal the presence of magma underplating, dyke swarms and crustal magmatic intrusion during CFB formation. However, the architecture of the magmatic system, the path of magma rising and the chemical evolution of the magma remain matters of debate (Ernst, 2019; Jerram and Widdowson, 2005; Magee et al., 2018; Mittal and Richards, 2021a, b). It also remains unclear how the magmatic systems and the associated volcanism evolve during rift evolution. Shallow magmatic reservoirs have been observed for the on-land well developed magmatic segment, together with deeper magmatic systems (Pagli et al., 2012; Medynski et al., 2015; Xu et al., 2020; Desissa et al., 2013; Didana et al., 2014). Studies of mid-oceanic ridges reveal the presence of axial melt lens 1-2 km deep, fed by episodic magma batches rising from the shallow asthenosphere (Carbotte et al., 2016; Marjanović et al., 2015). Furthermore, in the last years the emerging idea of a source-to-surface, vertically extended, *mush-magma-host rock* magmatic system has been suggested for various geological setting, with the deeper portion of the magmatic system feeding chambers in the

upper crust and/or the eruptions (Cashman et al., 2017; Lissenberg, et al., 2018; Edmonds et al., 2019; Sparks et al., 2019).

The Afar depression is an excellent place to study the magmatic system evolution and the crustal response in relation to the ongoing continental-oceanic transition. In this chapter I focused on the southern Red Sea rift in Central Afar along the Manda Hararo-Tendaho graben segment. I used a petrologic and geochemical approach to investigate the magmatism of the Afar Upper Stratoid flood basalts (hereafter US; 2.6-1.1 Ma) and the activity of the more localized Central Afar Gulf Series (hereafter CAG; 1.1-0.6 Ma) in order to investigate and interpret the magmatic system evolution and the crustal response during rift focusing in Central Afar.

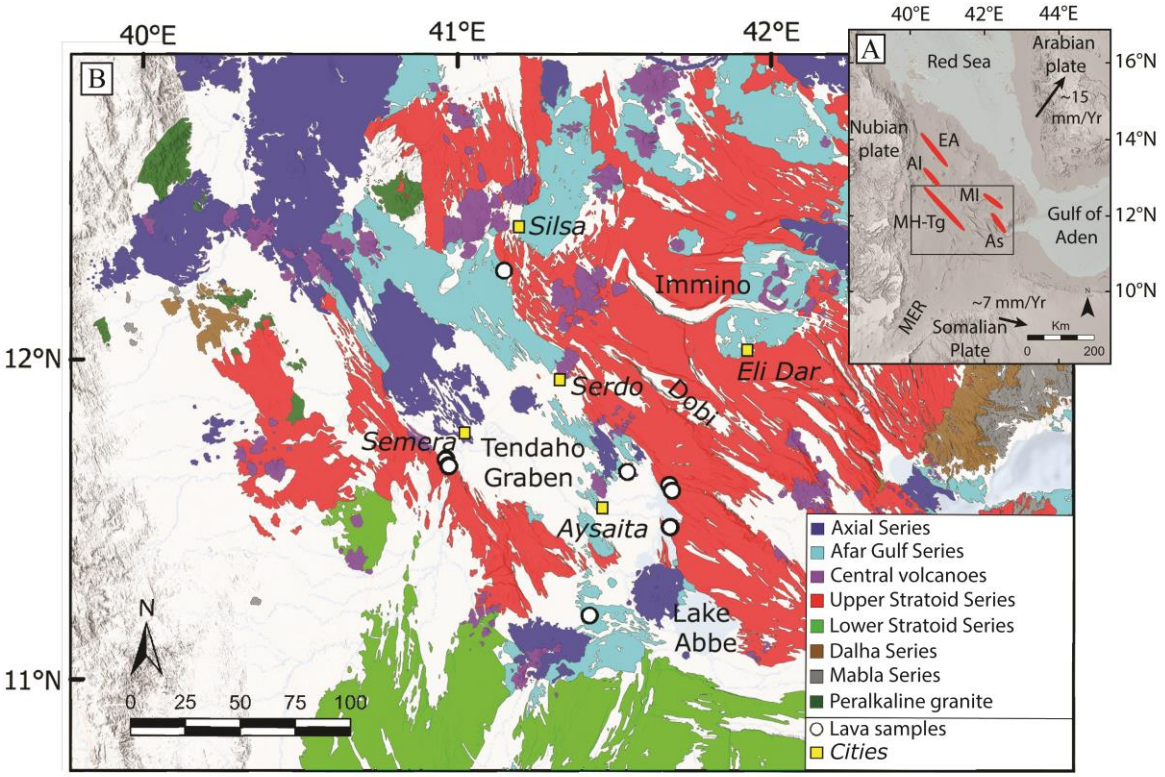

Fig. 4.1 (a) Multi-Directional Hillshade map of Afar with inland Red Sea and Gulf of Aden magmatic segments in red. Spreading vector with respect to Nubia fixed plate. The black box encloses the Central Afar represented in picture (b). EA, Erta Ale; Al, Alayta; MH-Tg, Manda Hararo-Tendaho graben; As Asal; MER, Main Ethiopian Rift. (b) Geological map of Central Afar modified from chapter 3.

4.2. Geological and volcanological background

The study area is located at the intersection of the northernmost portion of the East African Rift System (i.e., Main Ethiopian Rift, MER) with the Red Sea and Gulf of Aden rifts in the Afar

rift-rift-rift triple junction (Fig. 4.1a). In Afar, the transition from continental rifting to oceanic spreading is exposed subaerially (Bastow and Keir, 2011; Bastow et al., 2018; Makris and Ginzburg, 1987). The onset of the activity is thought to be related to the arrival of a mantle plume around 45 Ma and the emplacement of the flood basalt volcanic successions, which took place mainly over ∼1 Myr, at about 30 Ma (Ebinger et al., 1993; Hofmann et al., 1997; Kieffer et al., 2004; Pik et al., 1999). The rifting between the Arabia, Nubia and Somalian plates started around ~35 Ma in the east of the Gulf of Aden, at ~27.5-23 Ma in the south Red Sea and at ~25 Ma in the Afar region (Hughes et al., 1991; Watchorn et al., 1998; Barberi et al., 1972; Bosworth et al., 2005) while seafloor spreading started at ∼20 Ma in the Gulf of Aden (Fournier et al., 2010) and at ~5 Ma in the south-central Red Sea (Searle and Ross, 1975; Cochran, 1983).

Within Afar, volcano-tectonic reconstruction by Wolfenden et al. (2005) suggests that by 16 Ma the locus of strain of the Southern Red Sea migrated eastward from the western border to the central areas, accompanied by a narrowing of the active zone of extension until 7 Ma. Similarly, Kalb (1995) reveals a northeast migration of the paleo-depocenter formation across Southern Afar during ∼10–3 Ma suggesting a northeast migration of the strain location. Furthermore, according to geophysical and stratigraphic evidence, the locus of strain migrated from South to Central Afar, starting from 8 Ma (Wynn et al., 2008; Hammond et al., 2011). Around 1 Ma, after the emplacement of the US (2.6-1.1 Ma), the rift started to progressively localize the extension, from a diffuse distribution (i.e., Stratoid Series) to a localised distribution (i.e., magmatic segments), leading to the formation of the magmatic segment of Central Afar with the emplacement of the CAG Series (∼1.1-0.6 Ma; Gasse et al., 1983; Stab et al., 2016; Rooney, 2020b). Spanning in time between the end of the US and the beginning of the CAG, several silicic central volcanoes were formed and are indicated as the precursor of the magmatic segment development in Central Afar (Barberi and Santacroce, 1980; Lahitte et al., 2003a, b). The ongoing Axial activity (<0.6 Ma) of the Red Sea rift is observed along the Erta Ale Range in North Afar and the Manda Hararo-Tendaho graben in Central Afar (Fig. 4.1). The Tendaho graben started forming at ∼1.8 Ma (Acton et al., 1991, 2000) and it is now tens of km wide and hundreds of km long. It reaches 1000 m in height cutting the US (2.6-1.1 Ma) while CAG and Axial products are observed only inside the graben. According to Acocella (2010) the formation of the Tendaho graben is partially

due to the collapse induced by the voluminous eruption of the Stratoid and its magmatic and tectonic activity decreased in the last ~0.2 Ma after the development and on-land migration of the Gulf of Aden (Acocella, 2008).

A 30-km-wide and 35-km-depth sill-like region extending into the mantle, with an estimated magma volume of at least 500 km^3 has been suggested using magnetotelluric investigation in Central Afar (Desissa et al., 2013). The crust is ~25-30 km thick, getting thinner (~23 km) under the Manda Hararo segment (Ahmed et al., 2022; Hammond et al., 2011; Wang et al., 2021). Presence of melt associated with the ongoing activity in the area of the Manda Hararo-Tendaho graben has been imaged at 6-12 km (Guidarelli et al., 2011) and at 5-15 km deep (Didana et al., 2014) by means of seismic tomography and magnetotelluric data. In Central Afar, crustal scale seismic anisotropy is consistent with presence of a combination of stacked sills and vertical dikes (Hammond et al., 2014; Chambers et al., 2022) feeding eruption or ephemeral magma chambers in the upper crust. By means of petrological studies, Field et al. (2012a) identified a system of stacked sills from 1 to 5 km below the currently active Dabbahu volcano, in agreement with their storage depths estimates from seismology and InSAR analysis.

The US, as well as several other flood basalt deposits (Jerram and Widdowson 2005; Single and Jerram 2004), are dominated by basaltic lava successions but, at the same time, primary basalts are rare and primitive lavas have not been found in Central Afar, hindering the development of robust models of magma evolution for the more mafic terms. Furthermore, these magmas are chemically homogeneous and moderately fractionated, indicating that they resided and differentiated in the crust before being erupted. Lastly, these lavas are generally aphyric, making it difficult to study magma evolution by means of mineral chemistry. The CAG are instead less voluminous, still dominated by basaltic lava flows but slightly more porphyritic and mafic with respect to the Stratoid. To my knowledge, only the preliminary study made in chapter 3 has been carried out on the US and CAG, suggesting evolution by means of fractional crystallization for both Series and variation in the crustal storage, with the CAG ponding at ~5-7 km while no stationing in the upper crust was observed for the US.

4.3. Results

4.3.1. Rock classification and petrography

The whole-rock geochemistry and petrography of the US and CAG has been previously described (Chapter 3). The US and CAG Series are mainly basalt-basaltic andesites, with minor evolved products (Fig. 4.2). Both the Series are subalkaline, with transitional to tholeiitic affinity. The lavas of the US Series are mainly aphyric with rare micro-porphyritic or moderately porphyritic types; plagioclase is the most abundant phenocryst, while olivine and clinopyroxene are common only in the more primitive lavas. The CAG are micro-porphyritic or porphyritic with minor aphyric samples; plagioclase is the most abundant phenocryst phase, but olivine and clinopyroxene phenocrysts are also common (Fig. S4.1; Tab. S2.1). For this microanalytical study I selected five US and three CAG mafic samples of the area of the Tendaho graben in Central Afar, based on the petrographic (presence of phenocrysts) and chemical characteristics of the two Series. Six of the selected samples have been previously studied in chapter 3 while two US samples (Z16 and Z131; Tab. S2.1) have been selected from the Afar Repository of the University of Pisa and presented for the first time in this chapter. For both Series I have selected samples with MgO in the range 4-6 wt% (hereafter low-MgO samples and representing the majority of the erupted lavas, Fig. 4.2) and 6-8.5 MgO wt% (hereafter high-MgO samples) (Fig. 4.2; Tab. S2.1).

The selected US high-MgO samples are moderately porphyritic (10% vol.) and phenocrysts are mainly olivine and clinopyroxene with minor plagioclase. The US low-MgO range from nearly aphyric to plagioclase-dominated porphyritic samples with rare clinopyroxene and olivine (Fig. S4.1; Tab. S2.1).

The CAG high-MgO sample has an ophitic texture dominated by clinopyroxene and olivine with minor plagioclase. The CAG low-MgO are porphyritic (up to 20% vol.), plagioclase-dominated but showing an increase in size and abundance of clinopyroxene and olivine with respect to the US low-MgO samples. Both the CAG low-MgO samples show evidence of possible magma mingling in the thin sections (Fig. S4.1). Two different Fe-Ti oxides (Ti-magnetite and ilmenite) have been observed in all the samples. The groundmass is composed of plagioclase, clinopyroxene, Fe-Ti oxides and, occasionally, olivine.

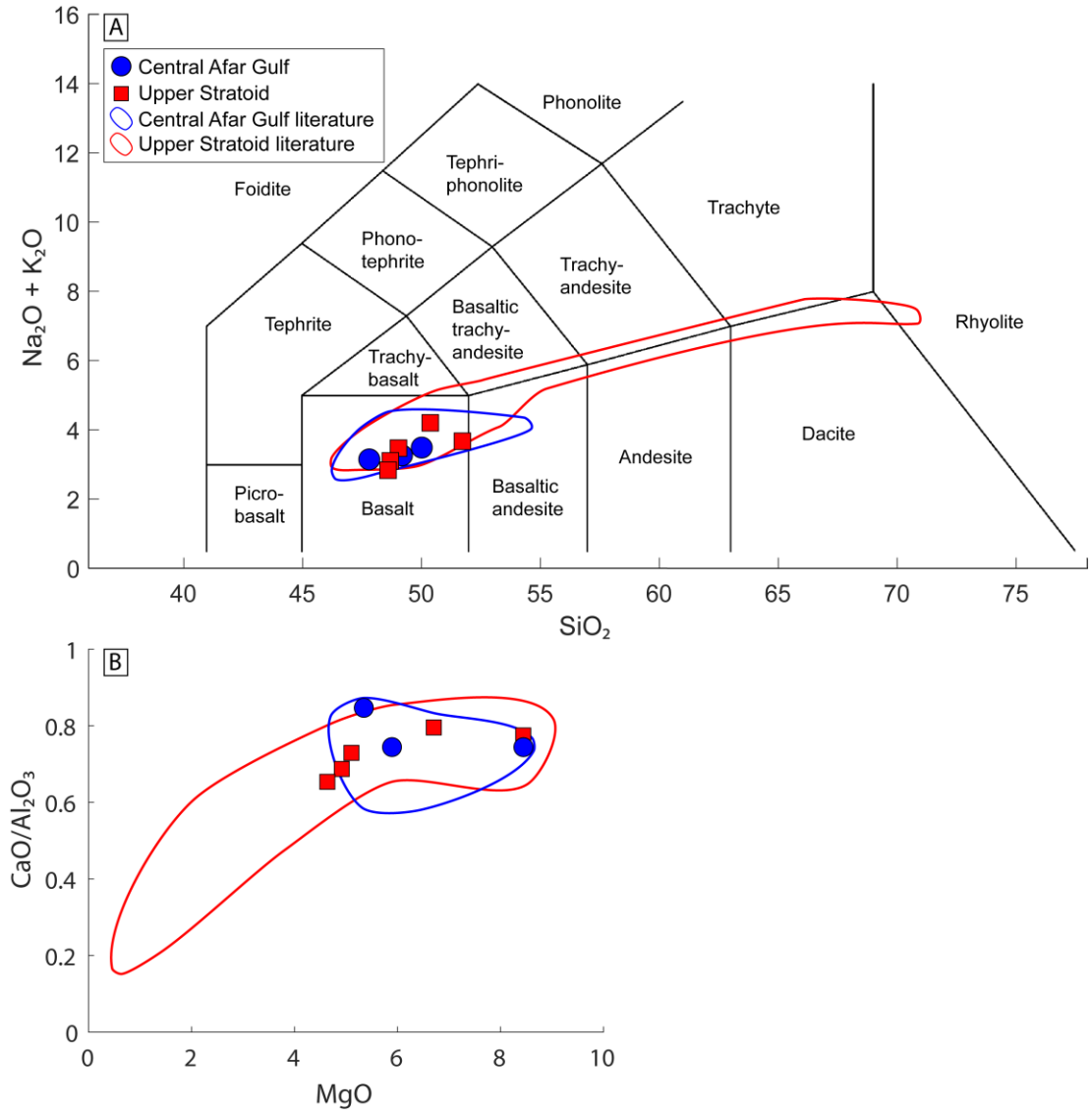

*Fig. 4.2 (a) TAS (Total Alkali vs Silica, wt%) classification diagram for US and CAG lavas. Data recalculated to 100% on a water-free basis. Total iron as FeOtot = FeO+Fe2O3*0.8998. (b) CaO/Al_2O_3 vs MgO variation diagrams (wt%) for US and CAG lavas.. All analyses are reported in Tab. S2.1. Fields are data from chapter 3, Feyissa et al. (2019) and Barberi and Santacroce (1980).*

4.3.2. Mineral chemistry

In this section I present the mineral chemistry results of plagioclase, clinopyroxene, olivine and Fe-Ti oxides for the two series (Fig. S4.3; Tab. S2.1).

4.3.2.1. Plagioclase

Plagioclase covers an overall similar compositional range in the two series, with phenocryst composition from bytownite to andesine (An_{29-88} for the US and An_{27-85} for the CAG) (Fig. 4.3a, b), and a bimodal distribution of the core composition (modes An_{67} and An_{83} for the US

and modes An_{71} and An_{78} for the CAG, Fig. 4.3c, d). The bimodality in the plagioclase core composition corresponds to the low-MgO and high-MgO rock groups (Fig. 4.3e, f, g, h).

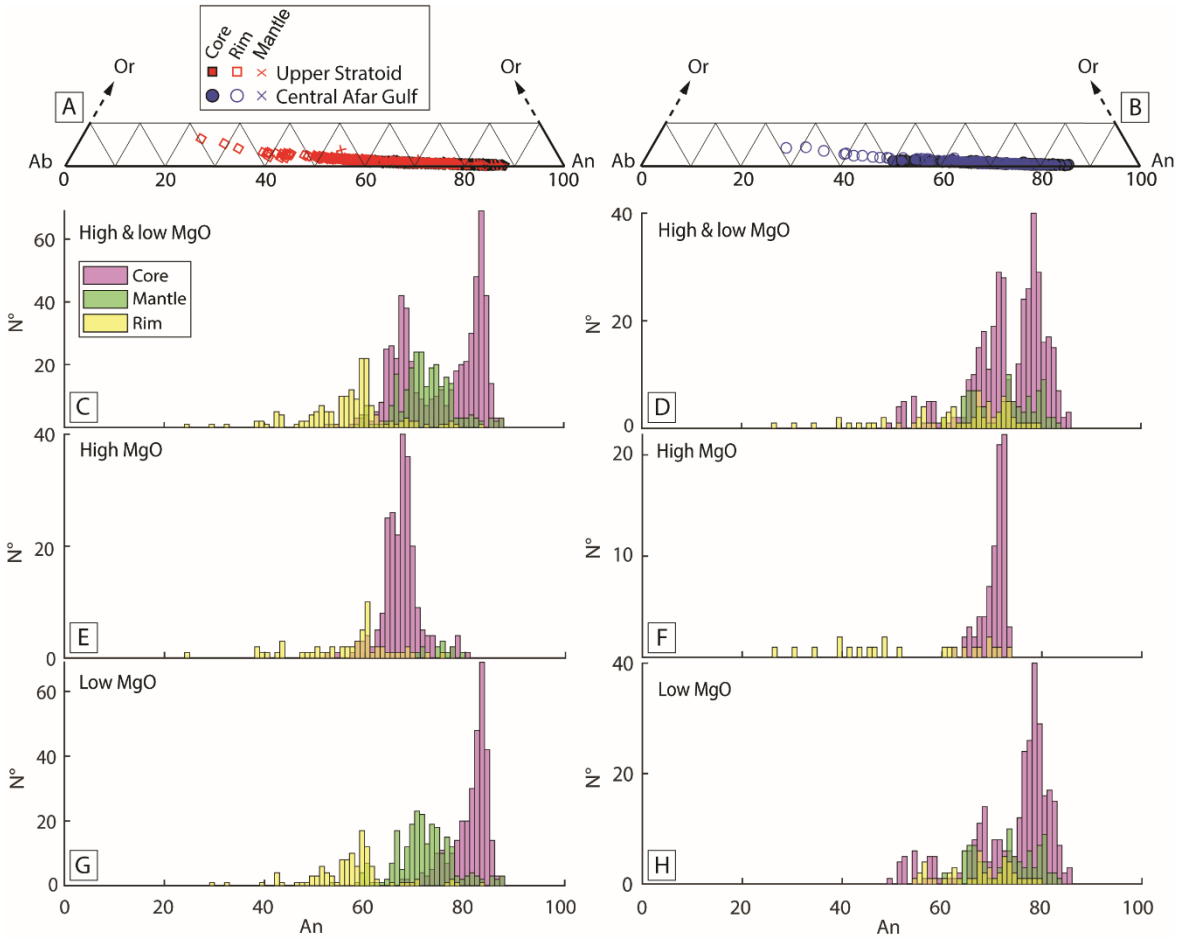

Fig. 4.3 (a, b) Feldspar (An-Ab-Or) classification diagrams of US (a) and CAG (b). (c-h) Feldspar histograms (An) for core, mantle and rim analyses of US and CAG. US high- and low-MgO samples (c), high-MgO (e) and low-MgO (g) samples are on the left side. CAG high- and low-MgO samples (d), high-MgO (f) and low-MgO (h) samples are on the right side. All EPMA data are reported in Tab. S2.1.

Regarding the US high-MgO samples, plagioclase phenocrysts are mainly normally zoned or unzoned, with core composition corresponding to the lower An mode (range An_{53-80} and mode An_{67}) and overlapping or lower An for the rim (range An_{24-76} and mode An_{60}) (Fig. 4.3e). However, few plagioclase crystals show a more complex zoning with an oscillation or rim to An-rich composition (An_{75-80} in Fig. 3e). In the US low-MgO samples the plagioclase crystals are normally zoned, with core composition corresponding to the higher An cores mode (range An_{54-88} and mode An_{83}) and a compositional gap with the lower An rim (range An_{29-84} and mode An_{59}). This gap between core and rim is partially covered by the mantle analyses (range An_{53-87} and mode An_{71}) (Fig. 4.3g). Regarding the CAG, the high-MgO samples have normally zoned or unzoned plagioclase, with core composition corresponding to the lower

An cores mode (range An_{63-74} and mode An_{72}) and overlapping or lower An for the rim (range An_{27-73}) (Fig. 4.3f). In the CAG low-MgO samples the plagioclase are normally and reversed zoned, with core composition corresponding to the higher An cores mode (An_{78}). The plagioclase core, mantle and rim analyses broadly overlap, with the cores having a major mode at An_{78} and two minor modes at An_{54} and An_{68} and mantle and rim ranging respectively An_{60-83} and An_{54-80} (Fig. 4.3h).

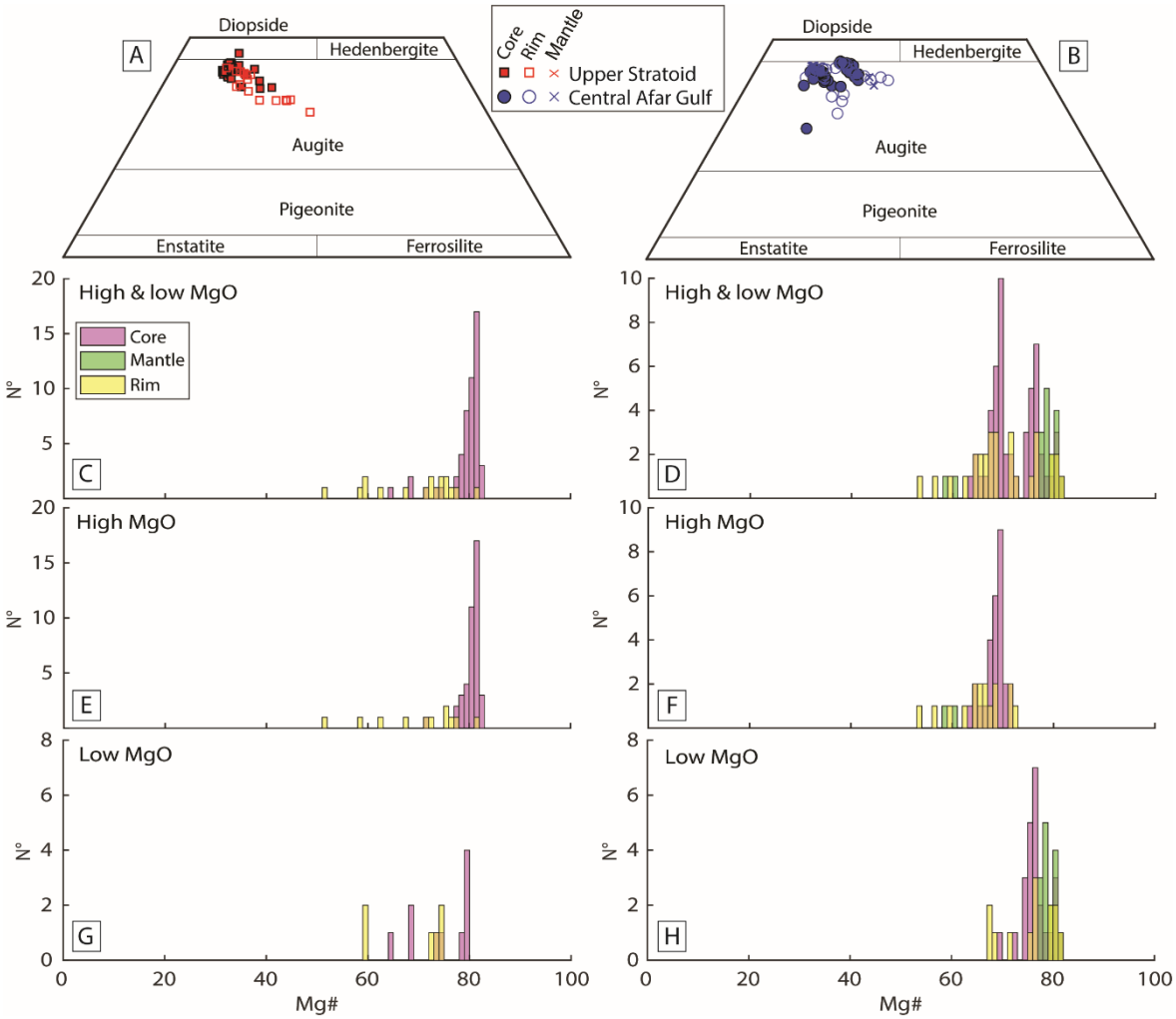

Fig. 4.4 (a, b) Clinopyroxene (En-Fs-Hd-Di) classification diagrams of US (a) and CAG (b). (c-h) Clinopyroxene histograms (Mg#) for core, mantle and rim analyses of US and CAG. US high- and low-MgO samples (c), high-MgO (e) and low-MgO (g) samples are on the left side. CAG high- and low-MgO samples (d), high-MgO (f) and low-MgO (h) samples are on the right side. All EPMA data are reported in Tab. S2.1.

4.3.2.2. Clinopyroxene

All the clinopyroxene of both series are augite, close to the diopside field, with a broadly similar distribution, with the exception of the CAG high-MgO sample, having a trend shifted toward the hedenbergite field (Fig. 4.4a, b). The two series have overall a similar

compositional range (range $Mg\#_{52-82}$ and $Mg\#_{54-81}$ for the US and CAG respectively) but with a unimodal distribution for the US core composition (mode $Mg\#_{81}$) and a bimodal distribution for the CAG core composition (mode $Mg\#_{69}$ and $Mg\#_{76}$) (Fig. 4.4c, d). The bimodality in the CAG core composition corresponds to the low-MgO and high-MgO rock groups (Fig. 4.3d, f, h).

Regarding the US, the high-MgO samples have normally zoned clinopyroxene with high Mg# values (range $Mg\#_{71-82}$ and mode $Mg\#_{81}$) and lower Mg# for the rim (range $Mg\#_{52-81}$) (Fig. 4.4e). The US low-MgO samples have few and unzoned clinopyroxene with variable Mg# for the core (range $Mg\#_{65-80}$) and overlapping Mg# for the rim (range $Mg\#_{59-75}$) (Fig. 4.4g). Regarding the CAG, the high-MgO samples have normally zoned or unzoned clinopyroxene with core composition corresponding to the lower Mg# mode (range $Mg\#_{64-72}$ and mode $Mg\#_{69}$) and overlapping or slightly lower Mg# for the rim (range $Mg\#_{54-73}$) (Fig. 4.4f). The CAG low-MgO samples have normally and, in some cases, reversely zoned clinopyroxene with core composition corresponding to the higher Mg# mode (range $Mg\#_{69-81}$ and mode $Mg\#_{76}$) and slightly higher Mg# for some mantle and rim (Fig. 4.4h).

4.3.2.3. Olivine

The US olivine have a wider compositional range (range Fo_{29-85}) with respect to the CAG (range Fo_{55-82}) and a bimodal distribution of core compositions (Fo_{74} and Fo_{83}) while the CAG have instead a unimodal distribution (Fo_{77}) (Fig. 4.5a, b, c, d). Despite the US bimodality not being related to the core composition of the low-MgO and high-MgO rock groups, variation between them has been observed (Fig. 4.5c, e, g). Iddingsite is present at the rim and along the fractures of some crystals and avoided as far as possible during the analysis.

Regarding the US, the high-MgO samples have olivine with normal zoning or unzoned with cores in the range Fo_{69-84} and modest intrasample variation (Fig. 4.5e; the bimodal distribution is due to distinct samples). The US low-MgO samples have few and normally zoned olivine with slightly lower Fo with respect to the high MgO samples (Fig. 4.5e, g). Regarding the CAG the high-MgO samples have olivine with normal zoning or unzoned with core composition corresponding to the higher Fo values of the CAG (range Fo_{76-82}; Fig. 4.5f). The low-MgO samples have olivine with normal zoning, with core composition corresponding to the lower Fo values of the CAG (range Fo_{74-80}; Fig. 4.5h).

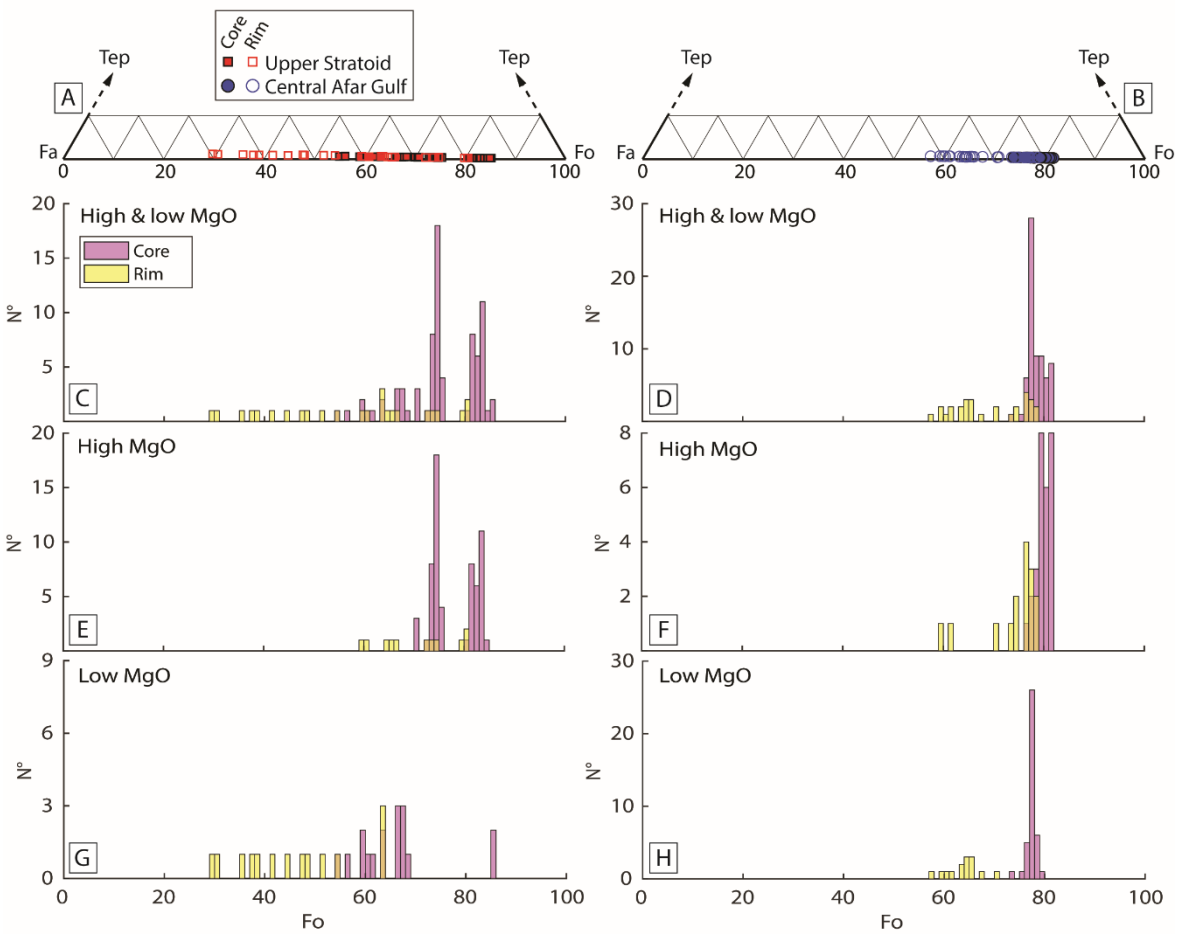

Fig. 4.5 (a, b) Olivine (Fo-Fa-Tep) classification diagrams of US (a) and CAG (b). (c-h) Olivine histograms (Fo) for core, mantle and rim analyses of US and CAG. US high- and low-MgO samples (c), high-MgO (e) and low-MgO (g) samples are on the left side. CAG high- and low-MgO samples (d), high-MgO (f) and low-MgO (h) samples are on the right side. All EPMA data are reported in Tab. S2.1.

4.3.2.4. Fe-Ti oxides

Fe-Ti oxides as accessory minerals have been observed in all samples, sometimes enclosed at the rim or mantle of phenocrysts. (Fig. S4.1). Both the US high and low-MgO samples have ilmenite and titanomagnetite with ulvöspinel component up to 78% (Fig. S4.2). No clear coexisting pairs have been found and, based on back scattered electron imaging and microanalytical analysis, ilmenite seems to precede titanomagnetite. Both CAG high and low-MgO samples have Ilmenite (except for one low-MgO sample) and titanomagnetite (Fig. S4.2). Furthermore, chromite has been observed in both the US and CAG high-MgO samples, always included in olivine with the exception of one analysis in the groundmass (Tab. S2.1).

4.3.3. Phenocrysts textures and chemical zoning

In this section I describe the texture and the core to rim major and trace element compositional profiles of 15 high-MgO US and 23 low-MgO US plagioclase phenocrysts, 5 high-MgO CAG and 21 low-MgO CAG plagioclase phenocrysts and 2 low-MgO CAG clinopyroxene phenocrysts analyzed by mean of EPMA (Fig. 4.6; all profiles in Fig. S4.4).

4.3.3.1. Upper Stratoid

The prevalent plagioclase type in US high-MgO samples is normally zoned, with homogeneous core with mean An_{67}, and high TiO_2 (mean 0.12 wt.%) and no or very thin rims, averaging An_{43} and showing an increase in TiO_2 (mean 0.15 wt.%) with respect to the core (Fig. 4.6a; Fig. S4.4). Distinctive crystals have been observed, sometimes with a sieved core, with core or mantle having high An (mean An_{77}) and low TiO_2 (mean 0.09 wt.%) (Fig. S4.4).

Two main types have been observed for the US low-MgO samples: I) homogeneous and rounded cores with high An (mean An_{82}) and low TiO_2 (mean 0.07 wt.%) and thin rims marked by an abrupt decrease in An (mean An_{53}) and increase in TiO_2 (mean 0.15 wt.%) (Fig. 4.6b); some have a resorbed core and slightly lower An, averaging An_{78} (Fig. S4.4). II) homogeneous rounded cores with high An (mean An_{82}) and low TiO_2 (mean 0.07 wt.%) mostly showing an abrupt normal zonation to an oscillatory or homogeneous mantle averaging An_{72} and showing an increase in TiO_2 (mean 0.10 wt.%) (Fig. 4.6c). Sometimes a gradual variation is observed in BSE images, confirmed by An and TiO_2 content (Fig. S4.4). The crystals show homogenous rims, with a decrease in An (mean An_{57}) and increase in TiO_2 (mean 0.13 wt.%) with respect to the mantle. Only two crystals show distinctive characteristics (Fig. S4.4) having a patchy and resorbed low An (mean An_{73}) and low TiO_2 (mean 0.09 wt.%) core and an oscillatory mantle (mean An_{68} and TiO_2 0.11 wt.%) or a reversely zoned mantle (mean An_{83} and TiO_2 0.07 wt.%). Both have a normally zoned rim with a decrease in An (mean An_{59}) and increase in TiO_2 (mean 0.14 wt.%).

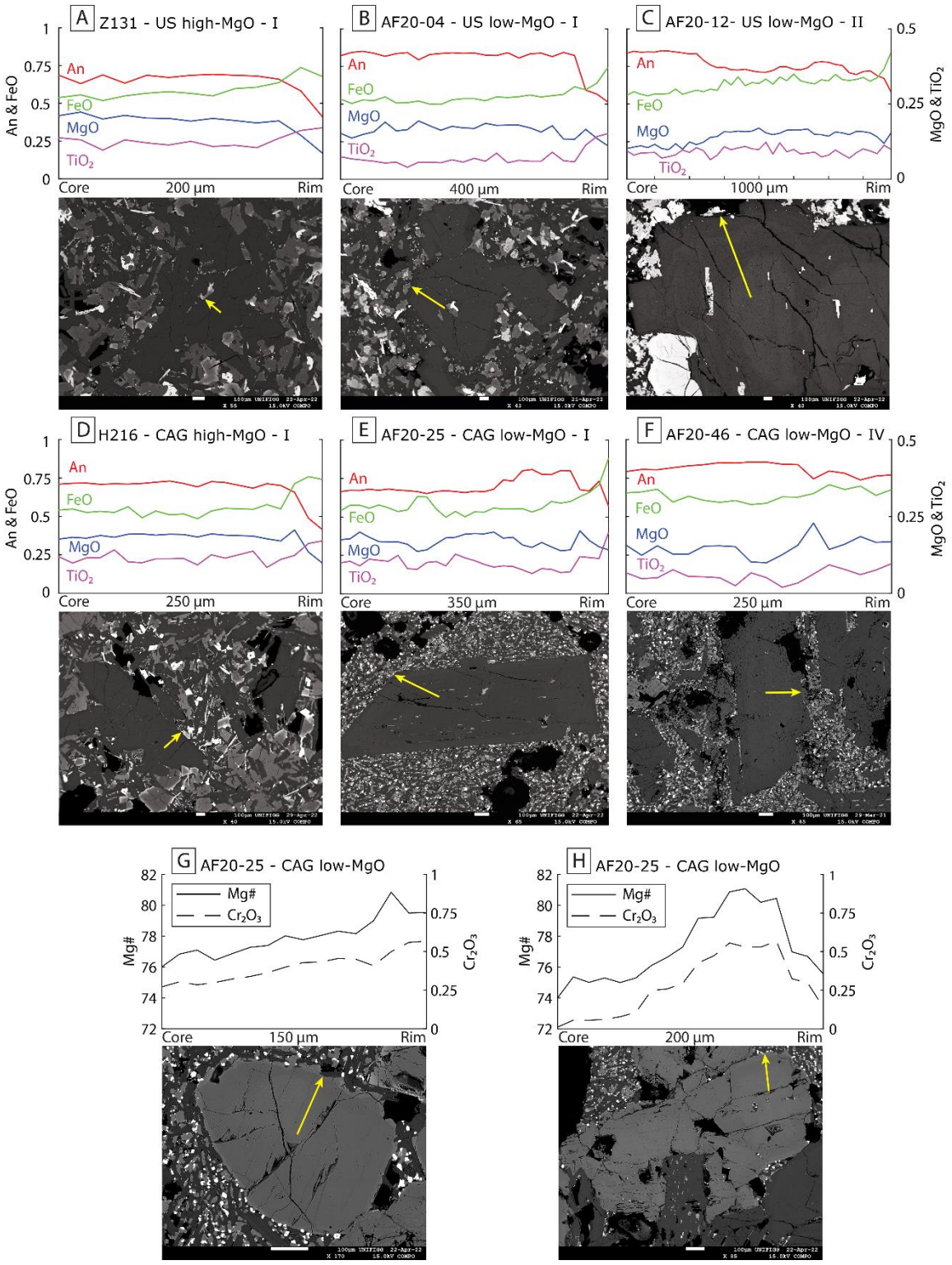

Fig. 4.6 (a-f) Representative plagioclase compositional profiles of anorthite content, FeO, TiO_2 and MgO concentration with relative SEM pictures for: (a) US high-MgO sample; (b, c) US low-MgO samples; (d) CAG high-MgO sample; (e, f) CAG low-MgO samples. The location of the analysis profiles is indicated with a yellow arrow in each SEM picture. All plagioclase profile and relative SEM pictures are in Fig. S4.4. (g, h) Clinopyroxene compositional profiles of Mg# content (Mg# = (Mg/(Mg + Fe^{2+}) × 100) and Cr_2O_3 concentration with relative SEM pictures for CAG low-MgO samples. The location of the analysis profiles is indicated with a yellow arrow in each SEM picture. Each profile is titled with the sample name, the Series name acronym, the low- or high-MgO group and the crystal typology number (description in text).

4.3.3.2. Central Afar Gulf

The plagioclase phenocrysts of high-MgO CAG samples have homogeneous cores with constant and relatively low An, averaging An_{70}, and high TiO_2 (0.11 wt.%); they have no or very thin rims, showing a decrease in An (mean An_{47}) and increase in TiO_2 (0.15 wt.%) with respect to the core (Fig. 4.6d; Fig. S4.4).

The low-MgO CAG plagioclase show overall more complexity with respect to the US and five different types of plagioclase have been recognized (Fig. 4.6e, f; Fig. S4.4): I) innerly resorbed and rounded cores with variable An (range An_{60-82}) and low TiO_2 (mean 0.09 wt.%), with complex mantles showing oscillatory and/or reverse zoning with An averaging An_{77} and overall similar or lower TiO_2 (mean 0.09 wt.%). The rims show a decrease in An (mean An_{65}) and increase in TiO_2 (mean 0.15 wt.%) (Fig. 4.6e; Fig. S4.4). II) Homogeneous or slightly oscillatory cores with high An (mean An_{74}) and low TiO_2 (mean 0.09 wt.%). An abrupt decrease in An (mean An_{66}) and slight increase in TiO_2 (mean 0.11 wt.%) marks the passage to mantles, sometimes having a small reverse zoned portion toward the rims with an increase in An. No or thin normally zoned rims (mean An_{60} and TiO_2 0.21 wt.%) have been observed (Fig. S4.4). III) Homogeneous cores with low An (mean An_{61}) and high TiO_2 (mean 0.13 wt.%) and slightly zoned mantle or rim with an increase of An (mean An_{68}) and decrease in TiO_2 (mean 0.11 wt.%) (Fig. S4.4). IV) Homogeneous or lightly oscillating rounded cores (one resorbed) with constant or gradual (one with a more marked step) slightly increasing An (range An_{68-85}) and constant low TiO_2 (mean 0.07 wt.%) (Fig. 4.6f; Fig. S4.4). No or normally zoned rims (mean An_{73} and TiO_2 0.09 wt.%) have been observed. V) Homogeneous or lightly oscillating rounded cores with gradual slight decrease in An (range An_{65-84}) and constant TiO_2 (mean 0.07 wt.%) (Fig. S4.4). No or normally zoned rims (mean An_{67} and TiO_2 0.10 wt.%) have been observed. One crystal shows distinctive characteristics (Fig. S4.4) having an innerly resorbed and rounded core with low An (mean An_{53}) and low TiO_2 (mean 0.11 wt.%) and reverse zoned rim with an abrupt increase of An (mean An_{79}) and similar TiO_2 (mean 0.10 wt.%).

Two low-MgO CAG clinopyroxene shows oscillatory and reverse zoning with rim and mantle reaching higher Mg# and Cr_2O_3 (respectively up to 81 and 0.57 wt.%) with respect to the cores (up to Mg# 77 and Cr_2O_3 0.32 wt.%; Fig. 4.6g, h).

4.3.4. Mineral-melt equilibrium and geothermobarometry

I used the plagioclase geothermobarometer of Putirka (2008) to calculate the pressure (eq. 25a, SEE = ±3.8 kbar) and temperature (eq. 24a SEE = ±36 °C) of crystallization. The clinopyroxene pressure and temperature of crystallization has been calculated using the Neave and Putirka (2017; SEE = ±1.4 kbar) and Putirka (2008; eq. 33 SEE = ±45 °C) respectively (Tab. S2.1). I used the whole rock analysis as melt composition according to Putirka (2008) and a water concentration input of 0.5 wt% according to evidence from literature of low water content of Afar mafic magmas (Field et al., 2012a, b, 2013; Natali et al., 2011; Gleeson et al., 2017) and to the MELTS best fit model of chapter 3. The equilibrium was checked based on the distribution coefficient $KD_{(An-Ab)}^{pl-liq}$ = 0.27 ± 0.11 at T ≥ 1050°C (Putirka, 2008) for the plagioclase and based on the distribution coefficient $KD_{(Fe-Mg)}^{cpx-liq}$ = 0.28 ± 0.08 for the clinopyroxene. I estimated the storage conditions of the magma based on the core and mantle analyses in equilibrium with the host rock. The corresponding depths have been derived assuming a 270 bar/km geobaric gradient (Best, 2013).

The US high-MgO samples clinopyroxene are in equilibrium with the host rock at overall 3-5 kbar (mean 3.8 ± 1.4 kbar) and 1145-1202 °C (mean 1174 ± 45 °C) (Fig. 4.7a). The plagioclase phenocrysts of US high-MgO samples are in equilibrium with the host rock at 1.8-3.4 kbar (mean 2.8 ± 3.8 kbar) with a temperature of 1160-1170C° (mean 1163 ± 36 °C) (Fig. 4.7b). The US low-MgO samples have clinopyroxene analyses in equilibrium with the host rock at 1.1-3 kbar (mean 2.1 ± 1.4 kbar) and 1126-1144 °C (mean 1132 ± 45 °C) (Fig. 4.7a). Regarding the US low-MgO samples plagioclase, the high An cores are in disequilibrium with their host rocks, while the lower An core and mantle (An_{66-82}) are in equilibrium with the whole rock at 3.6-5.2 kbar (mean 4.3 ± 3.8 kbar) and temperatures of 1173-1184 °C (mean 1179 ± 36 °C) (Fig. 4.7b). Moreover, according to the KD equilibrium test, few plagioclase of one low-MgO sample with low An (An_{69-76}) core analyses (Fig. S4.4b) crystallized at very shallow depth (equilibrium at <1 km of depth; Fig. 4.7b).

None of the CAG high-MgO samples clinopyroxene are in equilibrium with the host rock. The plagioclase of the CAG high-MgO sample are in equilibrium with the host rock at 3.7-4.4 kbar (mean 3.9 ± 3.8 kbar) with a temperature of 1158-1164 °C (mean 1161 ± 36 °C) (Fig. 4.7b). The CAG low-MgO clinopyroxene are in equilibrium at overall 3-5 kbar (mean 3.7 ± 1.4 kbar)

and 1146-1175 °C (mean 1164 ± 45 °C) (Fig. 4.7a). The plagioclase of the low-MgO CAG samples are in equilibrium at 1.2-4 kbar (mean 2.2 ± 3.8 kbar) with a temperature of 1164-1178 °C (mean 1173 ± 36 °C) (Fig. 4.7b).

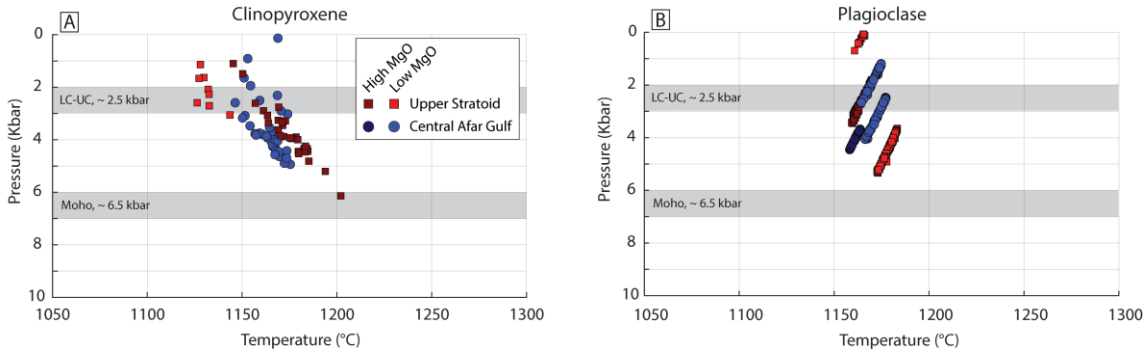

Fig. 4.7 a) Pressure and temperature estimates from clinopyroxene–melt pairs calculated with Neave and Putirka (2017; eq. 1) and Putirka (2008; eq. 33). SEE for the clinopyroxene-melt thermobarometer are ± 45 C° and ± 1.2 kbar. b) Pressure and temperature estimates from plagioclase–melt pairs calculated with Putirka (2008; eq.24a and 25a). SEE for the plagioclase-melt thermobarometer are ± 36 C° and ± 3.8 kbar. The depth of the Moho (23-25 km) and of the lower-upper crust limit (7-11 km) are from Hammond et al. (2011).

4.4. Discussion

4.4.1. Upper Stratoid magmatic evolution: insight from whole rock geochemistry

To better constrain the US magma evolution in the deep to shallow magmatic system indicated by the geothermobarometry estimates (overall 1.5-5 kbar; Fig. 4.7), I calculated the fractional crystallization liquid line of descent (LLD) and the resulting mineral phases composition using Rhyolite-MELTS (Gualda et., 2012) by means of AlphaMELTS software (Smith and Asimow, 2005). Due to the paucity of CAG analyses and, consequently, the lack of natural constraints to the model, I performed the modeling only for the US.

I used as starting composition the most mafic sample analyzed in this work (Z16, MgO wt% 8.3) and modeled liquid evolution for given P, T, fO_2 and H_2O wt%, by free-energy minimization at each ΔT step. Each run starts at the liquidus temperature (calculated by MELTS) and based on the clinopyroxene barometric estimates, I used 5 kbar and 1.5 kbar for the deeper and the shallower reservoirs respectively. According to estimations in previous works regarding volcanism within and surrounding Afar, I made water concentration range from 0.5 to 1.5 wt% (chapter 3; Field et al., 2012a, b, 2013; Natali et al., 2011; Peccerillo et

al., 2003; Gleeson et al., 2017) and fO_2 from QFM-0.5 to QFM-1 (chapter 3; Moor et al., 2013; Bizouard et al., 1980). For each initial P-T-H_2O-fO_2 fixed conditions combination, I decompressed the magma from 5 kbar to 1.5 kbar, letting the magma fractionate in the deep reservoir and started decompressing it at different degrees of evolution (8.3, 7, 6, 5 MgO wt%) and at different ΔP (20, 40, 60, 80 bar/C°; Armienti et al., 2008; Newcombe et al., 2020) (Fig. S4.6).

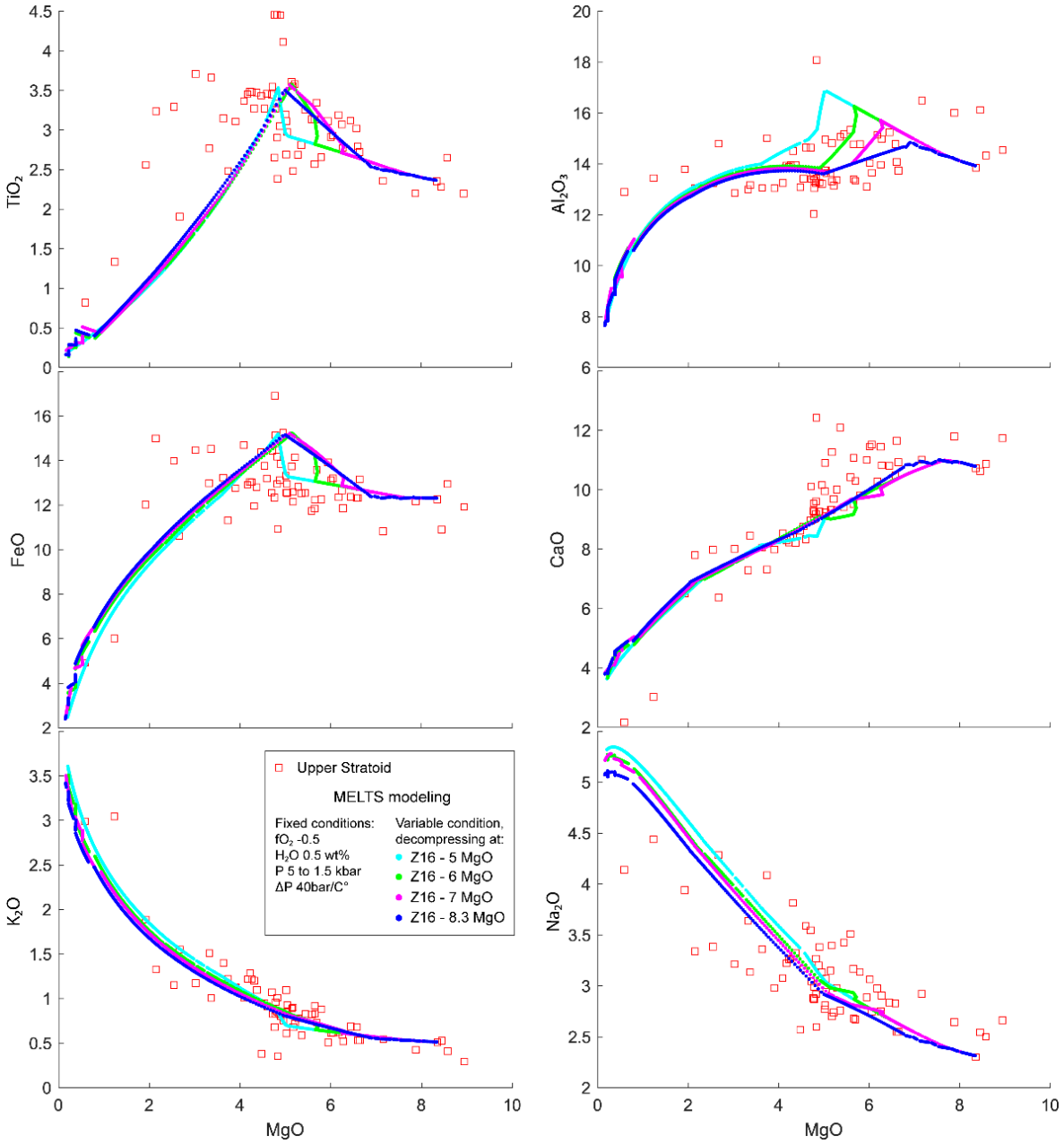

Fig. 4.8 Best fit modeled liquid line of descent for the US Series major element (wt%) by means of rhyolite-MELTS (Smith and Asimow, 2005; Gualda et al., 2012). Using fixed oxygen fugacity (QFM -0.5) and starting water content (0.5 wt.%) I modeled a polybaric system with magma rising at 5, 6, 7 and 8.3 MgO wt% (respectively pale blue, green, purple and blue line) from 5 kbar at 40bar/C° up to and 1.5 kbar. Data are from this work, Feyissa et al. (2019) and Barberi and Santacroce (1980). All the models are in Fig. S4.6.

My modeling fit wells the drop in FeO_t and TiO_2 due to *spinel-in* at MgO 4.5-5 wt % (Fig. 4.8; Fig. S4.6). According to the Al_2O_3 drop due to the *plagioclase-in,* the best fit is H_2O 0.5 wt% (or even lower; Fig. 4.8). Furthermore, the *plagioclase-in* composition given by MELTS best fit models (Fig. 4.8; An70-75) is in excellent agreement with the composition of the analyzed plagioclase in equilibrium with the whole rock (An66-82 and a mean of An72). Given this condition, magma rising at low ΔP (20 bar/C°) inhibits the crystallization of plagioclase for too long, overestimating the melt Al_2O_3 concentration, while magma rising at 40-60 bar/C° fit the drop and variability of Al_2O_3 (Fig. 4.8).

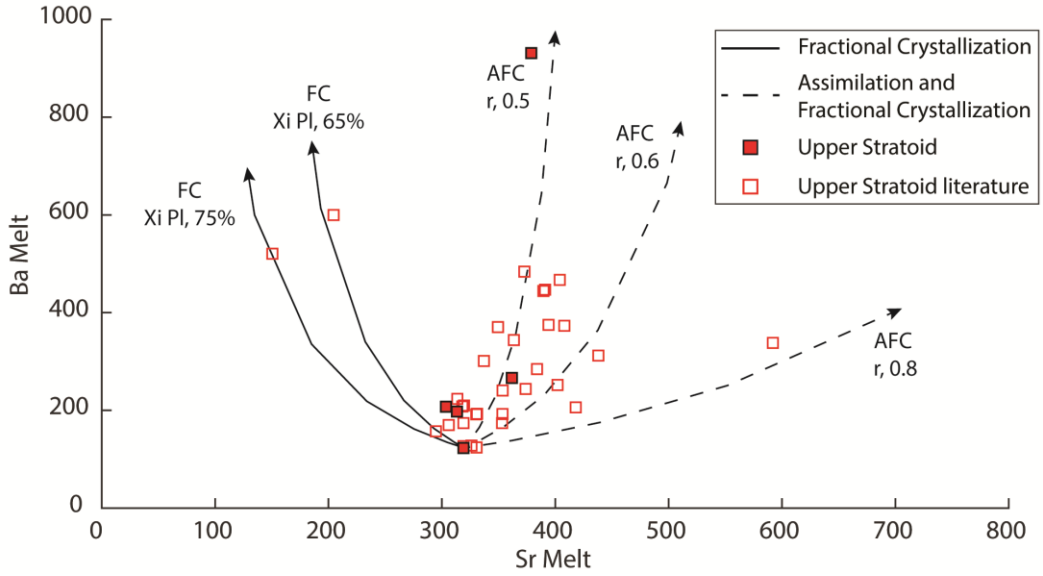

Fig. 4.9 Sr versus Ba whole rock analysis variation diagram. Solid lines show the variations due to fractional crystallization of a mineral assemblage composed of 65% and 75% of plagioclase (Xi, percentage of plagioclase involved in fractional crystallization) together with clinopyroxene, olivine and spinel. The dashed line shows the variations due to assimilation and fractional crystallization (AFC equation of DePaolo, 1981) assimilating at r 0.5, 0.6 and 0.8 (r = rate of assimilation/rate of fractional crystallization) a plagioclase rich mush (assimilant Sr 600 ppm and Ba 30 ppm) and crystallizing 70% of plagioclase (according to MELTS results between plagioclase start to crystalize and magma erupt at ~4 MgO wt%). For both FC and AFC I used the composition of the more mafic sample as starting composition (Z16, MgO wt% 8.3). The partition coefficient for olivine are from McKenzie and O'Nions, (1991; Sr 0.00019 and Ba 0.0003) for clinopyroxene are from McKenzie and O'Nions, (1991; Sr 0.13 and Ba 0.0005) and for spinel are from Elkins et al. (2008; Sr 0.0047 and Ba 0.0006). For the plagioclase the partition coefficients have been calculated using Blundy and Wood (1991; RT ln DSr=26800 – 26700XAn and RT ln DBa=10200 – 38200XAn; Sr 1.91 and Ba 0.23) according to MELTS results between 8-4 MgO wt% (An 72 and T 1130 C°). For the AFC the bulk-rock partition coefficient are 1.36 for Sr and 0.16 for Ba while for FC Xi Pl 65% are 1.26 for Sr and 0.15 for Ba and for FC Xi Pl 75% are 1.45 for Sr and 0.17 for Ba. Empty symbols are from chapter 3 and Feyissa et al. (2019).

However, the scattered Al_2O_3 at 4-6 MgO wt%, in accordance with the scattered and overall constant trend of Sr (Fig. 3.8e), could also be explained by mixing of similarly evolved

magmas with variable, but not strong, plagioclase fractionation, allowing the scattered distribution without decreasing of Al_2O_3 and Sr. Alternatively, assimilation of a plagioclase-rich mush could possibly explain the Al_2O_3 and Sr behavior. Using MELTS results I therefore modeled the Ba and Sr during assimilation and fractional crystallization (AFC equation of DePaolo, 1981). I used Ba and Sr of the plagioclase cores as the assimilant (Sr 600 ppm and Ba 30 ppm), assumed a 70% crystallization of plagioclase (according to MELTS results between plagioclase starting to crystalize and magma erupting at ~4 MgO wt%) and used the composition of the more mafic sample as starting composition (Z16, MgO wt% 8.3). I used literature KD values for olivine, clinopyroxene and spinel (McKenzie and O'Nions, 1991; Elkins et al., 2008) while plagioclase KD has been calculated using Blundy and Wood (1991) equations. I observe that the increase in Ba and Sr could be explained by AFC modeling with plagioclase Xi = 0.7 % and r = 0.5-0.6 (Xi = mass fraction plagioclase/mass fraction total solid phase and r = rate of assimilation/rate of fractional crystallization) arguing in favor of a plagioclase-rich mush in the US deep magmatic system (Fig. 4.9). In the possible scenario of plagioclase crystallizing less than the 70% estimated by MELTS, a decrease of the rate of assimilation is needed to fit the data.

4.4.2. Magmatic system architecture and dynamics

4.4.2.1. The deep and stable magmatic system of the Upper Stratoid volcanic phase

The US volcanic phase was characterized by voluminous eruptions of overall similar mostly aphyric and moderately evolved (MgO 6-4 wt%) magmas (Fig. 4.2; Fig. S4.1). Therefore, a similar magma storage, differentiation and ascent scenario persisted over an interval of time of ~1.5 Ma in the Central Afar region. The fact that most of the US lavas do not show evidence of shallow crystallization (i.e., < 3 kbar; Fig. 4.7) suggests that the basaltic magma differentiation occurred in a deep-seated, zoned magmatic system and that moderately evolved magmas rose directly to the surface. Considering the voluminous eruptions of the mostly aphyric US lavas and their unzoned plagioclase core, unperturbed melt-dominated portion/s, representing large eruptible magma bodies, can be envisaged in the magmatic system. However, the high An plagioclase of the low-MgO samples often show resorbed cores (Fig. 4.6; Fig. S4.4b) indicating disequilibrium with the carrying magma and in some

cases oscillatory mantles have been observed (Fig. 4.6c; Fig. S4.4b), suggesting polybaric convection and/or magma mixing and revealing a more complex magma dynamic.

The magmatic system was composed of magmatic reservoir/s in the lower crust (11-18 km depth) with high Mg# pyroxene and Fo-rich olivine, crystallizing from the high-MgO magma (Fig. 4.7a). It is also reasonable that the high An plagioclase found as cores (up to An_{88}) in disequilibrium with the host low-MgO magma crystallized from a high-MgO-like, or more mafic magma in the same or even deeper reservoir; this is confirmed by the calculated Sr equilibrium melt concentration (calculated using Blundy and Wood, 1991; see below, chapter 4.4.3.1), reaching 500 ppm and overall higher than the whole rock concentration of analyzed samples (300-400 ppm). The depth constraint from plagioclase mantles in equilibrium with the low MgO US (mean An_{72}) (~13-19 km) again points to storage in the lower crustal reservoirs (Fig. 4.7b). The possibility of plagioclase buoyancy justifying the presence of the An-rich resorbed cores of phenocrysts in the low-MgO samples can be evaluated by density calculations. Using DensityX (Iacovino and Till, 2019) at pressure and temperature obtained by the thermobarometer of the deep magmatic system and water concentration from 0.5 to 1 wt% I calculated the density of high-MgO silicate melt (2.69-2.78 g/cm^3) is equally or more dense than the plagioclase (up to An_{87}; bytownite 2.71 g/cm^3) and less dense than clinopyroxene and olivine (forsterite 3.27 g/cm^3 and enstatite 3.2 g/cm^3). With differentiation from high-MgO to low-MgO magmas the increase of FeO_t causes melt density to remain higher than 2.70 g/cm^3 with the exception of very low pressure conditions and high water concentration. The plagioclase crystals were therefore able to float, entrained in the differentiating magma of the upper part of the lower crust magmatic system and eventually erupted in the low-MgO lavas or stored in a plagioclase-dominated crystal mush. Clinopyroxene and olivine, instead, settled down to form a cumulate crystal mush at the base of the lower crust magmatic system, being only occasionally erupted with the high-MgO lava (Fig. 4.10).

In this scenario the rate of magma ascending from the mantle to the lower crust must be sufficiently high to allow the formation and the maintenance of a melt-dominated magmatic system in the lower crust (Solano et al., 2012; Annen et al., 2006; Cashman et al., 2017). Simultaneously, mush forming at the top of the reservoir due to plagioclase buoyancy, can create crystal poor and differentiate melt rich zones, just below the top host rock (Jackson

et al., 2018, 2003), as has been largely observed for silicic magma chambers (Deering et al., 2011; Bachmann and Bergantz, 2004; Forni et al., 2016; Dufek and Bachmann, 2010). Considering that the US are mostly moderately evolved, aphyric or nearly aphyric, and that, the rare low porphyritic sample (mostly targeted for this work) have largely high An plagioclase in disequilibrium with the host rock (i.e., Low-MgO lavas), this suggests that the US magma mostly rose directly to the surface from the upper portion of this lower crustal reservoir (Fig. 4.10).

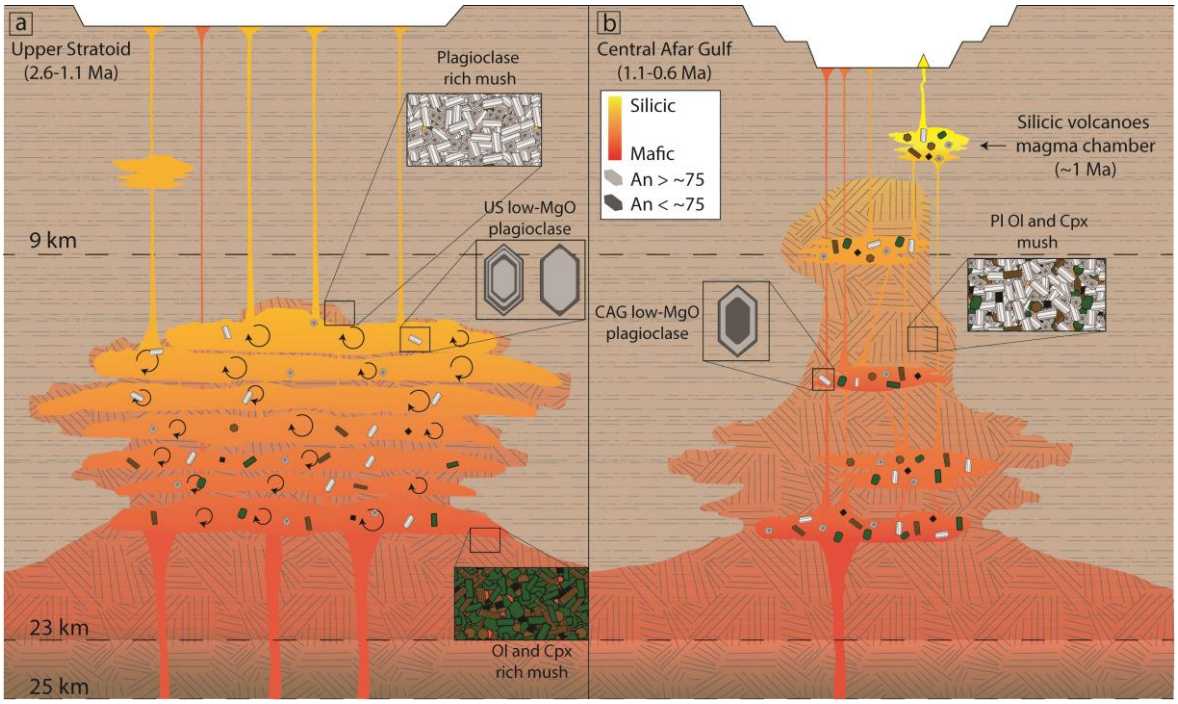

Fig. 4.10 Schematic cartoon depicting the magmatic system of US and CAG in Central Afar. a) The US are dominated by eruption of the moderately evolved, aphyric and homogeneous (4-6 MgO wt%) upper portion/s of a melt-dominated magmatic system, rising directly to the Surface. b) The CAG are dominated by a melt-poor magmatic system with respect to the US, with eruptions taking place through a series of small, crystal-rich and interconnected magma chambers. The sketch is not to scale, and the depth of the magmatic systems is approximative. The depth of the Moho (23-25 km) and of the lower-upper crust limit (9 km) are from Hammond et al. (2011). The plagioclase represent the main topology used for the interpretation. See text for more details.

4.4.2.2. The polybaric and interconnected magmatic system for the Central Afar Gulf volcanic phase

The CAG magmas are more variable in the whole rock chemical composition and crystal cargo, less voluminous and more porphyritic with respect to the US (Fig. 4.2; Fig. S4.1). Reverse and normal zoning observed in plagioclase profiles (Fig. 4.6; Fig. S4.4) indicates a highly dynamic storage system. Reverse zoning has been observed also in some low-MgO

samples clinopyroxene chemical profiles, showing an increase in Mg# and Cr_2O_3 at the mantle and rim (Fig. 4.6g, h). Furthermore, the low-MgO samples have higher An plagioclase and higher Mg# clinopyroxene, and similar Fo content for olivine with respect to the high-MgO samples. These characteristics indicate that the CAG were not fed directly by the melt-dominated portion of large, zoned reservoirs, as for the US, but suggest instead multiple, relatively small, crystal-rich, interconnected reservoirs (Fig. 4.10). Clinopyroxene of the high-MgO samples are in disequilibrium with the whole rock while CAG low-MgO samples clinopyroxene are in equilibrium at 11-18 km depth, similar to the US high-MgO clinopyroxene, and have reverse zoning indicating recharge events from a deeper reservoir (Fig. 4.6g, h; Fig. 4.7a). Plagioclase phenocrysts in equilibrium in different samples indicate crystallization depth from ~15 to 4 km (Fig. 4.7b), suggesting that the CAG magmatic system developed within a similar depth range (possibly shallower) compared to the US. However, despite the similar depth with respect to the US, the common presence of phenocrysts in the CAG indicate a major predisposition to stop and crystallize, while their crystal chemical variability indicates a more dynamic and interconnected storage system (Fig. 4.10).

4.4.3. Upper Stratoid and Central Afar Gulf magmatic evolution: insight from mineral compositional zoning

In this section I use major components and trace elements (e.g., An, TiO_2, Sr, Ba) measured in US and CAG plagioclase to reconstruct magma evolution in relation to intensive (e.g. pressure, temperature, water content) or extensive (e.g. magma mixing, assimilation) parameters. To this purpose, it has to be taken into account that chemical diffusion and crystallization kinetics can affect the redistribution of the element from the melt to minerals. Mg diffusion is fast in plagioclase and can therefore obliterate the information about magma composition. However, considering that Mg diffuses faster than other elements treated in this work (i.e., CaAl–NaSi interdiffusion, Ti, Sr and Ba; Grove et al., 1984; Cherniak and Watson 2020; LaTourrette and Wasserburg, 1998; Cherniak, 2002; Giletti and Casserly, 1994), the frequent variations observed for the MgO, as well as TiO_2, Sr and Ba variations (Fig. 4.6; Fig. 4.11a; Fig. S4.4b, d; Fig. S4.5B), suggest that diffusion did not strongly affect the compositions of the analyzed crystals. Kinetic effect, due to rapid growth of the crystals, could also affect the plagioclase mineral chemistry since the crystals do not have time to

equilibrate with the hosting melt. This process can be identified by the behavior of compatible and incompatible elements (Singer et al., 1995; Ginibre et al., 2002; Bezard et al., 2017). Incompatible elements (Fe, Ba, Mg, Ti) will be enriched by kinetic effect while compatible (Sr) will be depleted (Ginibre et al., 2002; Bottinga et al., 1966). In the analyzed US and CAG samples plagioclase, Sr and Ba behave coherently (Fig. 4.11a), increasing in the mantle/rim and arguing against the effect of kinetic processes.

Therefore, I interpret the variation in An, FeO_t, TiO_2, Sr, Ba and LREE as related to the changes in the magma composition. In the case of Mg, a recent work indicates that MgO partitioning coefficient in plagioclase depends on the C1–I1 structural phase transition (An_{60} at 1000 C; Mutch et al., 2022). Mutch et al. (2022) observed a positive correlation in the C1 (albite) domain and a negative correlation in the I1 (anorthite) domain between An and MgO. Accordingly, the plagioclase binary plots of this work show an increase in MgO before it starts decreasing at ~An_{65} (Fig. 4.11b). Furthermore, I observe a decrease and an increase of MgO in the mantle and or rim if the anorthite is respectively lower or higher than An_{65} (Fig. 4.6; Fig. S4.4). The observed MgO variations in the analyzed plagioclase seem to be related to the MgO mineral-melt partitioning and not to its concentration in the magma thus confirming the findings of Mutch et al. (2022). For this reason, MgO variations have not been used for the interpretation.

4.4.3.1. Fractional crystallization mixing and crystal mush assimilation recorded in Upper Stratoid crystals

The plagioclase in the US high-MgO samples mostly show no variation in An, TiO_2 and FeO_t, suggesting that they grow in a stable and unperturbed magma chamber (Fig. 4.6a; Fig. S4.4a). The US low-MgO samples plagioclase cores show overall constant composition of An, TiO_2 and FeO_t. At the core-rim transition, a decrease in An is accompanied by an increase in FeO_t and TiO_2 (Fig. 4.6b; Fig. S4.4b). Such decrease in An and increase in FeO_t and TiO_2 can be explained by mixing between similarly evolved magmas (4-6 MgO wt%) that have not reached the ilmenite saturation yet, allowing therefore a decrease in An and an increase in TiO_2 and FeO. This could be explained by a mixing between the lower and the upper portion of the lower crustal magmatic system, followed by magma rising directly to the surface (i.e., no mantle and thin rim), with the high An plagioclase carried by the ascent more mafic

magma and/or taken from the upper mush while rising (Fig. 4.10a). The lack of intermediate compositions suggests that the mush is isolated and/or the plagioclase in disequilibrium with the aphyric evolved melt of the magmatic system upper portion/s (as suggested by the high An plagioclase resorbed core). Mixing is also suggested by some plagioclase showing a decrease in An and increase in TiO_2 and FeO from core to mantle, similarly to the variations just described but less marked. Furthermore, this plagioclase (Fig. 4.6c; Fig. S4.4b) have a mantle showing coarse oscillations of An and TiO_2 suggesting mixing and polybaric convection before erupting (e.g., Streck, 2008; Ustunisik et al., 2014; Neave et al., 2014), while crystalizing the plagioclase An ~ 70 mantle in equilibrium with the melt (and in agreement with the plagioclase composition calculated by MELTS models). However, this reconstruction will not explain the strong increase in Sr, Ba and LREE of the US low-MgO samples plagioclase mantle and rim, reaching higher values (up to 1740, 420 and 3.6 ppm for Sr, Ba and Eu respectively) for the same An content with respect to the US high-MgO samples (Fig. 4.11a; Fig. S4.5). Assimilation of the plagioclase-rich mush forming in the upper portion/s of the lower crustal reservoir could explain the observed behavior of Sr and Ba, increasing in plagioclase mantle and rim during magma evolution in spite of plagioclase being the main mineral phase. To explain the behavior of US plagioclase Sr and Ba, I calculated their concentration in the melt that crystallized the analyzed plagioclase core, mantle and rim, using the KD calculated by means of Blundy and Wood (1991) equations. Then, using the average of the calculated melt composition of the plagioclase cores as starting material (Sr 390 ppm and Ba 147 ppm for the US low-MgO samples), I modeled the behavior of Ba and Sr in the melt during fractional crystallization (Rayleigh equation) and assimilation and fractional crystallization (AFC equation of DePaolo, 1981). I used literature KD for olivine, clinopyroxene and spinel (McKenzie and O'Nions, 1991; Elkins et al., 2008) while plagioclase KD has been calculated using the Blundy and Wood (1991) equations. I used the phase's mass fraction of the magma crystallizing in the lower crust (before it started to rise) according to MELTS results (only pyroxene at first and then 50% plagioclase and 50% pyroxene). Before plagioclase crystallization, due to their incompatibility in the pyroxene, the modeled Ba and Sr continue to increase in the evolving melt (dotted line in Fig. 4.12). Eventually, plagioclase starts crystallizing and Ba (incompatible) and Sr (compatible) concentrations are expected to respectively increase and decrease in the melt. However, the calculated melt in equilibrium with my analysis indicates both Ba and Sr concentration

continue to increase in the melt. I therefore modeled AFC using the analyzed Ba and Sr core concentration as the assimilant (Sr 600 ppm and Ba 30 ppm). I observe that the behavior of Ba and Sr could be explained by AFC modeling with plagioclase Xi = 0.5 % and r spanning from 0.3 to 0.6 (in agreement with the assimilation observed for the whole rock AFC model) (dashed lines in Fig. 4.12). As indicated for the whole rock modeling, the rate of assimilation can change if the plagioclase mass fraction fractionating is different with respect to MELTS results. Regarding the melt calculated for the high-MgO samples, the decreasing trend from core to rim of Sr and Ba seem to suggest evolution by mean of fractional crystallization (Fig.4.12).

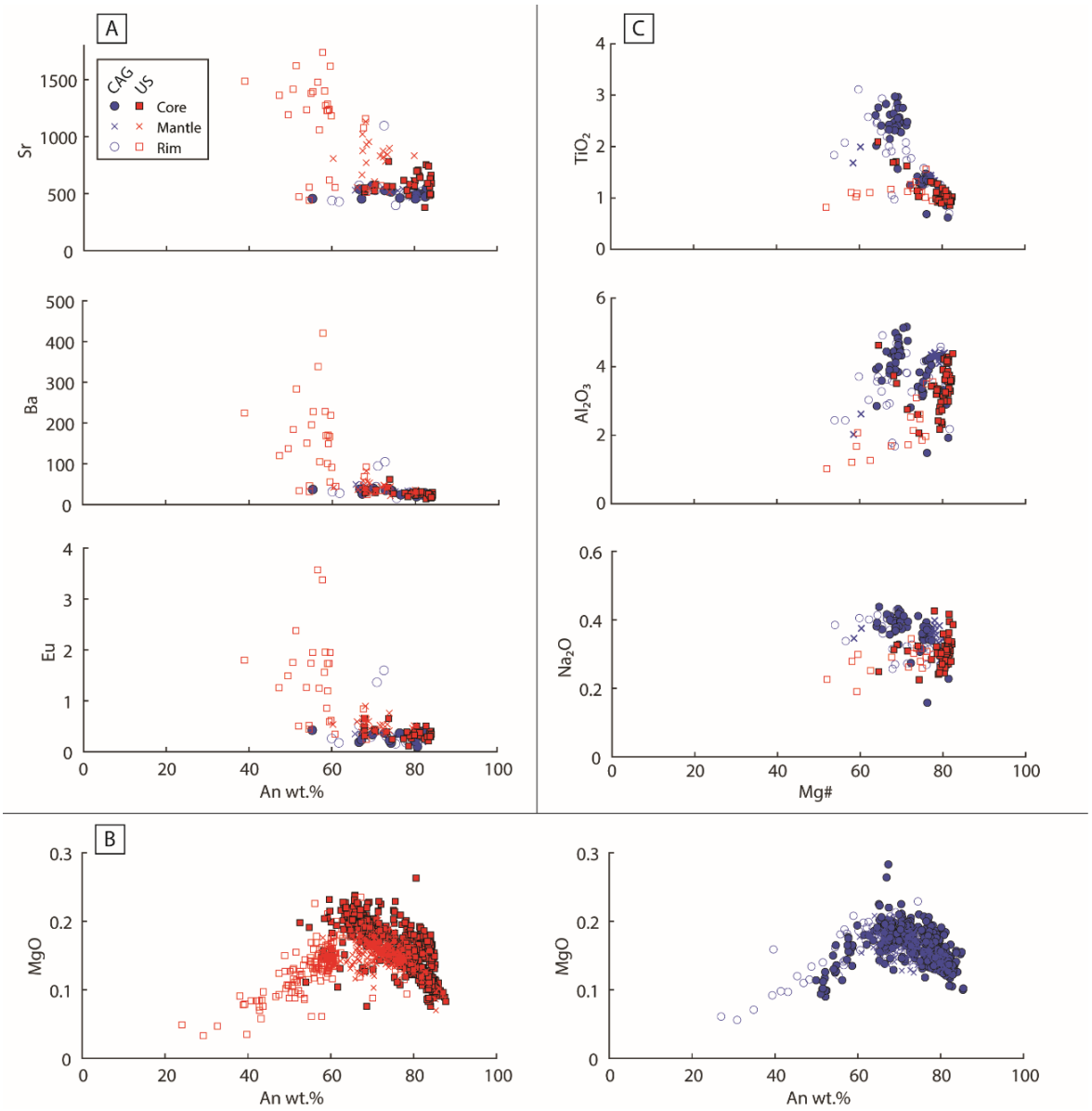

Fig. 4.11 a) Variation of Sr, Ba and Eu trace element concentrations versus An content of US and CAG plagioclase. All trace element variation diagrams are in Fig. S4.5 and the LA-ICP-MS data are listed in Tab. S2.1. b) Variation of MgO wt% versus An for US and CAG split in different diagrams to better show their trend and

the drop in MgO at An ~65. All variation diagrams are in Fig. S4.3 and the EPMA data are listed in Tab. S2.1 c) Variation of TiO_2, Al_2O_3 and Na_2O versus magnesium number (Mg# = (Mg/(Mg + Fe^{2+}) × 100) showing the differences between US and CAG. All variation diagrams are in Fig. S4.3 and the EPMA data are listed in Tab. S2.1.

So, based on my observations, the genesis of the widespread US is due to fractional crystallization together with a certain degree of mixing of similarly evolved magmas and assimilation of a plagioclase-rich mush within a deep (11-18 km) zoned reservoir. A deeper more mafic magma, possibly with high An plagioclase, mix with a shallower, aphyric, more evolved and Ba- and Sr-rich magma and rise, possibly tearing high An plagioclase from the mush, directly to the surface (Fig. 4.10a).

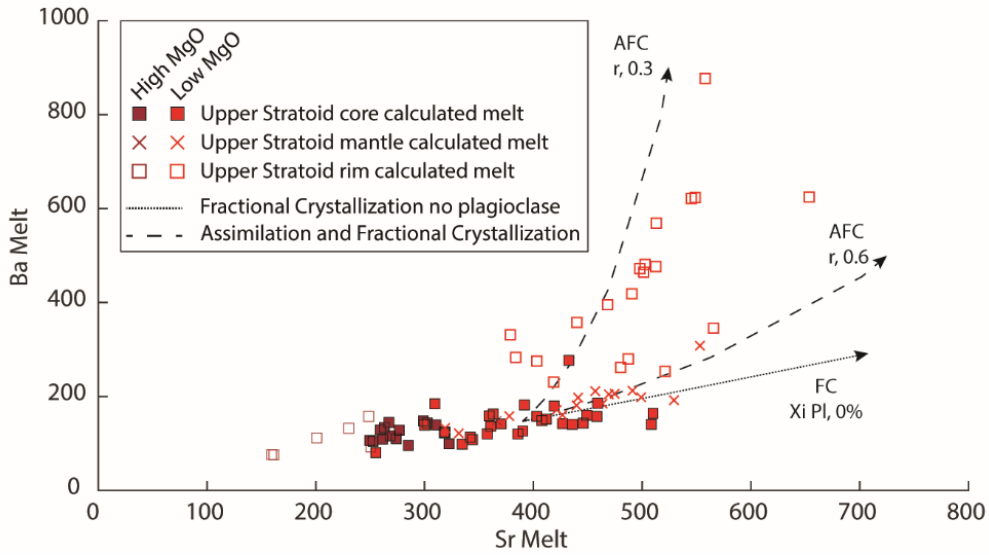

Fig. 4.12 Variation diagram of the Sr and Ba concentration of the melt calculated to be in equilibrium with core, mantle and rim EPMA analyses (full squares, crosses and empty squares respectively) of high-MgO and low-MgO samples plagioclase, calculated using Blundy and Wood (1991; T 1170 C° according to MELTS results). I modeled FC and AFC using the average melt composition of the low-MgO samples plagioclase cores (Sr 390 ppm and Ba 147 ppm) as starting material. The dotted line shows the variations due to fractional crystallization in absence of plagioclase (Xi, percentage of plagioclase involved in fractional crystallization). The dashed lines shows the variations due to assimilation and fractional crystallization (AFC equation of DePaolo, 1981), assimilating at r 0.3, 0.6 (r = rate of assimilation/rate of fractional crystallization) a plagioclase rich mush (assimilant Sr 600 ppm and Ba 30 ppm) and crystallizing 50% of plagioclase (according to MELTS results between 8-5 MgO wt%, in order to investigate magma behavior in the deep system before rising). The partition coefficients for olivine, clinopyroxene and spinel are the same as Fig. 4.9. For the low-MgO samples plagioclase the partition coefficients have been calculated using Blundy and Wood (1991; Sr 1.95 and Ba 0.25) according to MELTS results (An 70 and T 1170 C°).

4.4.3.2. Magma mixing, recharging events and mush interaction recorded in the Central Afar Gulf crystals

The CAG high-MgO samples plagioclase show no variation in An, TiO_2 and FeO_t, suggesting they grow in an overall stable and unperturbed reservoir (Fig. 4.6d; Fig. S4.4c). However, petrographic evidence of possible mixing within a zoned and/or between interconnected magmatic reservoirs is observed in the two analyzed CAG low-MgO samples (Fig. S4.1). Evidence of mixing has been observed in plagioclase with low An and sieved core and higher An and lower TiO_2 mantle (Fig. 4.6e; Fig. S4.4d). This indicates rising of a Ca-rich and TiO_2-poor mafic magma in a shallower reservoir (10-15 km depth) where it mixes with resident, more evolved, melt (Fig. 4.10b). Recharging events in the lower crust reservoirs (11-18 km; Fig. 7a) are suggested also by some clinopyroxene profiles showing increase in Mg# and Cr_2O_3 in the mantle and rim with respect to the core (Fig. 4.6g, h). Slight increase or decrease of An corresponding to inverse or no TiO_2 variations could suggest mixing between two compositionally similar magmas or diffusion obliterating the compositional variations (Fig. 4.6f; Fig. S4.4d). At the same time, decrease or increase in An has been observed in some plagioclase mantle/rim with no appreciable variation in TiO_2, suggesting variation in the intensive parameters (Fig. 4.6; Fig. S4.4d).

The CAG are enriched, with respect to the US, in TiO_2, Al_2O_3 and Na_2O for the same Mg# content, suggesting different trends for the two Series (Fig. 4.11a; Fig. S4.3). The high and increasing values of Na_2O and TiO_2 with decreasing Mg# are typical of alkaline magmas while a constant or slight decrease values are observed in the tholeiitic magmas (e.g. Nisbet and Pearce, 1977). This would suggest a more alkaline affinity for the CAG with respect to the US. However, the cooling rate could influence the clinopyroxene composition, in particular, an increase in cooling rate could explain the CAG clinopyroxene enrichment in Na_2O, Al_2O_3 and TiO_2 (Mollo et al., 2010; Giuliani et al., 2022). The elevated Na_2O and TiO_2 could also be explained by a melt-mush reaction with magma percolates through a troctolite mush due to the dissolution of olivine and plagioclase (Yang et al., 2019). Furthermore, regarding the olivine analyses, the CAG has lower NiO for the same Fo content with respect to the US (Fig. S4.3) that, according to Yang et al. (2019) experimental study, could suggest differences in the melt-mush interaction for CAG and US. I suggest that the observed clinopyroxene

variations are related to the cooling rate and melt-mush interaction instead of a different magma affinity.

The CAG magmatic system developed overall along the same depth range of the US but mixing and recharging events testify a different organization, with magma rising between small, crystal-rich and interconnected reservoirs (Fig. 4.10b).

4.5. Conclusive remarks

In this chapter difference in the magmatic system of US and CAG have been observed. The widespread US volcanism has been related to fractional crystallization together with a certain degree of mixing of similarly evolved magmas and assimilation of a plagioclase-rich mush (Fig. 4.8; Fig. 4.9; Fig. 4.11; Fig. 4.12) within a melt-dominated, slightly zoned, deep-seated (11-18 km) magmatic system (Fig. 4.6; Fig. 4.7). Moderately evolved US magmas rose from the top of this lower crust magmatic system directly to the surface (Fig. 4.10). The CAG show overall a similar depth range with respect to the US (or possibly shallower), but the erupted volume, the petrography characteristic (Fig. S4.1), and the mineral chemistry (Fig. 4.6; Fig. 4.11) indicate a different organization of the magmatic system, with magma more prone to stop and crystallize while rising between small, crystal-rich and interconnected reservoirs (Fig. 4.10).

5. Evidence of active magmatic rifting at the Ma'Alalta volcanic field

5.1. Introduction

The Afar rift is a triple junction where the Main Ethiopian Rift, Red Sea and the Gulf of Aden rift arms meet. Volcanism in Afar initiated ~30 Ma ago and was initially dominated by flood basalts (Hofmann et al., 1997). Most of the Afar depression is covered by the Stratoid Series, erupted between 4.5 and 1.1 Ma while, since at least ~1 Ma, active rifting and volcanism have focused to en-echelon axial magmatic segments (~70-km-long, ~20-km-wide) marking the current plate boundary of the rift (e.g., Dabbahu segment, Manda Hararo segment and Erta Ale segment) (Fig. 5.1a) (Oppenheimer et al., 1998; Wright et al., 2012; Medynski et al., 2013). Quaternary rift volcanism has also produced large volumes of lavas along the margin of the Afar depression, such as those erupted by the felsic stratovolcanoes of the Nabro-Mahlale alignment or Ma'Alalta stratovolcano (*marginal* volcanism) (Fig. 5.1a; Barberi et al., 1970, 1974b). Furthermore, several felsic central volcanoes are also located in Central Afar (Barberi and Santacroce, 1980; Lahitte et al., 2003a, b). Despite the peculiarity of the felsic stratovolcanoes activity within Afar, current knowledge about their magma sources and plumbing system and their relationships with nearby magmatic segments is partial because of their remote location and because scientific interest has focused mainly on axial volcanism. However, the study of these central volcanoes is crucial in order to understand rift evolution, since they could act as precursors of the rift segment development, as suggested for Central Afar (Lahitte et al., 2003a).

The Ma'Alalta volcanic field (MVF hereafter) is located in Afar (Ethiopia), ~50 km north of Dabbahu volcano (Fig. 5.1). MVF consists of a felsic stratovolcano with summit nested calderas surrounded by more recent mafic lava flows and scoria cones, and felsic lava flows and domes. Due to its location at the edge of the Afar depression, the MVF was originally classified as a *marginal* unit (Barberi et al., 1974a; Wiart et al., 2005). However, little is known about the petrology, geochemistry and tectonics of MVF and how they relate to the tectonics of continental breakup in Afar.

In this study I provide new major and trace element analyses and the first pressure and temperature estimates of the MVF rock samples. The rocks were collected during the French-Italian campaigns in 1967-1973 (Varet et al., 1978; Barberi et al., 1977;

http://repositories.dst.unipi.it/index.php/afar-repositories). I integrated the volcanological, geochemical and petrological analyses with remote sensing based mapping and local earthquake catalogs. I combined the diverse datasets in order to understand the nature of the MVF magmatic production and the relationship of the felsic stratovolcanoes with rift segments and the current magmatic and tectonic activity of Afar.

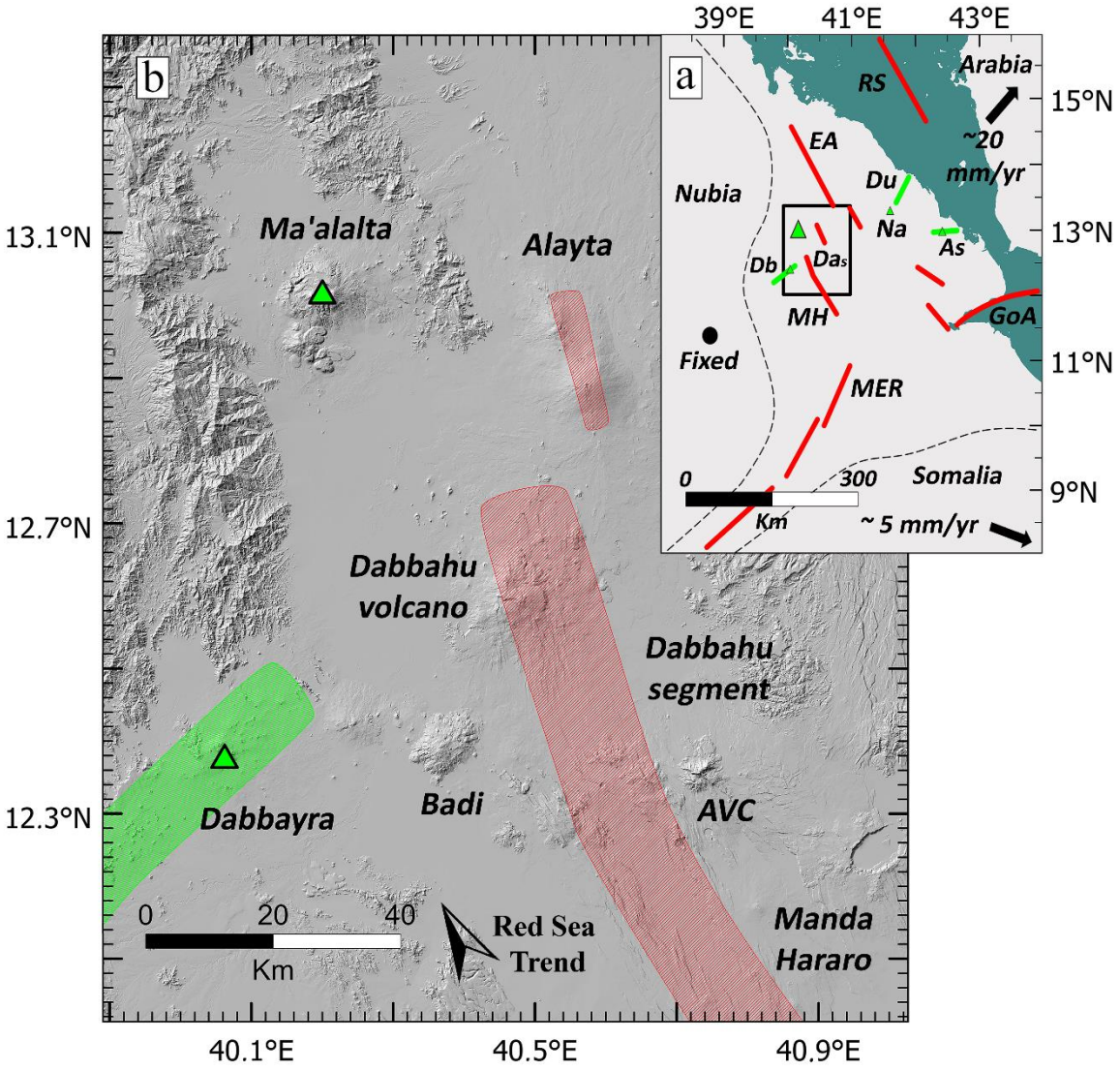

Fig. 5.1 a) Regional tectonic map showing the three diverging plates (Nubia, Arabia and Somalia) and the main structures. In red the magmatic segments and in green marginal volcanoes (triangles) and transverse structures (segments). E-A - Erta'Ale; MH - Manda Hararo; Das - Dabbahu segment; Na - Nabro; Du - Dubbi; As - Assab range; Db - Dabbayra; MER - Main Ethiopian Rift; GoA - Gulf of Aden; RS - Red Sea. The black box marks the location of the area shown in 1b. b) Topography of the MVF (SRTM DEM). AVC - Ado'Ale volcanic complex. In red the magmatic segments and in green marginal volcanoes (triangles) and transverse structures (green shading).

5.2. Geological and volcanological background

5.2.1. The Afar depression

The Afar depression is a triple junction between the Red Sea, Gulf of Aden, and Main Ethiopian rifts, created by the divergent motions of the Nubian, Arabian and Somalian plates. Afar is flanked by the Ethiopian Plateau to the west, by the Somalian Plateau to the south-east and the Danakil Block and Ali-Sabieh Block to the east. Initiation of volcanic activity in Ethiopia is thought to be caused by a mantle plume that produced the Ethiopian flood basalts (Marty et al., 1996; Pik et al., 1999; Kieffer et al., 2004) with the majority of the volume of basaltic magma erupted over only ~1 Myr at about 30 Ma (Zumbo et al., 1995; Hofmann et al., 1997). Starting from the Oligocene, magmatic activity occurred inside the newly forming Afar rift floor, and progressively migrated towards the current magmatic segments through the Miocene (Wolfenden et al., 2005; Stab et al., 2016).

The Afar rift floor is mainly covered by the Stratoid series (4-1 Ma), followed by the Gulf Basalt formation (1.1-0.6 Ma) (Barberi et al., 1980; Kidane et al., 2003; Stab et al., 2016) while magmatism and extension are currently mainly localized to axial magmatic segments within the rift (Hayward and Ebinger, 1996; Wright et al., 2006; Fig. 5.1). In central and northern Afar, these magmatic segments (e.g., Dabbahu, Manda Hararo and Erta Ale) are oriented NNW-SSE, which is the orientation of the Red Sea (Fig. 5.1). The magmatic segments consist of fissural eruptions associated with extensional fractures sometimes related to shield volcanoes (Oppenheimer et al., 1998; Wright et al., 2006; Ferguson et al., 2010; Field et al., 2012b, 2013; Medynski et al., 2015, 2016; Hagos et al., 2016). Volcanism close to the margins of the Afar floor is also reported. Barberi et al. (1970, 1974b) described transverse alignments of volcanoes (e.g., Dabbayra, Assab and Dubbi) situated both east and west of the magmatic segments in Afar (green segment in Fig. 5.1a) and oriented nearly orthogonally to the Red Sea trend. Furthermore, they also classified stratovolcanoes on either side of the rift, such as Nabro and Ma'Alalta, as marginal volcanoes (green triangles in Fig. 5.1a). These are large stratovolcanoes that produced caldera-forming explosive eruptions (Barberi et al., 1974a; Wiart et al., 2005; Oppenheimer et al., 2019) and lava flows generally more alkaline with respect to the tholeiitic-transitional axial volcanism (Civetta et al., 1975; De Fino et al., 1978; Donovan et al., 2018). The most recent eruption of a marginal

volcano was in 2011 at Nabro, which produced basaltic to basaltic trachyandesite tephra and lava (Hamlyn et al., 2018; Donovan et al., 2018). The MVF is located in the Northern sector of Afar, where the extension rate is ~20 mm/yr in a ~NE-SW direction (Fig. 5.1) (McClusky et al., 2010).

5.2.2. The Ma'Alalta volcanic field

The MVF is surrounded by outcrops of Jurassic limestones, meta-sediment and meta-volcanic of the Neoproterozoic basement and is dominated by a 1745 m high stratovolcano with nested calderas elongated NE-SW, approximately perpendicular to the Red Sea trend. The outer caldera is approximately 8 x 5 km and the inner one is 5 x 2.5 km. At the base of the MVF sequence, Barberi et al. (1970) identified fissural basaltic lava flows, underlying three ignimbrite sheets alternated with pumice fall layers and, before the emplacement of the third ignimbrite unit, and basaltic scoriaceous deposits with associated small scoria cones. On top of this succession, they recognized obsidian flows, pyroclastic layers and porphyritic trachyte flows and domes that built the stratovolcano. The most recent products are felsic lava domes and obsidian flows, erupted along NNW-SSE fissures south of the stratovolcano. Barberi et al. (1974a) distinguished an earlier stratovolcano-building phase with felsic non-peralkaline lavas and a later phase that produced large-volume ignimbrites, intra-caldera domes and lava flows of peralkaline composition, particularly rich in sanidine phenocrysts (Barberi et al., 1970). The felsic domes and flows south of the stratovolcano are more peralkaline and silica-rich with respect to the stratovolcano products and they are nearly aphyric (Barberi et al., 1970, 1974a). Wiart et al. (2005) proposed a satellite-based map suggesting that the stratovolcano is flanked to the west and south-west by felsic domes and lava flows but also by recent mafic cinder cones and NNW-SSE fissural lava flows and to the east by more weathered and eroded lavas, named "Old Lava". K-Ar age determinations gave 0.55 ± 0.05 Ma for a lava sample at the base of the stratovolcano, and 0.12 ± 0.05 Ma for a pantellerite obsidian south of the stratovolcano (Barberi et al., 1972).

5.3. Results

5.3.1. Geological map of MVF and relative chronology of the volcanic units

In this chapter I used petrographic analysis (Tab. S2.1), rock classification (Fig. 5.2; Tab. 5.1) and the reconstructed distribution and relative chronology of the erupted products by means of satellite observations, in order to investigate the MVF volcanic units in the context of the two identified different phases of activity (Fig. 5.3).

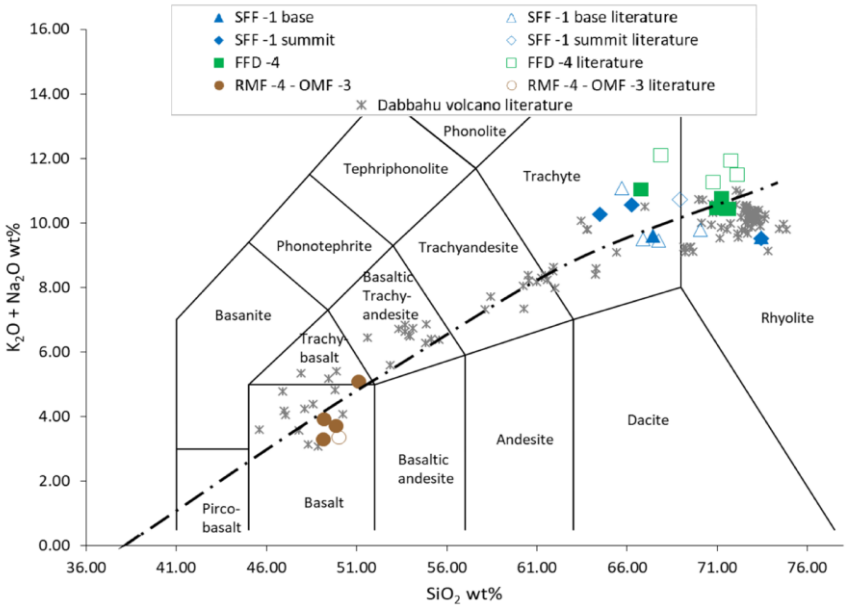

Fig. 5.2 TAS (Total Alkali vs Silica) classification diagram for MVF volcanic products. Data recalculated to 100% on a water-free basis. The Dabbahu volcano whole rocks are from Field et al. 2013 and Barberi et al. 1975b. The dashed line represents the limit between subalkaline-alkaline fields (Irvine and Baragar, 1971). SFF-1, Stratovolcano Felsic Flows; FFD-4, Felsic Flows and Domes; RMF-4 - OMF-3, Recent-Old Mafic Flows.

The first phase started at 0.55 ± 0.05 Ma (Barberi et al., 1972) with the formation of the stratovolcano and was later affected by a caldera-forming stage, producing trachytic-rhyolitic lava flows and ignimbrites (Fig. 5.3; Fig. 5.2). This activity was followed by the second phase (0.12 ± 0.05 Ma; Barberi et al., 1972) producing multi-vent mafic and felsic eruptions. This phase produced a NNW-SSE-trend of fissural basaltic-trachybasaltic lava flows and cinder cones and rhyolitic-trachytic lavas and domes (Fig. 5.3; Fig. 5.2).

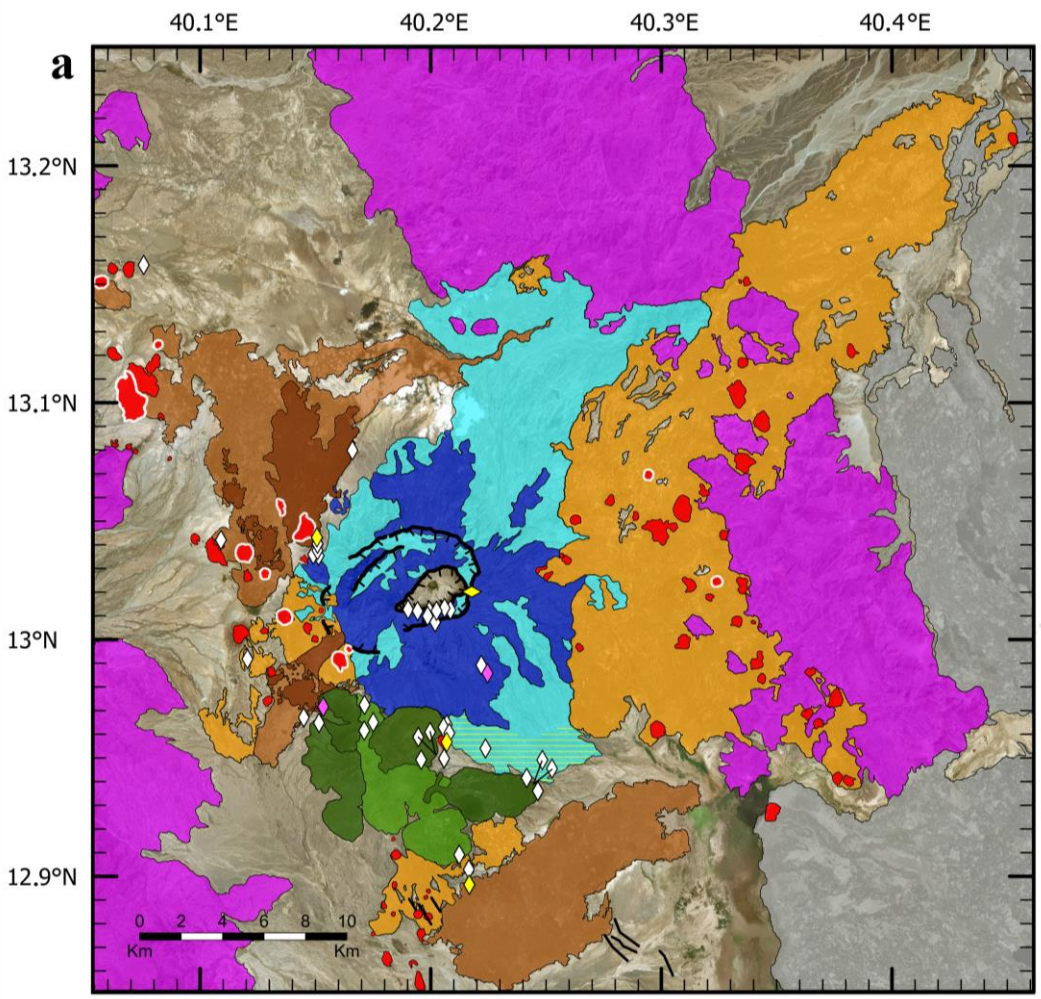

b

Ma'Alalta Volcanic Field

		Volcanic structures	Main structural trends	Rock composition	Age
Second Phase	FFD-4 / RMF-4	The darker portion of FFD-4 and RMF-4 are morphologically younger. Mafic flows are associated with fissural vents and cinder cones.	NNW-SSE	Rhyolite and minor trachyte, peralkaline; basat to trachybasalt, transitional	0.12 ± 0.05 Ma
	OMF-3		NE-SW and NNW-SSE		
First Phase	CFI-2	Mainly ignimbrites but also tuff and pumice (yellow stripes) associated with the stratovolcano	NE-SW	Trachyte, metaluminous to peralkaline	
	SFF-1	Felsic lava flows erupted from the stratovolcano	NE-SW	Trachyte and minor rhyolite, metaluminous to peralkaline	0.55 ± 0.05 Ma

Eroded cinder cones
Well preserved cinder cones
Neoproterozoic basement & Jurassic sediments
Alayta lava flows
Caldera rim
Fault
Samples

Fig. 5.3 a) Geological map of the MVF, combining petrographic analysis, Landsat 5 satellite images, SRTM DEM and morphological observation. The horizontal diamond as in Fig. 2.2. The pink diamonds represent the literature dated samples (the one of FFD-4 is located in the original sampling map but not in the collection) while the yellow ones are the samples used for the geothermobarometry Estimates. b) Stratigraphic column showing the main characteristics of the MVF deposits and their chronological order. SFF-1, Stratovolcano Felsic Flows; CFI-2, Calderas Felsic Ignimbrites; OMF-3, Old Mafic Flows; RFM-4, Recent Mafic Flows; FFD-4, Felsic Flows and Domes. The numbers represent the reconstructed chronological order from the lower (1) to the higher (4) deposits. Ages from Barberi et al. (1972).

5.3.1.1. The stratovolcano and caldera-forming phase (first phase)

Based on the available samples of the first phase, two stages can be distinguished: a mainly effusive stage, consisting of metaluminous to peralkaline trachytic-rhyolitic rocks building the central edifice, called the stratovolcano felsic flows (SFF-1); a caldera-forming stage, consisting of metaluminous to peralkaline trachytic pyroclastic flow deposits, called calderas felsic ignimbrites (CFI-2) which include the final felsic activity of the calderas (Fig. 5.3; Tab. 5.1; Tab. S2.1). I observed an upward variation in size, type and abundance of phenocrysts from the base (samples collected on the flank of the stratovolcano, south and northwest with respect to the crater) to the top of the stratovolcano (samples collected in close proximity of the crater) felsic lava flows (Fig. 5.2). The seven samples from the top have up to 40 vol% of phenocrysts consisting of alkali feldspar reaching one cm in size, and minor plagioclase, fayalite, slightly pleochroic clinopyroxene and, in one sample, arfvedsonite (Fig. 5.4; Fig. S5.1a; Tab. S2.1). Plagioclase is mainly andesine and minor oligoclase (Ab51-68An26-47), alkali feldspar is mainly anorthoclase (Ab63-72Or15-36), clinopyroxene is augite (Wo38-44 Fs23-57) (Fig. S5.2a; Tab. S2.1). Apatite and Fe-Ti oxides are the main accessory phases. The groundmass is holocrystalline or nearly so, and it is composed of the same crystals as the phenocrysts except for fayalite. Two samples from the top rim of the inner caldera display phenocrysts of quartz in addition to alkali feldspar and minor pleochroic clinopyroxene, arfvedsonite and aenigmatite (Fig. S5.1b; Tab. S2.1). The three samples from the base of the stratovolcano have lower phenocryst abundance (up to 20 vol%) and smaller phenocryst in size compared to samples from the top (Fig. 5.4; Fig. S5.1c; Tab. S2.1). Also, no minerals indicative of peralkalinity are observed (e.g., arfvedsonite, aenigmatite).

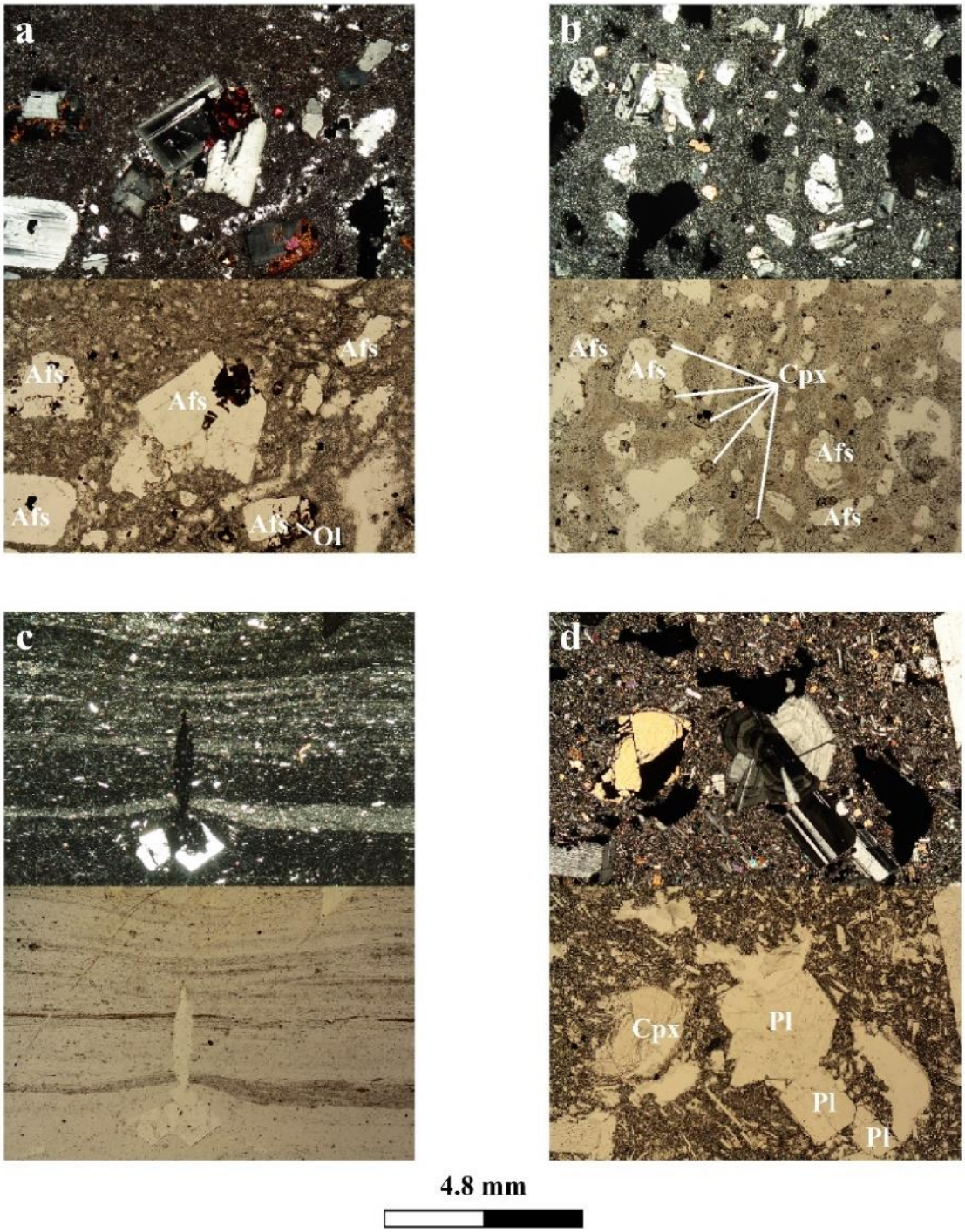

Fig. 5.4 Transmitted light petrographic images of MVF representative samples. a) G28, Stratovolcano Felsic Flows top; b) D177, Stratovolcano Felsic Flows bottom; c) G23, Felsic Flows and Domes; d) K35, Recent Mafic Flows. Cpx, Clinopyroxene; Afs, Alkali feldspar; Pl, Plagioclase; Ol, Olivine. Location and petrographic details of the samples are in Tab. S2.1.

Tab. 5.1 Major and trace element composition of MVF whole rocks.

	First Phase				
	Stratovolcano felsic lava flows, SFF-1				
	Base			Top	
Sample	D 169	D 177	G33	K39	G28
SiO_2 (wt%)	73.28	65.89	71.9	65.13	63.65
TiO_2	0.26	0.70	0.28	0.58	0.89
Al_2O_3	9.86	15.41	9.73	14.76	15.77
FeO_{tot}	6.00	3.48	5.84	5.15	5.26
MnO	0.21	0.07	0.21	0.20	0.18
MgO	0.21	0.69	0.21	0.37	0.55
CaO	0.40	1.93	0.39	1.55	1.95
Na_2O	5.15	4.72	5.01	5.79	5.63
K_2O	4.39	4.66	4.30	4.59	4.50
P_2O_5	0.05	0.18	0.04	0.16	0.29
L.O.I.	0.00	0.49	0.47	0.18	1.55
Sum	99.81	98.22	98.38	98.46	100.22
Mg#	5.83	25.97	5.98	11.29	15.61
Total Alkalis	9.54	9.38	9.31	10.38	10.13
A.I.	1.34	0.83	1.33	0.98	0.90
Peralkaline Rock type	P	-	P	-	-

	Second Phase								
	Felsic lava flows and domes, FFD-4					Old and recent mafic lava flows, OMF-3 - RMF-4			
Sample	G3	G10	G18	G14	G23	D170	G8	G16	G20
SiO_2 (wt%)	65.68	71.07	70.83	70.26	70.20	48.56	48.26	50.80	49.10
TiO_2	0.46	0.30	0.29	0.31	0.30	1.79	2.47	2.72	2.29
Al_2O_3	13.89	13.09	13.31	12.96	12.95	17.88	15.04	15.73	15.10
FeO_{tot}	5.35	3.78	3.93	3.56	3.67	8.53	9.52	11.42	9.59
MnO	0.24	0.12	0.13	0.11	0.12	0.14	0.16	0.19	0.17
MgO	0.23	0.12	0.18	0.11	0.13	7.21	7.77	4.69	7.25
CaO	1.59	0.51	0.69	0.52	0.52	11.33	10.67	8.27	10.89
Na_2O	6.02	5.60	5.64	5.59	5.94	2.71	2.61	3.74	2.80
K_2O	4.86	4.79	4.80	4.66	4.68	0.56	1.24	1.32	0.86
P_2O_5	0.08	0.05	0.05	0.05	0.05	0.32	0.39	0.49	0.43
L.O.I.	0.49	0.06	0.14	0.18	0.35	0.50	-	-	-
Sum	98.89	99.49	99.99	98.31	98.91	99.29	98.13	99.37	98.48
Mg#	7.07	5.32	7.50	5.18	5.90	59.93	59.09	42.10	57.23
Total Alkalis	10.88	10.39	10.44	10.25	10.62	3.03	3.85	5.06	3.66
A.I.	1.09	1.10	1.09	1.10	1.15	0.27	0.37	0.48	0.37
Peralkaline Rock type	C	C	C	C	C	-	-	-	-

Tab. 5.1 (continued)

	First Phase				Second Phase								
	Stratovolcano felsic lava flows, SFF-1				Felsic lava flows and domes, FFD-4					Old and recent mafic lava flows, OMF-3 - RMF-4			
Sample	K39	G33	G28	D177	G23	G10	G14	G3	G18	G16	G20	D170	G8
Li	26.8	54	18.1	23.7	27.9	16.9	17.7	18.4	19.1	10.0	6.3	4.1	5.4
Be	6.6	14.1	5.1	3.4	5.5	5.6	5.1	2.92	5.4	1.79	1.16	0.88	1.30
Sc	6.5	7.0	10.8	5.7	1.87	2.65	2.62	3.26	1.83	25.1	34	35	29.6
V	3.4	<3	14.4	34	<0.2	<3	<3	0.72	1.04	317	314	251	300
Cr	1.34	2.04	2.80	1.40	1.80	1.35	<1	<1	0.73	15.1	288	177	287
Co	0.98	0.10	2.77	5.3	0.27	0.18	0.03	0.15	<0.1	35	39	37	40
Ni	0.60	<0.7	1.94	2.96	0.29	<0.7	<0.7	0.79	0.29	17.6	81	69	103
Cu	7.1	<11	12.1	12.7	21.6	<11	<11	11.9	<3	42	79	47	63
Zn	152	306	132	56	163	130	131	105	135	118	116	68	93
Ga	29.8	37	25.3	20.5	31.0	29.6	29.2	28.7	30.4	20.1	16.7	16.4	18.1
Rb	126	261	108	126	126	125	124	79	109	32.9	21.4	12.8	29.1
Sr	79	<12	232	109	<4	<12	<12	<12	8.4	327	365	402	463
Y	77	196	67	30.8	80	80	81	53	83	38	26.2	20.9	25.0
Zr	791	2070	657	289	734	738	745	457	697	223	155	115	179
Nb	152	371	122	65	130	132	136	96	130	44	36	25.8	41
Mo	3.5	3.5	2.29	2.62	7.0	4.7	4.9	2.14	1.88	2.04	1.56	1.01	1.81
Cs	0.85	1.46	<1	0.72	1.32	1.50	1.42	<1	0.42	0.38	0.22	<1	0.25
Ba	691	26.9	1065	567	4.7	10.9	<6	44	17.5	345	317	207	386
La	99	260	86	56	105	109	110	70	99	33	25.1	19.2	27.8
Ce	210	526	182	111	223	231	234	152	209	69	53	41	59
Pr	23.3	57	19.8	12.3	24.9	25.3	25.5	17.1	23.4	8.5	6.6	5.1	7.4
Nd	85	202	73	43	92	94	93	65	88	34	26.6	21.0	29.6
Sm	16.1	38	13.7	8.0	17.5	17.5	17.5	12.3	17.2	7.5	5.7	4.4	6.1
Eu	2.94	2.80	3.16	1.30	1.14	1.14	1.12	1.60	1.28	2.33	1.93	1.58	2.02
Gd	13.4	34	12.2	6.7	14.9	15.5	15.8	10.9	15.0	7.2	5.3	4.6	5.6
Tb	2.20	5.7	2.01	1.07	2.45	2.55	2.58	1.73	2.43	1.16	0.84	0.70	0.84
Dy	13.5	35	12.0	6.0	14.5	15.3	15.3	10.0	14.8	6.8	4.8	4.0	4.7
Ho	2.75	7.1	2.43	1.20	2.95	3.04	3.03	1.98	2.94	1.34	0.95	0.78	0.90
Er	8.2	21.2	7.3	3.33	8.4	8.8	8.8	5.7	8.5	3.8	2.64	2.18	2.43
Tm	1.22	3.13	1.06	0.48	1.25	1.27	1.27	0.85	1.24	0.55	0.37	0.29	0.34
Yb	7.7	19.7	6.7	2.82	7.7	8.0	8.1	5.5	7.8	3.31	2.23	1.84	2.07
Lu	1.16	2.88	1.01	0.40	1.15	1.18	1.19	0.84	1.17	0.51	0.34	0.27	0.30
Hf	18.1	48	15.4	8.3	17.5	18.0	17.9	10.8	16.5	5.5	3.8	2.91	4.2
Ta	9.1	22.5	7.2	4.4	7.9	8.0	8.0	5.5	7.7	2.84	2.18	1.71	2.60
W	1.90	na	na	0.87	1.61	na	na	na	0.88	0.57	0.36	na	0.41
Pb	14.7	25.6	13.1	12.3	32.3	13.8	12.7	7.6	16.5	5.2	4.6	2.85	2.79
Th	13.9	39	13.3	11.6	14.9	15.9	16.0	9.0	14.4	4.5	2.95	2.18	3.5
U	4.1	11.0	3.8	3.4	4.2	4.3	4.2	2.32	3.6	1.25	0.81	0.53	0.98
La/Yb	12.9	13.2	12.9	19.8	13.8	13.6	13.6	12.7	12.7	10.0	11.2	10.4	13.4
La/Sm	6.2	6.9	6.3	7.0	6.0	6.2	6.3	5.7	5.7	4.4	4.4	4.3	4.6
Eu/Eu*	0.59	0.23	0.73	0.53	0.21	0.21	0.20	0.41	0.24	0.95	1.05	1.06	1.03

Note: C, Comendite; P, Pantellerite; L.O.I., Loss Of Ignition; A.I., Agpaitic index. Total iron as FeO, Eu = (Sm_N+Gd_N)/2, na = not analyzed.*

5.3.1.2. The multi-vent mafic and felsic phase (second phase)

During the second phase, fissural eruptions occurred along a ~35 km long NNW-SSE trending zone. I identified three groups of products - old mafic lava flows (OMF-3), felsic lava flows and domes (FFD-4) and recent mafic lava flows (RMF-4) - erupted by fissural vents with numerous cinder cones forming monogenetic and polygenetic small volume volcanic edifices distributed along the NNW-SSE trending zone (Fig. 5.3).

The FFD-4 mainly occur south-west of the stratovolcano (Fig. 5.3). The samples are comendite rhyolite and minor trachyte lavas, scarcely porphyritic or aphyric (Fig. 5.2; Tab. 5.1; Tab. S2.1). Sanidine and clinopyroxene (hedenbergite Wo43-46Fs51-55; Fig. S5.2b; Tab. S2.1) are the main phenocrysts but fayalite, aenigmatite and arfvedsonite can be found in some samples (Fig. 5.4; Fig. S5.3; Tab. S2.1). The groundmass varies from holocrystalline to hypohyaline and it is dominated by alkali feldspar, clinopyroxene and Fe-Ti oxides with sporadic fayalite, apatite and plagioclase.

The OMF-3 and RMF-4 groups (Fig. 5.3) are basalt and trachybasalt lava flows and cinder cones (Fig. 5.2; Tab. 5.1; Tab. S2.1) that differ in their morphological features and degree of weathering (Fig. 5.5a, b). The majority of OMF-3 lavas and poorly preserved cinder cones (Fig. 5.5a) are east of the volcano, while the RMF-4, associated to relatively well-preserved cinder cones (Fig. 5.5b), are located along the northern sector of the NNW-SSE trending zone and at its southern tip. All the mafic products show olivine, clinopyroxene and plagioclase phenocrysts, with large variations in their relative abundance (Fig. 5.4; Fig. S5.4; Tab. S2.1). The groundmass is from hypohyaline to hypocrystalline, with clinopyroxene, plagioclase and opaques. In the mafic samples, plagioclase is labradorite to bytownite (Ab17-44, An54-82), olivine is Fo77-84 (the tephroite component is Tp0.4-0.2) and clinopyroxene is augite with minor diopside (Wo39-45, Fs9-16) (Tab. S2.1; Fig. S5.1c). Presence of reversed zoning in clinopyroxene, plagioclase and olivine crystals has been observed. In one case (sample G8), the large variation of clinopyroxene cores composition in the augite field towards the hedenbergite endmember (Wo41-48, Fs9-32) compared to the more homogeneous rims (Wo43-47, Fs9-13) indicates mixing processes with evolved and peralkaline lavas. Sample D170 show common reverse zoning in olivine, again an evidence of mixing of magmas with different degrees of chemical evolution.

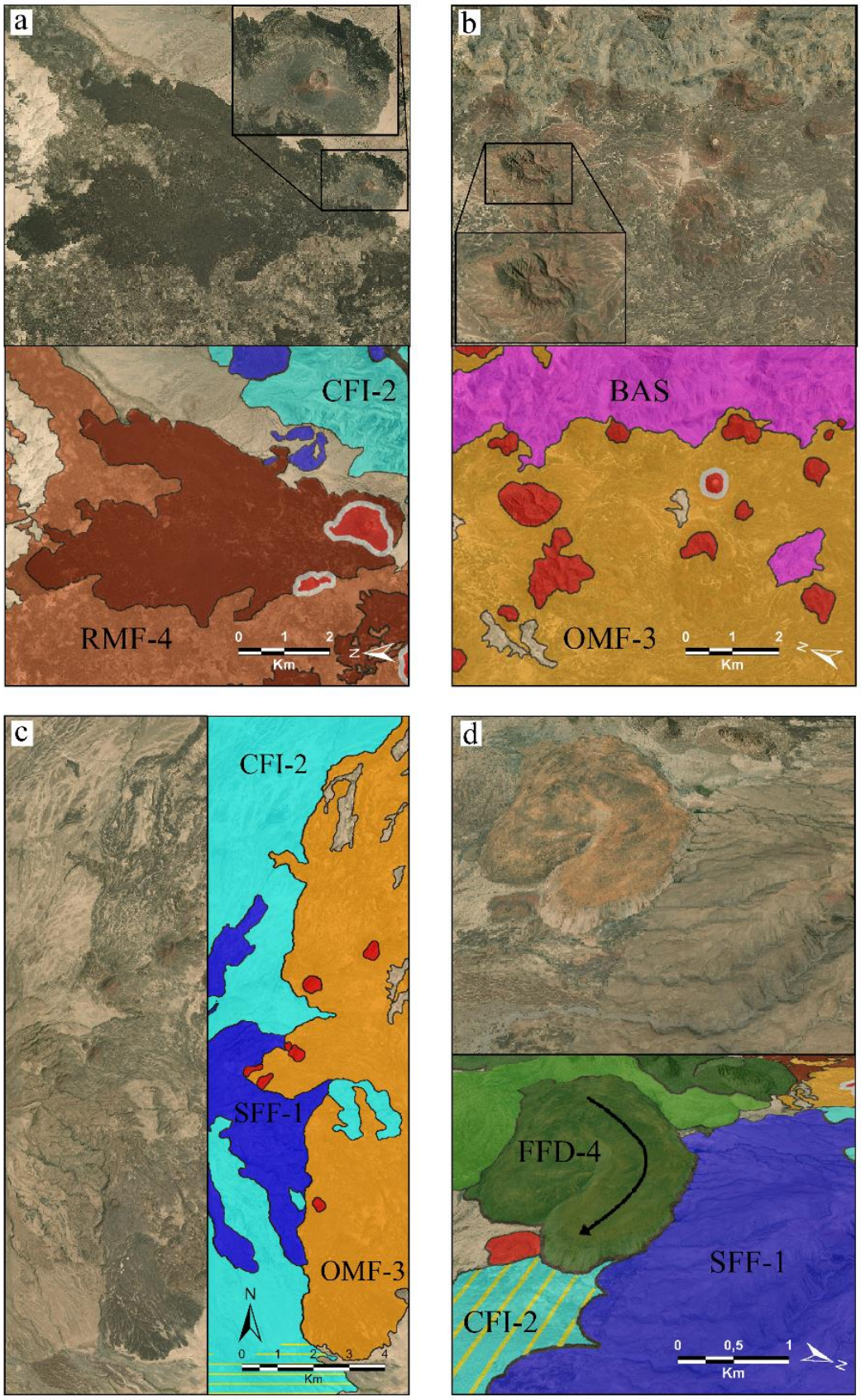

Fig. 5.5 Pairs of satellite images and the relative geological map. SFF-1, Stratovolcano Felsic Flows; CFI-2, Calderas Felsic Ignimbrites; OMF-3, Old Mafic Flows; RFM-4, Recent Mafic Flows; FFD-4, Felsic Flows and Domes; BAS basement. Locations are shown in Fig. S5.5.

5.3.1.3. Relative chronology of the volcanic units

The oldest products of MVF are the SFF-1, dated at 0.55 ± 0.05 Ma (Barberi et al., 1972), followed by the CFI-2 (Fig. 5.3b). I can identify at least two major explosive events that produced ignimbrite deposits, based on the presence of two calderas.

My interpretation of the relationship between the first phase and the OMF-3 differs from Wiart et al. (2005). I suggest that the sharp and relatively straight contact (N-S) on the eastern side of the stratovolcano (Fig. 5.5c), and the outcropping of the OMF-3 products on the western flank of the stratovolcano (Fig. S5.5) indicate that they post-date the stratovolcano. Otherwise, the pyroclastic flows responsible for the ignimbrites would be easily emplaced on the OMF-3 east of the stratovolcano due to their proximity to the edifice and the absence of a topographic boundary. This would lead to an irregular contact due to the overlapping of the ignimbrites and a fan-like geometry of the felsic flows (instead of an abrupt stop at the contact with the OMF-3; Fig. 5.5c; Fig. S5.5). Regarding the western flank of the stratovolcano, it is unlikely that the OMF-3, if emplaced before it, would result in topographic continuity (similar slope and altitude; Fig. S5.5) with the edifice and not covered by the stratovolcano products. Moreover, an outcropping portion of the ignimbrite deposit on the eastern flank of the stratovolcano is completely surrounded by OMF-3 mafic lava flows. These last observations indicate that the products of the first phase were deposited before the OMF-3. Based on the degree of erosion of lava flows and cinder cones, I classify OMF-3 as older than RMF-4 (Fig. 5.5a, b; Fig. S5.5). The FFD-4 south of the stratovolcano is dated by Barberi et al. (1972) at 0.12 ± 0.05 Ma. At the small scale the well preserved fan-like geometry of the northernmost lava flow of FFD-4 (preserved also in the portion where FFD-4 and RMF-4 are not in contact) indicates that FFD-4 precedes RMF-4 but, at the same time, the undulated front at the contact with the basalts (Fig. S5.5) would suggest the opposite. Due to these uncertain observations of the only contact between RMF-4 and FFD-4 and the heterogeneous color and surface morphology of both RMF-4 and FFD-4 (darker and lighter portions in Fig. 5.3) I suggest that they were likely emplaced during roughly the same time period. Despite the lack of certainty about their age relationship, as a whole they are the youngest products of the MVF eruptive history as they are emplaced after the stratovolcano activity, which also influences the flow directions of the upper products (Fig. 5.5d; Fig. S5.5).

5.3.2. Major and trace element geochemistry

In this chapter I present the major and trace element analysis of the MVF phases and compare them with the well-studied Dabbahu axial volcano (e.g., Field et al. 2013 and Barberi et al. 1975b; Fig. 5.1) in order to investigate similarities and differences of the MVF volcanic activities with respect to axial segment volcanism. In the Total-Alkali vs Silica diagram (TAS; Fig. 5.2), the analyzed MVF rocks (Tab. S2.1) fall in the basalt, trachybasalt, trachyte and rhyolite fields and define a compositional gap (Daly Gap), from 51 to 64 wt% SiO_2.

The SFF-1 rocks are mainly trachytes with few rhyolites (Fig. 5.2). The samples from the top of the edifice are prevalently peralkaline (comenditic trachyte and pantellerite), while the rocks at the base are metaluminous trachytes, although very close to peralkalinity, and a pantellerite (Tab. 5.1; Tab. S2.1). The variable degree of chemical evolution of the samples defines a differentiation trend of decreasing Al_2O_3, CaO, TiO_2 and P_2O_5, corresponding to fractionation of feldspar, pyroxene, Ti-Fe oxides and apatite, with nearly constant alkalies, while FeO_t increases in the most evolved rhyolitic samples (Fig. 5.6a). Accordingly, the elements Ba, Sr, Eu, strongly compatible in feldspars, reach the maximum depletion in the most evolved sample (Fig. 5.6b; Fig. 5.7).

The FFD-4 products are prevalently rhyolitic (Fig. 5.2) and are more silica- and alkali-rich and more peralkaline (comendite and comenditic trachyte) with respect to the SFF-1 samples taken as a whole (Tab. 5.1; Fig. 5.6; Tab. S2.1). The trace element patterns of FFD-4 samples are similar to each other and have greater negative anomalies in Sr, Eu, Ba, Ti and P compared to the stratovolcano (Fig. 5.7), which may indicate a higher degree of differentiation by fractionation of feldspar, Ti-Fe oxides and apatite. The G3 comenditic trachyte (the least evolved sample of the FFD-4) is the least enriched in REE and has the smallest negative Eu and Ba anomalies (Fig. 5.7) and shows the same ratios of highly incompatible elements (e.g., Zr/Nb; Fig. S5.6).

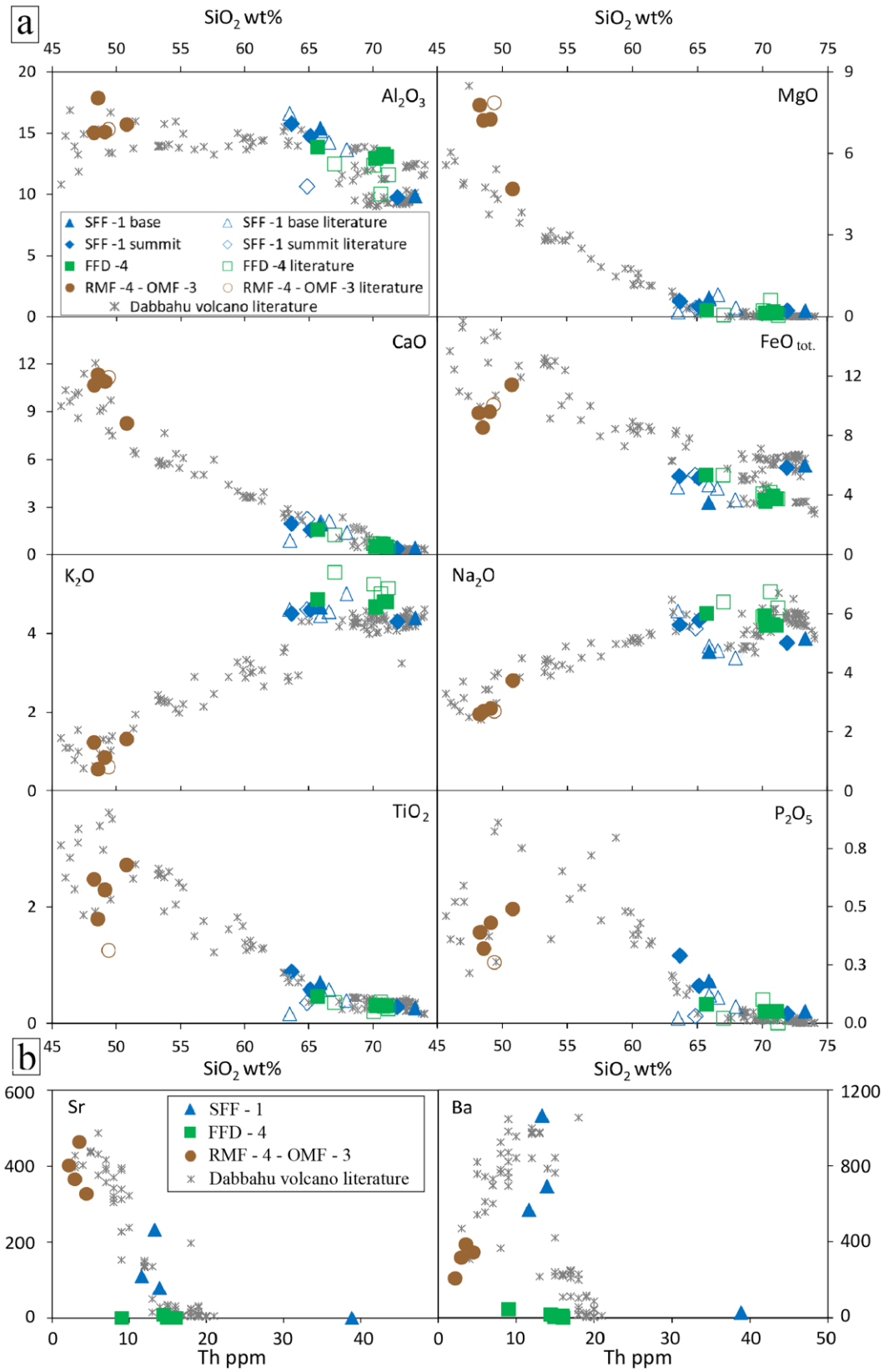

Fig. 5.6 a) Major element Harker diagrams. The Dabbahu volcano whole rocks analyses are from Field et al., 2013 and Barberi et al., 1975b. b) Ba and Sr trace element diagrams. The Dabbahu volcano whole rocks trace element analyses are from Hutchison et al. (2018). SFF-1, Stratovolcano Felsic Flows; FFD-4, Felsic Flows and Domes; RMF-4 - OMF-3, Recent-Old Mafic Flows.

The OMF-3 and RMF-4 products are basalts and trachybasalts (Fig. 5.2; Tab. 5.1; Tab. S2.1). All the samples have relatively low Mg# (<60) and are all olivine-hypersthene normative (Tab. S2.1). They all have no Eu negative anomalies (Fig. 5.7). Fractionation of olivine, clinopyroxene and Cr-spinel is active in the mafic reservoirs, as shown by the range in MgO and CaO (Fig. 5.6a) and Ni and Cr (Fig. S5.6).

Overall, the whole distribution of the compatible elements suggest differentiation by crystal fractionation of olivine, pyroxene, feldspar, Cr-spinel, Ti-Fe oxides and apatite starting from transitional basalts, as already proposed for Dabbahu volcano (Barberi et al., 1975b; Field et al., 2013; Fig. 5.6a; Fig. S5.6). The distribution of the incompatible elements is also similar to the Dabbahu volcano samples (Fig. S5.6; Fig. S5.7; Hutchison et al., 2018) with the exception of Y and Zr, slightly depleted in the MVF products for the same Th content. Moreover, the distribution of the MVF incompatible elements (Nb, Zr, Ta, Y Vs Th; Fig. S5.6; Fig. S5.7) show good positive correlations going through zero (e.g., Th/Rb = 0.12 ± 0.01, Nb/Zr = 0.20 ± 0.02) suggesting a genetic link between mafic and the whole felsic products. Due to the small dataset and to the presence of the Daly Gap, it is however difficult to give a certain reconstruction of the fractional crystallization evolution trend between mafic and felsic products. The comparison between the felsic rocks of SFF-1 and FFD-4 indicates different extent of fractional crystallization of feldspar, as suggested by the negative anomalies of Eu, Sr and Ba, and of apatite and Ti-oxide as indicated by the negative anomaly of P and Ti, respectively (Fig. 5.7). Moreover, the Sr and Ba are remarkably lower in FFD-4 for the same Th (or Nb and Zr) content with respect to SFF-1 (Fig. 5.6b). Since accumulation of feldspar in SFF-1 can be excluded because it is not confirmed by Al2O3 vs. SiO2 and trace element compositions (e.g., no positive Eu anomalies; Tab. 5.1; Fig. 5.6a; Fig 5.6), a major fractionation of feldspar for FFD-4 at the same evolution degree of SFF-1 is hypothesized. The trace element differences indicate that the two felsic rock suites were originated by different differentiation paths.

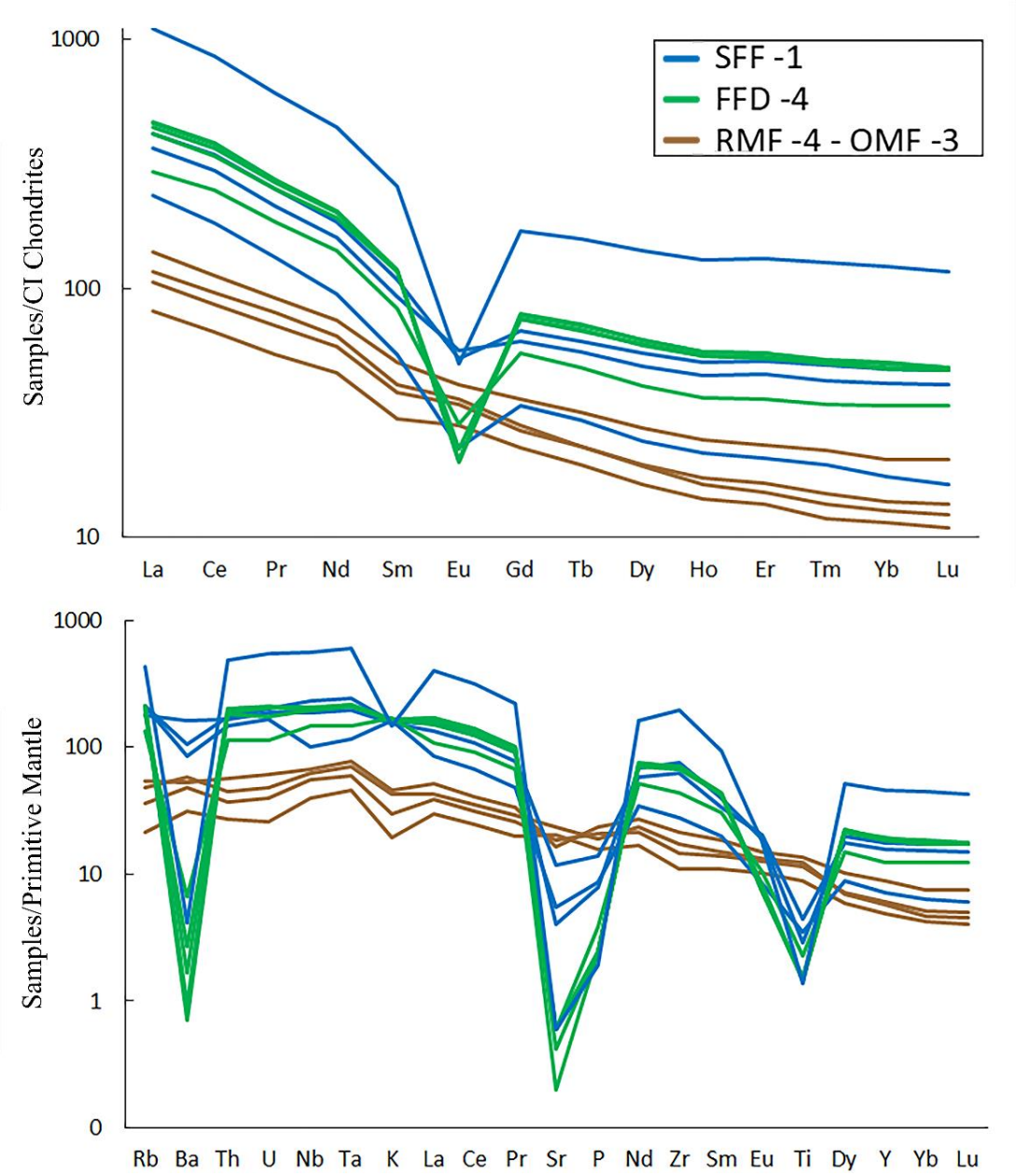

Fig. 5.7 Chondrite-normalized REE patterns and primitive mantle-normalized trace element spiderdiagrams. SFF-1, Stratovolcano Felsic Flows; FFD-4, Felsic Flows and Domes; RMF-4 - OMF-3, Recent-Old Mafic Flows. Normalizing values after McDonough et al. (1995).

5.3.3. Geothermobarometry

Four porphyritic samples, one trachyte of the first phase and three basalts of the second phase, were selected for mineral-melt geothermobarometry (Tab. 5.2; Fig. 5.3). The geothermobarometer of Masotta et al. (2013), based on the clinopyroxene-liquid equilibrium, was used for the stratovolcano trachyte. For the basalts I used the cpx-liquid thermometer of Putirka (2008; Eqn. 33) and the barometer of Neave and Putirka (2017). The feldspar-liquid and olivine-liquid equilibria of Putirka (2008; Eqn. 22, 24a, 24b and 25a) were

used for the stratovolcano trachyte and the basalts, respectively. For each sample, the whole rock analysis was used for the melt composition in equilibrium with the phenocrysts cores (Putirka, 2008). The output pressure of the clinopyroxene-liquid geothermobarometers was used as input for the other geothermobarometers. Water concentrations from 1 wt % to 3 wt % were used in the modelling. Mineral-melt equilibrium was checked based on the distribution coefficient $KD_{(Fe-Mg)}^{cpx-liq}$ = 0.09 - 0.37 for Masotta et al. (2013); $KD_{(Fe-Mg)}^{cpx-liq}$ = 0.27 ± 0.03 for Neave and Putirka (2017); $KD_{(Fe-Mg)}^{ol-liq}$ = 0.30 ± 0.03 for Putirka (2008); $KD_{(An-Ab)}^{pl-liq}$ = 0.10 ± 0.05 at T < 1050 °C and 0.27 ± 0.11 at T ≥ 1050 °C; $KD_{(An-Ab)}^{afs-liq}$ = 0.27 ± 0.18 for Putirka (2008).

The geothermobarometric calculations (Tab. 5.2) based on clinopyroxene of the SFF-1 trachyte indicate crystallization pressures on the order of 1.34-1.49 ± 1.15 kbar. The crystallization temperature was 914-925 ± 24 C° for clinopyroxene, 902-954 ± 36 °C for plagioclase, 857 ± 23 °C for alkali feldspar. A higher crystallization pressure is obtained for the RMF-4 mafic magma of the lava flow south of the stratovolcano (3.8-4.1 ± 1.4 kbar for clinopyroxene and 1.1-4.0 ± 3.8 kbar for plagioclase). The crystallization temperature was 1146-1176 ± 45 °C for clinopyroxene, 1091-1162 ± 36 °C for plagioclase and 1140-1178 ± 43 °C for olivine (only two analyses). The crystallization pressure obtained for the RMF-4 mafic magma of the lava flow north-west of the stratovolcano is still higher, 6.3-6.6 ± 1.4 kbar for clinopyroxene and 4.7-7.8 ± 3.8 kbar for plagioclase. The crystallization temperature was 1161-1193 ± 45 °C for clinopyroxene, 1134-1210 ± 36 °C for plagioclase and 1147-1184 ± 43 °C for olivine. Finally, the crystallization pressure obtained for the RMF-4 magma associated to a scoria cone in close proximity to the FFD-4 felsic centers, just south of the stratovolcano, is 2.5-2.8 ± 1.4 kbar. This estimation came from analysis of one clinopyroxene core and four rims which were found in equilibrium with melt. This is supported by ten analyses of rims close to the equilibrium range ($KD_{(Fe-Mg)}^{cpx-liq}$ = 0.31 and 0.32) giving crystallization pressures of 2.4-2.7 ± 1.4 kbar. The crystallization temperature for core and rim analyses in equilibrium is 1125-1155 ± 45 °C.

The corresponding depths can be derived assuming a 270 bar/km geobaric gradient (Best, 2013) and using clinopyroxene results because of the lower errors. The obtained crystallization pressures correspond to 5 km depth for the SFF-1 trachyte and to 9-10 km, 14-15 km and 23-24 km depths for the mafic products (Fig. 5.8).

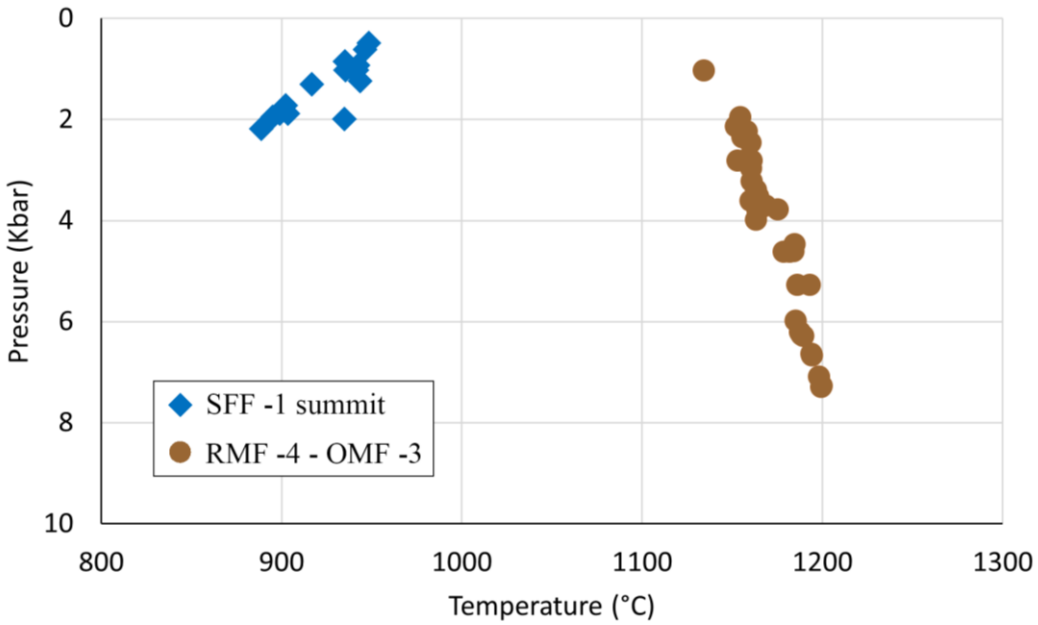

Fig. 5.8 Pressure and temperature estimates from clinopyroxene–melt pairs calculated with Neave and Putirka (2017; eq. 1) and Putirka (2008; eq. 33). SEE for the clinopyroxene-melt thermobarometer are ± 45 C° and ± 1.2 kbar.

5.3.4. Structures and seismicity

In this chapter I investigate the seismicity distribution, tectonic structures and cinder cones distribution and elongation of the MFV, in order to reveal the strain governing the MVF formation. I then compared the results of the MVF with the actual Central Afar NNW-SSE main trend (e.g., Manda Hararo, Erta Ale) and with the NNE-SSW trend of the Afar margin transverse alignments of volcanoes (e.g., Dabbayra, Assab and Dubbi).

En-echelon faults which are ~2 km long strike roughly parallel to the Red Sea trend and are clearly visible in the younger units at the southern tip of the MVF, and another NE-SW trend is defined by the elongation of the MVF calderas (Fig. 5.9). Furthermore, the distribution, morphology and elongation direction of the cinder cones is consistent with the two main trends (Fig. 5.9; Tab. 5.3). I identified three different groups of cinder cones based on their spatial distribution, and when the cone shapes were preserved, I also measured the direction of cone alignment using at least 3 cones closer than 400 m from each other, and the elongation direction using cones with aspect ratio > 1.4. The largest group of cinder cones is along the NNW-SSE trending zone west of the stratovolcano with up to 70 cones distributed along a zone striking 332° N, roughly parallel to the Red Sea trend. Also, the alignment of the cones within this group has a trend varying between 327° E and 351° E, and

the cones show predominant elongation varying from 321° E to 17° E, both sub-parallel to the Red Sea trend (Fig. 5.9). Altogether, the products of the second phase west of the stratovolcano occur over a ~35-km-long, NNW-SSE trend. East of the stratovolcano, two smaller groups of cones have been identified associated only with the OMF-3. A group of 19 cones show a trend of 317° N, similar to the western cones while the remaining 26 cones are aligned 49° N, parallel to the elongation direction of the calderas. Most of the cones east of the calderas are not elongated nor aligned (Fig. 5.9).

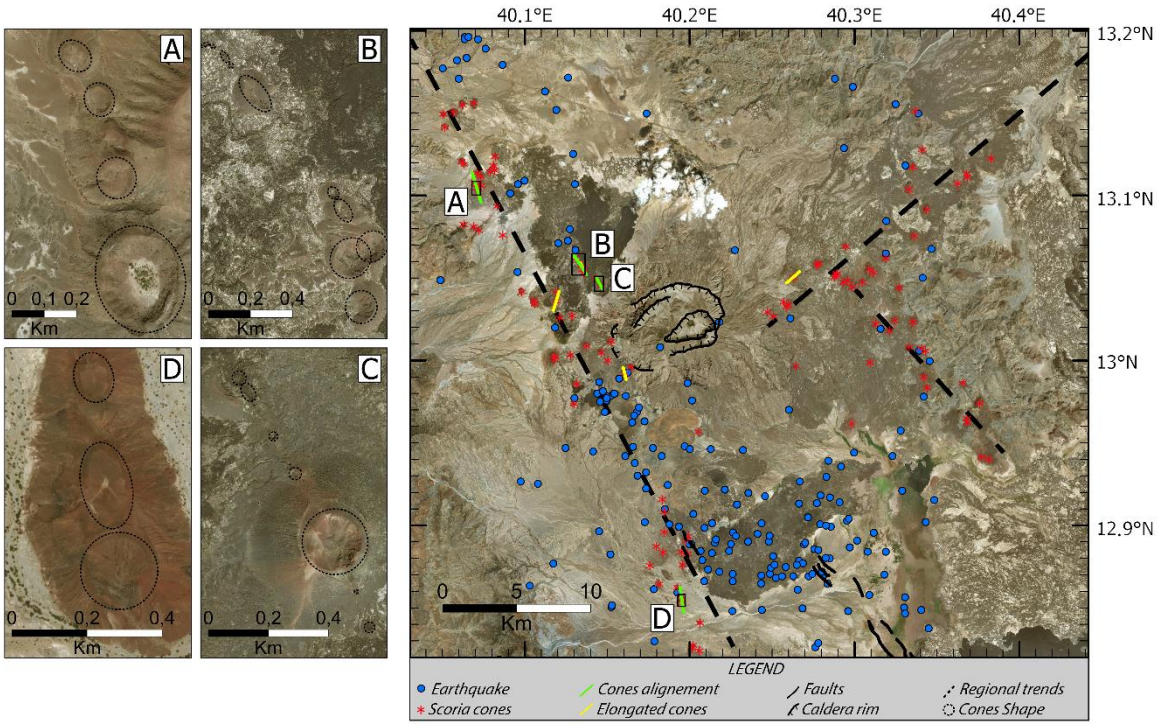

Fig. 5.9 Distribution of earthquakes (blue dots), cinder cones (red asterisks) and faults (solid black lines) of the MVF. Panels A, B, C and D show the elongated (351° E, 347° E, 17° E, 336° E and 321° E) and aligned (343° E, 327° E, 331° E and 351° E) cones (black dotted line).

The majority of the seismicity in MVF occurs along a ~35 km long, NNW-SSE trending region with the alignment of earthquakes corresponding to the largest group of cinder cones and to the recent flows (FFD-4 and RMF-4) (Fig. 5.9). The magnitude varies between 1.06 and 3.37 and give a mean of 2.22. Most earthquakes in the alignment are observed at the southern end with good correlation to where the most recent RMF-4 were erupted and where faults cutting these flows and surficial sediments occur. A smaller group of earthquakes is located in eastern parts of the MVF in the area between the OMF-3 and the basement, indicating this region is not the main locus of seismicity at present. No significant seismicity occurs at the MVF calderas.

Tab. 5.2 Pressure and temperature conditions of crystallization from mineral geothermobarometers. K39, SFF-1; D170, G20, G8, OMF-3 - RMF-4.

Sample		Clinopyroxene			Plagioclase			
K39	H_2O input		P_1	T_1	P input	H_2O input	P_2	T_2
	1%		1.34	925	1.5 Kbar	1%	2.7	954
	2%		1.41	919	1.5 Kbar	2%	2.1	928
	3%		1.49	914	1.5 Kbar	3%	1.7	902
		n°	15	15		n°	3	3
		SEE	± 1.15 kbar	± 24 °C		SEE	± 3.8 kbar	± 36 °C
G20	H_2O input		P_3	T_2	P input	H_2O input	P_2	T_2
	1%		4.1	1176	4 Kbar	1%	4.0	1162
	2%		3.9	1161	4 Kbar	2%	2.5	1125
	3%		3.8	1146	4 Kbar	3%	1.1	1091
		n°	11	11		n°	2	2
		SEE	± 1.4 kbar	± 45 °C		SEE	± 3.8 kbar	± 36 °C
D170	H_2O input		P_3	T_2	P input	H_2O input	P_2	T_2
	1%		6.6	1193	6.5 Kbar	1%	7.8	1210
	2%		6.5	1177	6.5 Kbar	2%	6.2	1171
	3%		6.3	1161	6.5 Kbar	3%	4.7	1134
		n°	7	7		n°	7	7
		SEE	± 1.4 kbar	± 45 °C		SEE	± 3.8 kbar	± 36 °C
G8	H_2O input		P_3	T_2				
	1%		2.8	1155				
	2%		2.6	1140				
	3%		2.5	1125				
		n°	5	5				
		SEE	± 1.4 kbar	± 45 °C				

Sample		K feldspar			Olivine			
K39	P input	H_2O input		T_2				
	1.5 Kbar	1%		857				
	1.5 Kbar	2%		857				
	1.5 Kbar	3%		857				
			n°	5				
			SEE	± 23 °C				
G20					P input	H_2O input		T_2
					4 Kbar	1%		1178
					4 Kbar	2%		1159
					4 Kbar	3%		1140
							n°	2
							SEE	± 43 °C
D170					P input	H_2O input		T_2
					6.5 Kbar	1%		1184
					6.5 Kbar	2%		1165
					6.5 Kbar	3%		1147
							n°	4
							SEE	± 43 °C

Note: n°, number of analyzed samples; SSE, Error Sum of Squares. Subscript indicates the reference work for the geothermobarometric calculation: 1, Masotta et al., 2013; 2, Putirka, 2008; 3, Neave and Putirka, 2017.

Tab. 5.3 Spatial distribution and elongation of the cinder cones.

	Main trend		Alignment		Elongation	
	Degree	N° of cones	Degree	N° of cones	Degree	Aspect ratio
NNW-SSE distribution of cones west of the stratovolcano	332° N	70	351° N	3	351° N	1.5
			327° N	6	347° N	1.4
			331° N	2 + pit craters	17° N	1.4
			343° N	4	336° N	1.55
					321° N	1.5
NNW-SSE distribution of cones east of the stratovolcano	317° N	19				
NE-SW distribution of cones east of the stratovolcano	49° N	26			49° N	1.65

5.4. Discussion

5.4.1. Evolution of the MVF: from caldera activity to rift segment development

Two main phases of activity were identified during the evolution of MVF, based on the integration of volcanological, geochemical, petrological, structural and seismological evidence.

The first phase began at 0.55 Ma (Barberi et al., 1972) with explosive and effusive activity from a central vent that built the stratovolcano. The two caldera structures suggest that the volcano was fed by a shallow crustal magma chamber, at ~5 km depth according to geobarometry applied to the lavas of the stratovolcano summit. This phase is dominated by structures trending NE-SW as indicated by the caldera elongation. Furthermore, this trend has been observed also in the NE-SW alignment of OMF-3 cinder cones east of the stratovolcano. This cinder cones alignment suggests that a tectonic structure orthogonal to the current rift axis (transverse alignment), existed during the formation of the stratovolcano and controlled the emplacement of the OMF-3 cinder cones aligned NE-SW. The large range in the concentrations of incompatible trace elements of SFF-1 indicate efficient differentiation processes in the crustal chambers leading from trachytes to peralkaline

rhyolites. An estimate of the extent of differentiation made using Zr as fractionation index due to its high incompatibility in peralkaline rocks indicates formation of the peralkaline rhyolite by 60% fractional crystallization starting from the trachytic melts. No mafic activity has been observed for the first phase meaning that the basic magmas could have remained at depth, unerupted, as suggested for some MER volcanoes (e.g., Peccerillo et al., 2003; Hutchison et al., 2016), or could be mostly covered by later activity and thus difficult to identify and distinguish from the later mafic products. It is also possible that the composition of the mafic products of the second phase represent the parental magma of the stratovolcano felsic products, erupted after the first phase and away from the stratovolcano. Since the stratovolcano is now heavily eroded and currently lacks any significant seismic activity, I suggest that it is now dormant or extinct.

During the second phase, both mafic and felsic magmas were erupted. The mafic magma storage depths range from ~9 to ~24 km, and the presence of reversed zoning in clinopyroxene, plagioclase and olivine crystals (Tab. S2.1; Fig. S5.2c), suggest a stacked plumbing system where the mafic magmas undergo differentiation by fractional crystallization and magma mixing. In addition, connections between the mafic and felsic feeding systems of the second phase are revealed by evidence of interaction between basalts and felsic magmas, indicated by the presence of two populations of clinopyroxene in the mafic lavas erupted nearby the sialic centers (as a whole Wo41-48 Fs9-32). This suggests that the mafic magmas encountered mush-like felsic pockets during ascent and captured high Fs clinopyroxene without other clear evidence of magma mixing. The felsic products of the second phase (0.12 Ma from Barberi et al., 1972) are mostly aphyric and effusive, systematically more evolved (except for G33) and more peralkaline compared to the stratovolcano products and occupy a very narrow chemical range. It is possible that these aphyric and acidic lavas originated from highly fractionated melts rising from a relatively deep reservoir slowly enough to allow efficient gas/melt decoupling, preventing explosive activity (Gonnermann and Manga, 2007); efficient crystal-melt separation in the magma chamber or adiabatic decompression-induced crystal resorption may explain the aphyric texture. However, their negative anomalies in Sr, Ba and Eu point toward the efficient crystal-melt separation as the reabsorption of feldspar would have canceled or at least mitigated these negative anomalies. This phase is characterized by the development of

structures parallel to the NNW-SSE Red Sea trend and a shift in activity to the western side of the stratovolcano, where the youngest structures including RMF-4, FFD-4 and cinder cones occur. The youngest volcanism and structures correlate spatially with the majority of the recent seismicity, suggesting that this region is the current locus of strain and magmatism. I also interpret that the seismicity at the southern end of the MVF is caused by faulting on NNW-SSE planes along the rift axis, as short en-echelon faults are mapped across a ~10 km wide axial zone (Fig. 5.9). En-echelon faults that can also feed fissure eruptions during episodes of magma migration.

The marked changes in the types of erupted products, the different magma chamber depths, the distribution of the recent seismic activity and the structural arrangement between the two evolutionary phases of the MVF, show that the recent activity of MVF differs from the first phase and it is now typical of an active magmatic rift segment.

A petrogenetic discussion of the magmatic evolution of MVF was not the focus of this work due to lack of mafic and intermediate products and of a complete sampling coverage of the area. I am aware that new studies on the stratovolcano, and in particular on the associated mafic products if outcropping, are needed to test my geochemical and petrological interpretation. Nevertheless, a process of fractional crystallization from transitional basalts to rhyolite, similar to those described for Dabbahu volcano (Barberi et al., 1975; Field et al., 2013), can be envisaged for the MVF products, with FFD-4 as a whole reaching a higher extent of differentiation with respect to SFF-1. I also show differences in Sr and Ba for the same degree of evolution (Zr or Th content) indicating differences in the fractionation process between the two felsic phases. I therefore speculate that the described chemical differences, in particular the different trace element concentration of felsic rocks between the two phases (Sr and Ba; Fig. 5.6b) are not only due to different degrees of fractional crystallization, but also due to major differences in the evolutionary processes. The major differences in the evolutionary processes are possibly linked to different P-T-H2O conditions of magma storage or variable extent of crustal assimilation that, combined with the differences regarding the erupted products and the geobarometric estimates, could be related to differences in the plumbing system architecture.

5.4.2. The MVF magma source and comparison to other rift volcanoes

Taken as a whole, the MVF products show a similar distribution of major and trace elements to Dabbahu volcano, except for the G33 lavas of the stratovolcano summit, reaching very high incompatible element contents (Fig. 5.6; Fig. S5.6; Fig. S5.7). In particular, the RMF-4 phase of MVF and the on-axis volcanism of Dabbahu volcano (Field et al., 2013) are both characterized by eruption of a significant volume of transitional mafic magmas. The recent mafic flows, just like at Dabbahu volcano, are associated with aphyric and obsidian-rich comendite erupted from several scattered vents and producing small volume domes or lava flows. Furthermore, the MVF first phase, unlike on-axis volcanoes (e.g., Dabbahu, Badi) and MVF second phase, show abundance of ignimbrites that could suggest different tectonic settings. In the off-axis activity of MVF stratovolcano the volatile phases may be able to exsolve, accumulate and lead to explosive eruptions while this could be prevented by magma degassing along axial segments.

Lithosphere thinning is an important process influencing the depth of partial melting in the rising asthenosphere beneath rift systems. The across- and along-rift variation in the extent of stretching and thinning of the lithosphere leads to partial melting by decompression at different depths, and consequently to different geochemical composition of the basaltic melts (Rooney, 2010). I compared the chemical composition of the MVF mafic products (MgO wt% > 4) to similar mafic rocks of other Afar volcanoes by means of rare earth element ratios (Fig. 5.10). I use the La/Sm ratio to evaluate the degree of partial melting and/or source enrichment and the ratio Tb/Yb for the depth of the melting column (Rooney 2010; Wang et al., 2002). In fact, magmas generated at a depth sufficient to have residual garnet in the source show a marked fractionation in the middle and heavy rare-earth elements (e.g., Tb/Yb, Dy/Yb; Wang et al., 2002). High pressure clinopyroxene of a spinel-lherzolite source behaves somewhat like garnet, but with much lower effect (Rooney, 2010).

I considered the marginal Nabro volcano (Donovan et al., 2018) and the transverse Assab range (Teklay et al., 2010), the on-axis Dabbahu volcano (Barberi et al., 1975b; Hoare et al., 2020), the Badi volcano in the Dabbahu segment (Ferguson et al., 2013), the products from the Dabbahu and Manda Hararo segments (Ferguson et al., 2013; Barrat et al., 2003) and the Erta Ale (Barrat et al., 1998) magmatic segment fissural products. As a whole, the mafic

products of these volcanic centers range from 0.8 to 3.8 in La_N/Sm_N and from 1.0 to 2.2 in Tb_N/Yb_N (Fig. 5.10), crossing the Tb_N/Yb_N values at the transition between the spinel- and the garnet-bearing mantle sources derived from magma modelling in the Basin and Range province (Wang et al., 2002). Contributions from melting a garnet-bearing lower crust can be ruled out due to the low crustal thickness, ranging from 15 km beneath the Danakil Depression to 25-30 km beneath the Danakil microplate (Hammond et al., 2011). The fractionation of garnet under water-saturated conditions observed in some arc settings (Alonso-Perez et al., 2009) can also be excluded given the lack of hydrous phases in Afar mafic volcanism. Therefore, I interpret the variation in Tb_N/Yb_N as the result of changes in the melting column depth due to variations in lithospheric thickness. The marginal volcanism (i.e., Nabro and Assab range) is related to a deeper, garnet-bearing source ($Tb_N/Yb_N > 1.8$), while the MVF is similar to the axial volcanism (i.e., Badi volcano, Dabbahu volcano, Dabbahu and Manda Hararo segments and Erta'ale) and is related to a shallower source ($Tb_N/Yb_N < 1.8$, spinel-lherzolite in the Wang et al. (2002) model for Basin and Range, while still in the garnet stability field according to Ferguson et al. (2013)). This difference is in agreement with the more evolved rifting stage (and thinner lithosphere) of the axial magmatic segments and strengthens the analogy between MVF recent volcanism and axial volcanism.

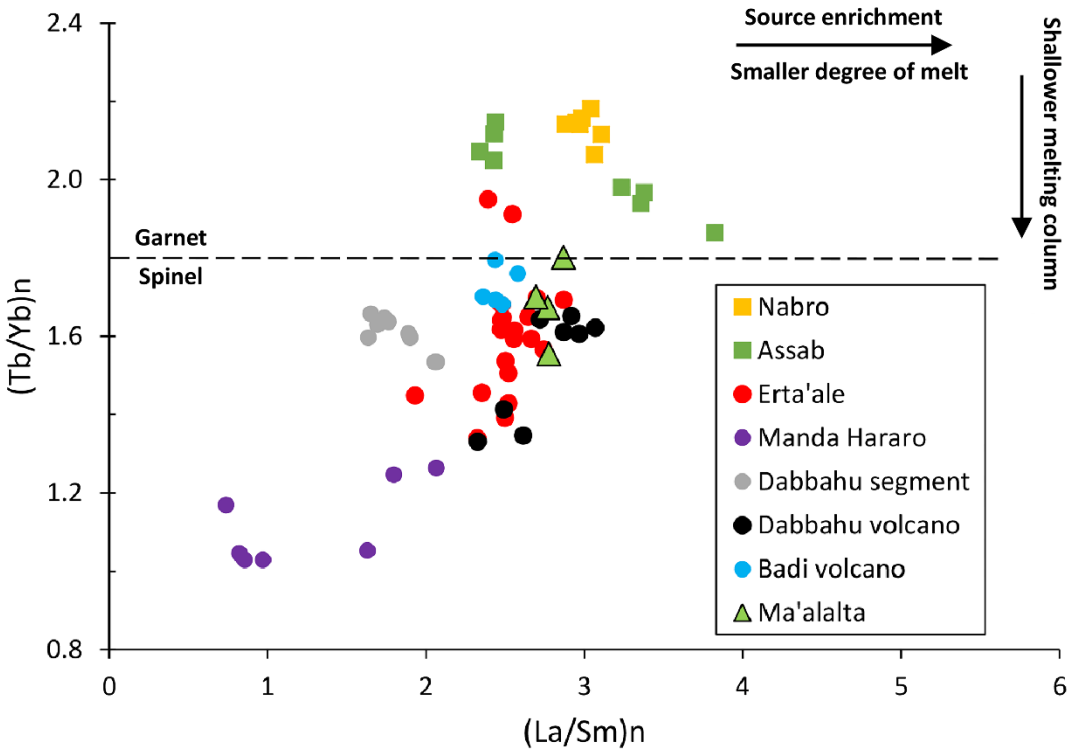

Fig. 5.10 Plot of Tb/Yb and La/Sm normalized to chondritic values (McDonough et al., 1995). Only samples with MgO greater than 4 wt% are plotted. The division between spinel and garnet-dominated melting is derived from

magma modelling in the Basin and Range province (Wang et al., 2002). As a comparison with the MVF, volcanism of different locations of the Afar region is shown: the marginal Nabro volcano (Donovan et al., 2018) and the transverse Assab range (Teklay et al., 2010), the on-axis Dabbahu volcano (Barberi et al., 1975b; Hoare et al., 2020), the Badi volcano in the Dabbahu segment (Ferguson et al., 2013), the products from the Dabbahu and Manda Hararo segments (Ferguson et al., 2013; Barrat et al., 2003) and Erta Ale (Barrat et al., 1998) rift axis fissural products. See text for explanation.

Therefore, I suggest that the geochemistry of the available mafic samples of the MVF, consistent with the other observations of this work, may be taken as an indication that the recent phase of the MVF is more typical of the axial volcanism. Additional work specifically on the MVF mafic rocks is necessary to fully define the mantle sources and melting conditions. However, based on several different lines of evidence from volcanology, geochemistry, seismicity and petrology, I propose that MVF evolved from an initial felsic central stratovolcano to an active magmatic segment.

Strain and magmatism are generally thought to progressively localize in-rift to narrow magmatic segments and the rift margin being progressively abandoned during magma-rich rifting (Hayward and Ebinger, 1996; Wolfenden et al., 2005). However, here I have presented evidence of a young axial segment close to the rift margin of Afar (Fig. 5.1; Fig. 5.3), suggesting that the process of strain localization may be more complex. Studies from Iceland suggest that rift zones can initiate as several subparallel overlapping rifts during incipient rifting. Some zones do not fully evolve like the Öræfajökull–Snæfell volcanic flank zone which initially developed on a pre-existing cross-rift structure and then was abandoned (Hards et al., 2000). On the other hand, subparallel overlapping rifts can be active at the same time in response to the plate migration with respect to a stable plume, like the Eastern and Western volcanic zones (LaFemina et al., 2005). Using this analogy, the origin of MVF could be linked to a pre-existing lithospheric weakness guiding where strain localizes (e.g., Muirhead et al., 2018; Lloyd et al., 2018; Robertson et al., 2016) or to the interaction between the plate-boundary and a hot-spot.

5.5. Conclusive remarks

The Study of the MVF allow to identify two phases of activity. The first phase (0.55 Ma; Barberi et al., 1972) is dominated by a stratovolcano with abundance of ignimbrite, with a shallow magma chamber (5 Km depth) and a NE-SW structural trend (Fig. 5.3; Fig. 5.8; Fig.

5.9). This phase is more affine to the transverse volcanism located at the Afar margins with respect to the axial segments. The second phase is dominated by mafic and felsic effusive magmatism, generated by a shallow partial mantling column, and evolving by means of fractional crystallization and magma mixing within a stacked plumbing system ranging from ~9 to ~24 km (Fig. 5.3; Fig. 5.6; Fig. 5.8; Fig. 5.10; Fig. S5.2). This phase is dominated by structures parallel to the NNW-SSE Red Sea trend and the recent seismicity indicate the second phase is the current locus of strain and magmatism (Fig. 5.9). The characteristics indicate that the second phase has to be considered as an active magmatic segment.

PART IV - Geodynamic evolution of the Afar Rift-Rift-Rift system

6. The origin of the Stratoid and the evolution of the Red Sea rift branch in Afar

6.1. The Stratoid Series

The systematic geochemical study carried out in this work allows for a detailed characterization of the Stratoid and reveals the variable petrological nature of the Series. In particular, the observed variations regarding the depth of the melting column (Fig. 3.11d, e) and the involved mantle reservoirs (Fig. 3.12) indicate that the spatial and temporal distinctions between Lower and Upper Stratoid (LS and US; Kidane et al., 2003) are related to changes in the conditions of primitive magma genesis. These observations clearly indicate different geological conditions in the origin of LS and US and therefore that the Stratoid are not a single Series as previously thought. Furthermore, similar variations have been observed in some younger lavas of the US (i.e., lavas of the region between Serdo and Silsa; Fig. 3.1; Fig. 3.12) indicating inner variability and revealing that the study of the Stratoid could be more challenging than previously thought as they are not an internally homogeneous volcanic phase.

6.2. The mantle source and rift evolution in Southern and Central Afar

The results of the Stratoid, Central Afar Gulf (CAG) and Ma'Alalta volcanic field (MVF) petrological study of this thesis are interpreted and integrated here with geophysical and stratigraphic literature evidence on magma storage, crustal structure and depocenter locations, in order to interpret the evolution of the on land portions of the Red Sea rift branch in Afar.

The geochemical results show that the LS (~4.5-2.6 Ma), were generated by a shallower melting column (< 60-100 km) with respect to the US, suggesting a more stretched and thinned lithosphere (Fig. 3.11d, e; Fig. 6.1a). In agreement with the observation of a stretched lithosphere, the isotopic signature indicates a major involvement of the DMM and PAL mantle source components during partial melting with respect to the more plume-like composition of the US (Fig. 3.12). The LS Series basalts outcrop only in Southern Afar (Fig. 3.1) and are temporally coeval with the development of the Hadar Basin depocenter in

Southern Afar (3.8-2.9 Ma; DiMaggio et al., 2015; Rooney, 2020b; Wynn et al., 2008; Fig. 3.1), which spatially corresponds to an area of thinned crust (~22 km; Hammond et al., 2011; Wang et al., 2021). I interpret these independent observations as evidence that the LS were produced during a phase of localized extension in Southern Afar, leading to melting of a relatively shallow mantle dominated by the DMM and PAL reservoirs. (Fig. 6.1a). These observations suggest an overall more mature stage of rifting for the LS with respect to the US. This interpretation is consistent with a number of geological and geophysical studies that interpret Red Sea related extension localized to the rift valley floor in South Afar during the Miocene (Hammond et al., 2011; Tesfaye et al., 2003; Wolfenden et al., 2005).

After the LS emplacement, the locus of Stratoid volcanism shifted dramatically from Southern to Central Afar to form the US during 2.6 to 1.1 Ma (Fig. 3.1). My data indicate that the US magmas were associated with a deeper melting column (> 60-100 km) with respect to the earlier LS Series and hence consistent with melting below a thicker lithosphere (Fig. 3.11d, e; Fig. 6.1b). Accordingly, the isotopic signature indicates a major involvement of the Afar plume component with respect to major DMM and PAL signals observed in the other studied Series (Fig. 3.12). These results are consistent with the locus of melting shifted NE to a new zone of extension in central Afar where the lithosphere had been less thinned, leading to a minor involvement of the shallow mantle (i.e., DMM and PAL reservoirs) and to a major influence of the Afar plume (Fig. 6.1b). I interpret the NE shift in volcanism, the deepening of the melting column, the isotopic signature and the geological evidence for a co-eval and pronounced change in fluvial depositional systems and locus of strain (Campisano, 2012; Di Maggio et al., 2015; Quade et al., 2008; Wynn et al., 2008), as indicative of a rift jump from the Pliocene rift in Southern Afar to the Pleistocene rift in Central Afar around the end of the Pliocene (Fig. 6.1b). I propose that the dramatic shift in strain and volcanism may have been triggered by tectonic reorganization caused by the triple junction moving north-eastward from the Hadar Basin to central Afar, possibly due to the on land spreading of the Gulf of Aden in the Tadjoura gulf at ca. 3 Ma (Daoud et al., 2011; Le Gall et al., 2015). My observation are in agreement with the regional reconstruction of the northeast migration of the Red Sea rift since 16 Ma (Wolfenden et al., 2005; Hammond et al., 2011), the inferred northeast migration of the triple junction (Tesfaye et al., 2003), and with the more local observations of the northeast migration of the depocenter during

~10-3 Ma along the Awash valley (Kalb, 1995). Furthermore, the rather continuous volcanic activity observed during the rift jump in Afar is in agreement with observations made on the relocation of two rift cycles observed in western Iceland (i.e., Snaefellsnes and the older NW rift of Iceland), separated by an unconformity indicating less than 200 Kyr hiatus in lava succession, and possibly overlapping in time (Hardarson et al., 1997).

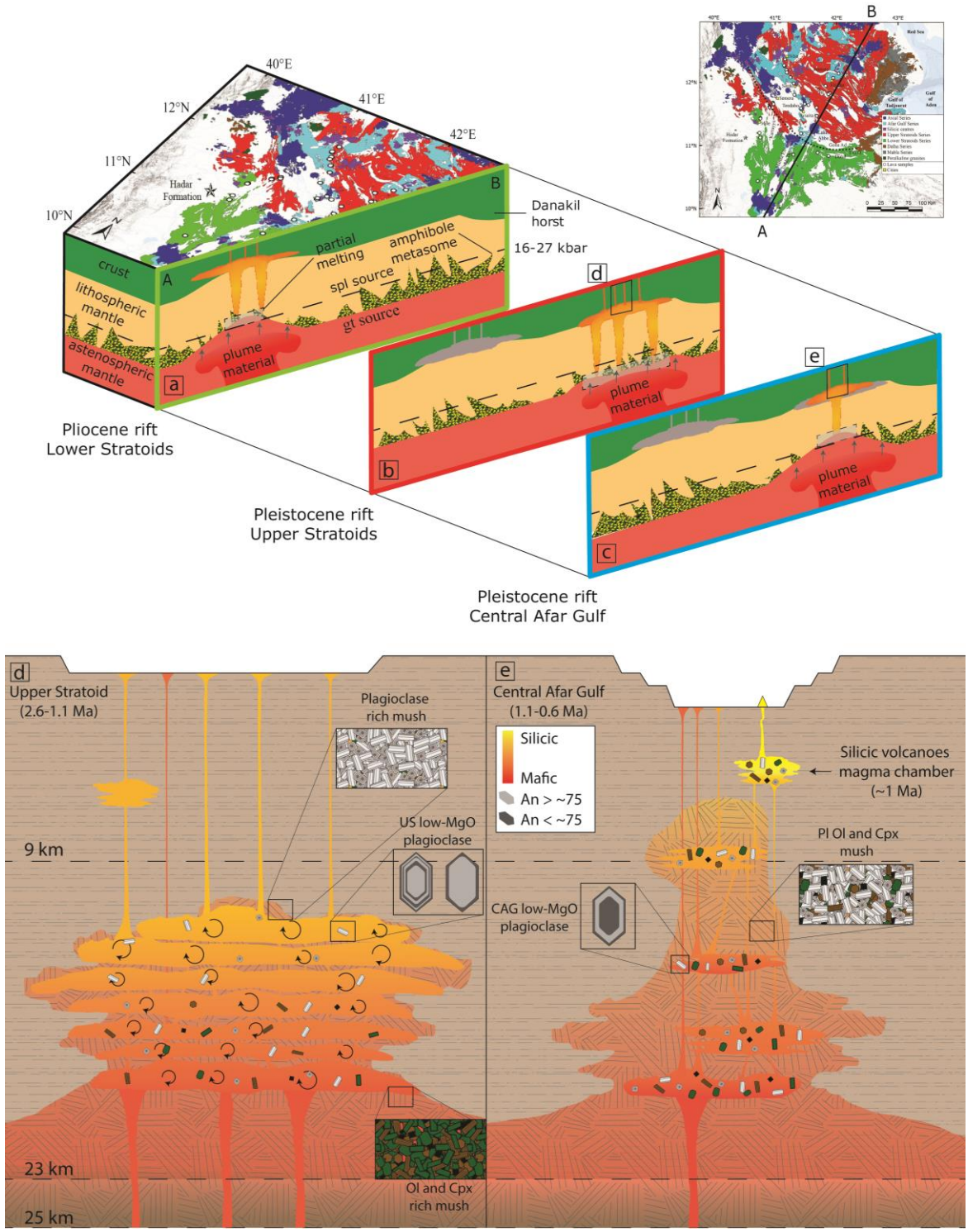

Fig. 6.1 Schematic cartoon depicting the partial melting and magmatic system evolution in Central and Southern

Afar. a-c) Schematic cartoon of the three mantle reservoirs (Afar plume, depleted mantle, and amphibole-bearing SCLM) involved in the partial melting of the three Series during rifting evolution in Afar last 4.5 Ma. A diffuse plume acting overall at regional scale can be envisaged, forming distinct plume heads of rising material in space and time. a) The Pliocene rift produced the LS Series from a shallow melting column associated with a thinned lithosphere. b) The jump of the rift relocates the Pleistocene rift north-east in Central Afar and led to the formation of the US Series from a deeper melting column associated with a thicker, less stretched lithosphere. c) The focalization of the Pleistocene rift led to a shallow melting column and a thinned lithosphere for the CAG Series mantle source. The sketch is not to scale, and the partial melting area is approximative. Spl, spinel; gt, garnet. See text for more details. d, e) Schematic cartoon depicting the magmatic system of US and CAG in Central Afar. d) The US are dominated by eruption of the moderately evolved, aphyric and homogeneous (4-6 MgO wt%) upper portion/s of a melt-dominated magmatic system, rising directly to the surface. e) The CAG are dominated by a melt-poor magmatic system with respect to the US, with eruptions taking place through a series of small, crystal-rich and interconnected magma chambers. The sketch is not to scale, and the depth of the magmatic systems is approximative. The depth of the Moho (23-25 km) and of the lower-upper crust limit (9 km) are from Hammond et al. (2011). See text for more details.

In the area between the towns of Serdo and Silsa (Fig. 3.1) some US and one CAG lavas (~1 Ma) show a shallower melting column and a marked increase in the DMM and PAL components (greater than the CAG) with respect to the US (Fig. 3.12). This could be explained by the persistent activity of the US weakening the lithosphere until it is destabilized and consumed (i.e., lithosphere detachment or dripping; Rooney at al., 2012b; Furman et al., 2016), leading to the thinning of the lithosphere and to the observed increase in PAL and DMM components at the expense of the Afar plume. These observations suggest the progressive focalization of the Pleistocene rifting from the US Series to the CAG Series along the Tendaho Graben at ~1 Ma.

After the eruptions of the US Series over a wide area and the formation of the silicic volcanoes, the rift activity changed again with the emplacement of the CAG Series (Fig. 3.1), the first recognized magmatic activity localized along the axial faults of the depression and associated with thinned crust in the Tendaho graben (Hammond et al., 2011). The CAG Series has been associated with the localization of strain (Rooney 2020b; Stab et al., 2016; Tesfaye et al., 2003). My results confirm this interpretation from a petrological point of view indicating a shallower melting column and a higher degree of melting for the CAG Series mantle source compared to the US (Fig. 3.11e, d; Fig. 6.1c). The isotopic signature indicates, in agreement with a less thick lithosphere, a major involvement of shallower DMM and PAL mantle source components with respect to the more plume-like composition of the US (Fig. 3.12). At the same time the CAG show a decrease of the DMM and PAL signature with

respect to the Serdo-Silsa lavas, suggesting that after this transitional phase of consuming the destabilized lithosphere, the involvement of shallower, colder and less weakened lithosphere leads to a decrease in the PAL components for the same depth of melting. I therefore indicate the CAG as a more mature stage of the rift with respect to the US and interpret them as the first volcanic activity associated with the progressive focusing of rifting in Central Afar (i.e., Pleistocene rifting; Fig. 6.1c).

6.3. The crustal magmatic system evolution during rift focusing in Central Afar

The US magmatic system developed in the lower crust (~11-18 km depth; Fig. 4.7a), allowing the formation of mush zones while preserving melt rich portions, moderately zoned, evolving by means of fractional crystallization, mixing and plagioclase-rich mush assimilation (Fig. 6.1d; Fig. 4.6b, c; Fig. 4.8; Fig. 4.12; Fig. S4.4b). Most of the US eruptions tap the moderately evolved, aphyric and homogeneous (4-6 MgO wt%) upper portion/s of this system and rise directly to the surface (Fig. 6.1d), possibly due to buoyancy of magma due to exsolved volatiles as a consequence of fractionation of anhydrous minerals and differentiation (Black and Manga, 2017) and/or because of plate spreading (Watanabe et al., 1999; Buck, 2006; Tibaldi, 2015). This reconstruction is in agreement with evidence of magma differentiation taking place in the lower and middle crust (Cashman et al., 2017; Sparks et al., 2018; Solano et al., 2012; Blundy and Annen, 2016; Annen et al., 2006), with evidence of current deep magmatic reservoir/s being present near the base of the crust in Afar (Desissa et al., 2013; Wang et al., 2021; Guidarelli et al., 2011; Didana et al., 2014; Ahmed et al., 2022; Hammond et al., 2011), and in general agreement with models of flood basalt magmatic systems (Black and Manga, 2017).

Roughly at 1 Ma, several silicic volcanoes developed in Afar producing a silicic volcanic phase in between the prevalently mafic US and the CAG (Fig. 3.1). This silicic phase marks an abrupt change in the magmatic system during rift evolution from the deep magmatic reservoirs of the US (11-18 km) to the shallow chambers of the silicic stratovolcano (Lahitte et al., 2003a). The study of MVF directly shows the presence of shallow magma chambers for the silicic volcanoes (~5 km; Tab. 5.2). This could suggest a decrease of the partial melting and/or an increase of the extension rate around 1 Ma, allowing magma to rise at shallower crustal level

due to decompression, pond and differentiate due to the decrease of new magmas input and possibly leading to an increase of the intruded magma volume. Furthermore, the geochemical and petrographic features of the MVF second phase are similar to the magmatic segments (i.e., Dabbahu, Erta Ale) and differ from the silicic volcanoes, indicating that localized rift extension can be heavily offset towards the rift margin and confirming that silicic volcanoes could act as precursor of rift development (Lahitte et al., 2003a).

The CAG magmatic system developed overall at the same depth range of the US (18-11 km; or possibly shallower as indicated by plagioclase; Fig. 4.7). However, the petrographic and micro analytical studies (Fig. 4.6e, f, g, h; Fig. S4.4d; Fig. S4.1; Fig. 4.11c) point out that the CAG rose through a mush-dominated crust and was more prone to stop and crystallize in small, interconnected and crystal rich magma chambers, indicating a different organization of the magmatic system (Fig. 6.1e). Considering the decrease of erupted volume from the US to the CAG (and to the silicic volcanic phase) and the increase in the degree of partial melting, an important volume of intruded material during the CAG activity is required. This is in agreement with geophysical, geodetic and seismic studies indicating the importance of magma intrusion during rifting in Afar (Keir et al., 2011; Wright et al., 2006), MER (Kendall et al., 2005; Corti, 2009) and Red Sea (Buck, 2006). Based on magnetic data, gravity data, surface geology, geochronology, and paleomagnetic studies Bridges et al. (2012) identify a 10 km wide zone of diking intruding the Tendaho graben in the last 0.8 Ma of extension, corresponding with the beginning of the CAG activity and supporting the substantial intrusive/subvolcanic activity. The study of the US and CAG crustal magmatic system could therefore suggest a transition from a possible subsolidus rock crust before the US, to melt-rich mushes after the rift relocalized in Central Afar (i.e., US activity), to crystal-rich mushes during rift focalization (i.e., CAG activity) with respect to the US.

7. Conclusion

In this thesis I investigated the petrology of the Stratoid flood basalt and younger volcanism (4.5-0.6 Ma), associated with the on land portion of the Red Sea branch and continental break up in Afar. This study leads to important observations regarding the evolution of the southern portions of the Red Sea rift and the associated magmatism:

I) Changes in the conditions of primitive magma genesis and in the mantle reservoirs partial melting revealed that the Lower and Upper Stratoid must be considered as two distinct Series and not one as previously thought. Furthermore, the Upper Stratoid characteristics suggest variations also within the Series.

II) The variations of the mantle source/s observed between the Series have been interpreted as related to the rift relocalization from South Afar (i.e., Lower Stratoid) to Central Afar (i.e., Upper Stratoid) at 2.6 Ma, before focalizing in Central Afar (i.e., Central Afar Gulf) at 1.1 Ma, marking the locus of the current continental break up.

III) The different crustal magmatic systems observed for the Upper Stratoid and Central Afar Gulf revealed an increase of the intruded material into the crust during the rift focalization, possibly indicating the formation of a crystal-rich mush storage system in the crust.

IV) The study of the Ma'Alalta volcanic field confirms the variation of the magmatic system after the Stratoid emplacement, and the role of silicic volcanoes as precursors of the rift development. This study also indicated that localized rift extension can be heavily offset towards the rift margins.

Acknowledgment

The years of my PhD has been a period full of great experiences, continuous learning and professional enrichment that led to a personal and professional growth. For this I am extremely thankful to my advisor Anna Gioncada and my co-advisor Carolina Pagli and Derek Keir for giving me the opportunity to undertake this journey, for helping, supporting and inspiring me during it and, above all, for doing all this in a friendly and lovely way.

I would like to acknowledge Dr. William Hutchison from the School of Earth and Environmental Sciences of the University of Andrews and Dr. Francesca Forni from the Department of Earth Sciences “Ardito Desio'' of the University of Milano for their precious and constructive comments that help improve the quality of the thesis.

I thank R. Ishak and M. Gemelli (Scanning Electron Microscope Laboratory, CISUP, University of Pisa), A. Orlando, E. Braschi (Electron Microprobe Laboratory, CNR-IGG of Firenze), A. Risplendente (Electron Microprobe Laboratory, University of Milano), L. Ghezzi (Inductively Coupled Plasma-Mass Spectrometry Laboratory, University of Pisa), M. Masotta (Laser Ablation-Inductively Coupled Plasma-Mass Spectrometer Laboratory, CISUP, University of Pisa) D. Mark and R. Dymock (NERC Argon Isotope Laboratory, Scottish Universities Environmental Research Centre) for their support during sample preparation and analytical acquisition. I thank R. Santacroce (University of Pisa) for discussions and support.

I thank the colleagues of the Addis Ababa University and the Ethiopian and Afar Regional governments for their support and help in organizing the February 2020 campaign. I also thank the drivers of the rental agency Ethioder, and the local policeman and guides of the different woredas for their logistic support during the campaign.

References

Acocella, V., Abebe, B., Korme, T., & Barberi, F. (2008). Structure of Tendaho Graben and Manda Hararo Rift: implications for the evolution of the southern Red Sea propagator in Central Afar. Tectonics, 27(4). https://doi.org/10.1029/2007TC002236

Acton, G. D., Stein, S., & Engeln, J. F. (1991). Block rotation and continental extension in Afar: A comparison to oceanic microplate systems. Tectonics, 10(3), 501-526. https://doi.org/10.1029/90TC01792

Acton, G. D., Tessema, A., Jackson, M., & Bilham, R. (2000). The tectonic and geomagnetic significance of paleomagnetic observations from volcanic rocks from central Afar, Africa. Earth and Planetary Science Letters, 180(3-4), 225-241. https://doi.org/10.1016/S0012-821X(00)00173-4

Ahmed, A., Doubre, C., Leroy, S., Keir, D., Pagli, C., Hammond, J. O., et al. (2022). Across and along-strike crustal structure variations of the western Afar margin and adjacent plateau: Insights from receiver functions analysis. Journal of African Earth Sciences, 192, 104570. https://doi.org/10.1016/j.jafrearsci.2022.104570

Alemseged, Z., Wynn, J. G., Geraads, D., Reed, D., Andrew Barr, W., Bobe, R., et al. (2020). Fossils from Mille-Logya, Afar, Ethiopia, elucidate the link between Pliocene environmental changes and Homo origins. Nature communications, 11(1), 1-12. https://doi.org/10.1038/s41467-020-16060-8

Alene, M., Hart, W. K., Saylor, B. Z., Deino, A., Mertzman, S., Haile-Selassie, Y., & Gibert, L. B. (2017). Geochemistry of Woranso–Mille Pliocene basalts from west-central Afar, Ethiopia: Implications for mantle source characteristics and rift evolution. Lithos, 282, 187-200. https://doi.org/10.1016/j.lithos.2017.03.005

Alonso-Perez, R., Müntener, O., & Ulmer, P. (2009). Igneous garnet and amphibole fractionation in the roots of island arcs: experimental constraints on andesitic liquids. Contributions to Mineralogy and Petrology, 157(4), 541-558. https://doi.org/10.1007/s00410-008-0351-8

Altherr, R., Henjes-Kunst, F., Puchelt, H., & Baumann, A. (1988). Volcanic activity in the Red Sea axial trough—evidence for a large mantle diapir. Tectonophysics, 150(1-2), 121-133. https://doi.org/10.1016/0040-1951(88)90298-3

Andres, M., Blichert-Toft, J., & Schilling, J. G. (2004). Nature of the depleted upper mantle beneath the Atlantic: evidence from Hf isotopes in normal mid-ocean ridge basalts from 79 N to 55 S. Earth and Planetary Science Letters, 225(1-2), 89-103. https://doi.org/10.1016/j.epsl.2004.05.041

Annen, C., Blundy, J. D., & Sparks, R. S. J. (2006). The genesis of intermediate and silicic magmas in deep crustal hot zones. Journal of Petrology, 47(3), 505-539. https://doi.org/10.1093/petrology/egi084

Armienti, P., Perinelli, C., & Putirka, K. D. (2013). A new model to estimate deep-level magma ascent rates, with applications to Mt. Etna (Sicily, Italy). Journal of Petrology, 54(4), 795-813. https://doi.org/10.1093/petrology/egs085

Armitage, J. J., Ferguson, D. J., Goes, S., Hammond, J. O., Calais, E., Rychert, C. A., & Harmon, N. (2015). Upper mantle temperature and the onset of extension and break-up in Afar, Africa. Earth and Planetary Science Letters, 418, 78-90. https://doi.org/10.1016/j.epsl.2015.02.039

Asimow, P. D., Dixon, J. E., & Langmuir, C. H. (2004). A hydrous melting and fractionation model for mid-ocean ridge basalts: Application to the Mid-Atlantic Ridge near the Azores. Geochemistry, Geophysics, Geosystems, 5(1). https://doi.org/10.1029/2003GC000568

Autin, J., Leroy, S., Beslier, M. O., d'Acremont, E., Razin, P., Ribodetti, A., ... & Al Toubi, K. (2010). Continental break-up history of a deep magma-poor margin based on seismic reflection data (northeastern Gulf of Aden margin, offshore Oman). Geophysical Journal International, 180(2), 501-519. https://doi.org/10.1111/j.1365-246X.2009.04424.x

Avanzinelli, R., Boari, E., Conticelli, S., Francalanci, L., Guarnieri, L., Perini, G., ... & Ulivi, M. (2005). High precision Sr, Nd, and Pb isotopic analyses using the new generation thermal ionisation mass spectrometer thermofinnigan triton-Ti®. Periodico di Mineralogia, 75(3), 147-166.

Ayalew, D., Jung, S., Romer, R. L., & Garbe-Schönberg, D. (2018). Trace element systematics and Nd, Sr and Pb isotopes of Pliocene flood basalt magmas (Ethiopian rift): A case for Afar plume-lithosphere interaction. Chemical Geology, 493, 172-188. https://doi.org/10.1016/j.chemgeo.2018.05.037

Ayalew, D., Pik, R., Bellahsen, N., France, L., & Yirgu, G. (2019). Differential fractionation of rhyolites during the course of crustal extension, Western Afar (Ethiopian rift). Geochemistry, Geophysics, Geosystems, 20(2), 571-593. https://doi.org/10.1029/2018GC007446

Bachmann, O., & Bergantz, G. W. (2004). On the origin of crystal-poor rhyolites: extracted from batholithic crystal mushes. Journal of Petrology, 45(8), 1565-1582. https://doi.org/10.1093/petrology/egh019

Baker, J., Peate, D., Waight, T., & Meyzen, C. (2004). Pb isotopic analysis of standards and samples using a 207Pb–204Pb double spike and thallium to correct for mass bias with a double-focusing MC-ICP-MS. Chemical Geology, 211(3-4), 275-303. https://doi.org/10.1016/j.chemgeo.2004.06.030

Baker, J., Snee, L., & Menzies, M. (1996). A brief Oligocene period of flood volcanism in Yemen: implications for the duration and rate of continental flood volcanism at the Afro-Arabian triple junction. Earth and Planetary Science Letters, 138(1-4), 39-55. https://doi.org/10.1016/0012-821X(95)00229-6

Barberi F, Bonatti E, Marinelli G, Varet J (1974b) Transverse tectonics during the split of a continent: Data from the Afar rift. Tectonophysics 23:17-29. https://doi.org/10.1016/0040-1951(74)90108-5

Barberi F, Borsi S, Ferrara G, Marinelli G, Santacroce R, Tazieff H, Varet J (1972) Evolution of the Danakil Depression (Afar, Ethiopia) in Light of Radiometric Age Determinations. The J Geol 80:720-729. https://doi.org/10.1086/627797

Barberi F, Borsi S, Ferrara G, Marinelli G, Varet J (1970) A discussion on the structure and evolution of the Red Sea and the nature of the Red Sea, Gulf of Aden and Ethiopia rift junction - Relations between tectonics and magmatology in the northern Danakil depression (Ethiopia). Philos Tr R S-A 267:293-311. https://doi.org/10.1098/rsta.1970.0037

Barberi F, Ferrara G, Santacroce R, Treuil M, Varet J (1975b) A Transitional Basalt-Pantellerite Sequence of Fractional Crystallization, the Boina Centre (Afar Rift, Ethiopia). J Petrol 16:22-56. https://doi.org/10.1093/petrology/16.1.22

Barberi F, Santacroce R (1980) The Afar Stratoid Series and the magmatic evolution of East African rift system. Bull Soc Géol France S7-XXII:891-899. https://doi.org/10.2113/gssgfbull.s7-xxii.6.891

Barberi F, Santacroce R, Varet J (1974a) Silicic peralkaline volcanic rocks of the Afar depression (Ethiopia). Bulletin Volcanologique 38:755-790. https://doi.org/10.1007/bf02596907

Barberi, F., Ferrara, G., Santacroce, R., & Varet, J. (1975a). Structural evolution of the Afar triple junction.

Barrat J, Fourcade S, Jahn B, Cheminée J, Capdevila R (1998) Isotope (Sr, Nd, Pb, O) and trace-element geochemistry of volcanics from the Erta'Ale range (Ethiopia). J Volcanol Geotherm Res 80:85-100. https://doi.org/10.1016/s0377-0273(97)00016-4

Barrat, J. A., Jahn, B. M., Fourcade, S., & Joron, J. L. (1993). Magma genesis in an ongoing rifting zone: The Tadjoura Gulf (Afar area). Geochimica et cosmochimica acta, 57(10), 2291-2302. https://doi.org/10.1016/0016-7037(93)90570-M

Barrat, J. A., Jahn, B. M., Joron, J. L., Auvray, B., & Hamdi, H. (1990). Mantle heterogeneity in northeastern Africa: evidence from Nd isotopic compositions and hygromagmaphile element geochemistry of basaltic rocks from the Gulf of Tadjoura and southern Red Sea regions. Earth and Planetary Science Letters, 101(2-4), 233-247. https://doi.org/10.1016/0012-821X(90)90156-R

Barrat, J. A., Joron, J. L., Taylor, R. N., Fourcade, S., Nesbitt, R. W., & Jahn, B. M. (2003). Geochemistry of basalts from Manda Hararo, Ethiopia: LREE-depleted basalts in Central Afar. Lithos, 69(1-2), 1-13. https://doi.org/10.1016/S0024-4937(03)00044-6

Bastow, I. D., & Keir, D. (2011). The protracted development of the continent–ocean transition in Afar. Nature Geoscience, 4(4), 248-250. https://doi.org/10.1038/ngeo1095

Bastow, I. D., Booth, A. D., Corti, G., Keir, D., Magee, C., Jackson, C. A. L., et al. (2018). The Development of Late-Stage Continental Breakup: Seismic Reflection and Borehole Evidence from the Danakil Depression, Ethiopia. Tectonics, 37(9), 2848-2862. https://doi.org/10.1029/2017TC004798

Beccaluva, L., Bianchini, G., Natali, C., & Siena, F. (2009). Continental flood basalts and mantle plumes: a case study of the Northern Ethiopian Plateau. Journal of Petrology, 50(7), 1377-1403. https://doi.org/10.1093/petrology/egp024

Belachew M, Ebinger C, Coté D, Keir D, Rowland J, Hammond J, Ayele A (2011) Comparison of dike intrusions in an incipient seafloor-spreading segment in Afar, Ethiopia: Seismicity perspectives. J Geophys Res. https://doi.org/10.1029/2010jb007908

Best MG (2013) Igneous and metamorphic petrology. John Wiley & Sons.

Bezard, R., Turner, S., Davidson, J., Schmitt, A. K., & Lindsay, J. (2017). Origin and evolution of silicic magmas in oceanic arcs; an in situ study from St Lucia, Lesser Antilles. Journal of Petrology, 58(7), 1279-1318. https://doi.org/10.1093/petrology/egx053

Bizouard, H., Barberi, F., & Varet, J. (1980). Mineralogy and petrology of Erta Ale and Boina volcanic series, Afar rift, Ethiopia. Journal of Petrology, 21(2), 401-436. https://doi.org/10.1093/petrology/21.2.401

Black, B. A., & Gibson, S. A. (2019). Deep carbon and the life cycle of large igneous provinces. Elements, 15(5), 319-324. https://doi.org/10.2138/gselements.15.5.319

Black, B. A., & Manga, M. (2017). Volatiles and the tempo of flood basalt magmatism. Earth and Planetary Science Letters, 458, 130-140. https://doi.org/10.1016/j.epsl.2016.09.035

Black, B. A., Karlstrom, L., & Mather, T. A. (2021). The life cycle of large igneous provinces. Nature Reviews Earth & Environment, 2(12), 840-857. https://doi.org/10.1038/s43017-021-00221-4

Blichert-Toft, J., Agranier, A., Andres, M., Kingsley, R., Schilling, J. G., & Albarède, F. (2005). Geochemical segmentation of the Mid-Atlantic Ridge north of Iceland and ridge–hot spot interaction in the North Atlantic. Geochemistry, Geophysics, Geosystems, 6(1). https://doi.org/10.1029/2004GC000788

Blundy, J. D., & Annen, C. J. (2016). Crustal magmatic systems from the perspective of heat transfer. Elements, 12(2), 115-120. https://doi.org/10.2113/gselements.12.2.115

Blundy, J. D., & Wood, B. J. (1991). Crystal-chemical controls on the partitioning of Sr and Ba between plagioclase feldspar, silicate melts, and hydrothermal solutions. Geochimica et Cosmochimica Acta, 55(1), 193-209. https://doi.org/10.1016/0016-7037(91)90411-W

Bonini, M., Corti, G., Innocenti, F., Manetti, P., Mazzarini, F., Abebe, T., & Pecskay, Z. (2005). Evolution of the Main Ethiopian Rift in the frame of Afar and Kenya rifts propagation. Tectonics, 24(1). https://doi.org/10.1029/2004TC001680

Bosworth, W., Huchon, P., & McClay, K. (2005). The red sea and gulf of aden basins. Journal of African Earth Sciences, 43(1-3), 334-378. https://doi.org/10.1016/j.jafrearsci.2005.07.020

Bottinga, Y., Kudo, A., & Weill, D. (1966). Some observations on oscillatory zoning and crystallization of magmatic plagioclase. American Mineralogist: Journal of Earth and Planetary Materials, 51(5-6), 792-806.

Bridges, D. L., Mickus, K., Gao, S. S., Abdelsalam, M. G., & Alemu, A. (2012). Magnetic stripes of a transitional continental rift in Afar. Geology, 40(3), 203-206. https://doi.org/10.1130/G32697.1

Brune, S., Corti, G., & Ranalli, G. (2017). Controls of inherited lithospheric heterogeneity on rift linkage: Numerical and analog models of interaction between the Kenyan and Ethiopian rifts across the Turkana depression. Tectonics, 36(9), 1767-1786. https://doi.org/10.1002/2017TC004739

Brune, S., Kolawole, F., Olive, J. A., Stamps, D. S., Buck, W. R., Buiter, S. J., ... & Shillington, D. J. (2023). Geodynamics of continental rift initiation and evolution. Nature Reviews Earth & Environment, 1-19. https://doi.org/10.1038/s43017-023-00391-3

Buck, W. R. (1986). Small-scale convection induced by passive rifting: the cause for uplift of rift shoulders. *Earth and Planetary Science Letters*, *77*(3-4), 362-372. https://doi.org/10.1016/0012-821X(86)90146-9

Buck, W. R. (1991). Modes of continental lithospheric extension. Journal of Geophysical Research: Solid Earth, 96(B12), 20161-20178. https://doi.org/10.1029/91JB01485

Buck, W. R. (2006). The role of magma in the development of the Afro-Arabian Rift System. Geological Society, London, Special Publications, 259(1), 43-54. https://doi.org/10.1144/GSL.SP.2006.259.01.05

Campisano, C. J. (2012). Geological summary of the Busidima formation (Plio-Pleistocene) at the Hadar paleoanthropological site, Afar Depression, Ethiopia. Journal of human evolution, 62(3), 338-352. https://doi.org/10.1016/j.jhevol.2011.05.002

Carbotte, S. M., Smith, D. K., Cannat, M., & Klein, E. M. (2016). Tectonic and magmatic segmentation of the Global Ocean Ridge System: a synthesis of observations. Geological Society, London, Special Publications, 420(1), 249-295. https://doi.org/10.1144/SP420.5

Cashman, K. V., Sparks, R. S. J., & Blundy, J. D. (2017). Vertically extensive and unstable magmatic systems: a unified view of igneous processes. Science, 355(6331), eaag3055. DOI: 10.1126/science.aag30

Castillo, P. R., Liu, X., & Scarsi, P. (2020). The geochemistry and Sr-Nd-Pb isotopic ratios of high 3He/4He Afar and MER basalts indicate a significant role of the African Superplume in EARS magmatism. Lithos, 376, 105791. https://doi.org/10.1016/j.lithos.2020.105791

Chambers, E. L., Harmon, N., Rychert, C. A., Gallacher, R. J., & Keir, D. (2022). Imaging the seismic velocity structure of the crust and upper mantle in the northern East African Rift using Rayleigh wave tomography. Geophysical Journal International, 230(3), 2036-2055. https://doi.org/10.1093/gji/ggac156

Chernet, T., & Hart, W. K. (1999). Petrology and geochemistry of volcanism in the northern Main Ethiopian Rift-southern Afar transition region. Acta Vulcanologica, 11, 21-42.

Cherniak, D. J. (2002). Ba diffusion in feldspar. Geochimica et Cosmochimica Acta, 66(9), 1641-1650. https://doi.org/10.1016/S0016-7037(01)00866-3

Cherniak, D. J., & Watson, E. B. (2020). Ti diffusion in feldspar. American Mineralogist: Journal of Earth and Planetary Materials, 105(7), 1040-1051.

Civetta L, de Fino M, Gasparini P, Ghiara M, La Volpe L, Lirer L (1975) Structural Meaning of East-Central Afar Volcanism (Ethiopia, T.F.A.I.). The J Geol 83:363-373. https://doi.org/10.1086/628098

Clapham, M. E., & Renne, P. R. (2019). Flood basalts and mass extinctions. Annual Review of Earth and Planetary Sciences, 47, 275-303. https://doi.org/10.1146/annurev-earth-053018-060136

Class, C., & Goldstein, S. L. (1997). Plume-lithosphere interactions in the ocean basins: constraints from the source mineralogy. Earth and Planetary Science Letters, 150(3-4), 245-260. https://doi.org/10.1016/S0012-821X(97)00089-7

Cochran, J. R. (1983). A model for development of Red Sea. Aapg Bulletin, 67(1), 41-69. https://doi.org/10.1306/03B5ACBE-16D1-11D7-8645000102C1865D

Cohen, A., Campisano, C., Arrowsmith, R., Asrat, A., Behrensmeyer, A. K., Deino, A., et al. (2016). The Hominin Sites and Paleolakes Drilling Project: inferring the environmental context of human evolution from eastern African rift lake deposits. Scientific Drilling, 21, 1-16. https://doi.org/10.5194/sd-21-1-2016

Corti, G. (2009). Continental rift evolution: from rift initiation to incipient break-up in the Main Ethiopian Rift, East Africa. Earth-Science Reviews, 96(1-2), 1-53. https://doi.org/10.1016/j.earscirev.2009.06.005

Corti, G. (2012). Evolution and characteristics of continental rifting: Analog modeling-inspired view and comparison with examples from the East African Rift System. Tectonophysics, 522, 1-33. https://doi.org/10.1016/j.tecto.2011.06.010

Corti, G., Agostini, A., Keir, D., Van Wijk, J., Bastow, I. D., & Ranalli, G. (2015b). Magma-induced axial subsidence during final-stage rifting: Implications for the development of seaward-dipping reflectors. Geosphere, 11(3), 563-571. https://doi.org/10.1130/GES01076.1

Corti, G., Bastow, I. D., Keir, D., Pagli, C., & Baker, E. (2015a). Rift-related morphology of the Afar Depression. In Landscapes and Landforms of Ethiopia (pp. 251-274). Springer, Dordrecht. https://doi.org/10.1007/978-94-017-8026-1_15

Corti, G., Bonini, M., Conticelli, S., Innocenti, F., Manetti, P., & Sokoutis, D. (2003). Analogue modelling of continental extension: a review focused on the relations between the patterns of deformation and the presence of magma. Earth-Science Reviews, 63(3-4), 169-247. https://doi.org/10.1002/2017TC004799

Courtillot, V., Achache, J., Landre, F., Bonhommet, N., Montigny, R., & Féraud, G. (1984). Episodic spreading and rift propagation: new paleomagnetic and geochronologic data from the Afar nascent passive margin. Journal of Geophysical Research: Solid Earth, 89(B5), 3315-3333. https://doi.org/10.1029/JB089iB05p03315

Courtillot, V., Jaupart, C., Manighetti, I., Tapponnier, P., & Besse, J. (1999). On causal links between flood basalts and continental breakup. Earth and Planetary Science Letters, 166(3-4), 177-195. https://doi.org/10.1016/S0012-821X(98)00282-9

d'Acremont, E., Leroy, S., Maia, M., Gente, P., & Autin, J. (2010). Volcanism, jump and propagation on the Sheba ridge, eastern Gulf of Aden: segmentation evolution and implications for oceanic accretion processes. Geophysical Journal International, 180(2), 535-551. https://doi.org/10.1111/j.1365-246X.2009.04448.x

Daoud, M. A., Le Gall, B., Maury, R. C., Rolet, J., Huchon, P., & Guillou, H. (2011). Young rift kinematics in the Tadjoura rift, western Gulf of Aden, Republic of Djibouti. Tectonics, 30(1). https://doi.org/10.1029/2009TC002614

De Fino M, Volpe L, Lirer L (1978) Geology and volcanology of the Edd-Bahar Assoli area (Ethiopia). Bulletin Volcanologique 41:32-42. https://doi.org/10.1007/bf02597681

de Moor, J. M., Fischer, T. P., Sharp, Z. D., King, P. L., Wilke, M., Botcharnikov, R. E., ... & Kelley, K. A. (2013). Sulfur degassing at Erta Ale (Ethiopia) and Masaya (Nicaragua) volcanoes: Implications for degassing processes and oxygen fugacities of basaltic systems. Geochemistry, Geophysics, Geosystems, 14(10), 4076-4108. https://doi.org/10.1002/ggge.20255

Deering, C. D., Bachmann, O., & Vogel, T. A. (2011). The Ammonia Tanks Tuff: Erupting a melt-rich rhyolite cap and its remobilized crystal cumulate. Earth and Planetary Science Letters, 310(3-4), 518-525. https://doi.org/10.1016/j.epsl.2011.08.032

Deniel, C., Vidal, P., Coulon, C., Vellutini, P. J., & Piguet, P. (1994). Temporal evolution of mantle sources during continental rifting: the volcanism of Djibouti (Afar). Journal of Geophysical Research: Solid Earth, 99(B2), 2853-2869. https://doi.org/10.1029/93JB02576

DePaolo, D. J. (1981). Trace element and isotopic effects of combined wallrock assimilation and fractional crystallization. Earth and planetary science letters, 53(2), 189-202. https://doi.org/10.1016/0012-821X(81)90153-9

Desissa, M., Johnson, N. E., Whaler, K. A., Hautot, S., Fisseha, S., & Dawes, G. J. K. (2013). A mantle magma reservoir beneath an incipient mid-ocean ridge in Afar, Ethiopia. Nature geoscience, 6(10), 861-865. https://doi.org/10.1038/ngeo1925

Didana, Y. L., Thiel, S., & Heinson, G. (2014). Magnetotelluric imaging of upper crustal partial melt at Tendaho graben in Afar, Ethiopia. Geophysical Research Letters, 41(9), 3089-3095. https://doi.org/10.1002/2014GL060000

DiMaggio, E. N., Campisano, C. J., Rowan, J., Dupont-Nivet, G., Deino, A. L., Bibi, F., et al. (2015). Late Pliocene fossiliferous sedimentary record and the environmental context of early Homo from Afar, Ethiopia. Science, 347(6228), 1355-1359. https://doi.org/10.1126/science.aaa1415

Donovan A, Blundy J, Oppenheimer C, Buisman I (2017) The 2011 eruption of Nabro volcano, Eritrea: perspectives on magmatic processes from melt inclusions. Contrib Mineral Petrol 173:1-23. https://doi.org/10.1007/s00410-017-1425-2

Dufek, J., & Bachmann, O. (2010). Quantum magmatism: Magmatic compositional gaps generated by melt-crystal dynamics. Geology, 38(8), 687-690. https://doi.org/10.1130/G30831.1

Duffield, W. A., Bullen, T. D., Clynne, M. A., Fournier, R. O., Janik, C. J., Lanphere, M. A., ... & Tesfai, T. (1997). Geothermal potential of the Alid volcanic center, Danakil Depression, Eritrea. US Geological Survey Open-File Report, 97-291.

Duraiswami, R. A., Bondre, N. R., Dole, G., Phadnis, V. M., & Kale, V. S. (2001). Tumuli and associated features from the western Deccan Volcanic Province, India. Bulletin of Volcanology, 63(7), 435-442. https://doi.org/10.1007/s004450100160

Ebinger CJ, Keir D, Ayele A, Calais E, Wright TJ, Belachew M, Hammond JO, Campbell E, Buck, WR (2008) Capturing magma intrusion and faulting processes during continental

rupture: seismicity of the Dabbahu (Afar) rift. Geophys J Int 174(3):1138-1152. http://dx.doi.org/10.1111/j.1365-246X.2008.03877.x

Ebinger, C. J., Yemane, T., Woldegabriel, G., Aronson, J. L., & Walter, R. C. (1993). Late Eocene–Recent volcanism and faulting in the southern main Ethiopian rift. Journal of the Geological Society, 150(1), 99-108. https://doi.org/10.1144/gsjgs.150.1.0099

Edmonds, M., Cashman, K. V., Holness, M., & Jackson, M. (2019). Architecture and dynamics of magma reservoirs. Philosophical Transactions of the Royal Society A, 377(2139), 20180298. https://doi.org/10.1098/rsta.2018.0298

Eid, B., Lhuillier, F., Gilder, S. A., Pfänder, J. A., Gebru, E. F., & Aßbichler, D. (2021). Exceptionally high emplacement rate of the afar mantle plume head. Geophysical Research Letters, 48(23), e2021GL094755. https://doi.org/10.1029/2021GL094755

Elkins, L. J., Gaetani, G. A., & Sims, K. W. W. (2008). Partitioning of U and Th during garnet pyroxenite partial melting: Constraints on the source of alkaline ocean island basalts. Earth and Planetary Science Letters, 265(1-2), 270-286. https://doi.org/10.1016/j.epsl.2007.10.034

Ernst, R. E., Liikane, D. A., Jowitt, S. M., Buchan, K. L., & Blanchard, J. A. (2019). A new plumbing system framework for mantle plume-related continental Large Igneous Provinces and their mafic-ultramafic intrusions. Journal of Volcanology and Geothermal Research, 384, 75-84. https://doi.org/10.1016/j.jvolgeores.2019.07.007

Farnetani, C. G., Hofmann, A. W., & Gupta, H. (2011). Mantle plumes. Encyclopedia of solid Earth geophysics. Springer, Dordrecht, 857-869. https://doi.org/10.1007/978-90-481-8702-7_132

Ferguson DJ, Barnie TD, Pyle DM, Oppenheimer C, Yirgu G, Lewi E, Kidane T, Carn S, Hamling I (2010) Recent rift-related volcanism in Afar, Ethiopia. Earth Planet Sci Lett 292(3-4):409-418. http://dx.doi.org/10.1016/j.epsl.2010.02.010

Ferguson DJ, Maclennan J, Bastow ID, Pyle D, Jones SM, Keir D, Blundy JD, Plank T, Yirgu G (2013) Melting during late-stage rifting in Afar is hot and deep. Nature 499(7456):70-73. http://dx.doi.org/10.1038/nature12292

Feyissa, D. H., Kitagawa, H., Bizuneh, T. D., Tanaka, R., Kabeto, K., & Nakamura, E. (2019). Transition from Plume-driven to Plate-driven Magmatism in the Evolution of the Main Ethiopian Rift. Journal of Petrology, 60(8), 1681-1715. https://doi.org/10.1093/petrology/egz043

Feyissa, D. H., Shinjo, R., Kitagawa, H., Meshesha, D., & Nakamura, E. (2017). Petrologic and geochemical characterization of rift-related magmatism at the northernmost Main Ethiopian Rift: Implications for plume-lithosphere interaction and the evolution of rift mantle sources. Lithos, 282, 240-261. https://doi.org/10.1016/j.lithos.2017.03.011

Field L, Blundy J, Brooker RA, Wright T, Yirgu G (2012a) Magma storage conditions beneath Dabbahu Volcano (Ethiopia) constrained by petrology, seismicity and satellite geodesy. Bull Volcanol 74(5):981-1004. http://dx.doi.org/10.1007/s00445-012-0580-6

Field L, Blundy J, Calvert A, Yirgu G (2013) Magmatic history of Dabbahu, a composite volcano in the Afar Rift, Ethiopia. Geol Soc Am Bull 125(1-2):128-147. http://dx.doi.org/10.1130/B30560.1

Field, L., Barnie, T., Blundy, J., Brooker, R. A., Keir, D., Lewi, E., & Saunders, K. (2012b). Integrated field, satellite and petrological observations of the November 2010 eruption of Erta Ale. Bulletin of Volcanology, 74(10), 2251-2271. https://doi.org/10.1007/s00445-012-0660-7

Foley, S., Musselwhite, D., & Van der Laan, S. R. (1999). Melt compositions from ultramafic vein assemblages in the lithospheric mantle: a comparison of cratonic and non-cratonic settings. In International Kimberlite Conference (7th: 1998) (pp. 238-246). Red Roof Design.

Forni, F., Bachmann, O., Mollo, S., De Astis, G., Gelman, S. E., & Ellis, B. S. (2016). The origin of a zoned ignimbrite: Insights into the Campanian Ignimbrite magma chamber (Campi Flegrei, Italy). Earth and Planetary Science Letters, 449, 259-271. https://doi.org/10.1016/j.epsl.2016.06.003

Fournier, M., Chamot-Rooke, N., Petit, C., Huchon, P., Al-Kathiri, A., Audin, L., ... & Merkouriev, S. (2010). Arabia-Somalia plate kinematics, evolution of the Aden-Owen-Carlsberg triple junction, and opening of the Gulf of Aden. Journal of Geophysical Research: Solid Earth, 115(B4). https://doi.org/10.1029/2008JB006257

Frizon de Lamotte, D., Fourdan, B., Leleu, S., Leparmentier, F., & de Clarens, P. (2015). Style of rifting and the stages of Pangea breakup. Tectonics, 34(5), 1009-1029. https://doi.org/10.1002/2014TC003760

Furman, T., & Graham, D. (1999). Erosion of lithospheric mantle beneath the East African Rift system: geochemical evidence from the Kivu volcanic province. In Developments in Geotectonics (Vol. 24, pp. 237-262). Elsevier. https://doi.org/10.1016/S0419-0254(99)80014-7

Furman, T., Nelson, W. R., & Elkins-Tanton, L. T. (2016). Evolution of the East African rift: Drip magmatism, lithospheric thinning and mafic volcanism. Geochimica et Cosmochimica Acta, 185, 418-434. https://doi.org/10.1016/j.gca.2016.03.024

Gale, A., Dalton, C. A., Langmuir, C. H., Su, Y., & Schilling, J. G. (2013). The mean composition of ocean ridge basalts. Geochemistry, Geophysics, Geosystems, 14(3), 489-518. https://doi.org/10.1029/2012GC004334

Gallacher, R., Keir, D., Harmon, N., Stuart, G., Leroy, S., Hammond, J. O. S., Kendall, J-M., Ayele, A., Goitom, B., Ogubazghi, G., & Ahmed, A. (2016). The initiation of segmented buoyancy-driven melting during continental breakup. Nature Communications, 7, [13110]. https://doi.org/10.1038/ncomms13110

Gasse, F., Fournier, M., Richard, O., & Ruegg, J. C. (1983). Notice explicative: carte géologique de la République de Djibouti à 1/100 000: Djibouti.

Ghiorso, M. S., & Sack, R. O. (1995). Chemical mass transfer in magmatic processes IV. A revised and internally consistent thermodynamic model for the interpolation and extrapolation of liquid-solid equilibria in magmatic systems at elevated temperatures and

pressures. Contributions to Mineralogy and Petrology, 119(2), 197-212. https://doi.org/10.1007/BF00307281

Giletti, B. J., & Casserly, J. E. D. (1994). Strontium diffusion kinetics in plagioclase feldspars. Geochimica et Cosmochimica Acta, 58(18), 3785-3793. https://doi.org/10.1016/0016-7037(94)90363-8

Ginibre, C., Wörner, G., & Kronz, A. (2002). Minor-and trace-element zoning in plagioclase: implications for magma chamber processes at Parinacota volcano, northern Chile. Contributions to Mineralogy and Petrology, 143(3), 300-315. https://doi.org/10.1007/s00410-002-0351-z

Giuliani, L., Vetere, F., Iezzi, G., Nazzari, M., Mollo, S., Behrens, H., ... & Ventura, G. (2022). Crystal-chemical variations of spinel, clinopyroxene, and plagioclase in MORB basaltic melt induced by continuous cooling. Chemical Geology, 594, 120765. https://doi.org/10.1016/j.chemgeo.2022.120765

Gleeson, M. L., Stock, M. J., Pyle, D. M., Mather, T. A., Hutchison, W., Yirgu, G., & Wade, J. (2017). Constraining magma storage conditions at a restless volcano in the Main Ethiopian Rift using phase equilibria models. Journal of Volcanology and Geothermal Research, 337, 44-61. https://doi.org/10.1016/j.jvolgeores.2017.02.026

Gonnermann HM, Manga M (2007) The fluid mechanics inside a volcano. Annu Rev Fluid Mech 39:321-356. http://dx.doi.org/10.1146/annurev.fluid.39.050905.110207

Govindaraju K (1980) Report (1980) on three GIT-IWG rock reference samples: Anorthosite from Greenland, AN-G; Basalte d'Essey-la-Côte, BE-N; Granite de Beauvoir, MA-N. Geostandard Newslett 4(1):49-138. https://doi.org/10.1111/j.1751-908X.1980.tb00274.x

Govindaraju K (1994) 1994 compilation of working values and sample description for 383 geostandards. Geostandard Newslett 18:1-158. https://doi.org/10.1046/j.1365-2494.1998.53202081.x-i1

Graham, D. W., Blichert-Toft, J., Russo, C. J., Rubin, K. H., & Albarède, F. (2006). Cryptic striations in the upper mantle revealed by hafnium isotopes in southeast Indian ridge basalts. Nature, 440(7081), 199-202. https://doi.org/10.1038/nature04582

Green, D. H. (1973). Experimental melting studies on a model upper mantle composition at high pressure under water-saturated and water-undersaturated conditions. Earth and Planetary Science Letters, 19(1), 37-53. https://doi.org/10.1016/0012-821X(73)90176-3

Green, D. H., Hibberson, W. O., Kovács, I., & Rosenthal, A. (2010). Water and its influence on the lithosphere–asthenosphere boundary. Nature, 467(7314), 448-451. https://doi.org/10.1038/nature09369

Griffiths, R. W., & Campbell, I. H. (1991). Interaction of mantle plume heads with the Earth's surface and onset of small-scale convection. Journal of Geophysical Research: Solid Earth, 96(B11), 18295-18310. https://doi.org/10.1029/91JB01897

Grove, T. L., Baker, M. B., & Kinzler, R. J. (1984). Coupled CaAl-NaSi diffusion in plagioclase feldspar: experiments and applications to cooling rate speedometry. Geochimica et cosmochimica Acta, 48(10), 2113-2121. https://doi.org/10.1016/0016-7037(84)90391-0

Gualda, G. A., Ghiorso, M. S., Lemons, R. V., & Carley, T. L. (2012). Rhyolite-MELTS: a modified calibration of MELTS optimized for silica-rich, fluid-bearing magmatic systems. Journal of Petrology, 53(5), 875-890. https://doi.org/10.1093/petrology/egr080

Guidarelli, M., Stuart, G., Hammond, J. O., Kendall, J. M., Ayele, A., & Belachew, M. (2011). Surface wave tomography across Afar, Ethiopia: Crustal structure at a rift triple-junction zone. Geophysical Research Letters, 38(24). https://doi.org/10.1029/2011GL046840

Haase, K. M., Mühe, R., & Stoffers, P. (2000). Magmatism during extension of the lithosphere: geochemical constraints from lavas of the Shaban Deep, northern Red Sea. Chemical Geology, 166(3-4), 225-239. https://doi.org/10.1016/S0009-2541(99)00221-1

Hagos M, Koeberl C, De Vries BVW (2016) The Quaternary volcanic rocks of the northern Afar Depression (northern Ethiopia): Perspectives on petrology, geochemistry, and tectonics. J African Earth Sci 117:29-47. http://dx.doi.org/10.1016/j.jafrearsci.2015.11.022

Halldórsson, S. A., Hilton, D. R., Scarsi, P., Abebe, T., & Hopp, J. (2014). A common mantle plume source beneath the entire East African Rift System revealed by coupled helium-neon systematics. Geophysical Research Letters, 41(7), 2304-2311. https://doi.org/10.1002/2014GL059424

Hamlyn J, Wright T, Walters R, Pagli C, Sansosti E, Casu F, Pepe S, Edmonds M, Kilbride BM, Keir D, Neuberg J, Oppenheimer C (2018) What causes subsidence following the 2011 eruption at Nabro (Eritrea). Progr Earth Planet Sci 5(1):1-15. http://dx.doi.org/10.1186/s40645-018-0186-5

Hammond, J. O., Kendall, J. M., Stuart, G. W., Keir, D., Ebinger, C., Ayele, A., & Belachew, M. (2011). The nature of the crust beneath the Afar triple junction: Evidence from receiver functions. Geochemistry, Geophysics, Geosystems, 12(12). https://doi.org/10.1029/2011GC003738

Hanan, B. B., & Graham, D. W. (1996). Lead and helium isotope evidence from oceanic basalts for a common deep source of mantle plumes. Science, 272(5264), 991-995. DOI: 10.1126/science.272.5264.991

Hanan, B. B., Blichert-Toft, J., Pyle, D. G., & Christie, D. M. (2004). Contrasting origins of the upper mantle revealed by hafnium and lead isotopes from the Southeast Indian Ridge. Nature, 432(7013), 91-94. https://doi.org/10.1038/nature03026

Hardarson, B. S., Fitton, J. G., Ellam, R. M., & Pringle, M. S. (1997). Rift relocation—a geochemical and geochronological investigation of a palaeo-rift in northwest Iceland. Earth and Planetary Science Letters, 153(3-4), 181-196. https://doi.org/10.1016/S0012-821X(97)00145-3

Hards VL, Kempton PD, Thompson RN, Greenwood PB (2000) The magmatic evolution of the Snaefell volcanic centre; an example of volcanism during incipient rifting in Iceland. J Volcanol Geotherm Res 99(1-4):97-121. https://doi.org/10.1016/S0377-0273(00)00160-8

Hart, S. R. (1984). A large-scale isotope anomaly in the Southern Hemisphere mantle. Nature, 309(5971), 753-757. https://doi.org/10.1038/309753a0

Hart, S. R., & Dunn, T. (1993). Experimental cpx/melt partitioning of 24 trace elements. Contributions to Mineralogy and Petrology, 113(1), 1-8. https://doi.org/10.1007/BF00320827

Hart, W. K., WoldeGabriel, G., Walter, R. C., & Mertzman, S. A. (1989). Basaltic volcanism in Ethiopia: constraints on continental rifting and mantle interactions. Journal of Geophysical Research: Solid Earth, 94(B6), 7731-7748. https://doi.org/10.1029/JB094iB06p07731

Hayward NJ, Ebinger CJ (1996) Variations in the along-axis segmentation of the Afar Rift system. Tectonics 15(2):244-257. https://doi.org/10.1029/95TC02292

Hoare L, Klaver M, Saji NS, Gillies J, Parkinson IJ, Lissenberg CJ, Millet MA (2020) Melt chemistry and redox conditions control titanium isotope fractionation during magmatic differentiation. Geochim Cosmochim Acta 282:38-54. https://doi.org/10.1016/j.gca.2020.05.015

Hofmann, A. W., Jochum, K. P., Seufert, M., & White, W. M. (1986). Nb and Pb in oceanic basalts: new constraints on mantle evolution. Earth and Planetary science letters, 79(1-2), 33-45. https://doi.org/10.1016/0012-821X(86)90038-5

Hofmann, C., Courtillot, V., Feraud, G., Rochette, P., Yirgu, G., Ketefo, E., & Pik, R. (1997). Timing of the Ethiopian flood basalt event and implications for plume birth and global change. Nature, 389(6653), 838-841. https://doi.org/10.1038/39853

Hooper, P. R. (1990). The timing of crustal extension and the eruption of continental flood basalts. Nature, 345(6272), 246-249. https://doi.org/10.1038/345246a0

Hughes, G. W., Varol, O., & Beydoun, Z. R. (1991). Evidence for Middle Oligocene rifting of the Gulf of Aden and for Late Oligocene rifting of the southern Red Sea. Marine and petroleum Geology, 8(3), 354-358. https://doi.org/10.1016/0264-8172(91)90088-I

Hutchison W, Mather TA, Pyle DM, Boyce AJ, Gleeson ML, Yirgu G, Blundy JD, Ferguson DJ, Vye-Brown C, Millar IL, Sims KW, Finch AA (2018) The evolution of magma during continental rifting: New constraints from the isotopic and trace element signatures of silicic magmas from Ethiopian volcanoes. Earth Planet Sc Lett 489:203-218. https://doi.org/10.1016/j.epsl.2018.02.027Get

Hutchison W, Pyle DM, Mather TA, Yirgu G, Biggs J, Cohen BE, Barfod DN, Lewi E (2016) The eruptive history and magmatic evolution of Aluto volcano: new insights into silicic peralkaline volcanism in the Ethiopian rift. J Volcanol and Geoth Res 328:9-33. https://doi.org/10.1016/j.jvolgeores.2016.09.010

Iacovino, K., & Till, C. B. (2019). DensityX: A program for calculating the densities of magmatic liquids up to 1,627 C and 30 kbar. Volcanica, 2(1), 1-10. https://doi.org/10.30909/vol.02.01.0110

Illsley-Kemp F, Keir D, Bull JM, Gernon TM, Ebinger C, Ayele A, Hammond O, Kendall JM, Goitom B, Belachew M (2018) Seismicity during continental breakup in the Red Sea rift of northern Afar. Journal of Geophysical Research: Solid Earth 123(3):2345-2362. https://doi.org/10.1002/2017JB014902

Irvine, T. N., & Baragar, W. R. A. (1971). A guide to the chemical classification of the common volcanic rocks. Canadian journal of earth sciences, 8(5), 523-548. https://doi.org/10.1139/e71-055

Jackson, M. D., Blundy, J., & Sparks, R. S. J. (2018). Chemical differentiation, cold storage and remobilization of magma in the Earth's crust. Nature, 564(7736), 405-409. https://doi.org/10.1038/s41586-018-0746-2

Jackson, M. D., Cheadle, M. J., & Atherton, M. P. (2003). Quantitative modeling of granitic melt generation and segregation in the continental crust. Journal of Geophysical Research: Solid Earth, 108(B7). https://doi.org/10.1029/2001JB001050

Jerram, D. A., & Widdowson, M. (2005). The anatomy of Continental Flood Basalt Provinces: geological constraints on the processes and products of flood volcanism. Lithos, 79(3-4), 385-405. https://doi.org/10.1016/j.lithos.2004.09.009

Kalb, J. E. (1995). Fossil elephantoids, Awash paleolake basins, and the Afar triple junction, Ethiopia. Palaeogeography, Palaeoclimatology, Palaeoecology, 114(2-4), 357-368. https://doi.org/10.1016/0031-0182(94)00088-P

Kebede, T., Koeberl, C., & Koller, F. (1999). Geology, geochemistry and petrogenesis of intrusive rocks of the Wallagga area, western Ethiopia. Journal of African Earth Sciences, 29(4), 715-734. https://doi.org/10.1016/S0899-5362(99)00126-8

Keir, D., Hamling, I. J., Ayele, A., Calais, E., Ebinger, C., Wright, T. J., et al. (2009). Evidence for focused magmatic accretion at segment centers from lateral dike injections captured beneath the Red Sea rift in Afar. Geology, 37(1), 59-62. https://doi.org/10.1130/G25147A.1

Keir, D., Pagli, C., Bastow, I. D., & Ayele, A. (2011). The magma-assisted removal of Arabia in Afar: Evidence from dike injection in the Ethiopian rift captured using InSAR and seismicity. Tectonics, 30(2). https://doi.org/10.1029/2010TC002785

Kendall, J. M., Stuart, G. W., Ebinger, C. J., Bastow, I. D., & Keir, D. (2005). Magma-assisted rifting in Ethiopia. Nature, 433(7022), 146-148. https://doi.org/10.1038/nature03161

Kidane, T., Courtillot, V., Manighetti, I., Audin, L., Lahitte, P., Quidelleur, X., et al. (2003). New paleomagnetic and geochronologic results from Ethiopian Afar: Block rotations linked to rift overlap and propagation and determination of a∼ 2 Ma reference pole for stable Africa. Journal of Geophysical Research: Solid Earth, 108(B2). https://doi.org/10.1029/2001JB000645

Kieffer, B., Arndt, N., Lapierre, H., Bastien, F., Bosch, D., Pecher, A., et al. (2004). Flood and shield basalts from Ethiopia: magmas from the African superswell. Journal of Petrology, 45(4), 793-834. https://doi.org/10.1093/petrology/egg112

Klemme, S., & O'Neill, H. S. (2000). The near-solidus transition from garnet lherzolite to spinel lherzolite. Contributions to Mineralogy and Petrology, 138(3), 237-248. https://doi.org/10.1007/s004100050560

Koptev, A., Burov, E., Calais, E., Leroy, S., Gerya, T., Guillou-Frottier, L., & Cloetingh, S. (2016). Contrasted continental rifting via plume-craton interaction: Applications to Central

East African Rift. Geoscience Frontiers, 7(2), 221-236. https://doi.org/10.1016/j.gsf.2015.11.002

Krans, S. R., Rooney, T. O., Kappelman, J., Yirgu, G., & Ayalew, D. (2018). From initiation to termination: a petrostratigraphic tour of the Ethiopian Low-Ti Flood Basalt Province. Contributions to Mineralogy and Petrology, 173(5), 1-22. https://doi.org/10.1007/s00410-018-1460-7

Kunz, K., Kreuzer, H., & Müller, P. (1975). Potassium-Argon age determinations of the Trap basalt of the south-eastern part of the Afar Rift. Afar depression of Ethiopia, 1, 370-374.

La Spina, G., Burton, M., Vitturi, M. D. M., & Arzilli, F. (2016). Role of syn-eruptive plagioclase disequilibrium crystallization in basaltic magma ascent dynamics. Nature communications, 7(1), 1-10. https://doi.org/10.1038/ncomms13402

LaFemina PC, Dixon TH, Malservisi R, Árnadóttir T, Sturkell E, Sigmundsson F, Einarsson P (2005) Geodetic GPS measurements in south Iceland: Strain accumulation and partitioning in a propagating ridge system. J Geophys Res: Solid Earth 110(B11). https://doi.org/10.1029/2005JB003675

Lahitte, P., Gillot, P. Y., & Courtillot, V. (2003a). Silicic central volcanoes as precursors to rift propagation: the Afar case. Earth and Planetary Science Letters, 207(1-4), 103-116. https://doi.org/10.1016/S0012-821X(02)01130-5

Lahitte, P., Gillot, P. Y., Kidane, T., Courtillot, V., & Bekele, A. (2003b). New age constraints on the timing of volcanism in central Afar, in the presence of propagating rifts. Journal of Geophysical Research: Solid Earth, 108(B2). https://doi.org/10.1029/2001JB001689

Lange, R. A., Frey, H. M., & Hector, J. (2009). A thermodynamic model for the plagioclase-liquid hygrometer/thermometer. American Mineralogist, 94(4), 494-506. https://doi.org/10.2138/am.2009.3011

LaTourrette, T., & Wasserburg, G. J. (1998). Mg diffusion in anorthite: implications for the formation of early solar system planetesimals. Earth and Planetary Science Letters, 158(3-4), 91-108. https://doi.org/10.1016/S0012-821X(98)00048-X

Lavayssiere, A., Rychert, C., Harmon, N., Keir, D., Hammond, J. O. S., Kendall, J-M., Doubre, C., & Leroy, S. (2018). Imaging lithospheric discontinuities beneath the northern East African Rift using S-to-P receiver functions. Geochemistry, Geophysics, Geosystems, 19(10), 4048-4062. https://doi.org/10.1029/2018GC007463

Le Gall, B., Daoud, M.A., Maury, R., Gasse, F., Rolet, J., Jalludin, M., Caminiti, A.-M., Moussa, N., (2015). Geological Map of the Republic of Djibouti. Centre d'Etude et de Recherche de Djibouti (CERD) and CCGM

Lezzerini, M., Tamponi, M., & Bertoli, M. (2013). Reproducibility, precision and trueness of X-ray fluorescence data for mineralogical and/or petrographic purposes. Atti Società Toscana Scienze Naturali Memorie, Serie A, 120, 67-73. https://doi.org/10.2424/ASTSN.M.2013.15

Lissenberg, C. J., MacLeod, C. J., & Bennett, E. N. (2019). Consequences of a crystal mush-dominated magma plumbing system: a mid-ocean ridge perspective. Philosophical

Transactions of the Royal Society A, 377(2139), 20180014. https://doi.org/10.1098/rsta.2018.0014

Lloyd, R., Biggs, J., Wilks, M., Nowacki, A., Kendall, J. M., Ayele, A., et al., (2018). Evidence for cross rift structural controls on deformation and seismicity at a continental rift caldera. Earth and Planetary Science Letters, 487, 190-200. https://doi.org/10.1016/j.epsl.2018.01.037

Longerich, H. P., Jackson, S. E., & Günther, D. (1996). Inter-laboratory note. Laser ablation inductively coupled plasma mass spectrometric transient signal data acquisition and analyte concentration calculation. Journal of analytical atomic spectrometry, 11(9), 899-904. https://doi.org/10.1039/JA9961100899

Lowenstern, J. B., Charlier, B. L., Clynne, M. A., & Wooden, J. L. (2006). Extreme U–Th disequilibrium in rift-related basalts, rhyolites and granophyric granite and the timescale of rhyolite generation, intrusion and crystallization at Alid volcanic center, Eritrea. Journal of Petrology, 47(11), 2105-2122. https://doi.org/10.1093/petrology/egl038

Maestrelli, D., Brune, S., Corti, G., Keir, D., Muluneh, A. A., & Sani, F. (2022). Analog and Numerical Modeling of Rift-Rift-Rift Triple Junctions. Tectonics, 41(10), e2022TC007491. https://doi.org/10.1029/2022TC007491

Magee, C., Stevenson, C. T., Ebmeier, S. K., Keir, D., Hammond, J. O., Gottsmann, J. H., ... & Jackson, M. D. (2018). Magma plumbing systems: a geophysical perspective. Journal of Petrology, 59(6), 1217-1251. https://doi.org/10.1093/petrology/egy064

Makris, J., & Ginzburg, A. (1987). The Afar Depression: transition between continental rifting and sea-floor spreading. Tectonophysics, 141(1-3), 199-214. https://doi.org/10.1016/0040-1951(87)90186-7

Manighetti, I., Tapponnier, P., Courtillot, V., Gruszow, S., & Gillot, P. Y. (1997). Propagation of rifting along the Arabia-Somalia plate boundary: The gulfs of Aden and Tadjoura. Journal of Geophysical Research: Solid Earth, 102(B2), 2681-2710. https://doi.org/10.1029/96JB01185

Marjanović, M., Carbotte, S. M., Carton, H., Nedimović, M. R., Mutter, J. C., & Canales, J. P. (2014). A multi-sill magma plumbing system beneath the axis of the East Pacific Rise. Nature Geoscience, 7(11), 825-829. https://doi.org/10.1038/ngeo2272

Marty, B., Appora, I., Barrat, J. A. A., Deniel, C., Vellutini, P., & Vidal, P. (1993). He, Ar, Sr, Nd and Pb isotopes in volcanic rocks from Afar: evidence for a primitive mantle component and constraints on magmatic sources. Geochemical Journal, 27(4-5), 219-228. https://doi.org/10.2343/geochemj.27.219

Marty, B., Pik, R., & Yirgu, G. (1996). Helium isotopic variations in Ethiopian plume lavas: nature of magmatic sources and limit on lower mantle contribution. Earth and Planetary Science Letters, 144(1-2), 223-237. https://doi.org/10.1016/0012-821X(96)00158-6

Masotta M, Mollo S, Freda C, Gaeta M, Moore G (2013) Clinopyroxene-liquid thermometers and barometers specific to alkaline differentiated magmas Contrib Mineral Petrol 166(6):1545-1561. ttps://doi.org/10.1007/s00410-013-0927-9

McClusky S, Reilinger R, Ogubazghi G, Amleson A, Healeb B, Vernant P, Sholan J, Fisseha S, Asfaw L, Bendick R, Kogan L (2010) Kinematics of the southern Red Sea-Afar Triple Junction and implications for plate dynamics. Geophys Res Lett 37(5). https://doi.org/10.1029/2009GL041127

McDade, P., Blundy, J. D., & Wood, B. J. (2003). Trace element partitioning on the Tinaquillo Lherzolite solidus at 1.5 GPa. Physics of the Earth and Planetary Interiors, 139(1-2), 129-147. https://doi.org/10.1016/S0031-9201(03)00149-3

McDonough, W. F., & Sun, S. S. (1995). The composition of the Earth. Chemical geology, 120(3-4), 223-253. https://doi.org/10.1016/0009-2541(94)00140-4

McKenzie, D. A. N., & O'nions, R. K. (1991). Partial melt distributions from inversion of rare earth element concentrations. Journal of Petrology, 32(5), 1021-1091. https://doi.org/10.1093/petrology/32.5.1021

Medynski S, Pik R, Burnard P, Dumont S, Grandin R, Williams A, Blard PH, Schimmelpfennig I, Vye-Brown C, France L, Ayalew D, Benedetti L, Yirgu G, ASTER team (2016) Magmatic cycles pace tectonic and morphological expression of rifting (Afar depression, Ethiopia). Earth Planet Sci Lett 446:77-88. https://doi.org/10.1016/j.epsl.2016.04.014

Medynski S, Pik R, Burnard P, Vye-Brown C, France L, Schimmelpfennig I, Whaler K, Johnson N, Benedetti L, Ayalew D, Yirgu G (2015) Stability of rift axis magma reservoirs: Spatial and temporal evolution of magma supply in the Dabbahu rift segment (Afar, Ethiopia) over the past 30 kyr. Earth Planet Sci Lett 409:278-289. https://doi.org/10.1016/j.epsl.2014.11.002

Medynski S, Pik R, Burnard P, Williams A, Vye-Brown C, Ferguson D, Blard PH, France L, Yirgu G, Seid JI, Ayalew D, Calvert A (2013) Controls on magmatic cycles and development of rift topography of the Manda Hararo segment (Afar, Ethiopia): insights from cosmogenic 3He investigation of landscape evolution. Earth Planet Sci Lett 367:133-145. https://doi.org/10.1016/j.epsl.2013.02.006

Meshesha, D., & Shinjo, R. (2008). Rethinking geochemical feature of the Afar and Kenya mantle plumes and geodynamic implications. Journal of Geophysical Research: Solid Earth, 113(B9). https://doi.org/10.1029/2007JB005549

Mittal, T., & Richards, M. A. (2021a). The magmatic architecture of continental flood basalts: 2. A new conceptual model. Journal of Geophysical Research: Solid Earth, 126(12), e2021JB021807. http://doi.org/10.1029/2021JB021808.

Mittal, T., Richards, M. A., & Fendley, I. M. (2021b). The magmatic architecture of continental flood basalts I: Observations from the Deccan Traps. Journal of Geophysical Research: Solid Earth, 126(12), e2021JB021808. https://doi.org/10.1029/2021JB021807.

Mohr, P. (1983). Ethiopian flood basalt province. Nature, 303(5918), 577-584. https://doi.org/10.1038/303577a0

Mollo, S., Del Gaudio, P., Ventura, G., Iezzi, G., & Scarlato, P. (2010). Dependence of clinopyroxene composition on cooling rate in basaltic magmas: Implications for thermobarometry. Lithos, 118(3-4), 302-312. https://doi.org/10.1016/j.lithos.2010.05.006

Morgan, W. J. (1972). Deep mantle convection plumes and plate motions. AAPG bulletin, 56(2), 203-213. https://doi.org/10.1306/819A3E50-16C5-11D7-8645000102C1865D

Muirhead JD, & Kattenhorn SA (2018) Activation of preexisting transverse structures in an evolving magmatic rift in East Africa. J Structural Geol 106:1-18. https://doi.org/10.1016/j.jsg.2017.11.004

Mutch, E. J., Maclennan, J., & Madden-Nadeau, A. L. (2022). The dichotomous nature of Mg partitioning between plagioclase and melt: Implications for diffusion chronometry. Geochimica et Cosmochimica Acta, 339, 173-189. https://doi.org/10.1016/j.gca.2022.10.035

Natali, C., Beccaluva, L., Bianchini, G., & Siena, F. (2011). Rhyolites associated to Ethiopian CFB: clues for initial rifting at the Afar plume axis. Earth and Planetary Science Letters, 312(1-2), 59-68. https://doi.org/10.1016/j.epsl.2011.09.059

Natali, C., Beccaluva, L., Bianchini, G., Ellam, R. M., Savo, A., Siena, F., & Stuart, F. M. (2016). High-MgO lavas associated to CFB as indicators of plume-related thermochemical effects: The case of ultra-titaniferous picrite–basalt from the Northern Ethiopian–Yemeni Plateau. Gondwana Research, 34, 29-48. https://doi.org/10.1016/j.gr.2016.02.009

Neave DA, Putirka KD (2017) A new clinopyroxene-liquid barometer, and implications for magma storage pressures under Icelandic rift zones. Am Mineral 102(4):777-794. https://doi.org/10.2138/am-2017-5968

Neave, D. A., Maclennan, J., Hartley, M. E., Edmonds, M., & Thordarson, T. (2014). Crystal storage and transfer in basaltic systems: the Skuggafjöll eruption, Iceland. Journal of Petrology, 55(12), 2311-2346. https://doi.org/10.1093/petrology/egu058

Nelson, W. R., Furman, T., van Keken, P. E., Shirey, S. B., & Hanan, B. B. (2012). OsHf isotopic insight into mantle plume dynamics beneath the East African Rift System. Chemical Geology, 320, 66-79. https://doi.org/10.1016/j.chemgeo.2012.05.020

Nelson, W. R., Hanan, B. B., Graham, D. W., Shirey, S. B., Yirgu, G., Ayalew, D., & Furman, T. (2019). Distinguishing plume and metasomatized lithospheric mantle contributions to post-flood basalt volcanism on the southeastern Ethiopian Plateau. Journal of Petrology, 60(5), 1063-1094. https://doi.org/10.1093/petrology/egz024

Newcombe, M. E., Plank, T., Zhang, Y., Holycross, M., Barth, A., Lloyd, A. S., ... & Hauri, E. (2020). Magma Pressure-Temperature-time paths during mafic explosive eruptions. Frontiers in Earth Science, 8, 531911. https://doi.org/10.3389/feart.2020.531911

Niida, K., & Green, D. H. (1999). Stability and chemical composition of pargasitic amphibole in MORB pyrolite under upper mantle conditions. Contributions to Mineralogy and Petrology, 135(1), 18-40. https://doi.org/10.1007/s004100050495

Nisbet, E. G., & Pearce, J. A. (1977). Clinopyroxene composition in mafic lavas from different tectonic settings. Contributions to mineralogy and petrology, 63(2), 149-160.

Oppenheimer C, Francis P (1998) Implications of longeval lava lakes for geomorphological and plutonic processes at Erta'Ale volcano, Afar. J Volcanol Geotherm Res 80(1-2):101-111. https://doi.org/10.1016/S0377-0273(97)00041-3

Oppenheimer C, Khalidi L, Gratuze B, Iverson N, Lane C, Vidal C, Sahle Y, Blegen N, Yohannes E, Donovan A, Goitom B, Hammond JOS, Keall E, Ogubazghi G, Mclntosh B, Büntgen U (2019) Risk and reward: explosive eruptions and obsidian lithic resource at Nabro volcano (Eritrea). Quaternary Sci Rev 226:105995. https://doi.org/10.1016/j.quascirev.2019.105995

Pagli, C., Wright, T. J., Ebinger, C. J., Yun, S. H., Cann, J. R., Barnie, T., & Ayele, A. (2012). Shallow axial magma chamber at the slow-spreading Erta Ale Ridge. Nature Geoscience, 5(4), 284-288. https://doi.org/10.1038/ngeo1414

Paton, C., Hellstrom, J., Paul, B., Woodhead, J., & Hergt, J. (2011). Iolite: Freeware for the visualisation and processing of mass spectrometric data. Journal of Analytical Atomic Spectrometry, 26(12), 2508-2518. https://doi.org/10.1039/C1JA10172B

Peccerillo, A., Barberio, M. R., Yirgu, G., Ayalew, D., Barbieri, M., & Wu, T. W. (2003). Relationships between mafic and peralkaline silicic magmatism in continental rift settings: a petrological, geochemical, and isotopic study of the Gedemsa volcano, central Ethiopian rift. Journal of Petrology, 44(11), 2003-2032. https://doi.org/10.1093/petrology/egg068

Peccerillo, A., Donati, C., Santo, A. P., Orlando, A., Yirgu, G., & Ayalew, D. (2007). Petrogenesis of silicic peralkaline rocks in the Ethiopian rift: geochemical evidence and volcanological implications. Journal of African Earth Sciences, 48(2-3), 161-173. https://doi.org/10.1016/j.jafrearsci.2006.06.010

Peccerillo, A., Mandefro, B., Solomon, G., Bedru, H., & Tesfaye, K. (1998). The Precambrian rocks from Southern Ethiopia: petrology, geochemistry and their interaction with the recent volcanism from the Ethiopian Rift Valley. Neues Jahrbuch Für Mineralogie-Abhandlungen, 237-262. https://doi.org/10.1127/njma/173/1998/237

Petrini, R., Joron, J. L., Ottonello, G., Bonatti, E., & Seyler, M. (1988). Basaltic dykes from Zabargad Island, Red Sea: petrology and geochemistry. Tectonophysics, 150(1-2), 229-248. https://doi.org/10.1016/0040-1951(88)90303-4

Pfänder, J. A., Jung, S., Münker, C., Stracke, A., & Mezger, K. (2012). A possible high Nb/Ta reservoir in the continental lithospheric mantle and consequences on the global Nb budget–Evidence from continental basalts from Central Germany. Geochimica et Cosmochimica Acta, 77, 232-251. https://doi.org/10.1016/j.gca.2011.11.017

Pik R, Deniel C, Coulon C, Yirgu G, Marty B (1999) Isotopic and trace element signatures of Ethiopian flood basalts: evidence for plume–lithosphere interactions. Geochim Cosmochim Acta 63(15):2263-2279. https://doi.org/10.1016/S0016-7037(99)00141-6

Pik, R., Deniel, C., Coulon, C., Yirgu, G., Hofmann, C., & Ayalew, D. (1998). The northwestern Ethiopian Plateau flood basalts: classification and spatial distribution of magma types. Journal of Volcanology and Geothermal Research, 81(1-2), 91-111. https://doi.org/10.1016/S0377-0273(97)00073-5

Pik, R., Marty, B., & Hilton, D. R. (2006). How many mantle plumes in Africa? The geochemical point of view. Chemical Geology, 226(3-4), 100-114. https://doi.org/10.1016/j.chemgeo.2005.09.016

Pilet, S., Baker, M. B., & Stolper, E. M. (2008). Metasomatized lithosphere and the origin of alkaline lavas. Science, 320(5878), 916-919. https://doi.org/10.1126/science.1156563

Putirka, K. D. (2008). Thermometers and barometers for volcanic systems. Reviews in mineralogy and geochemistry, 69(1), 61-120. https://doi.org/10.2138/rmg.2008.69.3

Quade, J., Levin, N. E., Simpson, S. W., Butler, R., McIntosh, W. C., Semaw, S., et al. (2008). The geology of Gona, Afar, Ethiopia. Geol. Soc. Am. Bull, 446, 1-31. https://doi.org/10.1130/2008.2446(01)

Robertson, E. A. M., Biggs, J., Cashman, K. V., Floyd, M. A., & Vye-Brown, C. (2016). Influence of regional tectonics and pre-existing structures on the formation of elliptical calderas in the Kenyan Rift. Geological Society, London, Special Publications, 420(1), 43-67. https://doi.org/10.1144/SP420.12

Rogers, N. W. (1993). The isotope and trace element geochemistry of basalts from the volcanic islands of the southern Red Sea. Geological Society, London, Special Publications, 76(1), 455-467. https://doi.org/10.1144/GSL.SP.1993.076.01.24

Rogers, N. W., Davies, M. K., Parkinson, I. J., & Yirgu, G. (2010). Osmium isotopes and Fe/Mn ratios in Ti-rich picritic basalts from the Ethiopian flood basalt province: No evidence for core contribution to the Afar plume. Earth and Planetary Science Letters, 296(3-4), 413-422. https://doi.org/10.1016/j.epsl.2010.05.027

Rooney TO (2010) Geochemical evidence of lithospheric thinning in the southern Main Ethiopian Rift. Lithos 117(1-4):33-48. https://doi.org/10.1016/j.lithos.2010.02.002

Rooney, T. O. (2017). The Cenozoic magmatism of East-Africa: Part I—Flood basalts and pulsed magmatism. Lithos, 286, 264-301. https://doi.org/10.1016/j.lithos.2017.05.014

Rooney, T. O. (2020a). The Cenozoic magmatism of East Africa: part V–magma sources and processes in the East African Rift. Lithos, 360, 105296. https://doi.org/10.1016/j.lithos.2019.105296

Rooney, T. O. (2020b). The Cenozoic magmatism of East Africa: Part IV–The terminal stages of rifting preserved in the Northern East African Rift System. Lithos, 360, 105381. https://doi.org/10.1016/j.lithos.2020.105381

Rooney, T. O., Hanan, B. B., Graham, D. W., Furman, T., Blichert-Toft, J., & Schilling, J. G. (2012b). Upper mantle pollution during Afar plume–continental rift interaction. Journal of Petrology, 53(2), 365-389. https://doi.org/10.1093/petrology/egr065

Rooney, T. O., Herzberg, C., & Bastow, I. D. (2012a). Elevated mantle temperature beneath East Africa. Geology, 40(1), 27-30. https://doi.org/10.1130/G32382.1

Rooney, T. O., Mohr, P., Dosso, L., & Hall, C. (2013). Geochemical evidence of mantle reservoir evolution during progressive rifting along the western Afar margin. Geochimica et Cosmochimica Acta, 102, 65-88. https://doi.org/10.1016/j.gca.2012.08.019

Rooney, T. O., Nelson, W. R., Ayalew, D., Hanan, B., Yirgu, G., & Kappelman, J. (2017). Melting the lithosphere: Metasomes as a source for mantle-derived magmas. Earth and Planetary Science Letters, 461, 105-118. https://doi.org/10.1016/j.epsl.2016.12.010

Rooney, T. O., Nelson, W. R., Dosso, L., Furman, T., & Hanan, B. (2014). The role of continental lithosphere metasomes in the production of HIMU-like magmatism on the northeast African and Arabian plates. Geology, 42(5), 419-422. https://doi.org/10.1130/G35216.1

Rosenthal, A., Foley, S. F., Pearson, D. G., Nowell, G. M., & Tappe, S. (2009). Petrogenesis of strongly alkaline primitive volcanic rocks at the propagating tip of the western branch of the East African Rift. Earth and Planetary Science Letters, 284(1-2), 236-248. https://doi.org/10.1016/j.epsl.2009.04.036

Rossi, M. J., & Gudmundsson, A. (1996). The morphology and formation of flow-lobe tumuli on Icelandic shield volcanoes. Journal of Volcanology and Geothermal Research, 72(3-4), 291-308. https://doi.org/10.1016/0377-0273(96)00014-5

Rudnick, R. & Gao, S. (2003). Composition of the Continental Crust. Treatise Geochem 3:1-64. https://doi.org/10.1016/B0-08-043751-6/03016-4

Salters, V. J., & Longhi, J. (1999). Trace element partitioning during the initial stages of melting beneath mid-ocean ridges. Earth and Planetary Science Letters, 166(1-2), 15-30. https://doi.org/10.1016/S0012-821X(98)00271-4

Sani, F., Ghinassi, M., Papini, M., Oms, O., & Finotello, A. (2017). Evolution of the northern tip of Afar triangle: Inferences from the Quaternary succession of the Dandiero—Massawa area (Eritrea). Tectonophysics, 717, 339-357. https://doi.org/10.1016/j.tecto.2017.08.026

Santarnecchi, E. (1978). Studio chimico e petrografico dei massicci riolitici intercalati nella parte superiore della serie Stratoide (depressione dell'Afar, Etiopia) (single cycle master's degree unpublished thesis). University of Pisa.

Saria, E., Calais, E., Stamps, D. S., Delvaux, D., & Hartnady, C. J. H. (2014). Present-day kinematics of the East African Rift. Journal of Geophysical Research: Solid Earth, 119(4), 3584-3600. https://doi.org/10.1002/2013JB010901

Schilling, J. G., Kingsley, R. H., Hanan, B. B., & McCully, B. L. (1992). Nd-Sr-Pb isotopic variations along the Gulf of Aden: Evidence for Afar mantle plume-continental lithosphere interaction. Journal of Geophysical Research: Solid Earth, 97(B7), 10927-10966. https://doi.org/10.1029/92JB00415

Schmeling, H. (2010). Dynamic models of continental rifting with melt generation. Tectonophysics, 480(1-4), 33-47. https://doi.org/10.1016/j.tecto.2009.09.005

Searle, R. C., & Ross, D. A. (1975). A geophysical study of the Red Sea axial trough between 20· 5° and 22° N. Geophysical Journal International, 43(2), 555-572. https://doi.org/10.1111/j.1365-246X.1975.tb00647.x

Self, S., Keszthelyi, L., & Thordarson, T. (1998). The importance of pahoehoe. Annual Review of Earth and Planetary Sciences, 26(1), 81-110. https://doi.org/10.1146/annurev.earth.26.1.81

Self, S., Schmidt, A., & Mather, T. A. (2014). Emplacement characteristics, time scales, and volcanic gas release rates of continental flood basalt eruptions on Earth. Geological Society of America Special Papers, 505, 319-337. https://doi.org/doi:10.1130/2014.2505(16)

Shaw, D. M. (1970). Trace element fractionation during anatexis. Geochimica et Cosmochimica Acta, 34(2), 237-243. http://dx.doi.org/10.1016/0016-7037(70)90009-8

Sifeta, K., Roser, B. P., & Kimura, J. I. (2005). Geochemistry, provenance, and tectonic setting of Neoproterozoic metavolcanic and metasedimentary units, Werri area, Northern Ethiopia. Journal of African Earth Sciences, 41(3), 212-234. https://doi.org/10.1016/j.jafrearsci.2005.04.004

Singer, B. S., Dungan, M. A., & Layne, G. D. (1995). Textures and Sr, Ba, Mg, Fe, K, and Ti compositional profiles in volcanic plagioclase: clues to the dynamics of calc-alkaline magma chambers. American Mineralogist, 80(7-8), 776-798. https://doi.org/10.2138/am-1995-7-819

Single, R. T., & Jerram, D. A. (2004). The 3D facies architecture of flood basalt provinces and their internal heterogeneity: examples from the Palaeogene Skye Lava Field. Journal of the Geological Society, 161(6), 911-926. https://doi.org/10.1144/0016-764903-136

Smith, P. M., & Asimow, P. D. (2005). Adiabat_1ph: A new public front-end to the MELTS, pMELTS, and pHMELTS models. Geochemistry, Geophysics, Geosystems, 6(2). https://doi.org/10.1029/2004GC000816

Solano, J. M. S., Jackson, M. D., Sparks, R. S. J., Blundy, J. D., & Annen, C. (2012). Melt segregation in deep crustal hot zones: a mechanism for chemical differentiation, crustal assimilation and the formation of evolved magmas. Journal of Petrology, 53(10), 1999-2026. https://doi.org/10.1093/petrology/egs041

Sparks, R. S. J., Annen, C., Blundy, J. D., Cashman, K. V., Rust, A. C., & Jackson, M. D. (2019). Formation and dynamics of magma reservoirs. Philosophical Transactions of the Royal society A, 377(2139), 20180019. https://doi.org/10.1098/rsta.2018.0019

Späth, A., Le Roex, A. P., & Opiyo-Akech, N. (2001). Plume–lithosphere interaction and the origin of continental rift-related alkaline volcanism—the Chyulu Hills volcanic province, southern Kenya. Journal of Petrology, 42(4), 765-787. https://doi.org/10.1093/petrology/42.4.765

Spencer, K. J., & Lindsley, D. H. (1981). A solution model for coexisting iron–titanium oxides. American mineralogist, 66(11-12), 1189-1201.

Stab, M., Bellahsen, N., Pik, R., Quidelleur, X., Ayalew, D., & Leroy, S. (2016). Modes of rifting in magma-rich settings: Tectono-magmatic evolution of Central Afar. Tectonics, 35(1), 2-38. https://doi.org/10.1002/2015TC003893

Steiner, R. A., Rooney, T. O., Girard, G., Rogers, N., Ebinger, C. J., Peterson, L., & Phillips, R. K. (2022). Initial Cenozoic magmatic activity in East Africa: new geochemical constraints on magma distribution within the Eocene continental flood basalt province. Geological Society, London, Special Publications, 518(1), 435-465. https://doi.org/10.1144/SP518-2020-262

Streck, M. J. (2008). Mineral textures and zoning as evidence for open system processes. Reviews in Mineralogy and Geochemistry, 69(1), 595-622. https://doi.org/10.2138/rmg.2008.69.15

Sun, S. S., & McDonough, W. F. (1989). Chemical and isotopic systematics of oceanic basalts: implications for mantle composition and processes. Geological Society, London, Special Publications, 42(1), 313-345. https://doi.org/10.1144/GSL.SP.1989.042.01.19

Tadesse, G., & Allen, A. (2005). Geology and geochemistry of the Neoproterozoic Tuludimtu Ophiolite suite, western Ethiopia. Journal of African Earth Sciences, 41(3), 192-211. https://doi.org/10.1016/j.jafrearsci.2005.04.001

Tazieff H, Marinelli G, Barberi F, Varet J (1969) Géologie de l'Afar septentrional. Bulletin Volcanologique 33(4):1039-1072. https://doi.org/10.1007/BF02597707

Teklay M, Scherer EE, Mezger K, Danyushevsky L (2010) Geochemical characteristics and Sr–Nd–Hf isotope compositions of mantle xenoliths and host basalts from Assab, Eritrea: implications for the composition and thermal structure of the lithosphere beneath the Afar Depression. Contrib Mineral Petrol 159(5):731-751. https://doi.org/10.1007/s00410-009-0451-0

Teklay, M., Scherer, E. E., Mezger, K., & Danyushevsky, L. (2010). Geochemical characteristics and Sr–Nd–Hf isotope compositions of mantle xenoliths and host basalts from Assab, Eritrea: implications for the composition and thermal structure of the lithosphere beneath the Afar Depression. Contributions to mineralogy and petrology, 159(5), 731-751. https://doi.org/10.1007/s00410-009-0451-0

Tesfaye, S., Harding, D. J., & Kusky, T. M. (2003). Early continental breakup boundary and migration of the Afar triple junction, Ethiopia. Geological Society of America Bulletin, 115(9), 1053-1067. https://doi.org/10.1130/B25149.1

Thirlwall, M. F. (2000). Inter-laboratory and other errors in Pb isotope analyses investigated using a 207Pb–204Pb double spike. Chemical Geology, 163(1-4), 299-322. https://doi.org/10.1016/S0009-2541(99)00135-7

Tibaldi, A. (2015). Structure of volcano plumbing systems: A review of multi-parametric effects. Journal of Volcanology and Geothermal Research, 298, 85-135. https://doi.org/10.1016/j.jvolgeores.2015.03.023

Turcotte, D. L., & Emerman, S. H. (1983). Mechanisms of active and passive rifting. In Developments in geotectonics (Vol. 19, pp. 39-50). Elsevier. https://doi.org/10.1016/B978-0-444-42198-2.50010-9

Ustunisik, G., Kilinc, A., & Nielsen, R. L. (2014). New insights into the processes controlling compositional zoning in plagioclase. Lithos, 200, 80-93. https://doi.org/10.1016/j.lithos.2014.03.021

Van Westrenen, W., Blundy, J. D., & Wood, B. J. (2001). High field strength element/rare earth element fractionation during partial melting in the presence of garnet: Implications for identification of mantle heterogeneities. Geochemistry, Geophysics, Geosystems, 2(7). https://doi.org/10.1029/2000GC000133

Varet, J. (1978). Geology of central and southern Afar (Ethiopia and Djibouti Republic) (map and 124 pp. report). Centre Natl. de la Rec. Sci., Paris.

Varet, J. (2018). Geology of Afar (East Africa). Springer. https://doi.org/10.1007/978-3-319-60865-5

Vigny, C., de Chabalier, J. B., Ruegg, J. C., Huchon, P., Feigl, K. L., Cattin, R., ... & Kanbari, K. (2007). Twenty-five years of geodetic measurements along the Tadjoura-Asal rift system, Djibouti, East Africa. Journal of Geophysical Research: Solid Earth, 112(B6). https://doi.org/10.1029/2004JB003230

Villmoare, B., Kimbel, W. H., Seyoum, C., Campisano, C. J., DiMaggio, E. N., Rowan, J., et al. (2015). Early Homo at 2.8 Ma from Ledi-Geraru, Afar, Ethiopia. Science, 347(6228), 1352-1355. https://doi.org/10.1126/science.aaa1343

Volker, F., Altherr, R., Jochum, K. P., & McCulloch, M. T. (1997). Quaternary volcanic activity of the southern Red Sea: new data and assessment of models on magma sources and Afar plume-lithosphere interaction. Tectonophysics, 278(1-4), 15-29. https://doi.org/10.1016/S0040-1951(97)00092-9

Vrba, E. S. (1988). Late Pliocene climatic events and hominid evolution. Evolutionary history of the “robust” australopithecines. In Grine, F.E. (1st ed.), Evolutionary History of the Robust Australopithecines (405-426). Routledge. https://doi.org/10.4324/9780203792667

Walker, G. P. (1991). Structure, and origin by injection of lava under surface crust, of tumuli,“lava rises”,“lava-rise pits”, and “lava-inflation clefts” in Hawaii. Bulletin of Volcanology, 53(7), 546-558. https://doi.org/10.1007/BF00298155

Wang K, Plank T, Walker JD, Smith EI (2002) A mantle melting profile across the Basin and Range, SW USA. J Geophys Res: Solid Earth 107(B1):ECV-5. https://doi.org/10.1029/2001JB000209

Wang, T., Gao, S. S., Yang, Q., & Liu, K. H. (2021). Crustal structure beneath the Ethiopian Plateau and adjacent areas from receiver functions: Implications for partial melting and magmatic underplating. Tectonophysics, 809, 228857. https://doi.org/10.1016/j.tecto.2021.228857

Watanabe, T., Koyaguchi, T., & Seno, T. (1999). Tectonic stress controls on ascent and emplacement of magmas. Journal of Volcanology and Geothermal Research, 91(1), 65-78. https://doi.org/10.1016/S0377-0273(99)00054-2

Watchorn, F., Nichols, G. J., & Bosence, D. W. J. (1998). Rift-related sedimentation and stratigraphy, southern Yemen (Gulf of Aden). In Sedimentation and Tectonics in Rift Basins Red Sea:-Gulf of Aden (pp. 165-189). Springer, Dordrecht. https://doi.org/10.1007/978-94-011-4930-3_11

Watts, E. J., Gernon, T. M., Taylor, R. N., Keir, D., Siegburg, M., Jarman, J., ... & Gioncada, A. (2020). Evolution of the Alu-Dalafilla and Borale volcanoes, Afar, Ethiopia. Journal of Volcanology and Geothermal Research, 408, 107094. https://doi.org/10.1016/j.jvolgeores.2020.107094

Wiart P, Oppenheimer C (2005) Large magnitude silicic volcanism in north Afar: the Nabro Volcanic Range and Ma’alalta volcano. Bull Volcanol 67(2):99-115. https://doi.org/10.1007/s00445-004-0362-x

Wolfenden, E., Ebinger, C., Yirgu, G., Deino, A., & Ayalew, D. (2004). Evolution of the northern Main Ethiopian rift: birth of a triple junction. Earth and Planetary Science Letters, 224(1-2), 213-228. https://doi.org/10.1016/j.epsl.2004.04.022

Wolfenden, E., Ebinger, C., Yirgu, G., Renne, P. R., & Kelley, S. P. (2005). Evolution of a volcanic rifted margin: Southern Red Sea, Ethiopia. Geological Society of America Bulletin, 117(7-8), 846-864. https://doi.org/10.1130/B25516.1

Wright TJ, Ebinger C, Biggs J, Ayele A, Yirgu G, Keir D, Stork A (2006) Magma-maintained rift segmentation at continental rupture in the 2005 Afar dyking episode. Nature 442(7100):291-294. https://doi.org/10.1038/nature04978

Wright TJ, Sigmundsson F, Pagli C, Belachew M, Hamling IJ, Brandsdóttir B, Keir D, Pedersen R, Ayele A, Ebinger C, Einarsson P, Lewi E, Calais E (2012) Geophysical constraints on the dynamics of spreading centers from rifting episodes on land. Nature Geoscience 5(4):242-250. https://doi.org/10.1038/ngeo1428

Wynn, J. G., Roman, D. C., Alemseged, Z., Reed, D., Geraads, D., & Munro, S. (2008). Stratigraphy, depositional environments, and basin structure of the Hadar and Busidima Formations at Dikika, Ethiopia. Geological Society of America Special paper, 446, 87-118. https://doi.org/10.1130/2008.2446(04)

Xu, W., Xie, L., Aoki, Y., Rivalta, E., & Jónsson, S. (2020). Volcano-wide deformation after the 2017 Erta Ale dike intrusion, Ethiopia, observed with radar interferometry. Journal of Geophysical Research: Solid Earth, 125(8), e2020JB019562. https://doi.org/10.1029/2020JB019562

Yang, A. Y., Wang, C., Liang, Y., & Lissenberg, C. J. (2019). Reaction between mid-ocean ridge basalt and lower oceanic crust: An experimental study. Geochemistry, Geophysics, Geosystems, 20(9), 4390-4407. https://doi.org/10.1029/2019GC008368

Yihunie, T., Adachi, M., & Yamamoto, K. (2006). Geochemistry of the Neoproterozoic metabasic rocks from the Negele area, southern Ethiopia: tectonomagmatic implications. Journal of African Earth Sciences, 44(3), 255-269. https://doi.org/10.1016/j.jafrearsci.2005.12.004

Zumbo V, Féraud G, Bertrand H, Chazot G (1995) 40Ar39Ar chronology of Tertiary magmatic activity in southern Yemen during the early Red Sea-Aden rifting. J Volcanol Geotherm Res 65(3-4):265-279. https://doi.org/10.1016/0377-0273(94)00106-Q

Quando mi è capitato di nascere,
la maggior parte dei miei simili si era allontanata da Dio.
E per colmare questo vuoto aveva scelto come nuovo culto
l'umanità con tutti i suoi ideali di libertà e di eguaglianza.
Tuttavia non so se per coscienza o per prudenza,
non riuscendo ad abbandonare completamente Dio,
né ad accettare fino in fondo l'umanità,
siamo rimasti come alla deriva del mondo in quella distanza
aristocratica da tutto comunemente chiamata decadenza.
Insomma siamo nati troppo tardi per Dio
e troppo presto per gli uomini.

G.G.